Modeling of LIBS Spectra Obtained in Martian Atmospheric Conditions

https://doi.org/10.18452/25303

DISSERTATION

zur Erlangung des akademischen Grades
doctor rerum naturalium (Dr. rer. nat.)
im Fach Physik (Spezialisierung Experimentalphysik)

eingereicht an der
Mathematisch-Naturwissenschaftlichen Fakultät
der Humboldt-Universität zu Berlin
von

M.Sc. Peder Bagge Hansen

Präsident (komm.) der Humboldt-Universität zu Berlin:
Prof. Dr. Peter Frensch

Dekan der Mathematisch-Naturwissenschaftlichen Fakultät:
Prof. Dr. Elmar Kulke

Tag der mündlichen Prüfung: 14.07.2022
Gutachter 1: Prof. Dr. Dr.h.c. Heinz-Wilhelm Hübers
Gutachter 2: Prof. Dr. Norbert Esser
Gutachter 3: PhD. Jörg Hermann

Abstract

Laser-induced breakdown spectroscopy (LIBS) is a type of atomic emission spectroscopy method. It is applied to analyse the elemental composition of a sample. It uses a laser pulse to ablate sample material into a luminous plasma. By recording the plasma emissions with a spectrometer, a LIBS spectrum is obtained from which knowledge about the composition of the sample can be gained. The first LIBS instrument in space was realised with the ChemCam instrument onboard the Curiosity rover. Since the rover's landing in 2012, it has explored the Martian surface in the Gale Crater. Due to its successful application, two additional Mars exploration rovers, equipped with LIBS instruments, arrived on Mars in 2021.

Motivated by existing challenges in analysing LIBS spectra and the increasing quantity of Martian LIBS data, this thesis investigates the modelling and simulation of LIBS spectra for the application to LIBS data in Martian atmospheric conditions. This is done with the aim of providing insights into the characteristics of Martian LIBS plasmas as well as developing tools to assist the analysis of real mission data. The modelling of LIBS spectra is based on a stationary plasma in local thermal equilibrium (LTE). The plasma is then divided into a series of homogeneous zones and spectra are simulated using radiative transfer along a one-dimensional line-of-sight through the plasma zones. By fits to synthetic test spectra, it is verified that plasmas with spatial gradients can be well described by a two-zone model. After this verification, the two-zone model is fitted to time-resolved LIBS spectra acquired in experimentally simulated Martian atmospheric conditions. It is found that most of the emissions are well described and that a two-zone model is a significant improvement over a one-zone model. From the fits, typical values of the plasma properties are obtained, and the effect of absorption is estimated to affect the strongest signals by a factor of one hundred. Furthermore, relative concentrations are estimated to within 25 % relative deviations from the reference values.

For the application to time-integrated LIBS data of samples with more complex compositions, a method of spectral unmixing is described and tested. The method consists of solving a system of linear equations between an input spectrum and a superposition of simulated spectra of various temperatures and densities, and some of the most important molecular features extracted from measured LIBS data. The outputs are an overview of the elemental contributions to the LIBS plasma, the temperatures and densities for describing the atomic emissions, and the line identification. From applications to synthetic test spectra and measured LIBS data in experimentally simulated Martian atmospheric conditions, the superposition is shown to describe the data well, with only a limited amount of over-fitting. Additionally, the line identification is verified using the method of multi-element Saha-Boltzmann plots. Finally, the spectral unmixing is applied to a LIBS spectrum from the ChemCam instrument. Although improvements should be done for this specific instrument, the results are promising, and the line-identification is shown to provide important insights into spectral interferences.

The results of this thesis show that spectral modelling based on LTE can be well applied to LIBS data in Martian atmospheric conditions. For time-resolved data, fits of a two-zone model can be used to obtain insights into the plasma as well as improved concentration estimates compared to the Saha-Boltzmann plot method. However, attention to non-equilibrium effects should be given at the earliest and latest stages of the plasma lifetime. For time-integrated spectra, i.e. real mission data, fits of the two-zone model are not feasible due to too long computation times. Instead, a superposition of spectra of different temperatures and densities, i.e. the spectral unmixing method, can be used. Although not directly allowing for quantitative concentration estimates, the method is a great tool to overview the large amount of information contained in the spectra.

Kurzfassung

Laser-induzierte Plasmaspektroskopie (LIBS) ist eine Methode der Atomemissionsspektroskopie und wird verwendet, um die elementare Zusammensetzung einer Probe zu analysieren. Dabei wird mit einem Laserpuls Probenmaterial abgelöst, welches sich zu einem leuchtenden Plasma entwickelt. Aus dem Spektrum der Plasmaemissionen lassen sich Informationen über die Zusammensetzung der Probe gewinnen. Das erste LIBS-Instrument im Weltraum ist das ChemCam-Instrument an Bord des Curiosity-Rovers, der seit seiner Landung in 2012 die Marsoberfläche in Gale Krater untersucht. Aufgrund der Erfolge von ChemCam wurden zwei weitere Mars-Rover ebenfalls mit LIBS-Instrumenten ausgestattet und sind seit 2021 auf dem Mars aktiv.

Wegen der zunehmenden Menge an LIBS-Daten von der Marsoberfläche sowie deren speziellen Herausforderungen bei der Analyse untersucht diese Arbeit, wie die Modellierung und Simulation von solchen LIBS-Spektren genutzt werden kann. Das Ziel ist es, Einblicke in die Eigenschaften von LIBS-Plasmen auf dem Mars zu erhalten und Modelle zu entwickeln, die bei der Analyse von realen Missionsdaten helfen können. Die Modellierung basiert sich auf einem stationären Plasma im lokalen thermischen Gleichgewicht (LTE). Das Plasma wird dabei in eine Reihe homogener Zonen unterteilt und Spektren werden mit dem Strahlungstransfer entlang einer eindimensionalen Sichtlinie durch diese Plasmazonen simuliert. Anhand synthetischer Testspektren mit bekannten räumlichen Temperatur- und Dichteverteilungen innerhalb des Plasmas wird gezeigt, dass solche Plasmen räumlichen Gradienten, durch ein Zwei-Zonen-Modell gut beschrieben werden können. Das Zwei-Zonen-Modell wurde anschließend an zeitaufgelöste LIBS-Spektren, die unter experimentell simulierten Mars Bedingungen gemessen wurden, angepasst. Dabei zeigt sich, dass die meisten Emissionen im gemessenen Spektrum mit der Simulation des Zwei-Zonen-Modells übereinstimmen und eine deutliche Verbesserung gegenübereiner Simulation mit einem Ein-Zonen-Modell zu beobachten ist. Aus den anpassungen ergeben sich typische Werte für die Plasmaeigenschaften. Es kann gezeigt werden, dass Absorption im Plasma insbesondere die stärksten Signale deutlich reduziert, teilweise um einen Faktor 100 oder mehr. Außerdem werden die relativen Konzentrationen mit einer geringen relativen Abweichung von 25 % von den Referenzwerten bestimmt.

Für die Anwendung auf zeitlich integrierte LIBS-Daten von Proben mit komplexeren Zusammensetzungen wird eine Methode der spektralen Entmischung beschrieben und getestet. Die Methode besteht aus der Lösung eines linearen Gleichungssystems zwischen einem Eingangsspektrum und einer Überlagerung von simulierten Spektren, die bei verschiedenen Temperaturen und Dichten berechnet wurden, sowie experimentell gemessenen Spektren von wichtigen Molekülbanden. Die Ergebnisse ermöglichen es, eine Übersicht über die verschiedenen Beiträge zum LIBS-Plasma zu erhalten und erlauben eine schnelle Identifizierung der Emissionslinien. Bei der Anwendung auf synthetische und gemessene LIBS-Testspektren zeigt sich, dass eine gute Übereinstimmung zwischen den Eingangsspektren und der Überlagerung von erzeugten Referenzspektren bereits mit einer geringen Anzahl an Referenzspektren erreicht werden kann. Zusätzlich wurde die Linienidentifizierung mit der Saha-Boltzmann-Plot Methode verifiziert. In einem nächsten Schritt wurde das entwickelte Verfahren der spektralen Entmischung auf ein LIBS-Spektrum, das auf dem Mars mit dem ChemCam-Instrument gemessen wurde, angewandt. Auch wenn das Verfahren noch weiter an die Daten des ChemCam Instruments angepasst werden muss, sind die ersten Ergebnisse vielversprechend und insbesondere die Linienidentifizierung liefert wichtige Erkenntnisse über spektrale Überlagerungen von Emissionslinien.

Die Ergebnisse dieser Arbeit zeigen, dass auf LTE basierende Modelle gut auf LIBS-Spektren angewendet werden können, die unter Marsbedingungen gemessen wurden. Für zeitaufgelöste Daten kann die Anpassung eines Zwei-Zonen-Modells verwendet werden, um Einblicke in das Plasma zu erhalten und um die Elementkonzentrationen mit einer höheren Genauigkeit zu bestimmen, als es mit der Saha-Boltzmann-Methode möglich wäre. Allerdings sollten Nicht-Gleichgewichtseffekte in den frühesten und spätesten Phasen der Plasmalebensdauer berücksichtigt werden. Für zeitlich integrierte Spektren, wie sie bei aktuellen Marsmissionen gemessen werden, sind Anpassungen durch ein Zwei-Zonen-Modell aufgrund von zu langen Rechenzeiten nicht durchführbar. Stattdessen kann durch die Methode der spektralen Entmischung eine Überlagerung von Spektren unterschiedlicher Temperaturen und Dichten verwendet werden. Diese Methode ermöglicht keine direkten quantitativen Bestimmungen der Elementkonzentrationen, ist aber ein hervorragendes Werkzeug, um einen Überblick über die große Menge an Informationen zu erhalten, die in den Spektren enthalten sind.

Contents

List of Abbreviations

CNSA	China National Space Administration
DLR	Deutsches Zentrum für Luft- und Raumfahrt
FOV	The field of view
FWHM	Full width at half maximum
ICCD	Intensified charge-coupled device
LIBS	Laser-induced Breakdown Spectroscopy
LSAW	Laser-supported absorption wave
LTE	Local thermal equilibrium
NASA	National Aeronautics and Space Administration
NELIBS	Nanoparticle enhanced LIBS
nnls	non-negative least squares
RMSE	Root-mean-square-error
RTE	Radiative transfer equation
pLTE	Partial local thermal equilibrium
SNR	Signal-to-noise ratio
UV	Ultraviolet

List of Symbols

A	Dimensionless coefficient for the correction term due to ions in Stark broadening formula
a	Strenght for the correction factor for the intensity response
A_{ik}	Einstein coefficient for spontaneous emission for uppper level i and lower level k
$Al_n^{(m)}$	Signal of the n'th' of the i'th template spectrum of aluminum
b_{instr}	Gaussian function for simulating instrumental broadening
B_{ik}	Einstein coefficient for stimulated emission for uppper level i and lower level k
B_{ki}	Einstein coefficient for absorption for uppper level i and lower level k
c	Speed of light
C_l	Wavelength span of the k'th peak
D	Stark shift parameter
dV	Infinitesimal volume element
dA	cross section of line-of-sight
E_i	Energy of i'th bound state in atom/ion/molecule
E_{rad}	Radiation energy of plasma in thermodynamic equilibrium
E_{exc}	Excitation energy of plasma in thermodynamic equilibrium
E_{ion}	Ionization energy of in thermodynamic equilibrium
E_{kin}	Kinetic energy of plasma in thermodynamic equilibrium
F	Experimental parameter in the description of the signal of emission lines
f	Correction factor for the intensity response
f_{12}	Oscillator strength of the transition from ground-state to first excited state
G	Gauss profile
$\langle \bar{g} \rangle$	Gaunt factor
h	Planck constant
I_λ	Line of sight radiance
$\hat{I}_\lambda$	Simulated spectrum comparable to measured spectrum
$\tilde{I}_\lambda$	Simulated spectrum comparable to measured and intensity calibrated spectrum
IR	Intensity response
$\mathrm{IR}_{\mathrm{rel}}$	Relative intensity response
k_B	Boltzmann constant.
L	Lorentz profile

m	Mass
m_i	Number density of i'th bound state in atom/ion/molecule
M_A	Mass relative to hydrogen atom
$m_{s,z,i}$	Population fraction of the species s in the ionic state z and in the electronic state i
$\tilde{n}$	Relative effective path of a zone in the plasma model
n_e	Electron density
N_D	Number of particles in the Debye sphere
$n_{e,c}$	Critical electron density for the onset of plasma schielding
$\tilde{N}_{\text{guess}}$	Sum of the relative effective path for the elements in the plasma
n_s	Population density of species s
$n_{s,z}$	Population fraction of the species s in the ionic state z
P	Voigt profile
P_{Al}	Template spectrum of aluminium for the unmixing database
$P_{Al,m_1,c_{low}}$	Matrix and concentration specific template spectrum of aluminium for the unmixing database
p_i	Signal of the i'th pixel
$p_{(bg),i}$	Signal of the background level of the i'th pixel
P_j	Signal of the j'th peak
r^2	Weighted squared residuals between simulated spectrum and input spectrum
R^2	Coefficient of determinant
SA	Self-absorption coefficient
s_{Al}	Score for the template spectrum of aluminium for the unmixing database
$s_{Al,m_1,c_{low}}$	Score for matrix and concentration specific template spectrum of aluminium for the unmixing database
s_m	Score of the m'th template spectrum.
T	Temperature
t	Time in seconds
V	Volume
v_{exp}	Expansion speed of plasma
w_i	Weight of the i'th pixel
X_{mj}	Rate of collisions from level m to level j
$Z_{s,z}$	Internal partition function of species s in ionic state z
α	Coefficient for stimulated emission and absorption
$\Delta\chi_z$	Correction to the ionization potential in vaccum due to Coloumb field of charged particles in the plasma
$\Delta\lambda_{Doppler}$	Doppler broadening as FWHM
$\Delta\lambda_{Stark}$	Stark shift
Δx	Length of plasma zone

Δt	Exposure time of a measurement
ϵ_0	Vacuum permittivity
ϵ	Coefficient for spontaneous emission
τ_{rel}	Relaxation time
λ	Wavelength
λ_{rel}	Diffusion length during relaxation time
λ_D	Debye length
Λ_e	Thermal De Broglie wavelength of the electron
$\chi_{s,z}$	Ionization potential of species s in the ionic state z
$\chi^0_{s,z}$	Ionization potential of species s in the ionic state z in vacuum
χ^2	Chi-square value

Chapter 1

Introduction

Laser induced breakdown spectroscopy (LIBS) is a type of atomic emission spectroscopy [1]. It is applied to analyse the elemental composition of a sample and it has recieved a lot of attention for its application in planetary exploration. For a LIBS measurement, a short and powerful laser pulse is focused onto the surface of the sample under investigation. The sample is thereby heated and a small amount of material is ablated into a short-lived plasma. Inside the plasma, atoms, ions, and simple molecules emit photons with energies/wavelengths that are characteristic for its type. These emissions can therefore be said to constitute fingerprints of the elemental composition. By recording the plasma emissions with a spectrometer, a LIBS spectrum is obtained and by analysing the spectrum, knowledge about the elemental composition of the sample can be gained. The process of conducting a LIBS measurement is shown schematically in Figure 1.0.1a and an example of a LIBS spectrum is shown in Figure 1.0.1b,c. In the spectrum a lot of spectrally narrow signals can be seen. These correspond to the light emitted from electron transitions in the atoms/ions. They are referred to as emission lines. Although with varying sensitivity, LIBS can in principle be used to detect any element in the periodic table [2].

A LIBS spectrum can be acquired within a short time. The duration of the laser pulse is typically in the order of nanoseconds and the plasma exists for less than one millisecond, depending on the atmospheric conditions. Usually none or a few repetitions are sufficient to get good signal-to-noise ratios (SNR) and the total time for obtaining a LIBS spectrum is usually limited by the read-out speed of the spectrometer system and/or the repetition rate of the laser. Furthermore, no sample preparation is required and one can therefore perform LIBS measurements of samples in their original context without any additional sampling steps and of targets in any physical state; solid, liquid or gaseous. Last but not least, LIBS can be used for remote sensing of targets up to several meters distance. As an example, remote elemental analysis at distances up to 90 m has been achieved [3]. These characteristics has made LIBS one of the most promising spectroscopic techniques [4]. On the other hand, LIBS is characterized by a low reproducibility. In an in-situ setting, this is partly due to non-fixed experimental parameters such as varying distances and angles between the target and the optics of the setup. But even in a laboratory-setting, where such experimental parameters may be fixed, the signal does not only depend on the concentration of the analyte, but also on the overall composition and aggregation of the sample [5]. Inevitably this complicates and puts high demands to the analysis of the data. Spatial and temporal characterizations of the LIBS plasma, such as temperature and species distributions, provide useful information when analysing the data. Such characteristics, however, depend strongly on the pressure and the composition of the atmosphere wherein the plasma is induced. For example inducing the plasma in inert gases such as helium or argon can be used to enhance certain emission lines or reduce plasma modelling efforts [6, 7].

The first LIBS instrument in space was realized with the ChemCam instrument onboard the Curiosity rover [8]. Since its landing in 2012, the Curiosity rover has explored the Martian surface. Using LIBS, the rover can perform analyses of several targets without repositioning of the rover and of targets inaccessible to its robotic arms such as cliff-sides. Thus, the Curiosity rover has acquired more than 800 000 LIBS spectra of 3000 different targets (as of May 2021 [9]). In 2021, two more LIBS instruments landed on the Martian

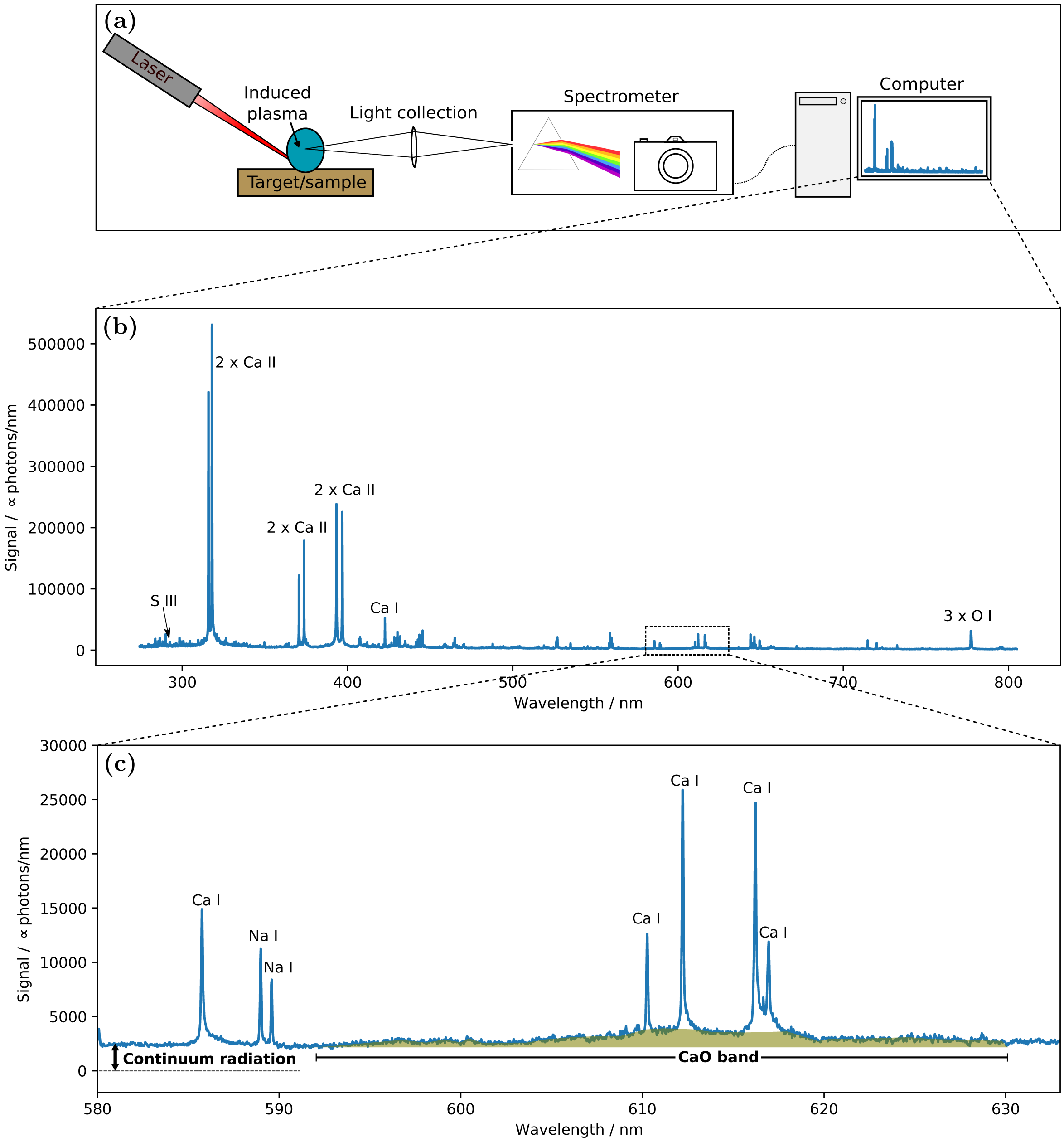

Figure 1.0.1: ***(a)*** *Schematic of the process of conducting a LIBS measurement. From left to right: a short laser pulse is focused onto the surface of the target. The laser induces a plasma and the plasma emissions are collected and recorded with a spectrometer.*
(b) *Example of a LIBS spectrum of a calcium sulfate sample. The spectrum can be seen to contain many spectrally narrow signals. As annotated in the figure, these so called emission lines correspond to the light emitted from electron transitions in specific atoms and ion.* ***(c)*** *Part of the spectrum in (b) shown in a smaller wavelength range. Here, the spectrum can be seen also to contain a background spectrum of continuum emissions as well as emissions from CaO molecules.*

surface. These instruments are equipped on the Mars 2020 Perseverance rover by NASA [10] and the Tianwen-1 Zhurong rover by the China National Space Administration (CNSA) [11]. The addition of two more LIBS instruments on Mars indicates its successful application and also means that even more Martian LIBS data will be acquired in the future. Due to the reduced pressure and different composition of the Martian atmosphere, the many efforts into characterising the plasma in argon or Earth's atmosphere are not directly applicable to Martian LIBS data. Improvements to approaches for analysing Martian LIBS data and insights into the plasma, specifically for Martian atmospheric conditions, are therefore of great value.

Generally, there are two approaches for the analysis of LIBS data. The first one is based on calibration models derived from laboratory LIBS data. In its most primitive form, a univariate calibration model is obtained from the concentration of an element and the signal of a single emission line. But as the signals in a LIBS spectrum is product of several factors, multivariate models are usually preferable [12, 13, 14]. In a multivariate approach, models are derived from larger sets of LIBS spectra of samples with various compositions measured in different sample matrices and possibly under different experimental conditions such as different distances between the sample and the optics of the experiment. The amount of necessary calibration data increases with the variation of the samples to be analysed. For practical reasons, this approach is therefore only applicable to the major elements or to groups of samples with limited compositional variations. A multivariate approach is currently being used for the quantification of the major elements by the ChemCam team [15, 16]. The other approach is based on physical models of the plasma emissions [17]. This approach only relies on the data available in the spectrum under analysis and it is therefore referred to as calibration-free. The approach can be applied for the quantification of both minor and major elements, however uncertainties related to the physical models limit the accuracy of this approach. On the other hand, the involvement of a physical model makes it easier to interpret the results that furthermore can be used for an improved understanding of the data. The most common calibration-free methods are the methods of Boltzmann or Saha-Boltzmann plots [18, 19]. Both methods are based on the identification of emission lines and their relative signals as predicted by the rate of spontaneous emission together with the assumption of a homogeneous plasma. Later proposed methods build upon the aforementioned by also including corrections for absorption of the emitted light inside the plasma [20, 21, 22]. Another and more emerging group of calibration-free methods are based on a more rigorous modelling/simulation of the plasma emissions [6, 23, 24, 25, 26, 27]. The simulations are based on the radiative transfer of the emissions through a model of the plasma. By also including instrumental effects, actual LIBS spectra can be simulated and directly compared or fitted to measured spectra. In the case of fitting, the output usually resembles the plasma density, temperature, and elemental concentrations. Although adding complexity, such rigorous modellings have the advantage of not relying on the assumption of a homogeneous plasma.

In this thesis, modelling and simulation of LIBS spectra are investigated for the application to LIBS data in Martian atmospheric conditions. More specifically, the goal of this thesis is to investigate the following key questions:

- How can LIBS spectra acquired in Martian atmospheric conditions be modelled by simplified models of the plasma?
- What can be learned from the models and what are the implications for the analysis of real mission data?
- How can spectral modelling be used as a tool for assisting the analysis of real mission data?

The structure of the thesis is as follows. In Chapter 2, the theoretical background of LIBS is described. This includes the generation of the plasma, its expansion and decay, and an overview of its characteristic emissions. Also, it includes the description of the thermodynamic state of local thermodynamic equilibrium which can be used for a simplified description of the plasma state. In Chapter 3, the experimental setup used for obtaining the LIBS data of this thesis is presented. Thereafter, the results obtained from characterizing the setup are presented. In Chapter 4, the methods for simulating and fitting LIBS spectra are presented. Then, examples of applications are presented and discussed. The examples of applications include both synthetic test and laboratory LIBS data acquired in experimentally simulated Martian atmospheric conditions. In Chapter 5, a method of spectral unmixing is presented and described. The method has emerged through the efforts described in the previous chapter. It can be applied to a LIBS spectrum in order to obtain fast but more qualitative results. Results from applications to synthetic and real laboratory LIBS data are presented and discussed as well as real mission data from the ChemCam instrument. Chapter 6 summarizes the main results of this thesis and concludes upon them.

Chapter 2

Theoretical Background

In this chapter, the theoretical background for the thesis is described. It starts with an overview of the basics of the LIBS plasma. This includes the plasma formation, expansion, and the characteristic emissions. The second part is about the thermodynamic state local thermal equilibrium (LTE). Herein, it is described how the atomic states and emissions are modelled under the assumption of LTE which form the basis of the later parts of this thesis.

2.1 Basics of LIBS Plasmas

2.1.1 Ablation and Plasma Formation

The first step in conducting a LIBS measurement is the generation of a plasma. The plasma formation starts with the target absorbing the incoming laser pulse. In the case of conducting materials, the incident laser is mainly absorbed by the acceleration of free electrons via the process of inverse Bremsstrahlung [2]. By collisions of the accelerated electrons, lattice atoms are heated and further free electrons are created enhancing the absorption. As phonon relaxation rates are on the order of picoseconds [28], the absorbed optical energy is converted into heat on a similar time scale [29]. In the case of non-conducting targets, the first free electrons are generated by multiphoton absorption and thereafter follows the same scheme as for conducting targets [2].

The subsequent plasma formation depends on the duration, energy, and wavelength of the laser pulse, but it can roughly be described by the processes of vaporization or ablation [30]. At laser irradiances below $\sim 1 \times 10^6\,\mathrm{W/cm^2}$, sample material is melted and vaporized forming a plasma near the sample surface. Due to different vaporization energies, some elements might be over-represented in the plasma compared to the target composition. This is known as elemental fractionization [31]. In LIBS, elemental fracitonization is an unwanted effect because that it makes it impossible, or at least very challenging, to equate the derived elemental composition of the plasma and the target of interest. At higher laser irradiances, around $1\,\mathrm{GW/cm^2}$, the absorbed energy from the laser greatly and quickly exceeds the latent heat of all the constituents of the target. Differences in thermodynamic properties, such as vaporization energies, therefore play a minor role and the composition of the plasma will be more representative of the target. At even higher laser irradiances, $>20\,\mathrm{GW/cm^2}$, the ejection of material is dominated by nonthermal processes and is more explosive in nature. Before the upper surface of the target can vaporize, the underlying layer has also reached the vaporization temperature. This leads to an explosion where sample material is ablated into the surroundings. Due to the wide use of laser ablation (welding, inductively coupled plasma atomic emission spectroscopy, inductively coupled plasma mass spectrometry), elemental fractionization has been widely investigated [31, 32, 33]. The general conclusion is that it can be considered negligible at sufficiently high laser irradiances of $>1\,\mathrm{GW/cm^2}$ [2]. During the plasma formation, the target material is ejected in a cone perpendicular to the target surface [34]. Typically reported values of the amount of ejected material are in the order of ten to hundreds of nanograms, depending on the laser parameters and the properties of the target [28].

The plasma formation is a complicated process where small differences in the targets such as different albedo, surface geometry and sample chemistry affect the resulting LIBS spectra strongly. Such effects are referred to as matrix effects [35, 36]. A great example of matrix effects are in nanoparticle enhanced LIBS (NELIBS). In NELIBS a micro-drop solution containing nanoparticles is deposited on the sample before a standard LIBS measurement is made. The added nanoparticles can contaminate the target negligibly ($<$ 0.04%), but significantly increases the coupling between the laser and the target leading to signal enhancement of certain emission lines by one or two orders of magnitudes [37]. In NELIBS this is a wanted effect, but for LIBS in general, such characteristics complicate the analysis and put high demands on calibration models. This is particularly true for analysing geological samples because of the high variety of minerals and rocks.

Due to the fast conversion of the optical energy of the laser into heat, the plasma is formed long before the end of a nanosecond laser pulse which is typically used for the plasma formation [29]. During the first part of the plasma formation, the induced plasma will be transparent to the incoming laser, but as more material is ejected the plasma can reach a critical electron density [1] given by

$$n_{e,c} \sim \frac{10^{27}}{\lambda^2} \,, \tag{2.1.1}$$

where $n_{e,c}$ is the critical electron density in m^{-3} and λ is the laser wavelength in microns. At the critical electron density, the plasma becomes opaque to the laser pulse and the remaining laser pulse is partially absorbed by the plasma and does not contribute to material removal. Instead, it is converted into heat inside the already formed plasma. This effect is known as plasma shielding and is especially well observed in breakdown of gases as an elongated shape of the plasma along the focal cone of the incoming laser [2, 38]. According to equation (2.1.1), the onset of plasma shielding depends on the wavelength of the laser. But as the electron density is affected by the amount of ablated material and the deposited energy, the onset of plasma shielding is a product of several factors. The effect of plasma shielding has been studied by pump-probe experiments. For nanosecond lasers with energies in the mJ range, 30% to 80% of the laser energy is usually absorbed in the plasma [39, 40].

2.1.2 Plasma Evolution and Characteristics

Due to the high internal pressure [41], the formed plasma expands with velocities exceeding the speed of sound [42]. From the expansion, a layer of compressed ambient gas forms a shock wave that propagates into the ambient gas. As the plasma expands, the internal pressure decreases and the expansion slows down. After some time, the shock wave therefore decouples from the plasma and transitions into the ambient gas and later degenerates into a sound wave. This is what produces the audible crack that is heard when conducting a LIBS measurement in non-vacuum conditions [43]. Eventually, the plasma stops expanding and is in a stage of confinement. In this stage, the dominant cooling effect transitions from adiabatic cooling to heat exchange with the background gas and radiative cooling [42, 44]. Finally, the plasma material re-solidifies and the plasma ends. The evolution of the plasma is shown schematically in Figure 2.1.1 with the approximate times scales for a plasma induced in Martian atmospheric conditions (0.7 kPa of mainly CO_2) with a nanosecond laser. The evolution and the different stages of the plasma are roughly universal, but the time scales and the internal structure (temperature and density profiles) vary strongly with the ambient atmospheric conditions, where especially the pressure has a big impact [6, 44, 45, 46, 47]. A heavy atmosphere works as walls confining the plasma. This results in a smaller, but longer lived plasma compared to plasmas in reduced pressure. For example, the plasma in Martian atmospheric conditions is roughly ten times bigger than in terrestrial conditions [48]. In [44], the influence of the pressure on the size of the LIBS plasma was studied systematically. At a pressure of 13 kPa the plasma expansion continued until ∼250 ns reaching a size of ∼2 mm. Reducing the pressure by a factor of ten, the expansion continued until ∼1500 ns reaching a size of 7 mm.

As a first approximation, the plasma expansion can be described by the Sedov point-blast model [49]. In the model, the expansion is driven by a large amount of energy deposited instantaneously in an infinitesimal small volume. The description is therefore only applicable when the pulse length and focal area of the laser are small compared to the dimensions of the plasma. Consequently, the earlier stage of the expansion is more

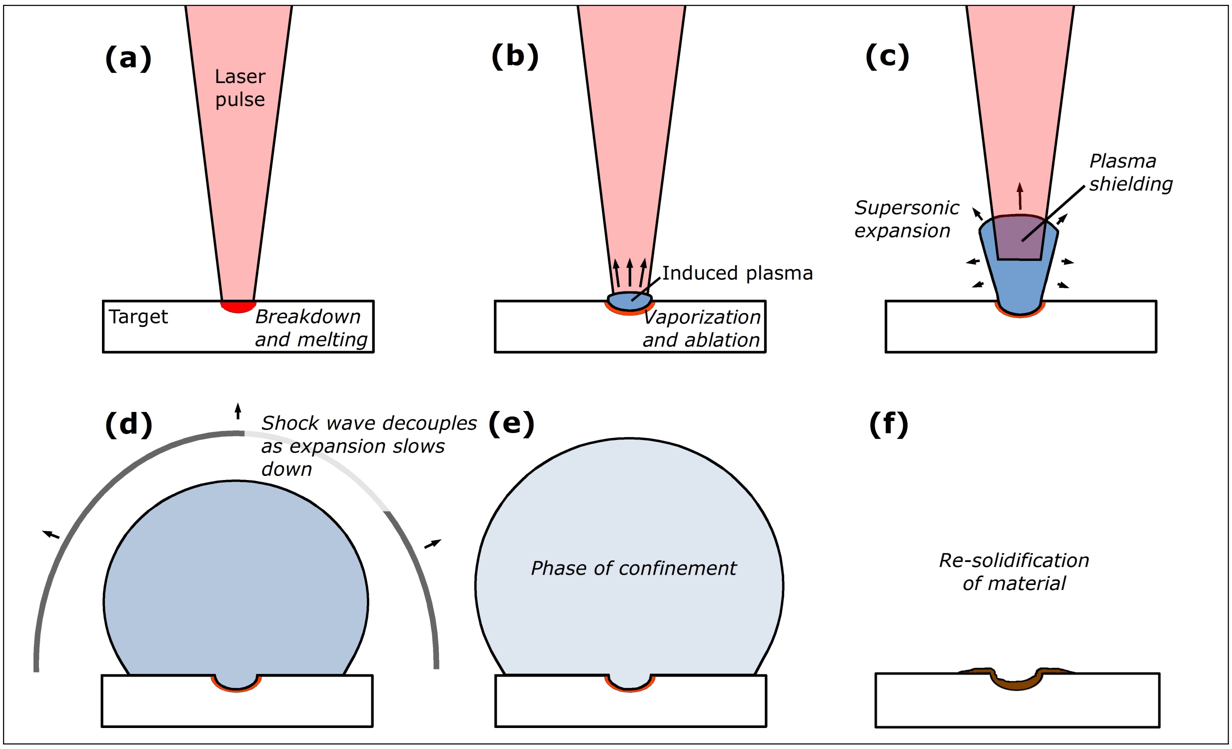

Figure 2.1.1: *Schematic of the evolution of a laser induced plasma in an atmosphere.* ***(a)*** *The incident laser breakdown and heats target material.* ***(b)*** *Material is vaporized and ablated into a plasma.* ***(c)*** *Due to the high internal plasma, the plasma expands supersonically into the background atmosphere. The remaining laser pulse is mostly absorbed by the already formed plasma.* ***(d)*** *As the pressure in the plasma decreases and simultaneously builds up in the compressed background, the expansion slows down and the shock wave decouples from the plasma.* ***(e)*** *The plasma expansion has slowed down further and the plasma now mostly cools of due to heat transfer.* ***(f)*** *The plasma has re-solidified.*

accurately described as a laser-supported absorption wave (LSAW) that includes the absorption of the incident laser in the already formed plasma, i.e plasma shielding [49, 50].

Many insights into the evolution and characteristics of the plasma have been obtained from hydrodynamic simulations of the plasma expansion and by time and space resolved measurements [51, 52, 53, 54, 55]. But the plasma evolution and its characteristics are a product of many different processes and vary with the experimental parameters. For plasmas induced with nanosecond lasers in the ultraviolet, the background gas is evacuated and pushed away by the formed plasma containing mostly target material. Using infrared lasers, the background gas is effectively mixed with the target material and the plasma is a little bigger with a slightly lower temperature [56]. The difference arises because of different rates of plasma shielding. In [57] the plasma expansion from a copper target into a 100 kPa pressure helium gas was simulated by a one-dimensional gas-dynamic model using a thermodynamic approach. The expansion model was coupled to a model for the plasma formation by a UV nanosecond laser. Their results include spatial profiles of target material, background gas, expansion velocities, and of the temperatures. A schematic of their obtained density and temperature profiles around 100 ns are shown in Figure 2.1.2. For enhancing the description of the profiles, the plasma has been divided into three regions according to the density of the copper atoms from the target and the background helium gas. A plume region from 0 mm to 0.6 mm containing only target material, a mixing region from 0.6 mm to 1 mm containing both target material and the background gas, and a background region from 1 mm and outwards containing only the background gas. The shock front is located at the position of maximum density inside the background region. The maximum temperature, of ~25 000 K was found to be in the mixing region. The temperature then decreases inwards towards the target surface and outwards towards the background region. At earlier times, 20 ns (not shown here), the maximum temperature was found in the plume and monotonically decreasing towards the background region and with a relatively smaller mixing region. The location of the maximum temperature is affected by the amount of plasma shielding that has the effect of shifting the location inwards towards the plume region. If plasma shielding is not considered, the maximum temperature would be located at the position of the shock front in the background region. In the case of an argon background gas at 50 kPa using a nanosecond UV laser, Hermann et. al. [6], showed that the plasma plume, containing the target material, was homogeneous and with all the temperature gradients in the background region. This allows for a simple description of the plasma plume and is one of the reasons why LIBS measurements sometimes are performed in an argon background gas. The homogeneity of the plasma plume was argued to be caused by the isolating properties of argon (mostly elastic collisions with elements from target materials due to large spacing between ground and first excited state of Ar I). There are not many modeling or experimental papers reporting about the internal structure of the LIBS plasma in Martian atmospheric conditions, but the thinner atmosphere is likely to be less isolating than that of argon. First results from spatially and temporally resolved measurements of LIBS plasmas induced in experimentally simulated Martian atmospheric conditions also indicate a more in-homogeneous plasma similar to that of Figure 2.1.2 [58].

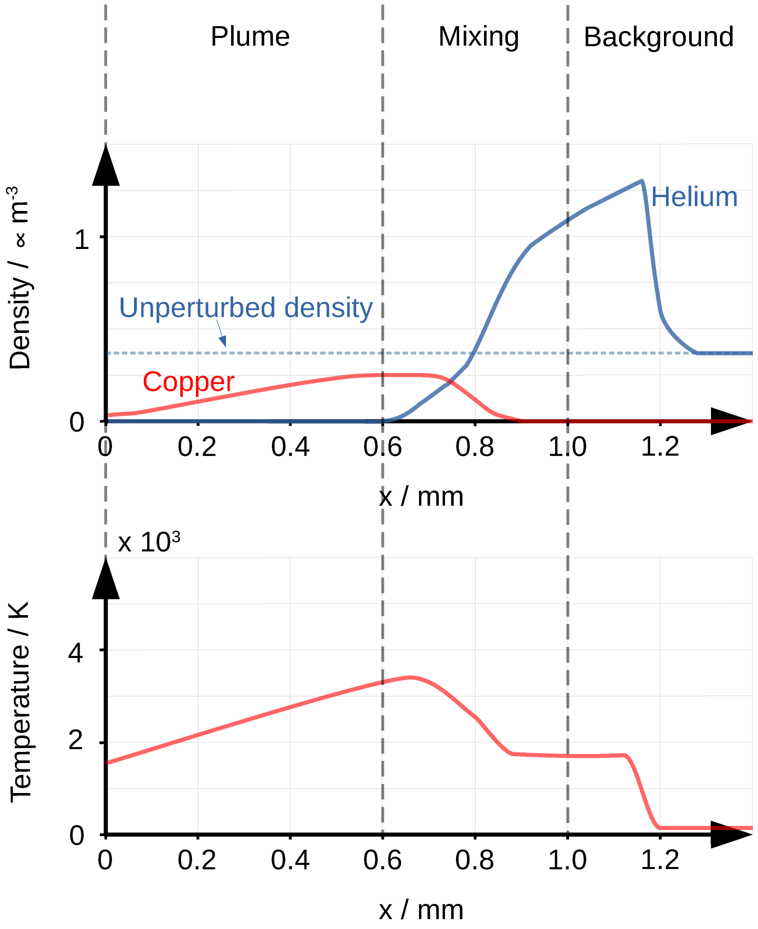

Figure 2.1.2: *Schematic representation of plasma density profiles (top) and temperature (bottom) at* ∼ 100 *ns after initiation of the laser. The profiles were obtained from the numerical simulation of the plasma formation of a copper target and the following expansion into a one atmospheric pressure helium background gas using a one dimensional gas-dynamics model [52]. As indicated by the density profiles, the background gas is evacuated from the plume region by the expanding copper vapour. The maximum temperature is found near in the mixing region, containing both copper and helium particles, and seen to decrease inwards towards the core region and outwards the background region.*

2.1.3 Plasma Emissions

The plasma consists of free electrons, ions, neutral atoms, and simple molecules. They all contribute to the emissions from the plasma. By the deceleration of free electrons in the plasma, typically in the vicinity of an ion, the electrons lose kinetic energy which is converted into radiation by the emission of photons. This is known as bremsstrahlung [2]. As the electron is free before and after the deceleration, bremsstrahlung is considered as a free-free transition. By the capture of a free electron, by typically a negative ion in the plasma, the excess kinetic energy can also be converted into radiation. This is known as recombination radiation [2]. As the electron is free before and bound in an ion or atom afterwards, such recombination can be considered as a free-bound transition. Finally, bound electrons inside atoms, ions, or molecules can make transitions between bound states and the excess energy can be converted into radiation by the emission of a photon. The emission spectra from bremsstrahlung and recombination are continuous and have little spectroscopic interest compared to the spectrally narrow emissions from the bound-bound transitions. The continuum spectra are therefore usually not exploited in the analysis of a LIBS spectrum. Instead, they are considered as an unwanted side effect. As both the spectra from bremsstrahlung and recombination depend on the square of the electron density, they are mostly observed in the early stage of the plasma and are usually removed in the pre-processing of the LIBS spectra or gated out in the experiment by applying a delay between the firing of the laser and the opening of the camera [59]. A schematic of the optical signal from a typical LIBS plasma is shown in Figure 2.1.3.

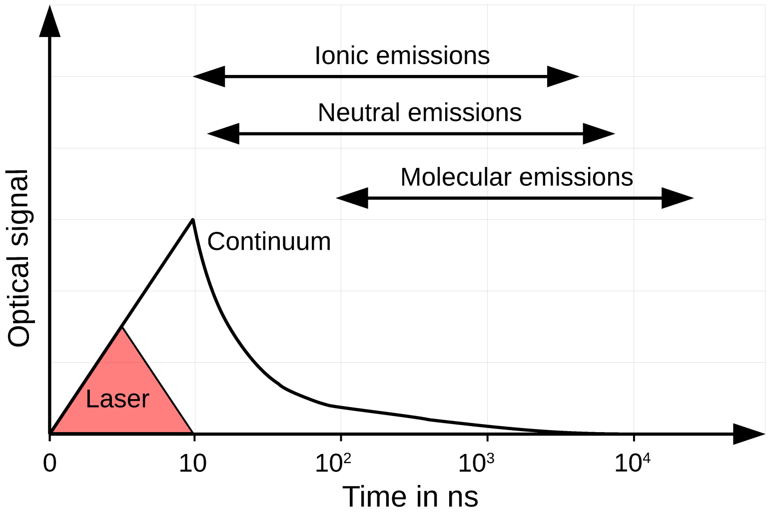

Figure 2.1.3: *Schematic of the optical signal from the plasma. During the first tens of nanoseconds, the plasma emission is dominated by continuum emission from recombination and bremsstrahlung. The continuum decays fast and the optical signal becomes dominated by ionic and neutral emissions from bound-bound transitions. Later, as the plasma cools further, simple molecules might form and also contribute to the optical signal.*

The emission and absorption of photons from the bound-bound transitions of ions, atoms or molecules are described by Einstein's radiation theory [60]. The processes involved are spontaneous emission, stimulated emission, and absorption. The processes are shown schematically in Figure 2.1.4 for a transition involving a bound state/level with an upper energy E_2 and lower energy E_1. As the bound states have well defined energies, the photons involved in these processes will also have well defined energies. This results in the characteristic and almost discrete emission lines in the LIBS spectra as exemplified in Figure 1.0.1b and c in the previous chapter. The rates of the processes are given by the Einstein coefficients that are due to intrinsic properties of the atoms/molecules only. The rate of generation of photons by spontaneous emission from the upper level E_2 to the lower level E_1 in a small volume, dV, of the plasma is

$$\frac{dI_{2\to1}}{dt} = m_2 \cdot A_{21} \cdot dV \ , \tag{2.1.2}$$

where A_{21} is the Einstein coefficient for spontaneous emission and m_2 is the population of the upper electronic level. A_{21} is equal to the probability per unit time for an electron to spontaneously decay from level E_2 to E_1 by the emission of a photon with energy $E_2 - E_1$.
The rate of generation of photons by stimulated emission is

$$\frac{dI_{2\to1}}{dt} = m_2 \cdot B_{21} \cdot \rho_{21} \cdot dV \ , \tag{2.1.3}$$

where B_{21} is the Einstein coefficient for stimulated emission and ρ_{21} is the spectral energy density of radiation with energies equal to the spacing between the two levels. B_{21} is the probability per unit time per unit spectral energy density that an electron in state E_2 decays to E_1 by the emission of a photon with energy $E_2 - E_1$.
The rate of generation of photons by absorption is

$$\frac{dI_{1\to2}}{dt} = -m_1 \cdot B_{12} \cdot \rho_{21} \cdot dV \ , \tag{2.1.4}$$

where B_{12} is the Einstein coefficient for absorption and m_1 is the number density of electrons in the level

E_1. B_{12} is the probability per unit time per unit spectral energy density that an electron in state E_1 absorbs a photon with energy $E_2 - E_1$ by jumping to the upper state E_2. The rate is negative since photons are absorbed. The Einstein coefficients for absorption and stimulated emission are equal in magnitude, but as the upper levels typically are less populated than the lower levels, the amount of stimulated emission is usually smaller.

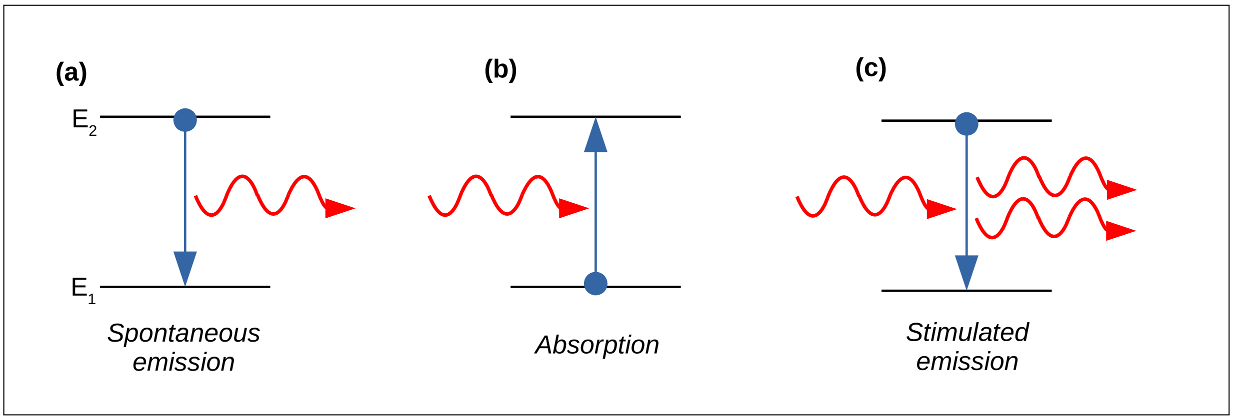

Figure 2.1.4: *Schematic drawing of the processes of **(a)** spontaneous emission, **(b)** absorption, and **(c)** stimulated emission.*

Due to the Heisenberg uncertainty principle, the photons emitted via bound transitions in an isolated atom or ion will have a small but finite line width. It is related to the inverse of the lifetime of the transition and is in the order of 1×10^{-5} nm for the stronger transitions. However, in LIBS plasmas that have a high temperature and a high pressure, Doppler and collisional broadening dominate the line profiles. Doppler broadening is caused by the Doppler shift in combination with thermal motion of the particles. It is described by a Gaussian profile with a full width at half maximum (FWHM) of [28]

$$\Delta\lambda_{Doppler} = \sqrt{\frac{8k_B \ln(2)}{mc^2}} \cdot \lambda_0 \ , \tag{2.1.5}$$

where k_B is the Boltzmann constant, m the mass of the emitting particle, c the speed of light, and λ_0 the center wavelength. Collisional broadening is broadening by collisions of charged particles in the plasma. This is called Stark broadening and caused by the Stark effect which is the electric analogue to the Zeeman effect [61]. The line profile due to Stark broadening is described by a Lorentzian profile. The Stark broadening is accompanied by a shift in center wavelength of the transition. The shift is usually a red shift and smaller than the width of the broadening. In the impact approximation the Stark broadening as the FWHM of a Lorentzian is given by[28]:

$$\Delta\lambda_{Stark} = \left[1 + 1.75A\left(1 - 4/3N_D^{-1/3}\right)\right] W_{\mathrm{FWHM}} \left(\frac{n_e}{10^{16}cm^{-3}}\right) \ , \tag{2.1.6}$$

where A is a dimensionless coefficient a correction term due to ions, N_D is the number of particles in the Debye sphere, n_e the electron density, and W_{FWHM} the impact broadening from electrons. A and W_{FWHM} are independent of the electron density and are slowly varying with the temperature. Neglecting the correction term for ions, the Stark broadening is proportional to the electron density and the shift is given by [28]

$$\Delta\lambda_{shift} \sim D\left(\frac{n_e}{10^{16}m^{-3}}\right) \ , \tag{2.1.7}$$

where D is the Stark shift parameter. A great amount of work in calculating and tabulating Stark broadening and shift parameters has been performed by Griem and Sahal-Bechot. The values are available at [62, 63]. Together the two databases cover the emission lines from many elements, but there are important emission lines not contained therein. The weak temperature dependence of the Stark parameters and the linear relation with the electron density, allow for the use of experimentally found Stark parameters (W_{FWHM} in equation (2.1.6) and D in (2.1.7)) and extrapolating the values to the relevant electron densities [64]. Reversely, the widths or shifts of an emission line can be used for determining the electron density when the Stark parameters are known. Combining the Doppler and the Stark broadening, the resulting line profile is obtained as a convolution of a Gaussian and a Lorentzian profile. It is called a Voigt profile and defined as

$$P(x) = \int_{-\infty}^{+\infty} L(x-u) \cdot G(u) \ du \ , \tag{2.1.8}$$

where L is the Lorentzian and G the Gaussian profile. The line profiles are normalized such that

$$\int_{-\infty}^{+\infty} P(\lambda) \ d\lambda = \int_{-\infty}^{+\infty} G(\lambda) \ d\lambda = \int_{-\infty}^{+\infty} L(\lambda) \ d\lambda = 1 \ . \tag{2.1.9}$$

2.2 Local Thermodynamic Equilibrium

2.2.1 Overview and Criteria

A detailed description of the plasma state involves knowledge about the population of bound electronic states of atoms and molecules and the states of the free electrons. Such information allows for the prediction of the plasma emission by the processes described in the previous section and is therefore necessary when modelling the plasma emissions and when simulating LIBS spectra. A detailed description of the plasma can in general be achieved by a complete kinetic description of the population and depopulation of states. This would involve all the relevant processes in the plasma, i.e. ionization by collisions, photo ionization, radiative and three-body recombination, collisional excitation/de-excitation processes, radiative decay, photo excitation and Bremsstrahlung processes [65]. In principle, the kinetic description should contain the complete history of the plasma, i.e. start at the moment where the first photons of the laser interacts with the target. This kind of description is therefore very complex and has, at the moment, little practical but mostly theoretical significance. Alternatively, a thermodynamic approach can be used for the detailed description of the plasma. The thermodynamic approach applied to the highly transient LIBS plasma is in the best case a good approximation, but due to its simplicity it is usually favoured over a kinetic description [66]. The big benefit of a thermodynamic approach is, that one does not need to consider the complete history of the plasma. Instead the plasma can, at a given time and position, be completely described statistical physics and a few thermodynamic parameters that can be derived from its spectrum.

If a plasma is in thermodynamic equilibrium, the population fractions of atomic and molecular electronic states are given by the Boltzmann distribution and the population ratio of two consecutive ionic states are given by the Saha-equation. Both as functions of the plasma temperature and electron density. The photon-energy-density is given by the Planck radiation curve which describes the radiation emittted from a blackbody. In units of $Wsr^{-1}m^{-3}$, and as a function of the wavelength λ, the Planck radiation curve is [2]

$$B(\lambda) = \frac{2hc^2}{\lambda^5} \frac{1}{\exp\left(\frac{hc}{\lambda k_B T_\lambda}\right) - 1}, \tag{2.2.1}$$

where h is Planck's constant, c is the speed of light, and λ the wavelength. As clearly indicated by the observation of the emission lines (see Figure 1.0.1, Chapter 1), the spectrum of a LIBS plasma is not that of a blackbody and the radiation is decoupled from any potential thermodynamic equilibrium. The decoupling is because that the mean free paths of the photons are larger than the dimensions of the plasma. The lack of absorptions in the plasma inevitably also affect the equilibrium distributions of the material of the plasma. Furthermore, the plasma is far from stationary and homogeneous and the macroscopic parameters such as its size and energy change rapidly. However, if the lack of excitation from absorption is negligible compared to excitations from collisions and if the macroscopic parameters change sufficiently slow throughout time and space, the state of the plasma material can still be well approximated by the standard equilibrium distributions by local and time dependent values of the temperature and densities. Such state is known as local thermodynamic equilibrium (LTE) [67]. The validity of the approximation of LTE in a plasma can be quantified by different criteria [65]. In an ionized plasma, the collisional excitation and ionization processes are dominated by interactions with free electrons. Classically this can be explained by the exchange of energy during collisions being much more efficient for particles of similar masses and that collisions of free electrons with bound electrons can be viewed as an electron-electron interaction. The criteria for LTE therefore all depend on the electron density. The first criterion is related to the escape of radiation/lack of absorption. It states that the rate of collisional processes from level m to higher levels should be ten times greater than the radiative decay from higher levels to the level m [65]

$$n_m \sum_{j>m} X_{mj} > 10 \cdot \sum_{j>m} n_j A_{jm} \ , \tag{2.2.2}$$

where n_m is the number density of the level m, X_{mj} the rate of collisions from level m to level j, and A_{jm} the Einstein coefficient for spontaneous emission. By applying some approximations, the inequality can be simplified to obtain the McWhirter criterion [65]

$$n_e > 1.6 \cdot 10^{-6} \cdot T^{1/2} \cdot (\Delta E)^3 \ , \tag{2.2.3}$$

where n_e is the electron density in m^{-3} and ΔE is the largest span between the two adjacent electronic levels of the considered atomic or ionic species and given in eV. The $(\Delta E)^3$ dependence is there since collisional cross section decreases as $1/\Delta E$ and optical transition increases as $(\Delta E)^2$. Choosing the largest span between two adjacent levels for ΔE therefore corresponds to the set of levels that is the most difficult to sustain in equilibrium when radiation escapes. As the spacing in energy between the levels usually decreases for higher excited levels, the ground state and the first excited stable state of the considered species is usually used such that $\Delta E = \Delta E_{21}$. If the electron density is lower than given by the McWhirter criterion, one can expect an overpopulation of the ground state with respect to the Boltzmann distribution. However, Boltzmann equilibrium might still be established among the higher excited levels. Such state is known as partial local thermodynamic equilibrium (pLTE) [65]. A second criterion for the possible existence of LTE is related to the transient nature of the LIBS plasma. This criterion states that the temporal variation of the plasma temperature and electron density should be low compared to the time for establishing equilibrium, i.e. the relaxation time

$$\frac{T(t+\tau_{rel}) - T(t)}{T(t)} << 1 \quad \& \quad \frac{n_e(t+\tau_{rel}) - n_e(t)}{n_e(t)} << 1, \tag{2.2.4}$$

where τ_{rel} is the relaxation time. A rough estimate on the relaxation time is given in [65] by equating it with the characteristic time of the slowest process. The slowest process is argued to be the collisional excitation of the ground state to the first excited state. The relaxation time is then given as

$$\tau_{rel} \sim \frac{6.3 \cdot 10^4}{n_e f_{12} \langle \bar{g} \rangle} \Delta E_{21} (k_b T)^{1/2} \exp\left(\frac{\Delta E_{21}}{k_b T}\right), \tag{2.2.5}$$

where f_{12} is the oscillator strength of the transition from ground-state (1) to first excited state (2) and $\langle \bar{g} \rangle$ is the Gaunt factor. ΔE_{12} and k_b are given in eV/K. A third criterion is the spatial analogue to equation (2.2.4). It states that the spatial variation of the plasma temperature and electron density should be low compared to the diffusion of particles during the relaxation time

$$\frac{T(x+\lambda_{rel}) - T(x)}{T(x)} << 1 \quad \& \quad \frac{n_e(x+\lambda_{rel}) - n_e(x)}{n_e(x)} << 1, \tag{2.2.6}$$

where λ_{rel} is the diffusion length during the time of relaxation and x is a measure of length. A rough estimate of the diffusion length during the relaxation time is again given in [65] as

$$\lambda_{rel} \sim 1.4 \cdot 10^{12} \frac{(k_b T)^{3/4}}{n_e} \left(\frac{\Delta E_{21}}{M_A f_{12} \langle \bar{g} \rangle} \right)^{1/2} \exp\left(\frac{\Delta E_{21}}{2 k_b T} \right), \tag{2.2.7}$$

where M_A is the relative mass of the considered species such that $M_{hydrogen}$ would be equal to one. The criteria in equation (2.2.4) and (2.2.6) are preferably rewritten by decay times and lengths

$$T/\left(\frac{dT}{dt}\right) >> \tau_{rel} \quad \& \quad n_e/\left(\frac{dn_e}{dt}\right) >> \tau_{rel} \ \text{ and} \tag{2.2.8}$$

$$T/\left(\frac{dT}{dx}\right) >> \lambda_{rel} \quad \& \quad n_e/\left(\frac{dn_e}{dx}\right) >> \lambda_{rel} \ , \tag{2.2.9}$$

where $T/\left(\frac{dT}{dt}\right)$ is the decay time and $T/\left(\frac{dT}{dx}\right)$ is the decay length of the temperature. They can be estimated from time and space resolved measurements of the temperature and electron density or roughly put equal to the plasma lifetime and the length of the plasma. If the criteria of equation (2.2.3), (2.2.8), and (2.2.9) are all satisfied in the plasma, it is likely that the state of LTE provides a good approximation and that the standard equilibrium distribtions can be used for the material of the plasma. From the criteria it is seen that a high electron density favors the existence of LTE. Towards the end of the plasma lifetime, the existence of LTE therefore seems unlikely due to the plasma becoming more and more neutral. In the beginning of the plasma lifetime the highest electron densities are found, but on the other hand the plasma also evolves more rapidly. The existence of LTE in a LIBS plasma is therefore not trivial and depends on the experimental conditions and times after plasma initiation. But, generally the higher the density and the slower the expansion speed is, the more likely it is that LTE is a good description. For LIBS plasmas induced in reduced pressures, such as in Martian atmospheric conditions, the fulfillment of the criteria therefore seem more difficult to fulfill due to the higher expansion speed and consequently lower density. Furthermore, the validity of LTE depends on the considered species via the ΔE terms. Metallic elements, are usually characterized by a low spacing of energy between adjacent levels. Consequently, the criteria are easily fulfilled in most plasmas. This is opposite to non-metals such as oxygen. For example, the value for ΔE to be used for neutral and singly ionized magnesium are 4.3 eV and 4.4 eV, respectively. The values for neutral and singly ionized oxygen are 9.5 eV and 9.9 eV, respectively. In a plasma, typical for martian atmospheric conditions in the confinement phase, of an electron density of $5 \times 10^{22}\,\mathrm{m}^{-3}$, electron temperature of 10 000 K, the relaxation time for neutral magnesium would be a few nanoseconds. The relaxation time for neutral oxygen would be around 15 milliseconds. The decay time of a Martian plasma is smaller than 1 milisecond and it is clear that the criterion of equation (2.2.8) would be easily satisfied for neutral magnesium whereas it would not be satisfied for neutral oxygen. For the McWhirter criterion, a minimum electron density for neutral magnesium would be $1.3 \times 10^{22}\,\mathrm{m}^{-3}$ and $1.4 \times 10^{23}\,\mathrm{m}^{-3}$ for neutral oxygen. The McWhirter criterion is therefore also easier satisfied for magnesium than for oxygen. The transitions used for the ΔE in the McWhirter criterion for magnesium and oxygen are the resonance transitions at 285 nm and 130 nm, respectively. They are both prone to self-absorption and the McWhirter criterion, calculated for optical thin conditions, might therefore be relaxed by a factor between one and ten depending on the amount of self-absorption. The discussion until now has been based on a Maxwellian velocity distribution of the free electrons in the plasma. The relaxation time for this is on the order of picoseconds and therefore very fast [28]. A Maxwellian distribution for the electrons therefore seem easily satisfied. The relaxation time for establishing equilibrium between the velocities of electrons and heavy particles is much longer and in the order of $0.01\,\mu$s to $1\,\mu$s [28]. As the excitation and de-excitation processes are dominated by the free electrons, deviation between the velocity distributions of electrons and heavy particles will have negligible effect on the distribution of the bound states of the material species.

The criteria given for the possible existence of LTE are thresholds based on appxromations [65]. If more accurate results are sought, where also the degree of departure is addressed, kinetic models of the plasma state are preferable. Such studies are found in [68] and [69]. In the latter, LTE is addressed by kinetic modelling of aluminium and tungsten states coupled to a simplified model of a laser induced plasma expanding in an argon background at two different pressures, 10 Pa and 1×10^5 Pa. By fitting the Boltzmann distribution, expected at LTE, to the atomic states predicted by the kinetic model, the departure from LTE was investigated. For the low pressure case, excitation equilibrium breaks down after ∼100 ns. At the higher pressure, the excitation equilibrium is maintained until ∼10 µs, but with a small and relatively short departure around 100 ns due to the fast plasma dynamics.

2.2.2 Calculation of Atomic State Distributions

Assuming LTE, the fraction $m_{s,z,i}$ of atomic states of the elemental species s in the ionic state z ($z = 0$ for neutrals) found in the electronic state i can be calculated from the Boltzmann distribution as function of the plasma temperature T and electron density n_e

$$m_{s,z,i} = \frac{g_i \exp\left(\frac{-E_i}{k_B T}\right)}{Z_{s,z}(T, n_e)} \ . \tag{2.2.10}$$

Here, k_B is the Boltzmann constant, g_i the degeneracy of the state i, E_i its energy and $Z_{s,z}$ the electronic partition function of the species s, z. The population ratio of two consecutive ionic states, $n_{s,z}$ and $n_{s,z+1}$, can be calculated by the Saha-equation

$$\frac{n_{s,z+1} n_e}{n_{s,z}} = \frac{2}{\Lambda_e^3} \frac{Z_{s,z+1}}{Z_{s,z}} \exp\left(-\frac{\chi_{s,z}}{k_B T}\right), \tag{2.2.11}$$

where Λ_e is the thermal De Broglie wavelength of the electron and $\chi_{s,z}$ is the ionization potential of the species s, z. In LIBS plasmas, the formation of anions can be assumed negligible [70]. The ionization potential is given by the ionization potential in vaccum plus a correction due to the Coulomb field of ions and free electrons in the plasma such that [71]

$$\chi_{s,z} = \chi^0_{s,z} - \Delta\chi_z \tag{2.2.12}$$

$$\Delta\chi_z = \frac{e(z+1)}{4\pi\epsilon_0 \lambda_D} \tag{2.2.13}$$

$$\lambda_D = \sqrt{\frac{\epsilon_0 k_B T}{e^2 \cdot (n_e + \sum_{s,z} z_s^2 n_{s,z})}} \ , \tag{2.2.14}$$

where, e is the electronic charge, λ_D the Debye length, ϵ_0 the vacuum permittivity, and $\chi^0_{s,z}$ the ionization potential in vacuum. The correction, $\Delta\chi_z$, is relatively low and between 0.03 eV and 0.3 eV for plasma densities between $1 \times 10^{22}\,\mathrm{m}^{-3}$ and $5 \times 10^{23}\,\mathrm{m}^{-3}$.

The partition function in (2.2.10) and (2.2.11) is calculated by the sum over the energies of the bound states of the considered species. As the number of bound electronic states is infinite, the sum for calculating the partition function diverges and the probability of finding an atom in its ground state at room temperature would be zero. This is known as the electronic partition function paradox [72]. Therefore, the number of states to include, when calculating the partition function needs to be limited. As the size of the atom increases with increasing energy, the size of the atom can be used to limit the sum together by considering the distance between the particles in the plasma. Another approach, is to limit the sum by only including states with energies lower than the ionization potential [71]. The ionization potential depends on the electron density, and therefore the partition function depends on the electron density even though the dependence is very weak. The electronic partition functions can therefore be calculated as

$$Z_{s,z} = \sum_{E_i < \chi_{s,z}} \exp\left(-\frac{E_i}{k_B T}\right). \tag{2.2.15}$$

The population fraction of an ionized state of a species is obtained from the system of equations resulting from the Saha-equation and a normalization condition

$$\begin{aligned}\frac{n_{s,II}n_e}{n_{s,I}} &= \frac{2}{\Lambda_e^3}\frac{Z_{s,II}}{Z_{s,I}}\exp\left(-\frac{\chi_{s,I}}{k_BT}\right),\\ \frac{n_{s,III}n_e}{n_{s,II}} &= \frac{2}{\Lambda_e^3}\frac{Z_{s,III}}{Z_{s,II}}\exp\left(-\frac{\chi_{s,II}}{k_BT}\right),\\ &\vdots\\ n_{s,I}+n_{s,II}+n_{s,III}+\cdots &= 1\ .\end{aligned} \tag{2.2.16}$$

The system of equations includes all possible ionization states, but due to the temperatures usually encountered in LIBS the higher ionized states can safely be neglected. As example, is the population of ionized states shown in Figure 2.2.1 for magnesium at two different electron densities and as a function of temperature. The calculations were done by considering states up till six times ionized (Mg I-VII). From the figure, it can be seen that Mg IV is the highest state with non negligible population density for temperatures below 50 000 K. By comparing the results for the lower and higher electron density value, it can be seen that an increase of electron density shifts the curve towards lower temperature but also broadens the temperature intervals wherein the different ionized state exists. Combining the Saha- and Boltzmann distributions, the population density of an electronic state i of an element s in the ionic state z is obtained by

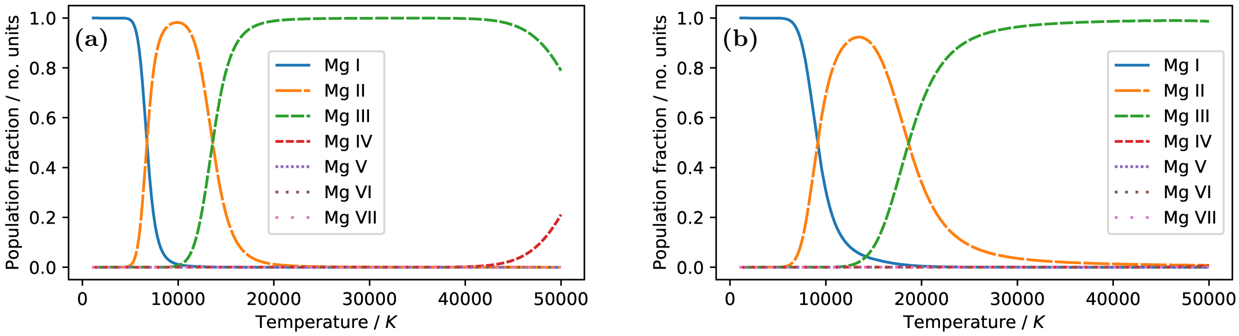

Figure 2.2.1: *Population fraction of ionized species of magnesium as a function of temperature calculated by solving equation* (2.2.16) *for two different electron densities:* ***(a)*** $1\times10^{22}\,\mathrm{m}^{-3}$, ***(b)*** $5\times10^{23}\,\mathrm{m}^{-3}$. *It is seen seen that the highest ionized state for temperatures below* 50 000 K *is Mg IV. Furthermore, the effect of the electron density can be inferred by comparing the two plots; increasing the electron density shifts the distribution towards higher temperatures but also widens the individual distributions. For example, are the populations of Mg I, Mg II and Mg III all non-negligible at a temperature of* ~15 000 K *at an electron density of* $5\times10^{23}\,\mathrm{m}^{-3}$ *while they are not coexisting for any temperature at the electron density of* $1\times10^{22}\,\mathrm{m}^{-3}$.

$$n_{s,z,i} = n_s \cdot n_{s,z} \cdot m_{s,z,i}, \tag{2.2.17}$$

where n_s is the total elemental number density of the considered element species s, $n_{s,z}$ the relative population of the ionic stage z as given by the Saha-equation (eq. 2.2.16) and $m_{s,z,i}$ the relative population of the electronic state as given by the Boltzmann distribution (eq. 2.2.10).

2.2.3 Calculation of Atomic Emissions

Given the population of atomic states, the atomic emission can be calculated by considering the radiative processes of spontaneous emission, stimulated emission, and absorption. The emission is calculated by propagating emission and absorption along the lines of sight (LOS) from the target and through the plasma to the detector of the LIBS set-up. A schematic of a LOS through the center of a plasma can be seen in Figure 2.2.2. The propagation of the radiation along a LOS, described by the spatial coordinate x, is then governed by radiative transfer equation (RTE)

$$\frac{dI_\lambda}{dx} = \epsilon_\lambda - \alpha \cdot I_\lambda, \tag{2.2.18}$$

where ϵ is the coefficient for spontaneous emission and α is the coefficient for stimulated emission and absorption. Assuming LTE, ϵ and α are, for a single and spectrally isolated emission line, given as

$$\epsilon_\lambda = A_{ul} \cdot n_{s,z,u} \cdot P_\lambda \cdot \frac{1}{4\pi c} \tag{2.2.19}$$

$$\alpha = h \cdot v \cdot \frac{dv}{d\lambda} \cdot (B_{lu} \cdot n_{s,z,u} - B_{ul} \cdot n_{s,z,l}) \cdot P_\lambda \cdot \frac{1}{c}\ , \tag{2.2.20}$$

where $n_{s,z,u}$ and $n_{s,z,l}$ are the number densities of the electronic levels u and l, respectively and given by equation (2.2.17) from the previous section. A_{ul}, B_{ul}, and B_{lu} are the Einstein coefficients for spontaneous emission, stimulated emission and absorption, respectively, c is the speed of light, and h is Planck's constant. P_λ is the line profile of the emission line and given by a Voigt profile. When considering multiple and superimposed emission lines, ϵ and α are obtained from the sum of the individual contributions from each emission line

$$\epsilon_\lambda = \epsilon_\lambda^{(1)} + \epsilon_\lambda^{(2)} + \epsilon_\lambda^{(3)} + \dots \tag{2.2.21}$$

$$\alpha = \alpha^{(1)} + \alpha^{(2)} + \alpha^{(3)} + \dots\ . \tag{2.2.22}$$

If also the continuum emissions were to be simulated, their emission and absorption coefficients would be included in equation (2.2.21) and (2.2.22). Inside a homogeneous plasma, i.e. a plasma with uniform temperature and densities, α_λ, β, and P_λ are independent of x and the RTE has the analytical solution

$$I_\lambda(x) = \frac{\epsilon_\lambda}{\alpha} + \left(I_{\lambda,x_0} - \frac{\epsilon_\lambda}{\alpha}\right) \exp\left(-\alpha \cdot x\right), \tag{2.2.23}$$

where $I_\lambda(x)$ is the spectral radiance at x along the LOS with units of photons per second per steradian per square meter per unit wavelength multiplied with the speed of light. I_{λ,x_0} is the spectral radiance at the beginning of the plasma and represents a boundary condition.

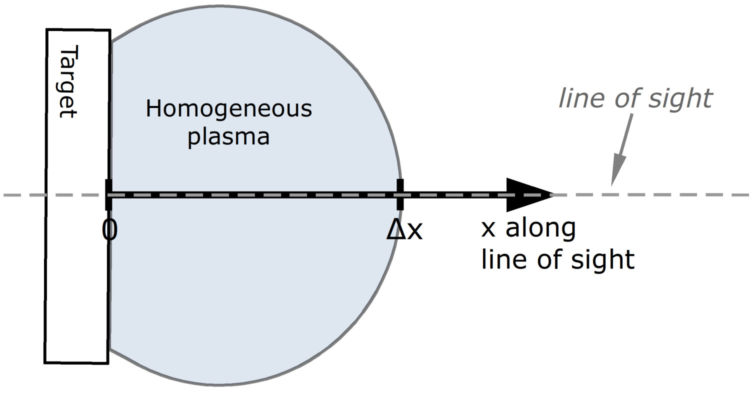

Figure 2.2.2: Schematic of a homogeneous LIBS plasma with a LOS through its center. The coordinate axis is located with origin at the surface of the target.

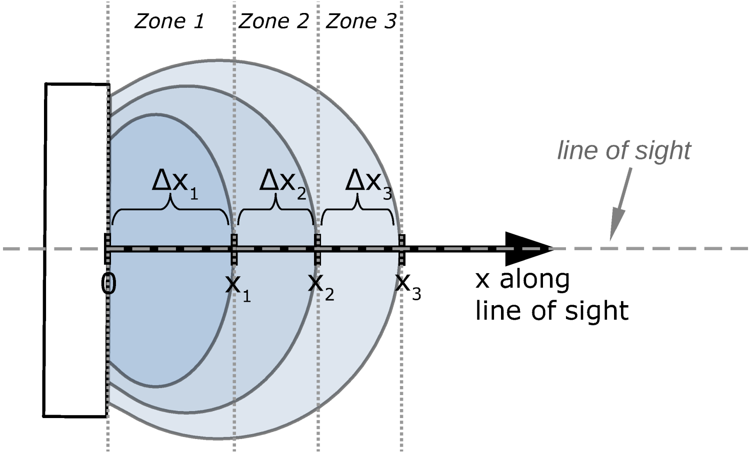

Figure 2.2.3: *Schematic of a inhomogeneous LIBS plasma divided into three zones wherein the plasma can be amused homogeneous.*

In the case of a non homogeneous plasma, the plasma can be divided into a chosen number of zones wherein the plasma can be assumed homogeneous [73]. This is illustrated in Figure 2.2.3 where the plasma is divided into three homogeneous zones. The emission is propagated from zone to zone using eq. (2.2.23) starting from the beginning of the first zone where $I_\lambda(x=0)=0$. As example the radiation after the first zone ($x=x_1$ in Figure 2.2.3) would be

$$I_{\lambda,x_1} = \frac{\epsilon_\lambda}{\alpha} + \left(0 - \frac{\epsilon_\lambda}{\alpha}\right)\exp\left(-\alpha \cdot \Delta x_1\right), \tag{2.2.24}$$

and after the second zone ($x=x_2$ in Figure 2.2.3) it would be

$$I_{\lambda,x_2} = \frac{\epsilon_\lambda}{\alpha} + \left(I_{\lambda,x_1} - \frac{\epsilon_\lambda}{\alpha}\right)\exp\left(-\alpha \cdot \Delta x_2\right), \tag{2.2.25}$$

where the radiance at $x=x_1$, i.e. I_{λ,x_1} from the previous equation, is used for the boundary condition. After the third zone, and at the end of the plasma ($x=x_3$), the radiance would be

$$I_{\lambda,x_3} = \frac{\epsilon_\lambda}{\alpha} + \left(I_{\lambda,x_2} - \frac{\epsilon_\lambda}{\alpha}\right)\exp\left(-\alpha \cdot \Delta x_3\right). \tag{2.2.26}$$

Since both ϵ_λ and α are directly proportional to the elemental densities (see equation 2.2.20 and 2.2.17), the LOS radiance depends uniquely on the product of the densities and the plasma length or the zone length in the multi zone description of the plasma. This will become important later in this thesis when fitting simulated spectra. In optical thin conditions the processes of absorption and stimulated emission are negligible and the radiative transfer equation simplifies to

$$\frac{dI_\lambda}{dx} = \epsilon_\lambda \ . \tag{2.2.27}$$

For a single zone, the LOS radiance is then equal to the product of the emission coefficient ϵ_λ times the length of the plasma zone

$$I_\lambda(x) = \epsilon_\lambda \cdot \Delta x \ . \tag{2.2.28}$$

In a multi zone description, the radiance is equal to the sum of the product of the emission coefficients times the zone lengths. In both cases the radiance is directly proportional to the elemental concentrations via equation (2.2.17) and (2.2.20). In the optical thick limit, i.e. in the limit of very strong absorption, the radiance goes towards the blackbody spectrum given by equation (2.2.1) in the previous section in the appropriate units. This can be seen in the solution for the RTE for the homogeneous plasma (equation 2.2.23) that reduces to

$$I_\lambda(x) = \frac{\epsilon_\lambda}{\alpha} = B_\lambda \ , \tag{2.2.29}$$

which is equal to the spectral radiance of a black body, B_λ, by Kirchhoff law of thermal radiation [27]. For assessing the effect of absorption on an emission line, a so called self-absorption coefficient (SA coefficient) can be calculated. It is defined as the spectrally integrated intensity calculated by neglecting the effect of absorption (equation 2.2.28) divided by the spectrally integrated intensity including absorption and stimulated emission (equation 2.2.23). For a LOS through a homogeneous plasma of length Δx it is [73]

$$SA = \frac{\int_\lambda \left(\epsilon_\lambda \cdot \Delta x\right)\ d\lambda}{\int_\lambda \left(\frac{\epsilon_\lambda}{\alpha} + \left(I_{\lambda,x_0} - \frac{\epsilon_\lambda}{\alpha}\right)\exp\left(-\alpha \cdot \Delta x\right)\right)\ d\lambda}\ , \tag{2.2.30}$$

where the integral is taken over the relevant wavelengths for the considered emission line. A SA coefficient of one means that absorption is negligible and that the emission line is optically thin. Thereby, the SA coefficient can be used to predict the signal of an observed emission lines in optical thin conditions.

An examples of the calculated atomic emissions from the Ca II resonance transition at 393 nm can be seen in Figure 2.2.4. The calculations were done with a single LOS through a homogeneous plasma for various calcium number densities/concentrations. The data for the emission line were taken from [63] and [74]. From Figure 2.2.4a it can be seen that for high calcium concentration the top of the emission line saturates. The saturation is at the balckbody value given by the temperature of the plasma, i.e. 12 000 K, as described by equation (2.2.29). The saturation leads to an increased FWHM of the line profile which is referred to as broadening due to self-absorption. The saturation can also be inferred by Figure 2.2.4b showing the spectrally integrated intensity of the emission line as a function of the calcium concentration. Such curve is usually referred to as a curve-of-growth (COG) [75]. Figure 2.2.4c shows the SA coefficient. It can be seen to rise above one as the density is increased. At low concentrations, the emission line is optically thin and the integrated intensity increases linearly with the concentration. At concentrations around $1 \times 10^{20}\,\mathrm{m}^{-3}$, absorption becomes important and the saturation of the emission line is seen by a decrease of the slope of the COG. The emissions from the Ca II lines has also been calculated for a plasma of two homogeneous zones. More specifically, a hot inner zone and a colder outer zone. The results are shown in Figure 2.2.5. The line profile is shown individually after the passage of the inner zone (halfway through the plasma) and after passage of both zones. After passage of the inner zone, the intensity of the emission line around the peak center is above the blackbody limit of the outer zone (with the lower temperature). The second zone therefore mostly works as an absorbing slap of material and only contributes to the emission at the peak flanks where the intensity is below the blackbody limit. The strong absorption at the peak center results in a reversed top. This is referred to as self-reversal. A reversed emission line top only happens when there is a drop in temperature along the LOS and is therefore an indication of spatial temperature gradients. The calculated emission of the Ca II line nicely illustrates the effect of absorption and its possible appearance in LIBS spectra. However, it is one of the most extreme cases for the following reasons. First, it is a ground state transition. This enhances absorption due to a high population of the ground state (equation 2.2.10). Furthermore it has a strong Einstein coefficient for spontaneous emission and a strong emitter is also a strong absorber due to the relation between the Einstein coefficients. The majority of the emission lines observed in LIBS spectra are less affected by absorption and emission lines that do not involve the ground state and with weaker Einstein coefficients, are usually not affected by absorptions to a good approximation.

The calculation of the LOS radiances in this section were all based on a stationary plasma, but due to the fast propagation of light through the plasma (the speed of light), any LIBS plasma can safely be assumed stationary when solving the RTE. If a time dependence is to be included, it can therefore be done by integrating the LOS radiance, in the stationary case, with different plasma temperatures and densities corresponding to different times.

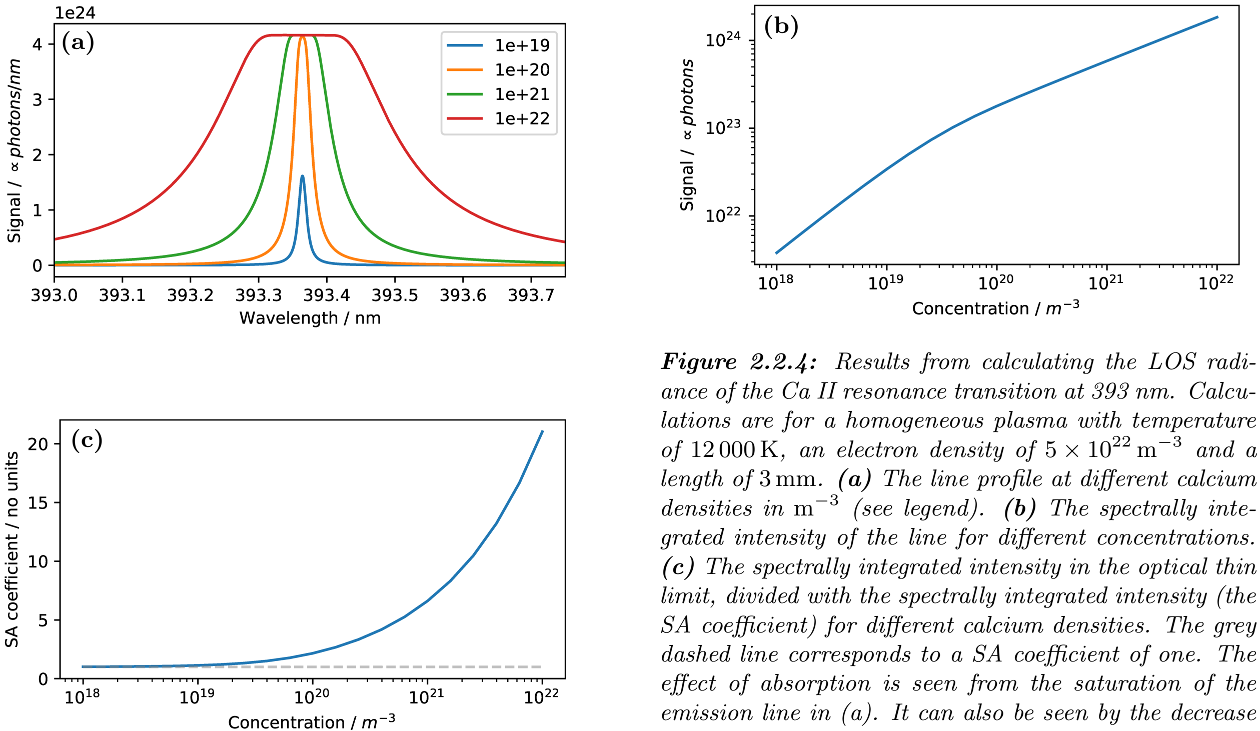

Figure 2.2.4: *Results from calculating the LOS radiance of the Ca II resonance transition at 393 nm. Calculations are for a homogeneous plasma with temperature of* 12 000 K*, an electron density of* $5 \times 10^{22}\,\mathrm{m}^{-3}$ *and a length of* 3 mm*.* ***(a)*** *The line profile at different calcium densities in* m^{-3} *(see legend).* ***(b)*** *The spectrally integrated intensity of the line for different concentrations.* ***(c)*** *The spectrally integrated intensity in the optical thin limit, divided with the spectrally integrated intensity (the SA coefficient) for different calcium densities. The grey dashed line corresponds to a SA coefficient of one. The effect of absorption is seen from the saturation of the emission line in (a). It can also be seen by the decrease in the slope of the curve in (b), and finally from the increase of the SA coefficient.*

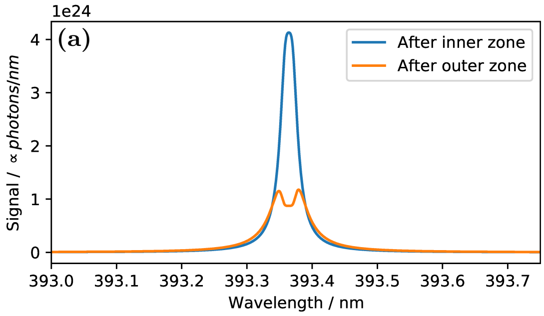

Figure 2.2.5: *Results from calculating the LOS radiance of the Ca II resonance transition at 393 nm. Calculations are for a plasma of two homogeneous zones with different temperatures; an inner zone of* 12 000 K *and an outer zone of* 8000 K*. The line profile of the emission line is shown after the passage of the inner zone (half-way through the plasma) and after the outer zone (at the end of the plasma). The outer and colder zone mainly absorbs the emission propagated in the first zone. The absorption is strongest at the peak center resulting in a reversed top.*

2.2.4 Boltzmann and Saha-Boltzmann plots

The method of Boltzmann and Saha-Boltzmann plots are the most common methods for determining the plasma temperature. It can be done without any additional experiments using only the information in the spectra in terms of the observed intensities of the emission lines. The method is therefore part of the calibration-free LIBS toolbox [17]. It is based on the equation for the atomic emissions in optical thin conditions and for a stationary and homogeneous plasma (equation 2.2.28). It is therefore best suited for LIBS spectra obtained with short integration times and even better for temporally and spatially resolved LIBS spectra [76].

The LOS radiance in optical thin conditions, as given by equation 2.2.23 from the previous section, is for a homogeneous and stationary plasma

$$I_\lambda = \epsilon_\lambda \cdot \Delta x \ , \tag{2.2.31}$$

For a single emission line from the elemental species s in the ionic stage z corresponding to an electron transition from the upper level u to the lower level l it can be written as

$$I_\lambda = P_\lambda \cdot A_{ul} \cdot n_s \cdot n_{s,z} \cdot g_u \cdot \frac{\exp\left(\frac{-E_u}{k_b \cdot T}\right)}{Z_{s,z}} \tag{2.2.32}$$

where P_λ is the line profile of the emission line, n_s the total density of the elemental species, $n_{s,z}$ is the population fraction of the ionized state of the line (see section 2.2.2) and where the population fraction of the upper electronic level, given by the Boltzmann distribution, has been written out explicitly. As the line profile is normalized, the spectrally integrated intensity is

$$I = A_{ul} \cdot n_s \cdot n_{s,z} \cdot g_u \cdot \frac{\exp\left(\frac{-E_u}{k_b \cdot T}\right)}{Z_{s,z}} \ . \tag{2.2.33}$$

As the plasma is assumed homogeneous and stationary, the light collection geometry, and other experimental parameters such as the exposure time of the LIBS measurement can be described by an unknown constant F. The exact value of F can be unknown, but it is equal for all emission lines in the spectrum. By multiplying the LOS radiance by F, the intensity as observed in a LIBS spectrum can be modelled. The units of the observed intensity will be in photons. For example, the observed intensity of three different emission lines from three different ionized states, but from the same species s, would then be

$$I_{s,I} = F \cdot A_{ul} \cdot n_s \cdot n_{s,I} \cdot g_u \cdot \frac{\exp\left(\frac{-E_u}{k_b \cdot T}\right)}{Z_{s,I}} \tag{2.2.34}$$

$$I_{s,II} = F \cdot A_{ul} \cdot n_s \cdot n_{s,II} \cdot g_u \cdot \frac{\exp\left(\frac{-E_u}{k_b \cdot T}\right)}{Z_{s,II}} \tag{2.2.35}$$

$$I_{s,III} = F \cdot A_{ul} \cdot n_s \cdot n_{s,III} \cdot g_u \cdot \frac{\exp\left(\frac{-E_u}{k_b \cdot T}\right)}{Z_{s,III}} \tag{2.2.36}$$

The final equations for the Saha-Boltzmann plot method follows from re-arranging the above equations and using the Saha relations between consecutive ionized states (equation (2.2.11))

$$\ln\left(\frac{I_{s,I}}{A_{ul} \cdot g_u}\right) = \ln\left(F \cdot n_s \cdot \frac{n_{s,I}}{Z_{s,I}}\right) - \frac{1}{k_b \cdot T} \cdot E_u \tag{2.2.37}$$

$$\ln\left(\frac{I_{s,II}}{A_{ul} \cdot g_u}\right) - \ln\left(\frac{2}{\Lambda_e^3 \cdot n_e}\right) = \ln\left(F \cdot n_s \cdot \frac{n_{s,I}}{Z_{s,I}}\right) - \frac{1}{k_b \cdot T} \cdot (E_u + X_I) \tag{2.2.38}$$

$$\underbrace{\ln\left(\frac{I_{s,III}}{A_{ul} \cdot g_u}\right) - \ln\left(\frac{4}{\Lambda_e^6 \cdot n_e^2}\right)}_{y^*} = \underbrace{\ln\left(F \cdot n_s \cdot \frac{n_{s,I}}{Z_{s,I}}\right)}_{b} - \underbrace{\frac{1}{k_b \cdot T}}_{a} \cdot \underbrace{(E_u + X_I + X_{II})}_{x^*} \tag{2.2.39}$$

By identifying several emission lines in a spectrum that involve different upper electronic levels or ionization stages but from the same considered species, their measured intensities can be substituted for the values of $I_{s,z}$. By plotting y^* versus x^*, linear regression can be performed and the parameters a and b can be determined. As seen from the equation, the plasma temperature is related to the value of a and an estimate of the plasma temperature can thereby be obtained. b can be seen to be related to the elemental concentration of the considered species and can be obtained by inserting the values of F, and $n_{s,I}/Z_{s,I}$. This is the method of Saha-Boltzmann plots. It should be noted that plotting y^*, requires an estimate of the electron density. The electron density can be determined separately by the Stark broadening or Stark shift of an emission line (equation (2.1.6) or (2.1.7) in section 2.1.3). When using emission lines from the same ionized stages, the method is referred to as the method Boltzmann plots. The method can also be applied using multiple elemental species. In that case the regression is a bit more complicated as there will be a b parameter for each species. The a parameter, giving the temperature, is the same for all species. In that case, the temperature estimate might be better confined as more emission lines can be utilized simultaneously.

Chapter 3

Experimentals

The experiments of this thesis were conducted using a high-resolution LIBS setup at the Institute of Optical Sensor Systems at the German Aerospace Center (DLR) in Berlin, Germany. This chapter contains an overview of the setup, the sample preparation and measurements, and results from characterizing the setup.

3.1 Overview of LIBS setup

The LIBS setup is built around an Echelle spectrometer (LTB Aryelle Butterfly) with an Intensified charge-coupled device (ICCD) detector (Andor iStar), a Q-switched Nd-YAG laser (Continuum), and an air tight chamber that can be pumped dry from air and filled with a Martian analogue gas mixture for the simulation of Martian atmospheric conditions. The timing of the laser and the detector is controlled by a control unit with an internal clock generator (LTB LIBS control box). This unit is part of the spectrometer system and is used for controlling the delay time between the laser pulse and the capturing of the light as well as the exposure time. A schematic of the setup can be seen in Figure 3.1.1. On the trajectory of the laser beam

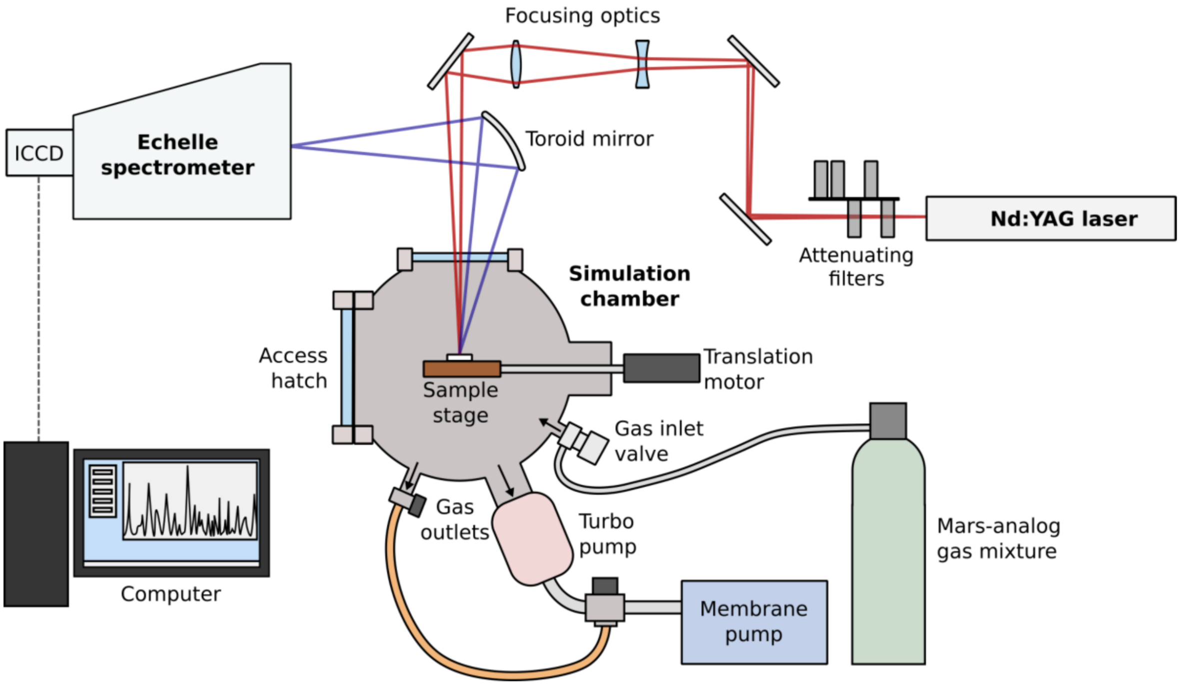

Figure 3.1.1: Schematic of the LIBS setup used for the measurements of this thesis. Figure taken from [77]. The setup is built around an Echelle spectrometer and contain an air tight chamber (simulation chamber) that allows for experimentally simulating Martian atmospheric conditions.

towards the sample, that is located inside the simulation chamber, the beam passes through a series of neutral density filters. These filters are used for attenuating the beam power. Behind the filters, the laser is guided through a window in the simulation chamber and focused at the position of the sample surface by the use of three mirrors and two lenses. The light from the induced plasma is collected by a toroid mirror that also focuses the plasma emission at the entrance slit of the spectrometer. A detailed descriptions of the LIBS setup is provided below.

3.1.1 Laser

The Q-switched Nd:YAG laser is operated at its fundamental wavelength of 1064 and with a repetition rate of 10 Hz. It has a pulse width of 6 ns and an output energy of 120.5 mJ as a top hat profile. Using different combinations of the neutral density filters the laser power, as measured at the location of a sample, can be adjusted to values between 0.4 mJ and 109.3 mJ. The diameter of the laser spot at the surface of a sample is approximately 300 μm.

3.1.2 Light Collection

The main component for collecting the plasma emissions is a toroid mirror that guides and focuses the light in two dimensions towards the entrance slit of the spectrometer. The toroid mirror has a focal length of 150 mm, in both dimensions, and is at placed 300 mm distance above the location of a sample and also at 300 mm distance in front of the spectrometer entrance slit. This results in a one-to-one imaging of the plasma onto the entrance slit. The size of the entrance slit is 50×50 μm^2 and limits the part of the plasma that is observed during a measurement. Therefore, the field of view of the spectrometer should be 50×50 μm^2. Between the spectrometer slit and the toroid mirror, two plane mirrors are placed for further guiding the plasma light onto the entrance slit. These mirrors are not shown in the schematic of the setup (Figure 3.1.1), but they further limit the angle of the plasma rays that reach the entrance slit, resulting in an acceptance angle of $\sim 6°$.

3.1.3 Spectrometer System

The spectrometer (LTB Aryelle Butterfly) can be switched between two spectral regimes; the UV range form 190 nm to 350 nm and the UV-VIS-NIR range from 270 nm to 850 nm. The switching is performed by a folding mirror that guides the plasma emission between two separate optical systems. All measurements for this thesis were performed in the UV-VIS-NIR configuration. The spectrometer works by splitting the plasma light in two dimensions using a prism and an Echelle grating. The Echelle grating separates diffraction orders in one dimension, while the prism disperses the spectrum within each diffraction order along the other dimension. This results in a two 2D spectrum of stripes with different but slightly overlapping wavelengths. This is illustrated in Figure 3.1.2. Figure 3.1.2a shows the raw detector image of the early LIBS plasma of a carbonate sample. The spectrum of the early plasma consists mainly of very broad emission lines and continuum emission. The orders are therefore easily seen. In Figure 3.1.2b, the orders are identified and in Figure 3.1.2c, the resulting spectrum can be seen. The spectrum was obtained by tracing pixel intensities along the different orders and plotting them against the corresponding wavelengths. Due to the blazed Echelle grating that varies as $(\sin(x)/x)^2$, each order is most sensitive in the central part [78]. This is the reason for the concave appearance of the spectrum for each order. In the spectrometer software, Sophi, spectra can be exported as raw detector images (Figure 3.1.2a) or as spectra (Figure 3.1.2c) with or without the order overlap in wavelengths removed. In the spectrometer there is a built in Hg lamp that can be used for automatic wavelength alignment in the software. The detector of the spectrometer system is an Andor iStar. It is a ICCD detector which allows for time gated measurements by varying the delay between the laser pulse and the activation of the detector (delay time) and the time interval within the detector is detecting photons (exposure time). Both the delay and the exposure time can be adjusted in steps of approximately 10 ns. The detector uses micro lensing, which results in a fill factor close to 100 %. When measuring spectral features smaller than or similar to the pixel size of the detector, a good fill factor of the detector is important for obtaining reliable intensities. This is

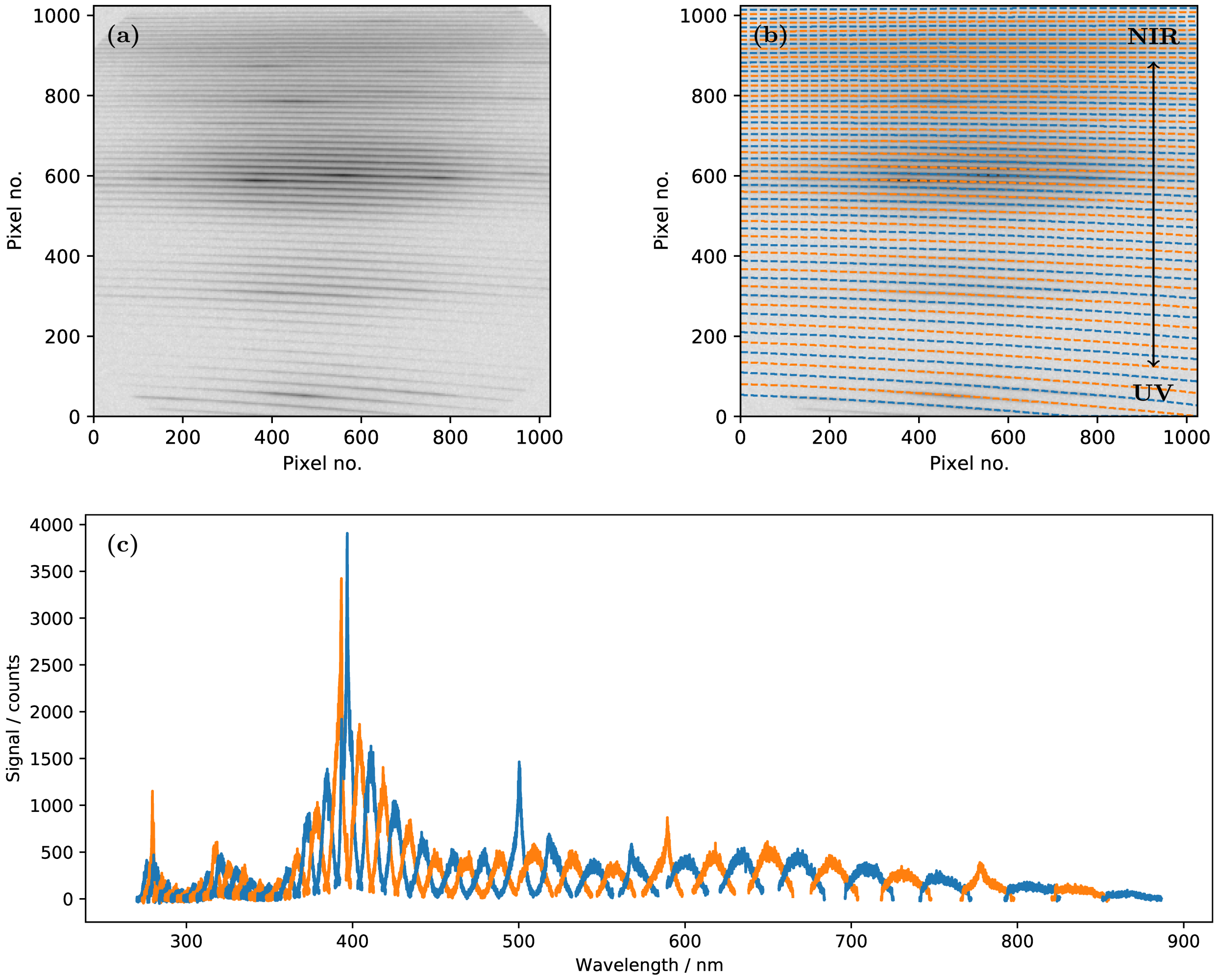

Figure 3.1.2: ***(a)*** *A raw detector image of the early LIBS plasma from a carbonate target.* ***(b)*** *The raw detector image with the orders identified.* ***(c)*** *The resulting spectra by plotting the intensities along the identified orders against the corresponding wavelengths.*

due to the finite size of the pixels and is illustrated schematically in Figure 3.1.3. Due to the high fill factor of the detector of the LIBS setup, the total intensity of emission lines are preferably calculated as the sum of pixel intensities. In cases of spectral features with characteristic widths (including broadening from the optics) larger than the pixel sizes, intensities can reliably be found by interpolation between the pixels and integration, i.e. fits of line profiles.

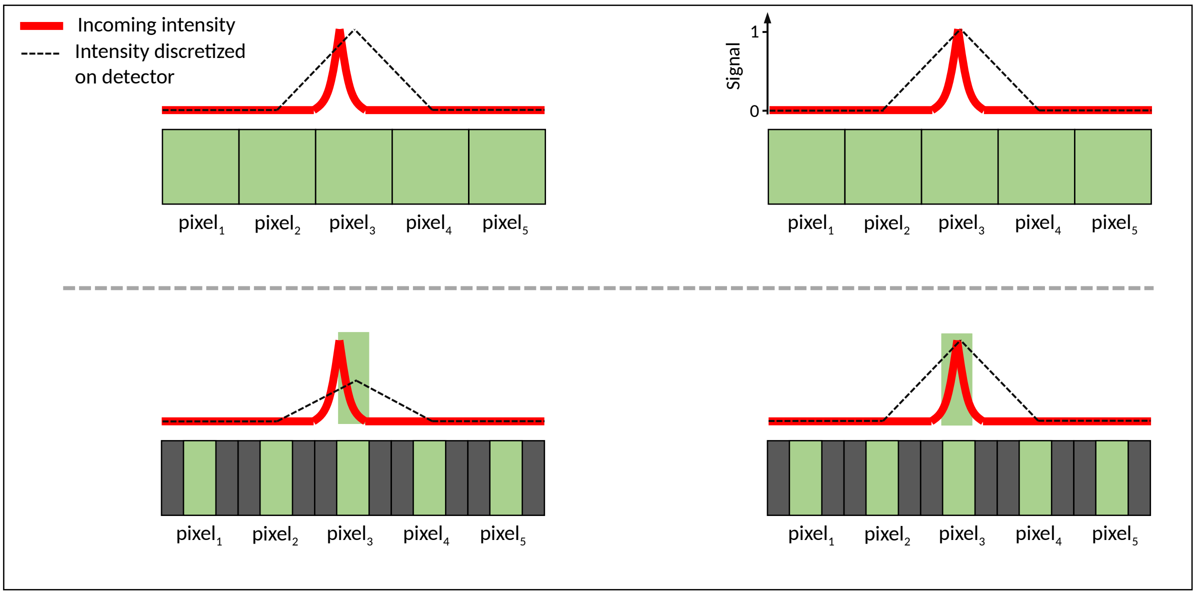

Figure 3.1.3: *Schematic of the effect of fill-factor. The green areas correspond to active area of the pixels in the detector. The dark areas correspond to inactive areas. Two peaks of equal intensity but slightly different wavelengths corresponding to slightly different positions on the detector are seen (red curves). In the case of a fill factor of 100% (top), the measured intensity would be equal for the two peaks. In the case of low fill factor (bottom), the measured intensity depends on the position on the detector even though the peaks have equal intensity. The black dashed lines indicate how discretized spectrum would appear from the detector image. From these lines it is seen that interpolation will not compensate the effect. From the lines showing the discretization of the detector, it can be seen that in the case of a good fill factor, the intensity is best derived by summing up pixel intensities rather than interpolating values between pixels and integrating.*

3.2 Sample Preparation and Measurements

Unless otherwise stated, the LIBS spectra in this thesis are from samples in form of pressed pellets. The pellets weights 1 g and have a cylindrical shape with a diameter of 1.4 cm and a height of approximately 0.4 cm. The pellets are from powders that have been grounded and mixed using a mortar and pestle and thereafter pressed. The pressing is done by applying five tons for ten minutes. As example, two pellets pressed from the four carbonates $CaCO_3$, $MgCO_3$, $MnCO_3$ and Na_2CO_3 can be seen in Figure 3.1.2. When mixing different powders for a pellet, the individual components are weighted by a scientific scale which allows for the calculation of reference concentrations. The uncertainty of the scale is less than 0.01 g. In this thesis, where only the concentrations of the major elements are considered, the uncertainty of the reference concentrations is therefore small when compared to the typical uncertainty obtained on the elements via LIBS.

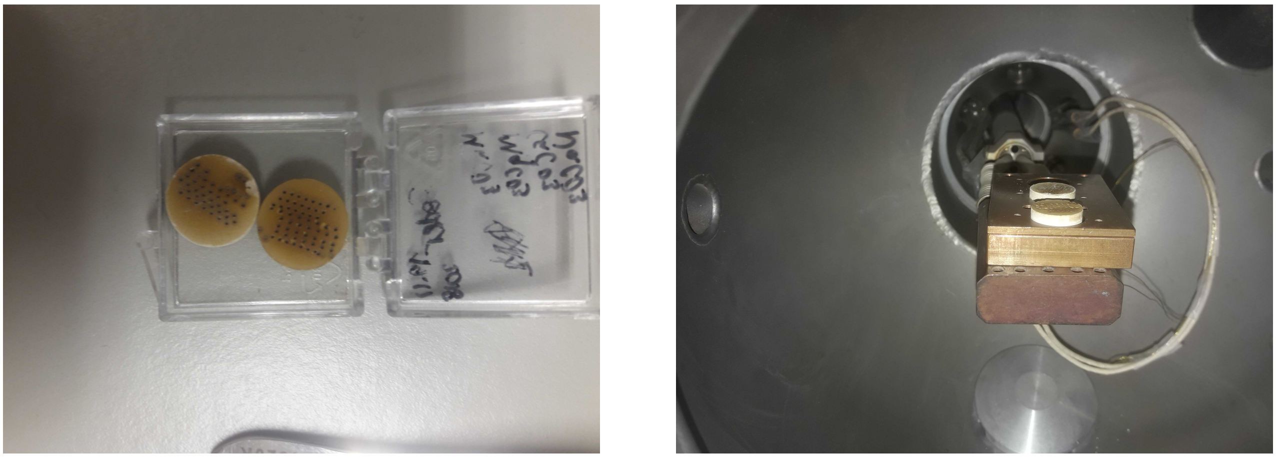

Figure 3.2.1: ***left:*** *A photo of two pellets from mixed carbonates. Small craters from LIBS measurements can be seen on the surface of the pellets.* ***right:*** *The pellets located in the simulation chamber wherein the measurements have been performed.*

3.3 Characterization of LIBS setup

3.3.1 Field of View

The field of view (FOV) was determined experimentally by the use of a green photo diode. By moving the diode around in the plane where samples usually are placed and measuring the intensity with the spectrometer (see Figure 3.3.1a), the FOV was measured. The results are summarized in Figure 3.3.1b,c,d. From the Figure it can be seen that the FOV changes when moving the diode in the y-direction. This is expected since the diode thereby moves in and out of the focal plane of the toroid mirror. It can also be seen that the FOV is bigger than expected from the slit width, i.e. $50 \times 50\ \mu\text{m}^2$ and a 1:1 projection in at least one of the dimensions at any y-position. At a y-position of 9 mm (Figure 3.3.1b) the size of the FOV in the z-direction seems to be around the expected whereas in the other dimension, the x-dimension, the field of view is around 1 mm. When decreasing the y-distance, i.e. increasing the distance between the toroid and the diode (Figure 3.3.1c,d), the FOV decreases in the x-dimension whereas it increases in the z-dimension. At a y-position of 1 mm, the field of view is symmetric. In conclusion, these measurements show that the alignment of the spectrometer is not optimal. As the setup is closed and its components not easily accessible, improving the alignment has been outside the scope of this thesis. However, the obtained insights have been important for the measurement strategies. For example, LIBS spectra to be fitted to simulated spectra (presented later in Chapter 4) have all been acquired at a sample surface positions corresponding to y-positions around 1 mm where the FOV is the smallest in any of the dimensions.

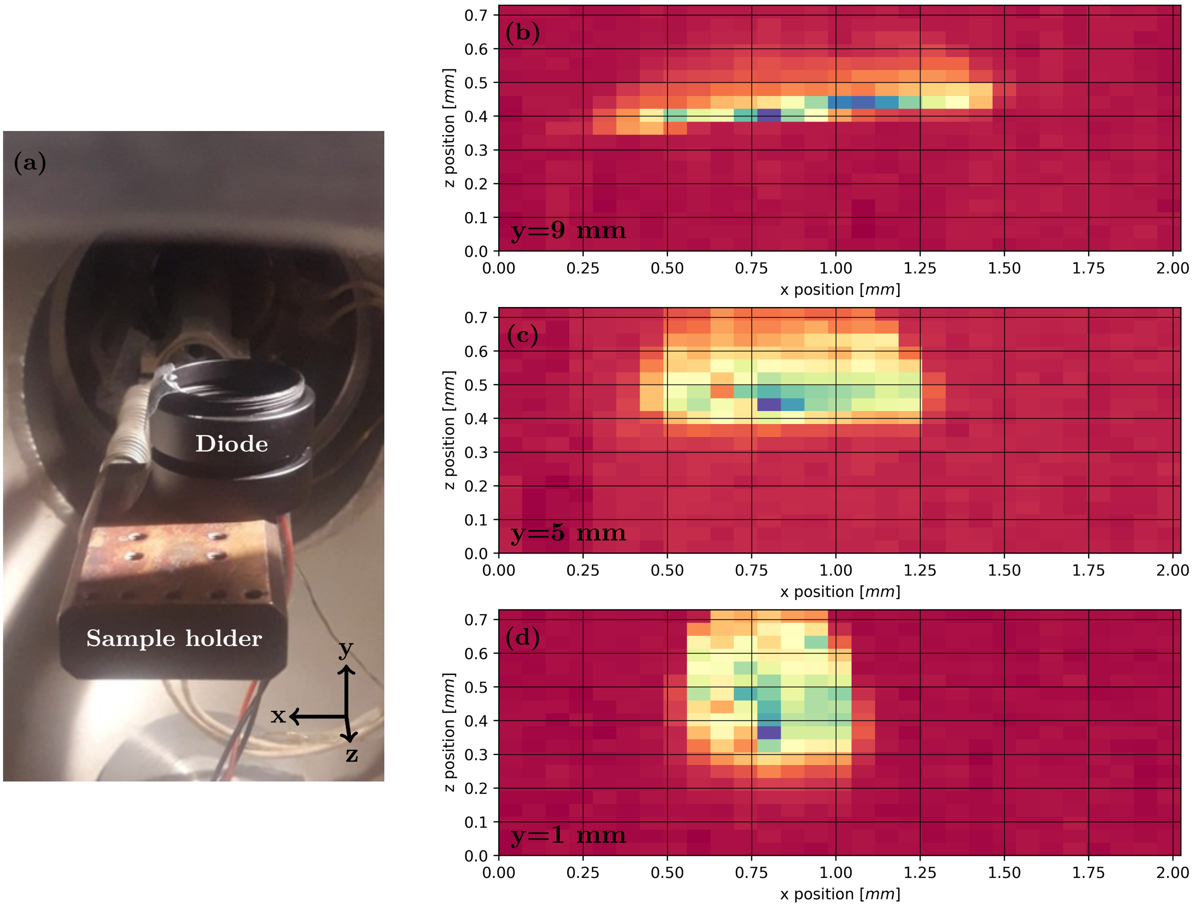

Figure 3.3.1: *Measurements of the field of view of the spectrometer by the use of a photo diode.* ***(a)*** *Picture of diode located at the sample holder inside the simulation chamber of the LIBS setup. By moving the diode around in the xz-plane and measuring the light with the spectrometer the field of view was estimated for different y-positions.* ***(b,c,d)*** *The field of view for different y-positions. Red corresponds to low values and blue to high values.*

3.3.2 Instrumental Broadening and Wavelength Alignment

The instrumental broadening was estimated using a fiber coupled Hg lamp. The characteristic spectral lines of the Hg lamp have a FWHM of around 0.002 nm. This is smaller than what can be resolved by the spectrometer (FWHM of ~ 0.03 in the VIS range [79]). The line profiles of the Hg lines, as measured by the LIBS setup, can therefore be assumed to be dominated by the broadening mechanisms of the spectrometer and thereby used as a measure of the instrumental broadening.

Due to spatial constraints from the air tight simulation chamber, the output fiber of the Hg lamp could not be placed at the exact same position where samples usually are located. Instead the fiber was located approximately 5 cm above the sample holder. At this position, the spectrum of the Hg lamp was measured 30 times. The median spectrum can be seen in Figure 3.3.2. Close-ups of the Hg I line at 296 nm and 546 nm, together with fits of a Gaussian and Voigt profile, are shown in Figure 3.3.3a and 3.3.3b, respectively. The Hg line at 296 nm is relatively week and the Gaussian and Voigt fits are equally good as indicated by the χ^2 values. The Hg line at 546 nm is stronger and has a higher signal to noise ratio (SNR). Comparing the χ^2 values for the two profiles for this line, it can be seen that the Voigt profile is a better description of the line profile, i.e. there is a non-negligible Lorentzian contribution to the instrumental broadening of the set-up. Nonetheless the Gaussian approximation of the line profile provides a visually good description. By fitting Voigt profiles to the Hg I lines at (296.7, 312.5, 365.0, 365.5, 404.6, 435.8, 546.0, 576.9, and 579.0) nm, the FWHM of the Gaussian and Lorentzian parts have been determined and plotted against the wavelength in Figure 3.3.4. As seen from the Figure, the instrumental broadening increases for increasing wavelengths. It can also be seen that the Gaussian part of the Voigt profile is approximately two times larger than the Lorentzian part. The deconvolution of Hg lines into a Gaussian and Lorentzian part is difficult and it is expressed by the relatively big uncertainties in the fitted widths. This is partly due to noise, but also partly due to a pure Gaussian actually providing a reasonable description of the line profiles (see Figure 3.3.3). The FWHM for different wavelengths has therefore also been obtained from the fits of pure Gaussian profiles. These results are shown in Figure 3.3.4. Here, the linear increase of the broadening with increasing wavelengths is more evident and it can be seen to be well described by the linear function $FWHM(\lambda) = 9.149 \times 10^{-5} \cdot \lambda + 8.417 \times 10^{-3}$ nm. Therefore, extrapolation of the FWHM for smaller and larger wavelengths seems more convincing for this case than for the Voigt fits. Given this, and that the Gaussian part of the Voigt profile is the biggest (twice as big as the Lorentzian), it is reasonable to approximate the instrumental broadening by a convolution of a Gaussian function with a width described by the linear function in Figure 3.3.5.

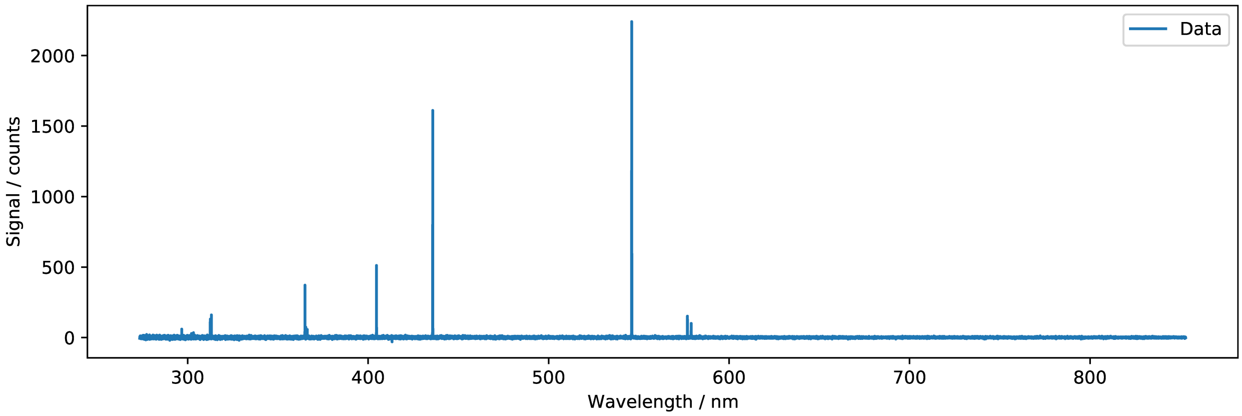

Figure 3.3.2: *The median spectrum of the Hg lamp spectra as measured by the LIBS setup. All the peaks origins from Hg I emission lines.*

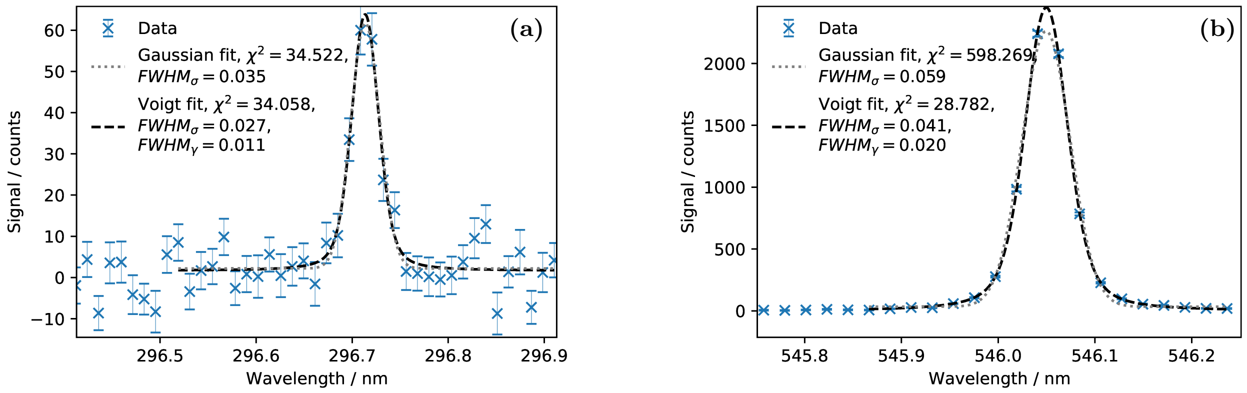

Figure 3.3.3: *Close-up of two Hg I lines investigated for the instrumental broadening.* ***(a)*** *The Hg I line at 297 nm.* ***(b)*** *The Hg I line at 546 nm. The vertical bars indicate the uncertainties as derived from the standard deviation of the 30 repetitions. Voigt and Gaussian profiles have been fitted to the emission lines and the parameters for describing the widths as well as the minimized χ^2 values are indicated. $FHWM_\sigma$ and $FHWM_\gamma$ correspond to the widths of the Gaussian and Lorentzian part, respectively, of the Voigt profile. By comparing the χ^2 values for the Gauss and Voigt fits to the line in* ***(b)*** *it can be concluded that the Voigt profile is a better description of the line profile. Nonetheless, the Gaussian part of the Voigt is twice as big as the Lorentzian and a pure Gaussian profile also provides a fair description.*

In conclusion, a Gaussian function will be used for the description of the instrumental broadening of the setup throughout this thesis. However, it is important to note that in special cases, such as when deriving the electron density from measured line profiles in the LIBS data, the Lorentzian part of the instrumental broadening might be important. For example, the FWHM, due to Stark broadening of the strong Ca II doublet at ~315 nm is equal to 0.022 nm at an electron density of $5 \times 10^{22}\,\mathrm{m}^{-3}$. Ignoring the Lorentzian part of the instrumental broadening for this doublet would lead to an error in the estimated electron density of about 15 %. Depending on the Stark widths of the lines, the error can be larger or smaller. For the H-α, that is usually preferred for the estimation of the electron density, the error would be negligible at an electron density of $5 \times 10^{22}\,\mathrm{m}^{-3}$.

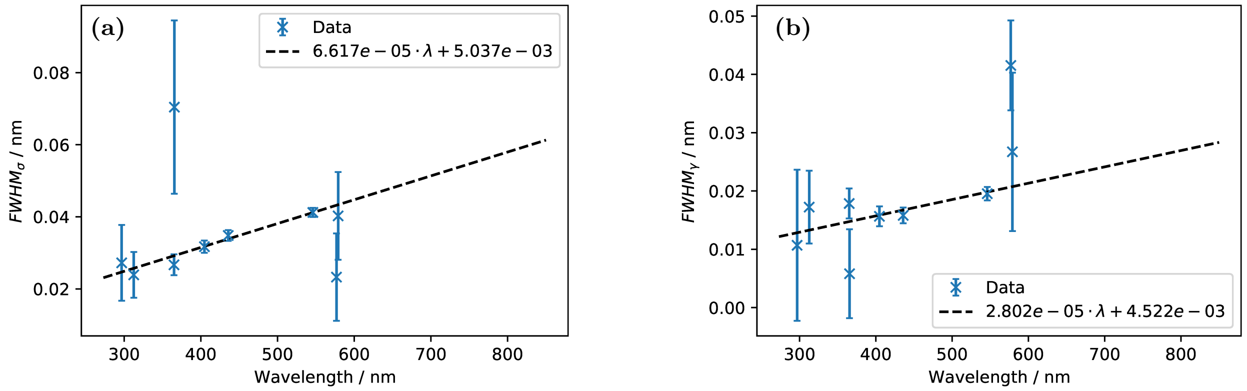

Figure 3.3.4: *The FWHM of the Hg lines from fits of Voigt profiles plotted against the center wavelengths of the lines. The vertical bars indicates the uncertainties as obtained from the fits.* ***(a)*** *The Gaussian width of the Voigt profile and* ***(b)*** *the Lorentzian width. Linear functions have been fitted to the data and are also seen. The linear functions indicate a non-constant broadening with wavelengths, but as the extracted widths have relatively high uncertainties, the fitted linear functions also comes with large uncertainties. The varying uncertainties are because of the varying signal to noise ratio of the utilized Hg lines.*

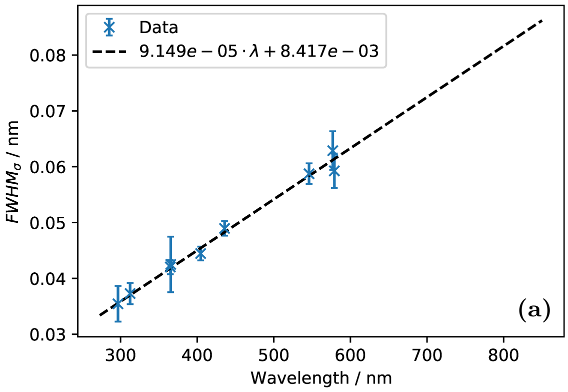

Figure 3.3.5: *The width/broadening of the Hg lines from fits of pure Gaussians plotted against the center wavelengths of the lines. A linear function is seen to describe the broadening for different wavelengths well.*

By comparing the center wavelengths of the Hg lines, as derived from the Gaussian fits, with the reference values from the NIST database [74], an evaluation of the automatic wavelength calibration has been obtained. The deviations between the fitted and the reference wavelengths are shown in Figure 3.3.6a against the center wavelengths of the lines and in Figure 3.3.6b against the horizontal position of the lines in the 2D detector image. From the deviation versus the horizontal pixel a clear trend of increasing offset with decreasing pixels can be seen, whereas the trend for the deviation for different wavelengths is less clear. A linear function of the horizontal pixel and the wavelength has been fitted to the deviation. The function with the best fitted parameters is

$$f(p, \lambda) = 1.049 \cdot 10^{-4} \cdot p - 6.643 \cdot 10^{-6} \cdot \lambda - 7.299 \cdot 10^{-2} \, , \tag{3.3.1}$$

where p is the horizontal pixel number and λ the wavelength in nm. The deviation as predicted by equation (3.3.1) versus the measured deviation is shown in Figure 3.3.7. From the figure it is seen that the deviation is well described by the function that therefore can be used for correcting the wavelength axis.

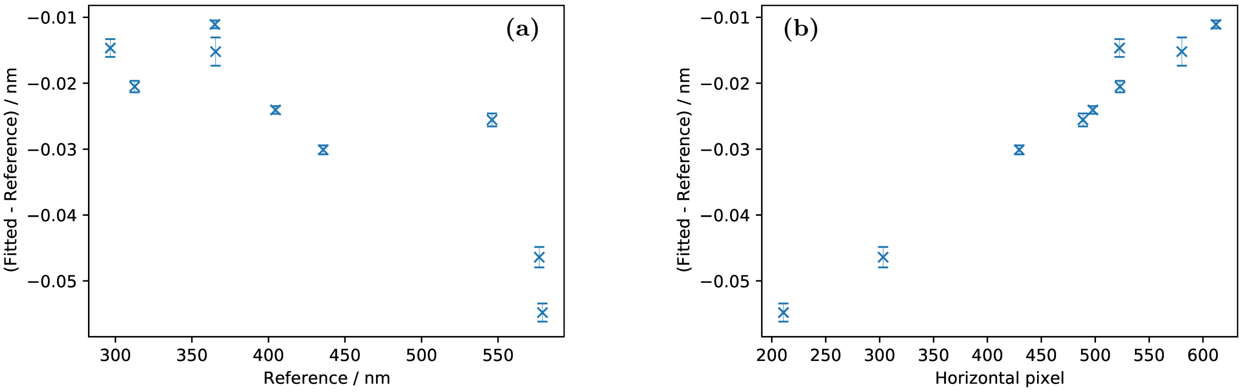

Figure 3.3.6: ***(a)*** *The difference in center wavelengths obtained from fits of pure Gaussians and the reference values from the NIST database as predicted by equation* (3.3.1) *plotted against the center wavelengths.* ***(b)*** *The deviations in (a) plotted against horizontal pixel in the 2D detector image.*

The correction has been tested on a measured LIBS spectrum of a carbonate sample in Martian atmospheric conditions and with a delay time of 1250 ns and a 50 ns gate width. In Figure 3.3.8, a close-up the spectrum showing a Ca I emission line can be seen with and without the wavelength correction (equation (3.3.1)). After applying the correction, the Ca I line can be seen to have the same center wavelength in the two consecutive Echelle orders. This should be the case and the correction is thereby verified. In Figure 3.3.9, a close-up of a Mg II emission line can be seen. The line has been fitted with a Voigt profile and the derived center wavelength has been compared to the reference value from the NIST database. There is a deviation of 0.015 nm. The Mg II line has a small positive Stark shift of 3.09×10^{-3} nm at a temperature of 10 000 K and an electron density of $1 \times 10^{23}\,\mathrm{m}^{-3}$. To explain the shift by the Stark effect, it would require an electron density of $5 \times 10^{23}\,\mathrm{m}^{-3}$.

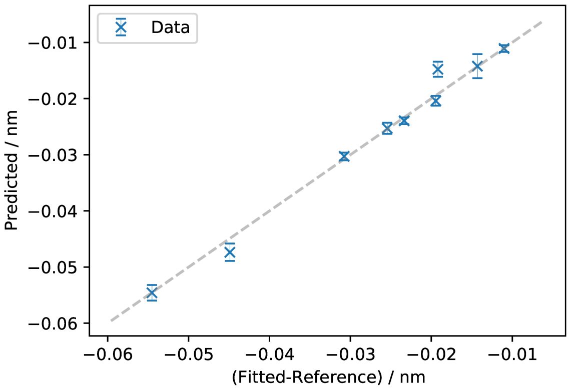

Figure 3.3.7: *The wavelength deviation as predicted by equation* (3.3.1) *plotted against the measured deviation. The equation is seen to describe the deviation well and will therefore be used for correcting the wavelengths of the measured spectra.*

At such electron density the FWHM, due to Stark broadening, would be 0.1 nm which is much broader than the observed width. The shift can therefore be attributed to uncertainties in the wavelength calibration. In conclusion the deduced wavelength correction will be applied to all spectra of this thesis. But even after the correction, smaller deviations can be expected and will be addressed when relevant.

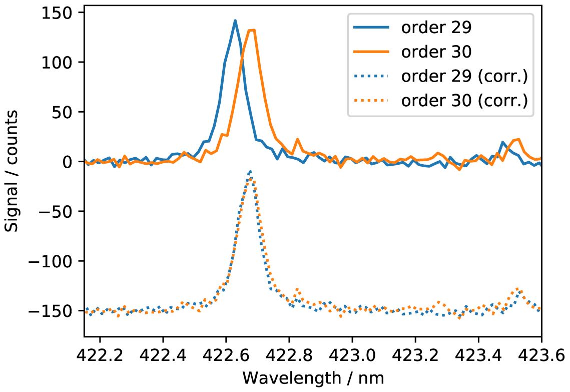

Figure 3.3.8: *A close-up of a Ca I emission line in the LIBS spectrum of a carbonate sample. The emission line is seen in two consecutive orders (order 29 and 30) before and after the applying wavelength correction. The corrected spectrum is shown with a negative offset. After the correction it is seen that the emission line has the same center wavelength in the two orders.*

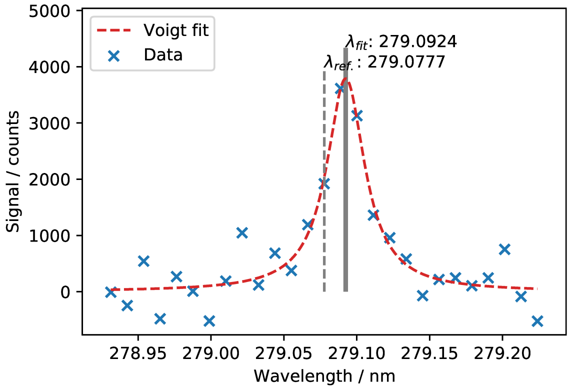

Figure 3.3.9: *A close-up of a Mg II emission line in the LIBS spectrum of a Carbonate sample. The wavelength correction has been applied to the spectrum. The emission line has been fitted with a Voigt profile and the center wavelength extracted* (λ_{ref})*. The fitted value is seen to deviate from the reference value* (λ_{ref})*. The uncertainty in the fitted value is indicated by the width of the horizontal line. The deviation can not be attributed to Stark shift and must be due to uncertainties in the wavelength calibration even after applying the wavelength correction.*

3.3.3 Intensity Response

The intensity response is a function of wavelength and covers the transformation from counts in the detector to more physical units such as photons or photons per nm emitted by a source. The response function is therefore important for comparing spectra obtained from different setups or for the comparison of measured and simulated spectra. In principle the intensity response can be deduced from the optical components of the setup. But as this is rather complicated, the response is usually determined experimentally by measuring the spectrum of a calibrated light source whose spectrum is known.

For the intensity response of this setup, a fiber coupled broadband plasma lamp was used. The reference spectrum of the lamp is shown in Figure 3.3.10. The reference spectrum was obtained by a colleague at the DLR using already intensity calibrated spectrometers (AvaSpec-Mini). The reference spectrum is not known absolutely, but only relatively. The intensity response of the setup can therefore only be determined relatively for the different wavelengths. As for the determination of the instrumental broadening, the output fiber of the plasma lamp could not be placed exactly at the position of the samples. Instead it was placed ∼5 cm above. Nonetheless, the path of the light from the plasma lamp goes through the same optical objects as the light from an induced plasma would do. The measured spectrum of the plasma lamp is shown in Figure 3.3.11. The intensity response, obtained by the measured spectrum divided by the reference spectrum, is shown in Figure 3.3.12a. The calibration of a spectrum is then done by multiplying the measured signal with the inverse of the intensity response, i.e. the inverse of the curve in Figure 3.3.12a. In Figure 3.3.12b, the relative statistical uncertainty of the intensity response is shown. It can be seen to be below 1.5 % at most wavelengths, but also to be very big at at the lowest and highest wavelengths. This is due to the low response of the setup at these wavelengths. Consequently, wavelengths below 273 nm will be cut away. Ideally, the intensity response is determined from a source with a flat and smooth spectrum. This is not the case of the plasma lamp for wavelengths larger than 800 nm, where two large peaks can be seen (Figure 3.3.10). As the reference spectrum was obtained from a spectrometer with a much smaller spectral resolution than this setup, the determined intensity response around these peaks might be prone to larger errors. Consequently, wavelengths higher than 800 nm will also be cut away.

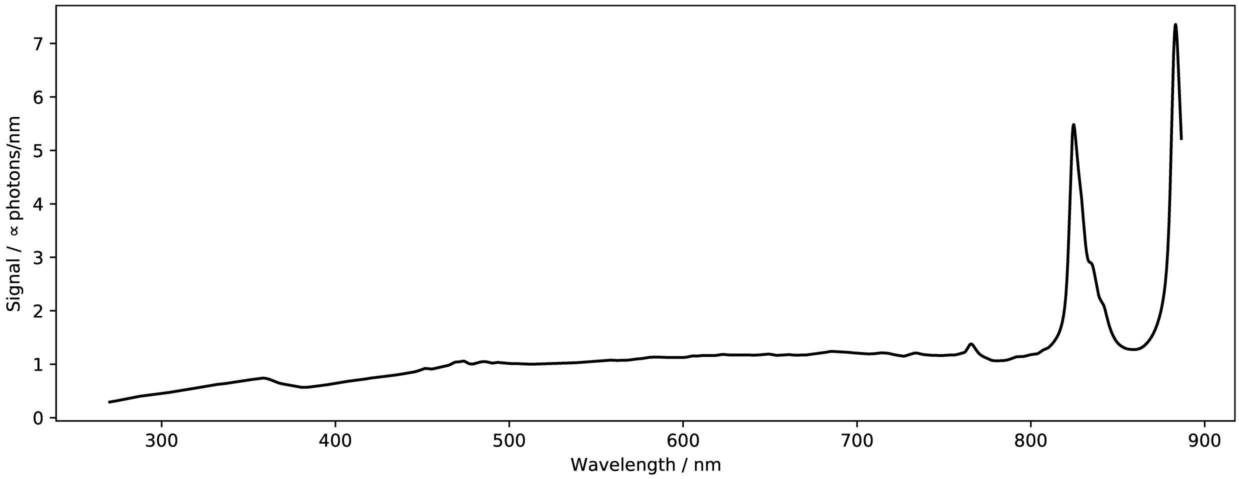

Figure 3.3.10: *Reference spectrum of the lamp used for the intensity calibration.*

In Figure 3.3.13, a spectrum is shown with and without the intensity calibration. The spectrum is of a carbonate sample recorded with zero delay time. Thereby it contains a non negligible background spectrum from continuum emissions. By comparing the non-calibrated and calibrated spectra (Figure 3.3.13a and b) it can be seen that the calibrated spectrum appears smoother than the non-calibrated as many of the "bumps" from the blaze function are removed. In the close-up showing the calibrated spectrum in the UV range (Figure 3.3.13c), it can be seen that the spectrum in the different orders align well. However, this is not the case for the orders at the higher wavelengths. This is exemplified in Figure 3.3.13d, where a ∼25 % discrepancy at the order overlap around 540 nm is pointed out. At this position, the spectrum consists of continuum radiation that is slowly varying and the discrepancy of 25 % is therefore considered as an uncertainty in the intensity calibration. This uncertainty is much larger than expected from the statistical uncertainty of the intensity response which is around 1.5 % (see Figure 3.3.12b). The estimation of the intensity response has been done in three separate experiments. The experimental data that provided the best results, evaluated by calibrating spectra containing continuum emission such as in Figure 3.3.13, are the ones shown here.

In order to correct the intensity response function, the discrepancies at the order overlaps were studied more systematically and for more LIBS spectra. Generally, it was found that the discrepancies at the order overlaps in the UV are small/negligible but that they get larger for larger wavelengths where it appears as if the spectrum in each order was tilted counter clockwise (see Figure 3.3.13d). As the spectrum in each order

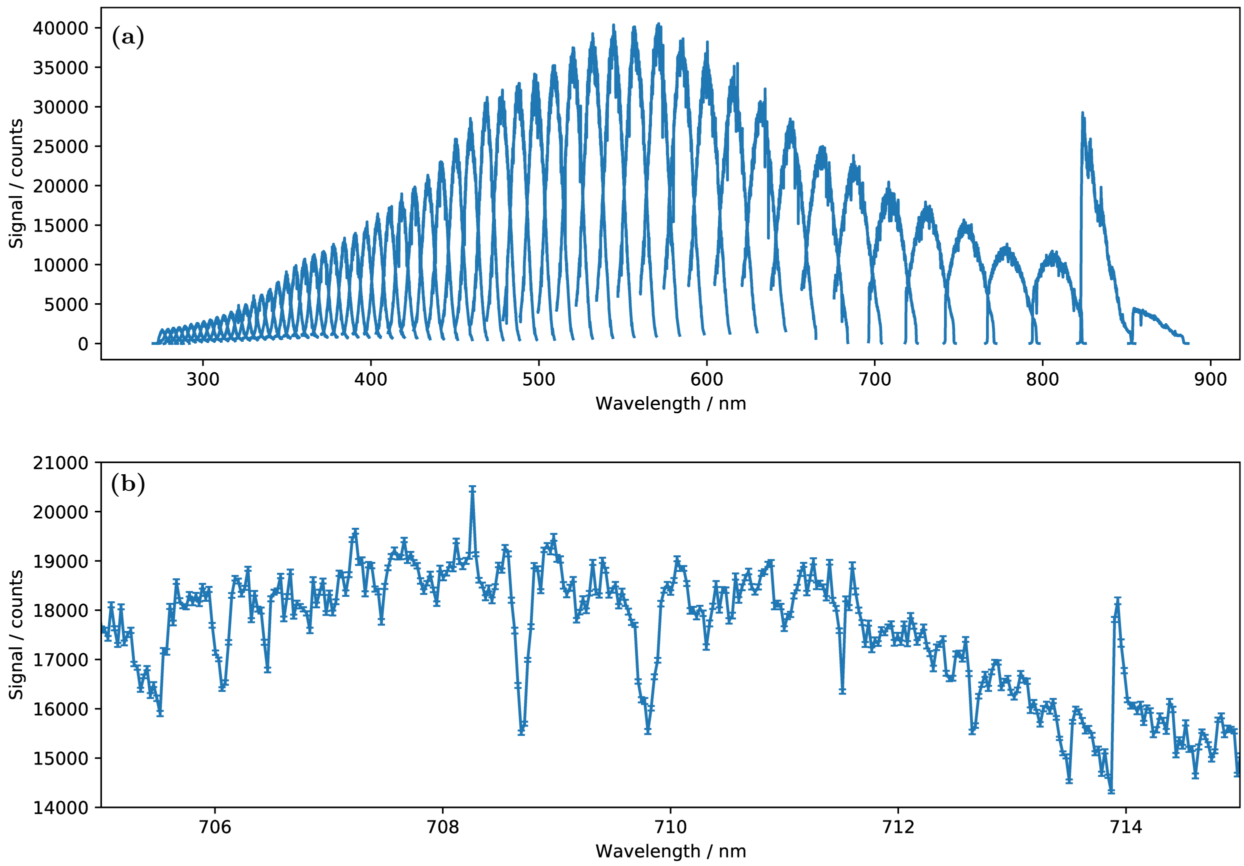

Figure 3.3.11: *Measured spectrum of the plasma lamp.* ***(a)*** *The median spectrum of 60 repetitions.* ***(b)*** *close-up of the median spectrum at around 700 nm. The horizontal bars indicates the uncertainties as obtained from the standard deviation of the repetitions. Here some spikes are seen in the otherwise smooth spectrum. These cannot be attributed to noise since they are larger than the statistical fluctuations marked by the horizontal bars.*

is determined by the pixels in the horizontal direction, the tilted appearance could be due to a systematic and increasing underestimation of the signal of the plasma lamp towards the right edge of the raw detector image (see Figure 3.1.2). Such systematic underestimation could be explained by a misalignment of the plasma lamp with the optical axis of the spectrometer. By misalignment of the plasma lamp, the conversion from the raw detector image into a spectrum, that is made in a fixed pattern by the spectrometer software, could thereby be disturbed. As the order overlap is bigger in the UV part of the spectrum, mostly the central part of the detector image is used for the generation of the spectra is this range. A systematic and increasing underestimation of the intensity towards the right edge of the detector image, would therefore also explain why the discrepancies are observed to be smaller in the UV range. Following this hypothesis, a correction factor, f, for the intensity of each order of a measured spectrum is introduced as

$$f(p) = 1 + (1024 - p) \cdot a \ , \tag{3.3.2}$$

where p is the horizontal pixel in the raw detector image and a is a parameter describing the strength of the correction. The number 1024 corresponds to the right most horizontal pixel. The correction factor can be considered as a first order correction. As the correction factor is to be applied in each order, the overall shape of the intensity response will be kept. By demanding that the pixels in two consecutive orders at the wavelength of the order overlap have equal intensities, after applying the intensity response, a system of linear

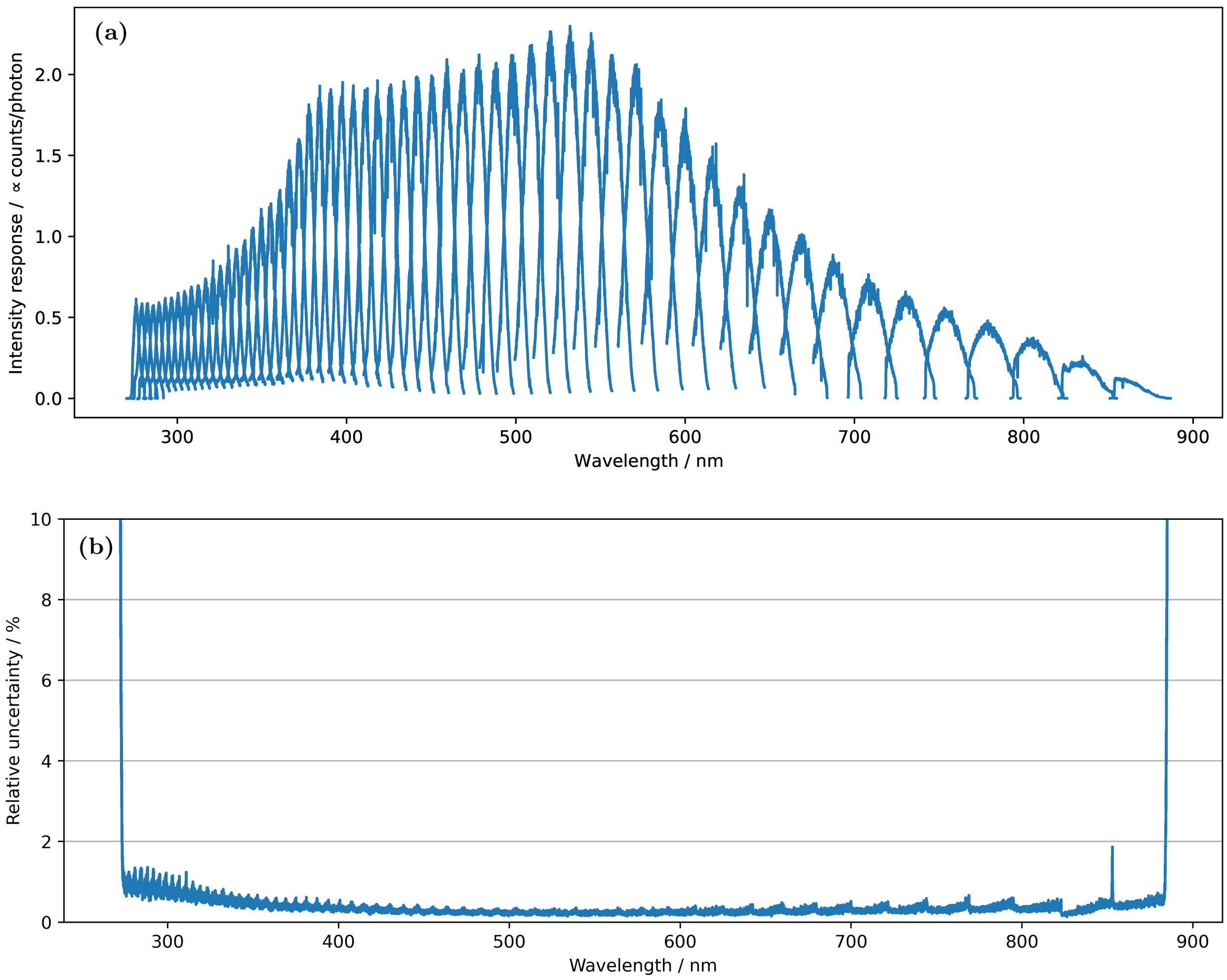

Figure 3.3.12: ***(a)*** *The determined intensity response of the setup.* ***(b)*** *The statistical uncertainty of the intensity response obtained from the uncertainties of the measured spectrum (Figure 3.3.11).*

equation can be obtained for the parameter a of the correction:

$$\begin{aligned}
I_{order_1,\lambda_{1,2}} \cdot (1 + (1024 - p_{order_1,\lambda_{1,2}}) \cdot a) &= I_{order_2,\lambda_{1,2}} \cdot (1 + (1024 - p_{order_2,\lambda_{1,2}}) \cdot a) \\
I_{order_2,\lambda_{2,3}} \cdot (1 + (1024 - p_{order_2,\lambda_{2,3}}) \cdot a) &= I_{order_3,\lambda_{2,3}} \cdot (1 + (1024 - p_{order_3,\lambda_{2,3}}) \cdot a) \\
I_{order_3,\lambda_{3,4}} \cdot (1 + (1024 - p_{order_2,\lambda_{3,4}}) \cdot a) &= I_{order_4,\lambda_{3,4}} \cdot (1 + (1024 - p_{order_4,\lambda_{3,4}}) \cdot a) \\
&\vdots
\end{aligned} \tag{3.3.3}$$

where $I_{order_1,\lambda_{1,2}}$ is the pixel intensity in order 1 at the wavelength of overlap between order 1 and 2, $\lambda_{1,2}$. $p_{order_1,\lambda_{1,2}}$ is the horizontal pixel number in order 1 at the wavelength of order overlap. The equation can be expanded for several LIBS spectra. This has been done using nine different LIBS spectra all displaying a good amount of continuum radiation just like the spectrum in Figure 3.3.13. By solving the system of equation using linear least squares, a value for a of -0.00037 is obtained. In Figure 3.3.14, the LIBS spectrum of a Martian regolith simulant can be seen. The spectrum is shown without any intensity calibration, with intensity calibration, and with intensity calibration and the additional correction given by equation (3.3.2). This spectrum was not among the nine spectra used for determining the strength of the correction (the value of a). From the figure, it can be seen that the correction provides a smoother transition between the spectra in the different orders. The correction is therefore included in the intensity response and thereby utilized in the intensity calibration of the spectra of this thesis. Finally, calibrated and un-calibrated spectra can be distinguished by the units of the intensity that will be in either photons or counts, respectively.

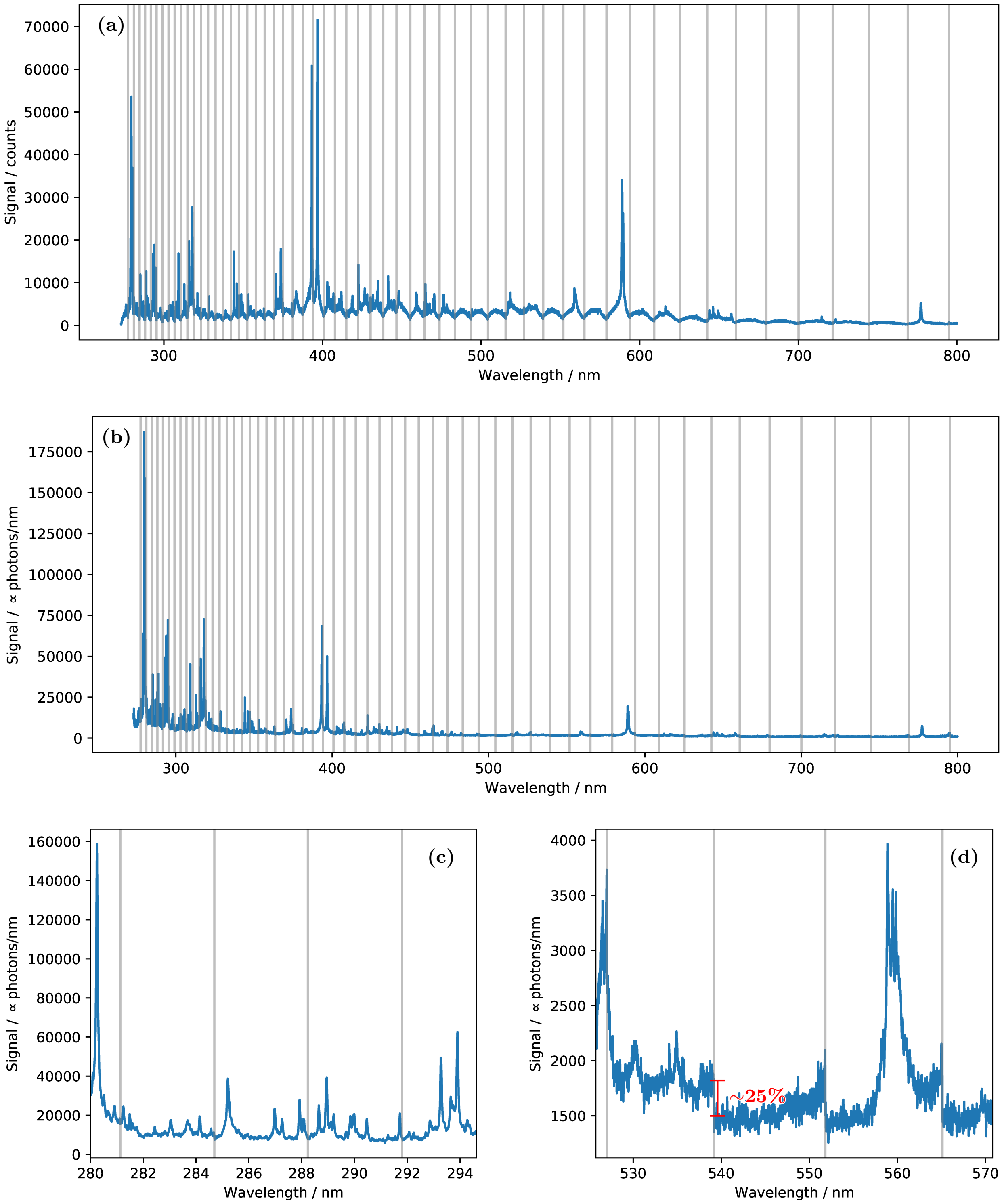

Figure 3.3.13: *LIBS spectrum of a carbonate target. The spectrum was acquired with delay time less than 50 ns and with an exposure time of 50 ns. The horizontal lines indicate the order overlaps.* ***(a)*** *Un-calibrated spectrum.* ***(b)*** *Intensity calibrated spectrum.* ***(c,d)*** *close-up of the calibrated spectrum in different wavelength ranges.*

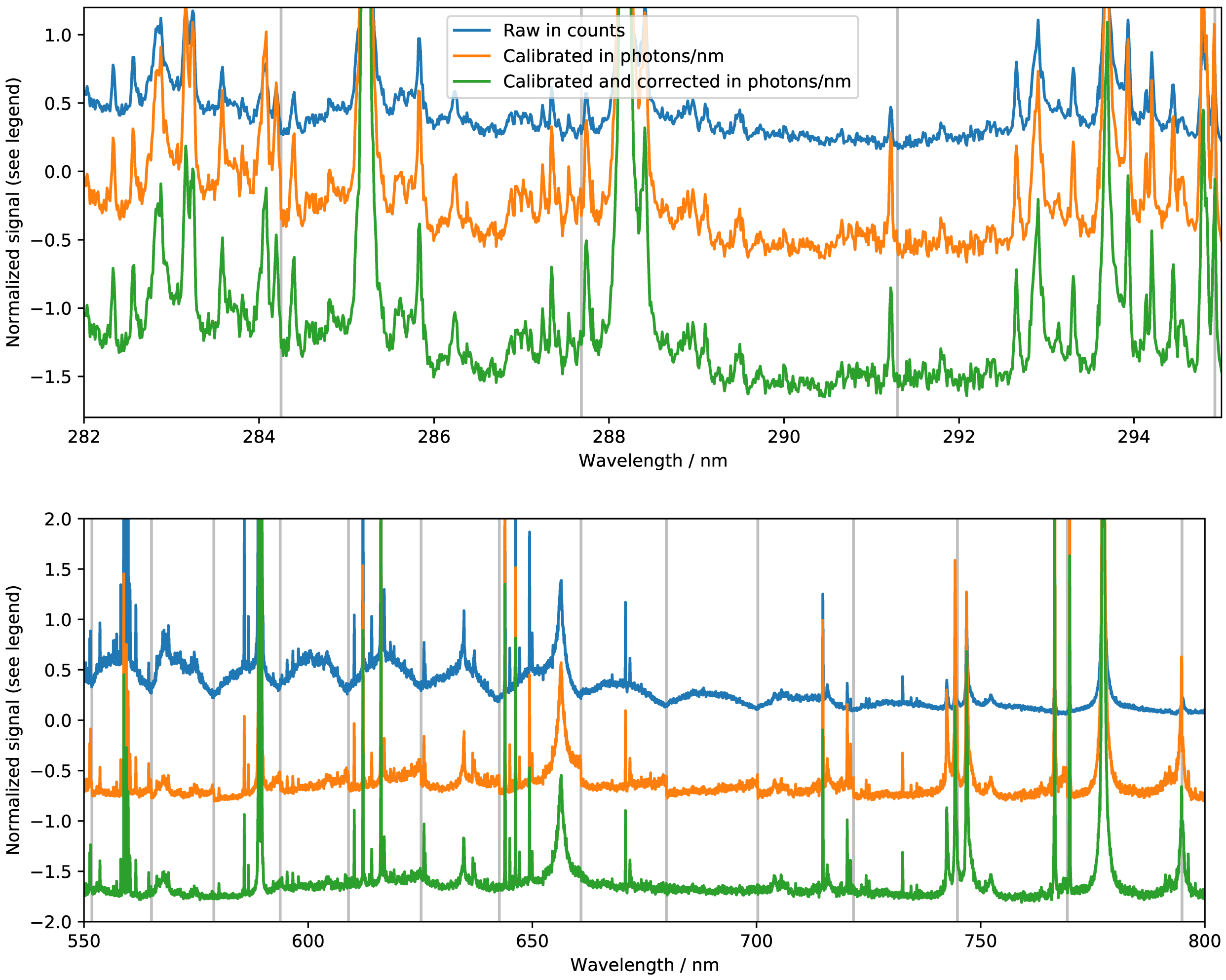

Figure 3.3.14: *The LIBS spectrum of a Martian regolith simulant. The spectrum is shown in the UV and in the NIR range and shown without any calibration (blue curve) with the intensity calibration (orange curve) and with the intensity calibration and the correction by* (3.3.2) *(green line). The spectra are normalized and shown with an offset. The intensity units are given in the legend. The horizontal lines indicates the order overlaps. By comparing the spectra, it can be seen that the correction leads to a more smooth transition between the orders.*

3.3.4 Spectral Noise

The noise in the spectra comes from different sources. The main sources are the generation of thermal electrons in the detector, during a measurement, the read out noise from the electronics in the detector, and finally the photon noise due to the stochastic process of detecting the incoming photons. The two first terms are independent of any incoming light and are well seen in blank spectra, i.e. spectra without any light source. This noise will be referred to as the zero'th level noise. An example of a blank spectrum is seen in Figure 3.3.15. In the blank spectrum, the zero level noise can be seen to decrease with increasing wavelengths. This is a consequence from how the spectra are generated from the raw 2D detector images. As seen from the detector image in Figure 3.1.2b, the spacing between the orders decreases with increasing wavelengths. Therefore, the intensities at the higher wavelengths are obtained from fewer pixels (less vertical binning) and thereby less zero level noise. By gathering the intensity values of the blank spectrum in smaller wavelength ranges and plotting them in histograms, it can be seen that the zero level noise is well described by a Gaussian profile with a width decreasing exponentially towards higher wavelengths. This is shown in Figure 3.3.16. The Gaussian distribution of the noise will become important later in this thesis when extracting peaks and estimating their uncertainties (Chapter 4) and 5).

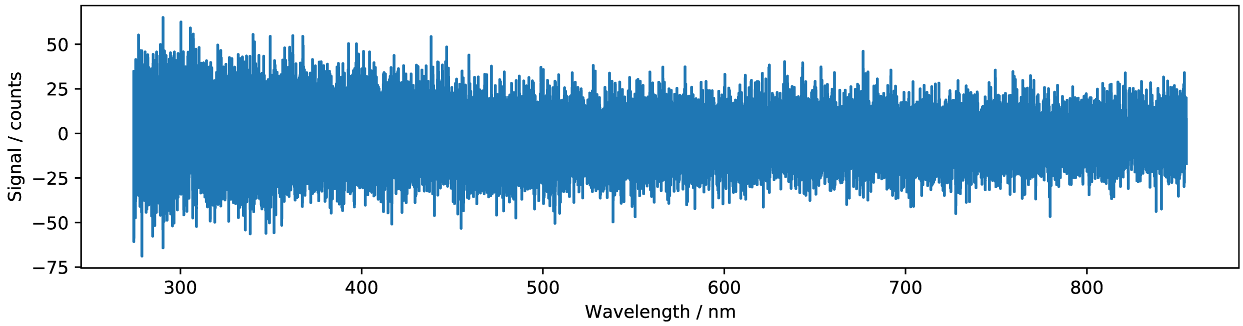

Figure 3.3.15: *Spectrum obtained without any light source in a dark room. Since no or very few photons have been detected, the spectrum is dominated by thermal and read out noise.*

Opposite to the zero'th level noise, the photon noise is dominant at high detector counts. In the spectra of the plasma lamp for the determination of the intensity calibration, there are lots of counts. The noise in these spectra is therefore dominated by the photon noise. That means that the root-mean-square-error (RMSE) in the intensity of the 60 repetitions should be well described as

$$RMSE(y) = \sqrt{y \cdot g} \ , \tag{3.3.4}$$

where y is the spectrum of the plasma lamp obtained as the mean of the many repetitions and g is the spectrometer gain. This function has been fitted to the RMSE obtained from the repetitions of the plasma lamp spectrum and the gain is found to be 9. The results are summarized in Figure 3.3.17.

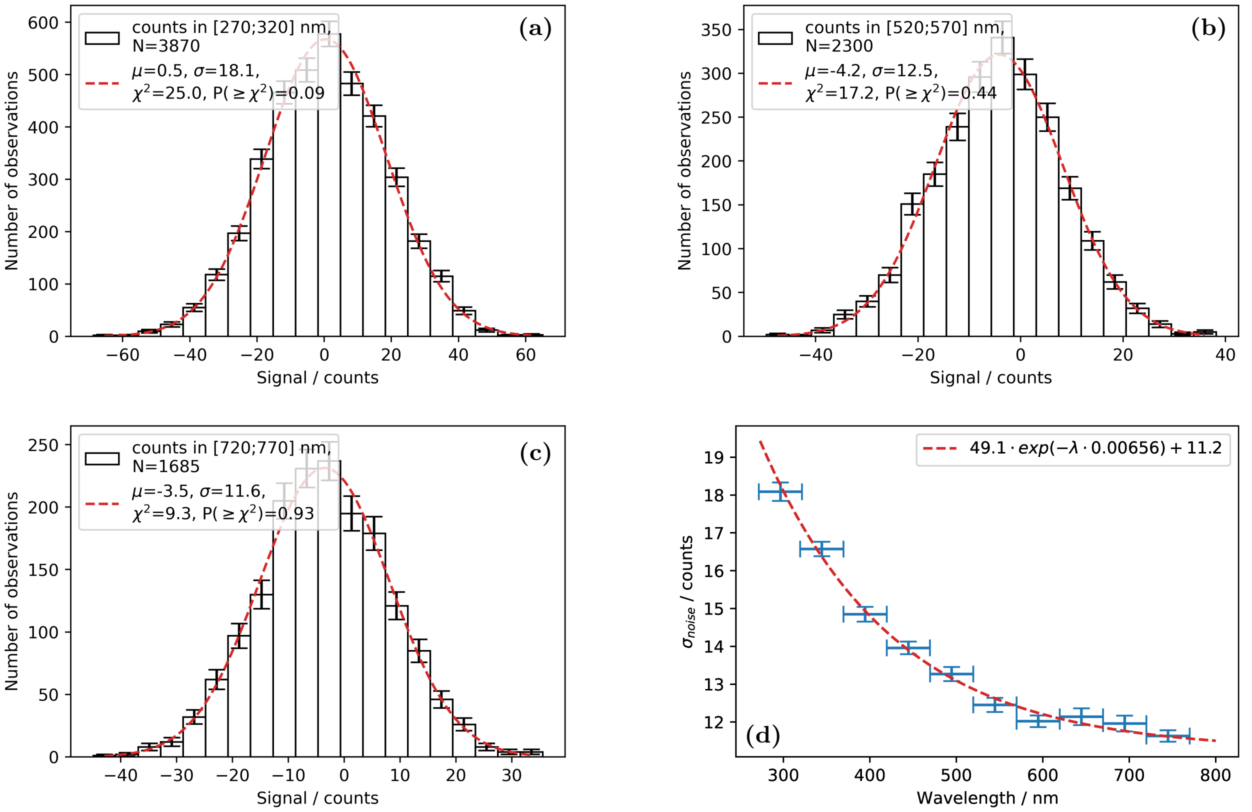

Figure 3.3.16: ***(a-c)*** *The counts in the spectrum of Figure 3.3.15 binned for different wavelength areas and shown as histograms together with fits of Gaussian functions.* μ *are the mean of the Gaussians and* σ *are the widths. From the* χ^2 *probabilities, it can be seen that the noise is well explained by the Gaussian functions.* ***(d)*** *The widths from the Gaussian profiles plotted against wavelengths. The horizontal bars indicates the wavelength range wherein the intensities were binned and fitted. The vertical bars indicate the uncertainty of the widths as obtained from the fits. From* ***(d)*** *it is seen that the Gaussian widths for different wavelengths are well modelled by an exponential function.*

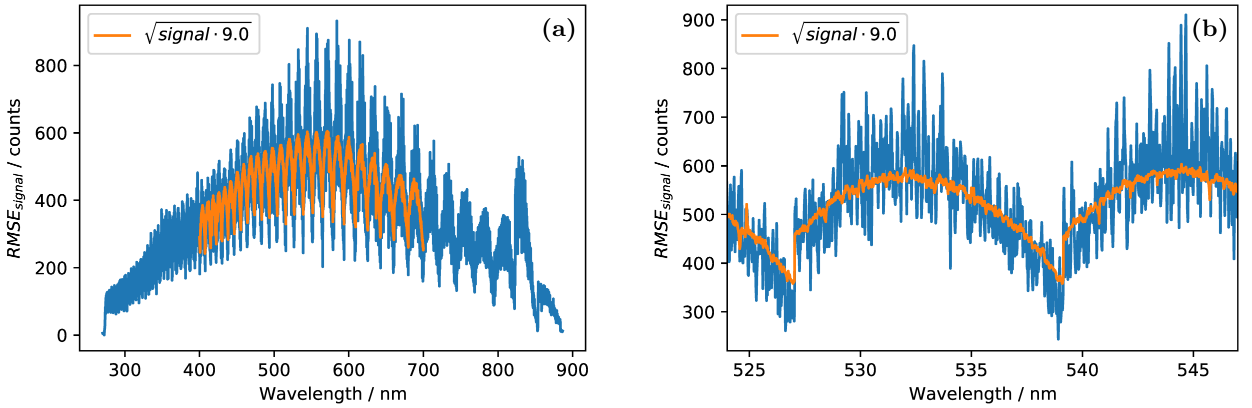

Figure 3.3.17: *The RMSE of the intensities in the spectrum of the plasma lamp (blue curve) shown together with the expected fluctuation (equation 3.3.4) from photon noise with a spectrometer gain of 9 (orange curve).* ***(a)*** *Full spectral range.* ***(b)*** *Close-up. From the plots it seen that the RMSE is well explained by the photon noise with a gain of 9.*

Chapter 4

Simulation and Fits of LIBS Spectra

In this chapter, it is first described how LIBS spectra are modeled and simulated from a plasma divided into homogeneous zones along a LOS. Thereafter, a method of fitting simulated spectra to an input spectrum is described. Finally, the simulation and fits of spectra is applied to both synthetic test spectra and measured time-resolved LIBS data obtained in Martian atmospheric conditions. Most of the matter of this chapter has been published in an article [80].

4.1 Modelling and Simulation of LIBS Spectra

4.1.1 Plasma Model

The model of the plasma is that of a stationary plasma in LTE. In LTE, the state of the plasma is completely described by a set of plasma properties, i.e. the plasma temperature and the densities of the species (see Chapter 2). The modelling of the plasma is therefore reduced to modelling these properties along the relevant LOSs through the plasma. The LIBS setup used in this thesis has a small field of view with a small acceptance angle of approximately 0.25 mm^2 and 6°, respectively (see Chapter 3). A schematic of the field of view is shown in Figure 4.1.1a. For comparison, it is shown on top of a LIBS plasma with a size of 3.5 mm corresponding to the approximate size of a plasma after ~200 ns in Martian atmospheric conditions. For the simulation of spectra, the light collection geometry will be approximated by a single LOS through the center of the plasma as shown in Figure 4.1.1b. As the plasma emission is only observed along this single LOS, the plasma properties need only to be modeled along that. This results in a one-dimensional plasma model. The validity of the single LOS approximation depends on the variation of the plasma properties along the width of the actual field of view. That is, the variation across an area of approximately 0.25 mm^2. Shortly after initiation of the plasma, the size of the plasma is smaller than 0.5 mm and the single LOS approximation is obviously not a good approximation. After ~200 ns of expansion, the size of the LIBS plasma in Martian atmospheric condition would be around 3.5 mm [58]. At this time, the length of the plasma is seven times larger than the field of view and the single LOS approximation is more reasonable. For example, assuming a linear temperature variation of 8000 K across the plasma (orthogonal to the LOS in Figure 4.1.1b), the variation inside the field of view would only be one seventh of that, i.e. 1150 K. At later times, when the plasma might have expanded further, the single LOS approximation might be better and likewise if the plasma core is more homogeneous.

Along the LOS, the plasma is assumed to be composed of a series of homogeneous zones. While plasma temperature, electron density and lengths of the zones can vary independently from zone to zone, the elemental densities are constrained to follow the same distribution resulting in equal relative elemental concentrations in all the zones:

$$\frac{n_{i,zone_1}}{n_{j,zone_1}} = \frac{n_{i,zone_2}}{n_{j,zone_2}} = \dots \ , \tag{4.1.1}$$

where i and j refer to the elements. A schematic drawing of such a plasma is shown in Figure 4.1.2. Due

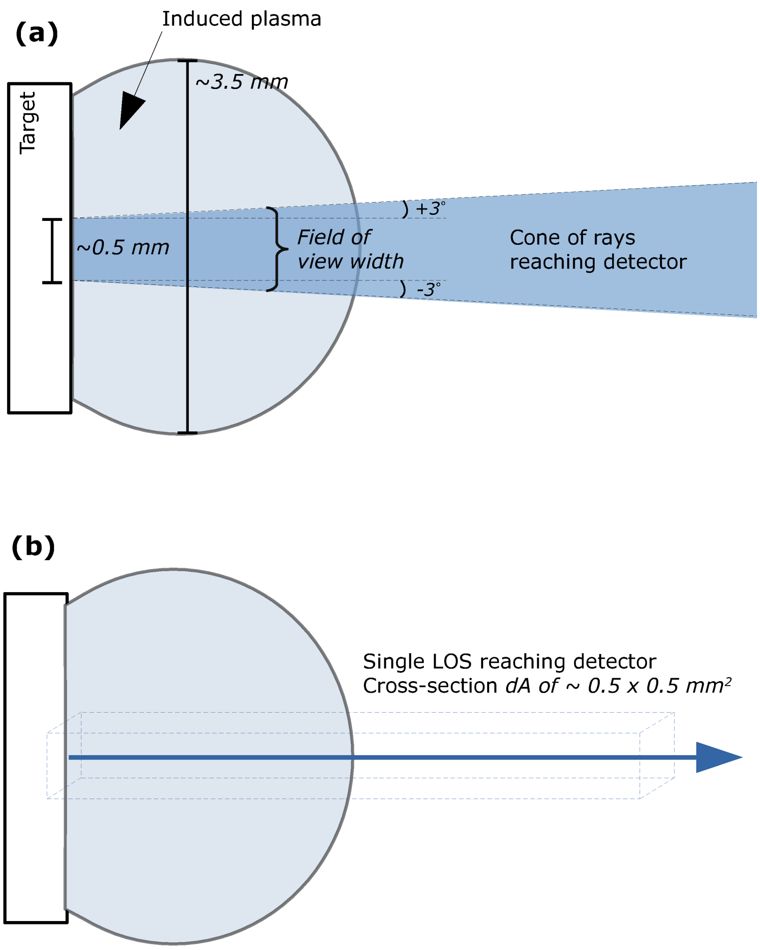

Figure 4.1.1: ***(a)*** *Schematic of the light collection and a LIBS plasma after a few hundred nanoseconds. The LOSs/rays passing through the plasma that reaches the detector of the setup are marked. These rays make up the field of view of the spectrometer. The width in both dimensions of the field of view is smaller than the dimension of the plasma (~0.5 mm versus 3.5 mm).* ***(b)*** *Single LOS approximation of the field of view.*

to the assumption of equal relative concentrations, the elemental densities are conveniently modelled by the elemental densities in the first zone, $n_{s,0}$, which is closest to the sample surface, and by relative values in the following zones described by the relative distribution n_{rel}. n_{rel} is thereby equal for all elements but can vary independently from zone to zone. As example, the concentration of element i in zone k is given as:

$$n_{i,zone_k} = n_{i,0} \cdot n_{rel,k} \ . \tag{4.1.2}$$

As discussed in Chapter 2 and illustrated in Figure 2.1.2, the elements originating from the atmosphere and the sample/target have significantly different distributions. This is also obvious from the fact that the atmosphere by definition fills out the entire laboratory or simulation chamber whereas the target material is ejected from the target surface and therefore much more localized. Ideally, one would have two different elemental distributions, i.e. two sets of values for n_{rel}. One for the elements of the target material and one for the elements of the atmospheric material. For this model, only the distribution of the target material will be considered. This is done to simplify the modelling. The lack of an individual distribution for the atmospheric component, means that concentration estimates cannot be obtained for elements of the sample that are also present in the atmosphere/background gas. For Martian atmospheric conditions, these are the elements of C and O. Differences in atomic masses of the elements of the target material might lead to smaller or larger deviations from the approximation of equal relative relative concentrations. This is usually refereed to as as elemental segregation and can be caused by higher expansion velocity distribution of the lighter elements. Segregation of elements in LIBS plasmas has been studied experimentally in [46] and [81] for deuterium and hydrogen and in [82] for nickel, iron and aluminum. In [46], the segregation of hydrogen and deuterium was studied in a low pressure argon environments from 100 Pa to 500 Pa. It was concluded that segregation could lead to measurement uncertainties of 50 %. It was also argued that the uncertainties could be reduced by going to earlier observation times and that segregation would be negligible at increased pressures. The last hypothesis was confirmed in [81] where the segregation of deuterium and hydrogen was found negligible at atmospheric pressure and likewise in [82] where no segregation between nickel, iron and aluminium was observed. Lastly, the plasma will be assumed non-reactive by neglecting the formation of molecules. The validity of this assumption also depends on the time of observing the plasma and on the reactants, i.e. the composition of the target. Carbon and Oxygen form strong bonds that might persist at temperatures up to ~10 000 K whereas other molecules such as CaO, MnO, MgO and NaO mostly exist at temperatures below 5000 K. This is because of difference dissociation energies.

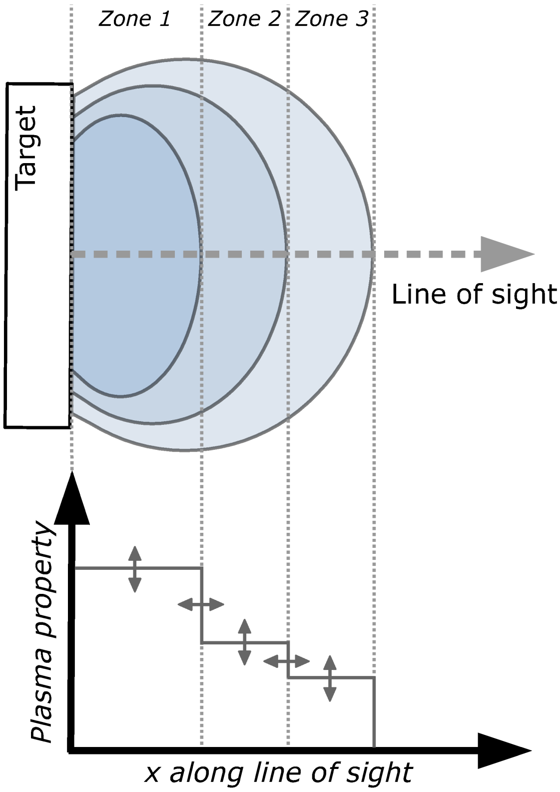

Figure 4.1.2: *Schematic drawing of the LIBS plasma divided into three homogeneous zones along the line of sight through the center of the plasma (top). Additionally, it is shown how the plasma properties may vary from zone to zone (bottom).*

4.1.2 Modelling of Spectra

The modelling and simulations of LIBS spectrum are based on the LOS radiance calculated from the one dimensional radiative transfer (equation (2.2.23) in Chapter 2) and the plasma model described above. But for simulating spectra comparable to measurements, the instrumental broadening and the intensity response of the setup need to be considered. As described in Chapter 3, the instrumental broadening can be well described by a Gaussian function with a FWHM increasing linearly with increasing wavelengths (see Figure 3.3.5 in Chapter 3). Consequently, the instrumental broadening will be modelled by convolution of the LOS radiance with this Gaussian function. A simulated spectrum, comparable to a measured spectrum, can thereby be written as

$$\hat{I}_\lambda\left(\lambda;\vec{T},\vec{n}_e,\vec{n}_0,\vec{n}_{\mathrm{rel}},\vec{\Delta x},\Delta t\right)=I_\lambda\left(\lambda;\vec{T},\vec{n}_e,\vec{n}_0,\vec{n}_{\mathrm{rel}},\vec{\Delta x}\right)\cdot dA\cdot\Delta t\cdot \mathrm{IR}(\lambda)*b_{\mathrm{instr}}(\lambda)\ , \tag{4.1.3}$$

where I_λ is the LOS radiance at a wavelength λ (equation (2.2.23) in Chapter 2), $\vec{T}$ a vector containing the temperatures of the zones, $\vec{n}_e$ the electron densities, $\vec{n}_0$ the elemental densities in the first zone and $\vec{n}_{\mathrm{rel}}$ the relative elemental concentration in the following zones according to equation (4.1.2), and $\vec{\Delta x}$ containing the lengths of the zones. dA is the cross section of the LOS, Δt the exposure time of the measurement, and IR the absolute intensity response function of the setup covering the transformation from the radiance at the end of the LOS to counts in the detector. Finally, $*b_{\mathrm{instr}}$ denotes the convolution with the Gaussian function for simulating the instrumental broadening. As the intensity response of the setup was determined relatively (Figure 3.3.12 Chapter 3) the absolute response can be written as the relative response times an unknown wavelength independent factor F

$$\mathrm{IR}(\lambda) = F \cdot \mathrm{IR}_{\mathrm{rel}}(\lambda). \tag{4.1.4}$$

Instead of multiplying by the IR in equation (4.1.3), the measured spectra are calibrated relatively using $\mathrm{IR}_{\mathrm{rel}}$ and only the unknown factor F remains on the right hand side. For simplicity F is redefined to also contain the product of the LOS cross section and the exposure-time ($dA \cdot \Delta t$). As F only depends on experimental parameters, it will be referred to as the experimental parameter. A simulated spectrum, comparable to measured and calibrated spectra, can then be written as

$$\tilde{I}_\lambda\left(\lambda; \vec{T}, \vec{n}_e, \vec{n}_0, \vec{n}_{\mathrm{rel}}, \vec{\Delta x}, F\right) = I_\lambda\left(\lambda; \vec{T}, \vec{n}_e, \vec{n}_0, \vec{n}_{\mathrm{rel}}, \vec{\Delta x}\right) \cdot F * b_{\mathrm{instr}}(\lambda)\ , \tag{4.1.5}$$

where $\tilde{I}_\lambda = \hat{I}_\lambda / \mathrm{IR}_{\mathrm{rel}}$. Since the LOS radiance depends uniquely on the product of the elemental densities and the zone lengths (see Chapter 2), it is convenient to define the effective path of the first zone as

$$\vec{\tilde{n}}_0 = \vec{n_0} \cdot \Delta x_{zone_1} \tag{4.1.6}$$

and in analogue to the relative concentrations in eq. (4.1.2), also to define the relative effective path $\vec{\tilde{n}}_{\mathrm{rel}}$ for the description of the effective path in the following zones. Equation (4.1.5) can then be written as

$$\tilde{I}_\lambda(\lambda; \vec{T}, \vec{n}_e, \vec{\tilde{n}}_0, \vec{\tilde{n}}_{\mathrm{rel}}, F) = I_\lambda(\lambda; \vec{T}, \vec{n}_e, \vec{\tilde{n}}_0, \vec{\tilde{n}}_{\mathrm{rel}}) \cdot F * b_{\mathrm{instr}}(\lambda)\ , \tag{4.1.7}$$

which contains fewer input parameters as compared with equation (4.1.5). For the modelling of a spectrum in a two-zone approximation there will be $6 + K$ input parameters: one for the value of F, two for the value of the temperature, two for the electron density, one value for the relative effective path $\tilde{n}_{\mathrm{rel}}$, and K values for $\tilde{n}_0$, where K is the number of elements in the plasma. For the modelling of a spectrum in an N-zone approximation there will be $3N + K$ parameters.

4.1.3 Spectral Database

For enabling the simulations of spectra, a custom database containing the necessary data for evaluating the LOS radiances has been build around the NIST Atomic Spectra Database [74]. The necessary data are comprised of the ionization energies and electronic levels of the atomic species, and the wavelengths, Einstein coefficients, and Stark parameters of the transitions of the species. With the exception of Stark parameters, the NIST database contains all the necessary data. NIST has been compiled from data collected and critically evaluated by the NIST team throughout several years. Although limited to critically evaluated data, the database contains a total of 112,230 atomic electronic levels and 285,000 emission lines where approximately 42 % of them are given with Einstein coefficients and the remaining atomic constants for evaluating LOS radiances. For the database of this thesis, the atomic data for the most relevant and less exotic elements have been downloaded for wavelengths between 100 nm and 2000 nm. Using the electronic levels, electronic partition functions have been pre-calculated and tabulated for different values of temperatures and ionization potentials according to equation (2.2.15) in Chapter 2. This has been done for species up to at least four times ionized. By interpolation of the tabulated values, partition function values can quickly be accessed. An example of the electronic partition functions of calcium can be seen in Figure 4.1.3.

In spite of the impressive number of emission lines with Einstein coefficients, several emission lines where no Einstein coefficients are available from the NIST database have been encountered. Some of these gaps for the elements of Al, Ag, Ca, Ti, Mn, O, P, C, and Fe have been closed sporadically throughout this thesis using the data from the Kurucz database (Kurucz CD-ROM No. 23) [83]. The Kurucz database is compiled from semi-empirical calculation and for some elements it seems more complete in terms of numbers of lines. For

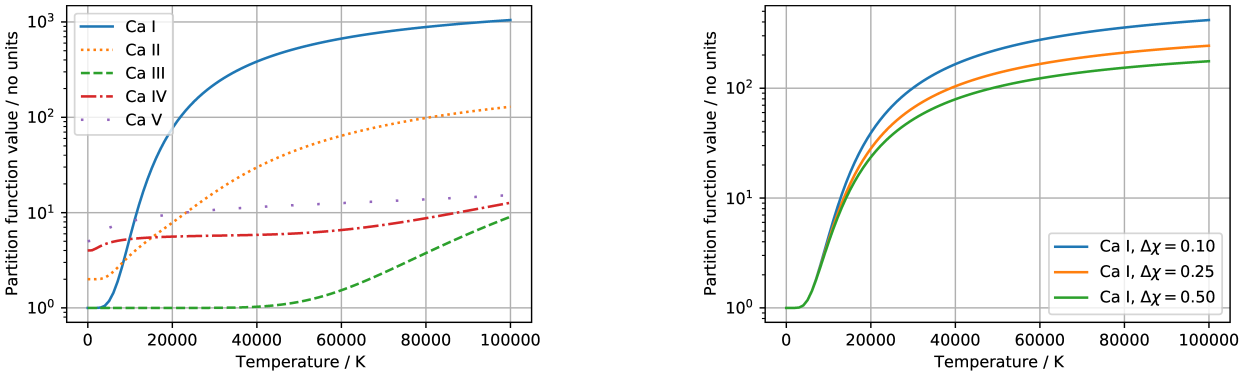

Figure 4.1.3: *Example of calculated internal partition functions of Ca species using the NIST data. The values have been evaluated using equation* (2.2.15) *from Chapter 2.* ***Left:*** *Different species with an ionization lowering of* 0.1 eV*.* ***Right:*** *Neutral calcium but for different values of the ionization potential lowering.*

example, the NIST database contains 718 emission lines with Einstein coefficients from Cr I-IV in the range of 200 nm to 1000 nm whereas the Kurucz contains more than 10 000. Until now, a total of 241 lines have been added (see Appendix B) and for Cr only the data from Kurucz is used. In summary, a total of 53 elements is contained in the custom database resulting in a total of 72646 lines with wavelengths between 100 nm and 2000 nm. An overview of the elements and number of emission lines can be seen in Figure 4.1.4.

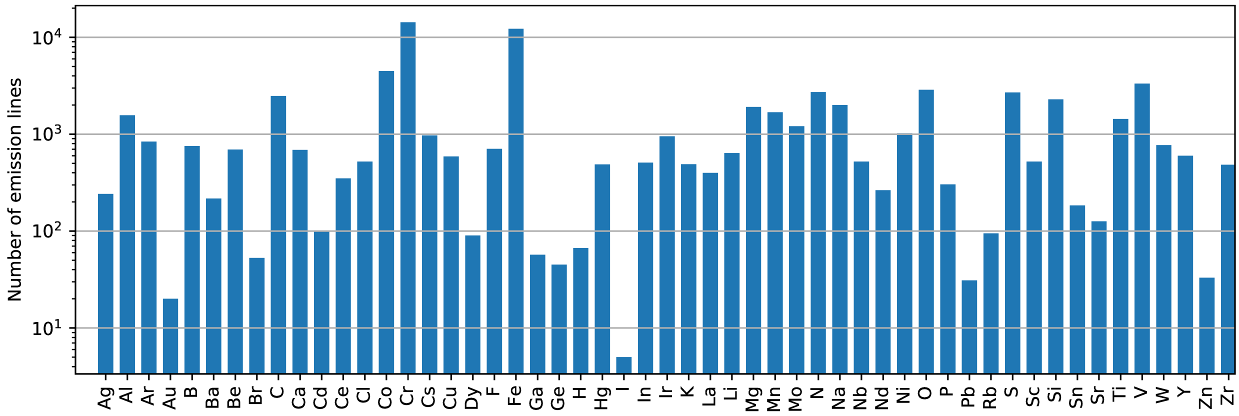

Figure 4.1.4: *Overview of the elements contained in the database and the number of lines from each element with wavelength within* 100 nm *and* 2000 nm *with the sufficient atomic parameters for calculating their intensities. The number of emission lines varies with the elements due to their different internal structure, but also due to the completeness of the NIST database. For example the NIST database only contains five lines for iodine (I) with Einstein coefficients. They are all below* 210 nm*, but iodine emission lines have been observed in LIBS spectra in the visible range [84].*

The Stark broadening and Stark shift parameters, for evaluation the line profiles, have mainly been taken from the STARK-B database [63]. The database contains the Stark parameters as predicted by the impact approximation. The parameters are given by fitting coefficients, a_0, a_1, a_2, b_0, b_1, and b_2 for also describing the weak temperature dependence as

$$\log(W_{\mathrm{FWHM}}) = a_0 + a_1 \cdot \log(T) + a_2 \cdot \log(T)^2 \tag{4.1.8}$$

$$D/W_{\mathrm{FWHM}} = b_0 + b_1 \cdot \log(T) + b_2 \cdot \log(T)^2 \ , \tag{4.1.9}$$

where W_{FWHM} and D are the Stark broadening and Stark shift parameter, respectively (see equation (2.1.6) and (2.1.7) in Chapter 2). The coefficients are given for different perturbers (free electrons and different ions), but in order to simplify the calculations only the coefficients for free electrons will only used in this thesis. Thereby, the contribution from the ions in the plasma is neglected. For the strong Ca II resonance transitions at 393 nm and 396 nm, the broadening from singly ionized helium is one tenth of the broadening from electrons with both perturbers at an density of $1 \times 10^{23}\,\mathrm{m}^{-3}$ and a temperature of 10 000 K [63]. This is smaller than the approximate accuracy of the calculated values that is around 20 % [63]. The STARK-B database contains the parameters for many LIBS relevant emission lines, but not for all of them. For example, within the wavelength range of 285 nm to 9000 nm there are Stark parameters for 16 different Na I multiplets corresponding to 109 individual emission lines. On the other hand, there are no data for Mn I lines at any wavelengths. The STARK-B database has therefore been supplemented with parameters tabulated in the GRIEM database [62] and experimentally found values or theoretical predictions found elsewhere in the literature [64, 85, 86, 87, 88, 89, 90, 91, 92]. Adding additional Stark parameters has been done sporadically when encountering important lines without any. However, this work is far from done and the majority of the downloaded lines do not have any Stark parameters. This is due to a combination of no values being available in the literature, but also due to the large amount of manual work involved in the process of finding and adding the values from different sources. Ideally, I would perform own calculations of Stark parameters via the formulas and descriptions referenced in e.g. [63], but gathering the theoretical knowledge and understanding for doing so is outside the scope of this thesis. The same goes for experimentally determining the parameters. Instead, the Stark broadening parameters of missing lines are determined by interpolating and extrapolating the literature values using a simple heuristic function. This approach is motivated by reported regularities of the Stark broadening parameters. For example, in [93] a good linear correlation between the Stark widths and the effective principal quantum number for singly ionized aluminum is pointed out. Another example is for hydrogen in [92] where their results are directly utilized in the database of this thesis (for hydrogen only). For finding suitable heuristic functions for the interpolation and extrapolation of the other species (element and ion state), the Stark broadening of all the emission lines with Stark parameters from the literature has been evaluated at an electron density of $1 \times 10^{22}\,\mathrm{m}^{-3}$ and a temperature of 10 000 K. It was then found that the Stark widths, of a given atomic species, correlate reasonably well with the reciprocal of the ionization energy in vacuum minus the energy of the upper level of the emission lines. More specifically, the following function was found to provide a fair description of the literature Stark parameters and therefore used as the main function for the interpolation and extrapolation

$$W^* = \frac{500^2}{\lambda^2} \cdot W_{\mathrm{FWHM}}\bigg|_{T=10\,000\,\mathrm{K}, n_e=1\,\times\,10^{22}\,\mathrm{m}^{-3}} = \frac{a_{s,z}}{(\chi_{s,z} - E_u)^{b_{s,z}}}. \tag{4.1.10}$$

In the above equation, W_{FWHM} is the Stark width of an emission line from the element e in the ionized stage z, λ is the wavelength in nm, $\chi_{s,z}$ the ionization energy of the species, and E_u the upper energy level for the emission line, both in eV. The species-dependent coefficients a and b are to be fitted. Contrary to the literature values from STARK-B, the function in equation (4.1.10) contains no temperature dependence and interpolation and extrapolation will be done at a fixed temperature of 10 000 K. The $1/(\chi_{s,z} - E_u)$ dependence in the function can be motivated by considering the rate of collisional excitations and de-excitations. As addressed in relation to the McWhirter criterion in Chapter 2, collisions are more efficient between levels with closely spaced energies. As the spacing between the energy levels decreases for higher excited states (hydrogenic approximation) the highly excited states, and especially those near the ionization limit, will have a high rate of collision induced transitions and thereby a large Stark broadening due to a shortened lifetime. Examples of fits of equation (4.1.10) are shown in Figure 4.1.5 for neutral and singly ionized species of Al, C, O and Fe. For Al I, Al II, C I, O I and O II, the literature values spans more than one order of magnitude but the RMSE of the fits is at most 38 %. It can thereby be concluded that equation (4.1.10) provides a much better approximation of the Stark broadening values from the literature than that of a fixed value. For C II the results are more cumbersome which can be seen by the RMSE of the fit which is 75 %. For Fe I and Fe II, no obvious correlation between the Stark width and the upper energy level is seen. Consequently, equation (4.1.10) is not used, but rather a constant function as indicated by the labels of the plots. In Figure 4.1.6 the results for Ca, Mg, Mn and Na are shown. For Ca I-II, Mg I-II, Mn II and Na I the RMSE is at most 51 % in spite of the Stark values spanning three orders of magnitudes. For Mn I the values are more scattered and no clear trend is seen. This can partly be due to the small span of upper energy (E_u) of the available data or the relation of equation (4.1.10) being too simple. For Na II, no literature values have been found and no interpolation or extrapolation for the upper energies of the emission lines can be done. In case of no litterature values, the Stark broadening parameter is set to 0.002 nm at an electron density of $1 \times 10^{22}\,\mathrm{m}^{-3}$ and varying linearly with the electron density with no temperature dependence. Fits of equation (4.1.10) to more atomic species can be found in the Appendix A. It should be mentioned that equation (4.1.10) was chosen in a trial-and-error approach and that there surely exist better functions where also the spectral series, within a given species, are treated individually such as in [94]. For the case of missing Stark shift parameters, no interpolation or extrapolation has been done. Emission lines without any Stark shift parameters are therefore set to a default value of zero. Since the Stark shift for many lines is small compared to the Stark broadening, the lack of Stark shift parameters has less significance on the line profile and is therefore less critical. A comparison of the Stark broadening and shift parameters can be seen in Figure 4.1.7. The figure shows a histogram of the ratio of the Stark width and the Stark shift parameter (for lines with literature values only). As indicated in the figure, 50 % of the emission lines are at least 4.9 times as broadened as they are shifted and 75 % are at least 2.2 times as broadened as they are shifted (median of 4.9 and upper quartile of 2.2 as annotated in the figure).

Many of the downloaded emission lines will have negligible signal in LIBS spectra. These are emission lines with small Einstein coefficients and/or emission lines involving highly excited electronic or ionic states. The number of lines in the database (Figure 4.1.4) can therefore be reduced and thereby also reducing the computation time when simulating a spectrum. For the reduction, emission line intensities have been calculated via equation (2.2.23) from Chapter 2 for a LOS of length 3 mm through a homogeneous plasma for different temperatures ranging from 5000 K to 50 000 K, electron densities ranging from $1 \times 10^{22}\,\mathrm{m}^{-3}$ to $5 \times 10^{24}\,\mathrm{m}^{-3}$, and elemental concentrations ranging from $1 \times 10^{20}\,\mathrm{m}^{-3}$ to $5 \times 10^{23}\,\mathrm{m}^{-3}$. Each emission line from each element was calculated separately. As measured LIBS spectra typically have a SNR lower than 1/1000, emission lines with signals lower than 1/1000 of the maximum emission line signal, in all of the combinations of temperatures and densities, were removed from the database. This resulted in approximately half of the emission lines being removed. An overview of the number of lines for each element before and after the reduction can be seen in Figure 4.1.8a for wavelengths ranging from 100 nm to 2000 nm and in 4.1.8b for the wavelengths ranging from 270 nm to 805 nm corresponding approximately to the utilized wavelength range of the LIBS setup of this thesis (see Chapter 3).

For the reduced database in the smaller wavelength range (Figure 4.1.8b) an overview of the completeness of the Stark broadening parameters can be seen in Figure 4.1.9. Figure 4.1.9a shows the percentage of the total emission with Stark broadening parameters and Figure 4.1.9b shows the percentage of the number of the emission lines with Stark broadening parameters. The total emission was calculated with the following parameters: $\Delta x = 3\,\mathrm{mm}$, $T = 15\,000\,\mathrm{K}$, $n_e = 1 \times 10^{23}\,\mathrm{m}^{-3}$, and $n_0 = 1 \times 10^{22}\,\mathrm{m}^{-3}$. From the figures it can be seen that the Stark coverage in total emission is better than the coverage for the number of lines. This means that the stronger emission lines are better covered than the weaker lines. This is a result from hand-picking literature values of mainly the stronger emission lines not contained in the STARK-B database. It can also be seen that the majority of the emission lines do not have any Stark parameters and thereby described by the default value (FHWM of 0.002 at $n_e = 1 \times 10^{22}\,\mathrm{m}^{-3}$). Nonetheless, 57 % of the elements have more than 50 % of their total intensity (at the above mentioned plasma properties) covered with literature values or by interpolations via (4.1.10).

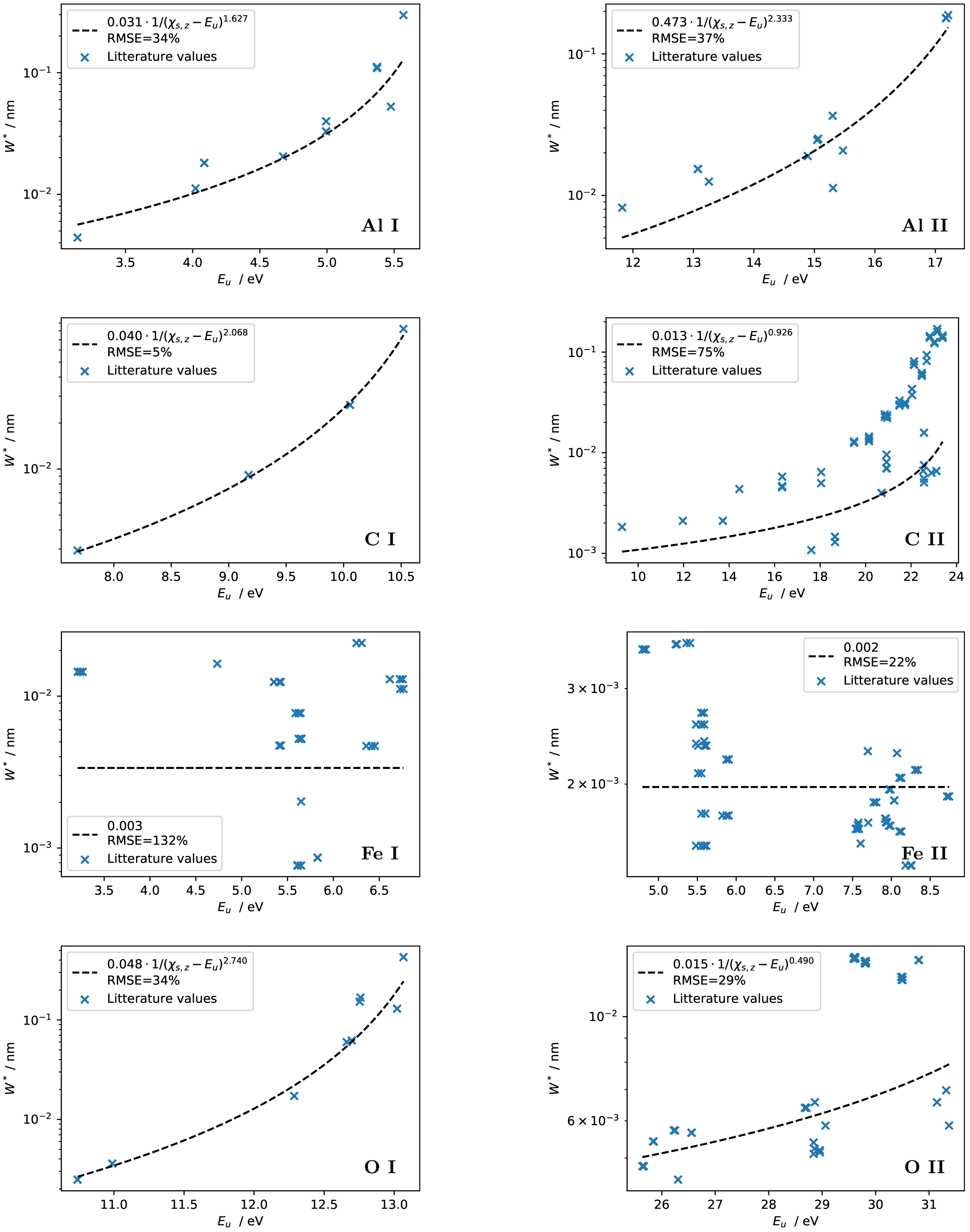

Figure 4.1.5: *Results from fitting the function of equation (4.1.10) to the literature values of the Stark broadening parameters of different atomic species. The fitted functions are used for assigning Stark broadening parameters to emission lines with no literature values.*

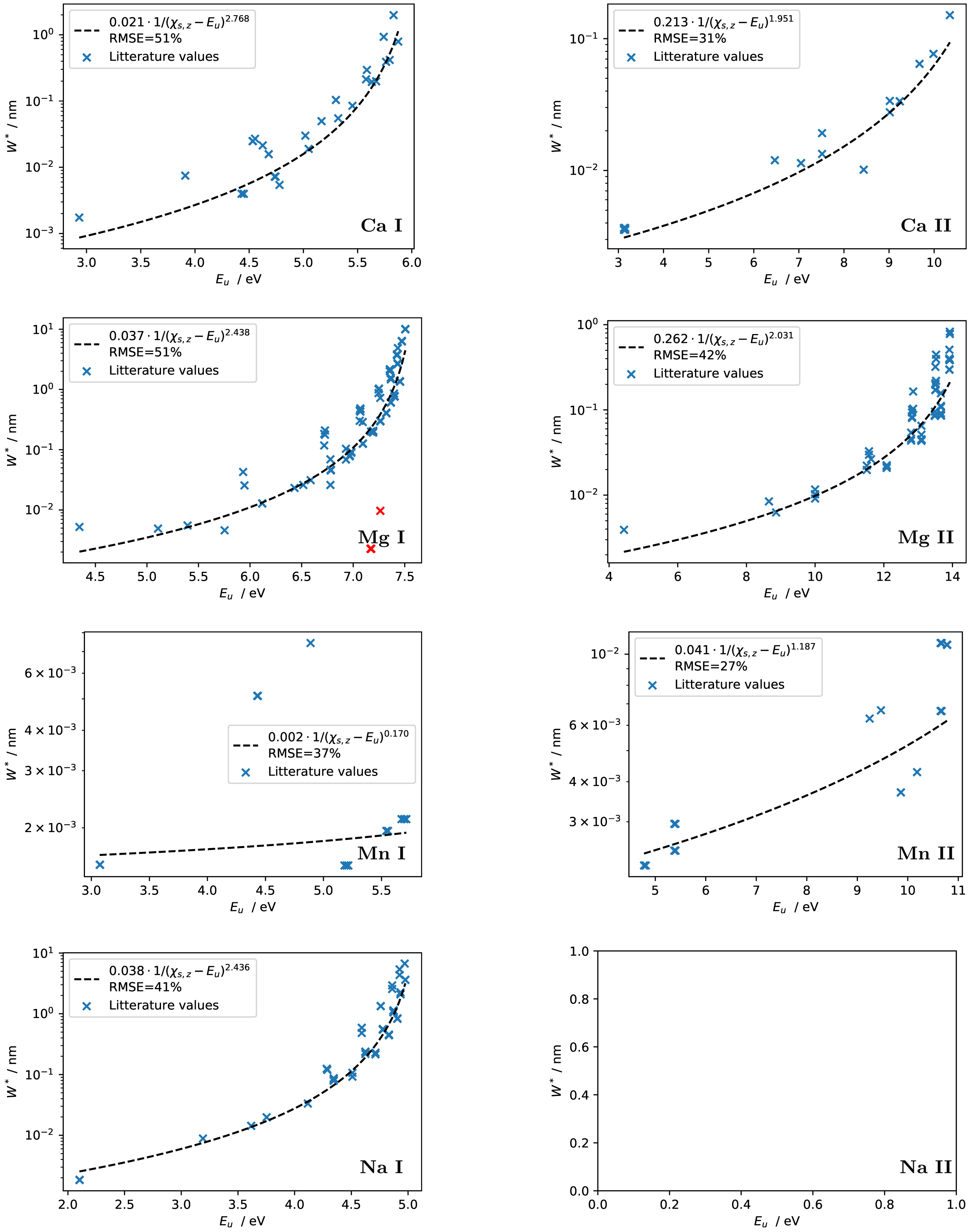

__Figure 4.1.6:__ Same as Figure 4.1.5 but for atomic species that will be important later in this chapter. In the fit for Mg I, two outliers have been identified and excluded from the fit (red crosses). No Stark parameters have been found for Na II emission lines. Consequently, the plot for Na II is empty.

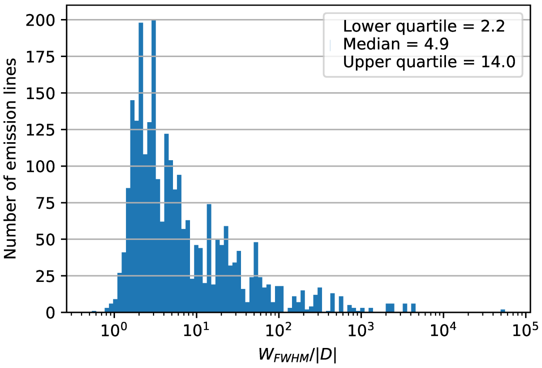

Figure 4.1.7: *Histogram showing the relative Stark broadening and Stark shift parameters for the emission lines in the database with literature values. The lower quartile, median and the upper quartile are noted. From the distribution it can be seen that the Stark broadening is bigger than the Stark shift. More specifically it is seen from the upper quartile that 75 % of the emission lines have a FWHM, due to Stark broadening, that is more than twice as big as the Stark shift.*

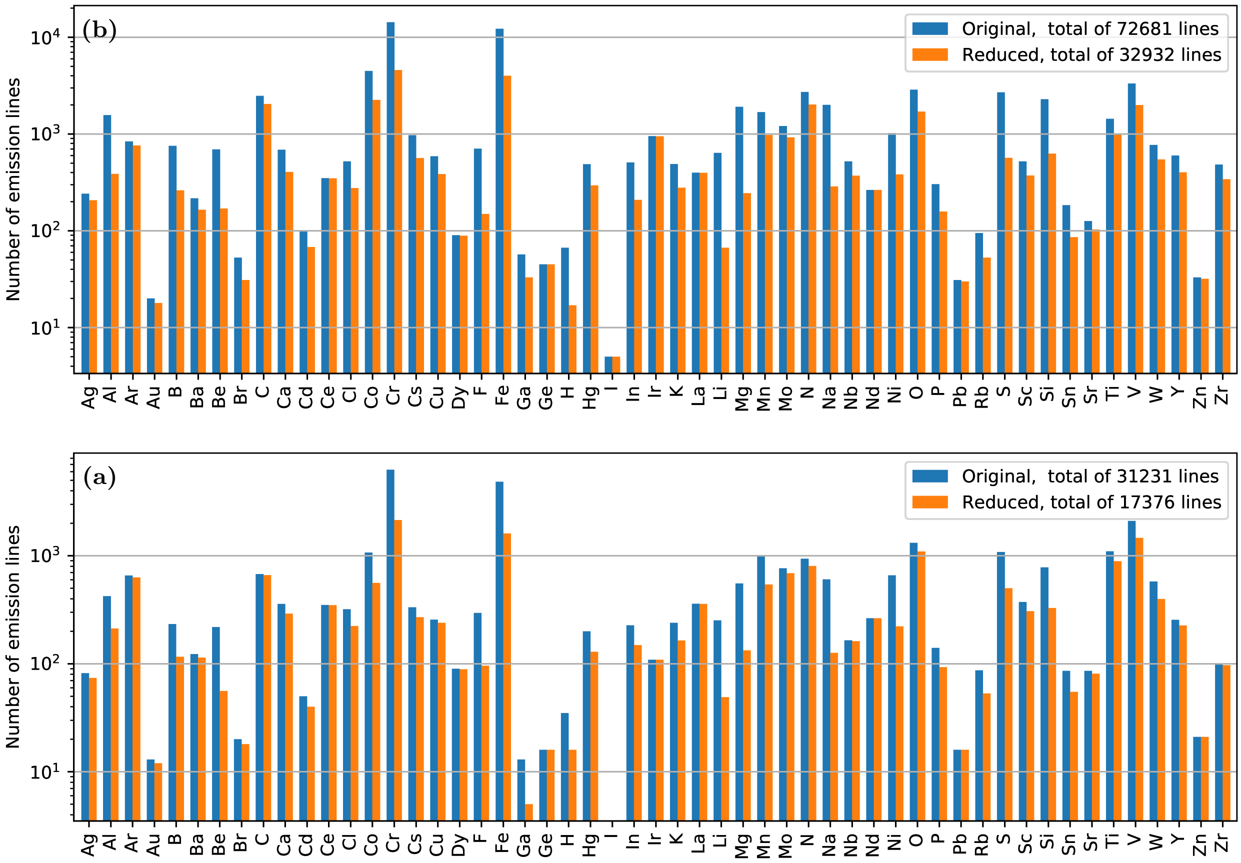

Figure 4.1.8: *The number of emission lines in the original database and the reduced database where emission lines predicted to have negligible intensity have been removed. The reduced database contains approximately half the emission lines of the original one.* ***(a)*** *In the spectral range from* 100 nm *to* 2000 nm *and* ***(b)*** 270 nm *to* 805 nm *which is the wavelength range of the LIBS setup of this thesis.*

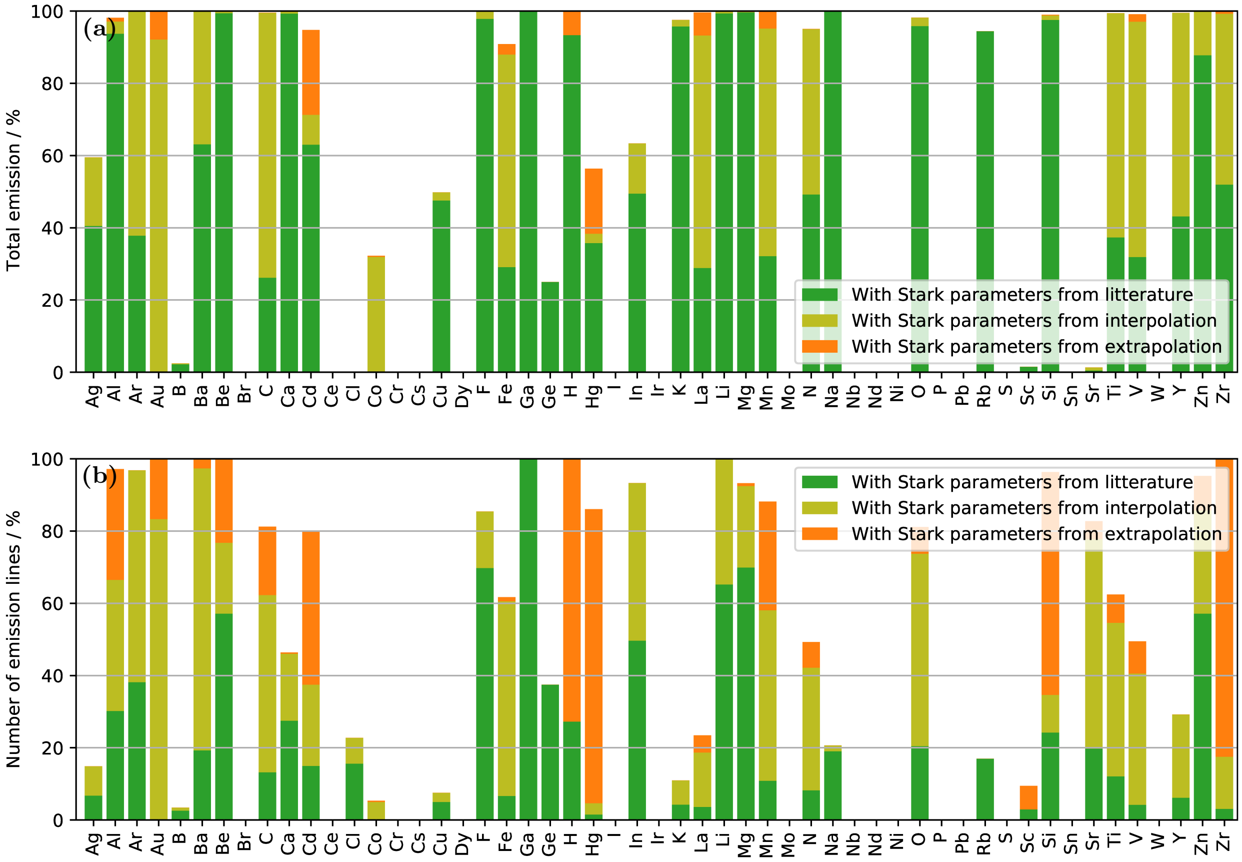

Figure 4.1.9: *Overview of the Stark broadening coverage of the emission lines in the database and for the range of* 270 nm *to* 805 nm. ***(a)*** *Stark broadening parameter coverage given as the percentage of the total intensity of each element calculated from a LOS though a single zone with the properties* $\Delta x = 3\,\mathrm{mm}$, $T = 15\,000\,\mathrm{K}$, $n_e = 1 \times 10^{23}\,\mathrm{m^{-3}}$, *and* $n_0 = 1 \times 10^{22}\,\mathrm{m^{-3}}$. ***(b)*** *Stark broadening parameter coverage given as the number of emission lines from each element. The coverage can be seen to be better in terms of intensities than in terms of number of emission lines.*

The uncertainties of the ionization energies, energy levels, and wavelengths from the NIST database are all small and negligible compared to the wavelength resolution of the setup, broadening mechanisms from the plasma, and the effects from the approximations and assumptions for the plasma model, e.g. LTE or the discretization of the plasma parameters along LOS. However, the Stark broadening parameters and the Einstein coefficients have larger uncertainties that are not always negligible. For example, the Einstein coefficients for the two strong Ca II resonance transitions at 393.4 nm and 396.8 nm have stated uncertainties of $\leq$25 %. These lines are very relevant for LIBS as they can be seen in almost every LIBS spectrum of a sample containing just a small amount of calcium. Generally, the Einstein coefficients have stated uncertainties between $\leq$0.03 % and $\geq$50 %. To obtain an overview of the uncertainties linked to the database, the uncertainties of the Einstein coefficients as stated by NIST have been propagated to the emissions calculated for a LOS through a homogeneous plasma of typical plasma properties to LIBS. The same has been done for the uncertainties of the Stark parameters assuming an uncertainty of 20 % or 50 % for lines with and without literature values, respectively. The results are shown in Figure 4.1.10. From the figure it can be seen that the uncertainty for many of the elements are dominated by the uncertainties in the Einstein coefficients. In the NIST database [74] the uncertainties are given with only an upper bound. In propagating the Einstein coefficient uncertainties the upper bound was used and the propagated uncertainty is therefore a conservative estimate and likely to be smaller in reality. From the figure it can also be seen that uncertainties of the Stark parameter have smaller influence on the emissions and for some elements like carbon and oxygen it is practically zero. This is because that the emission lines from these elements are free from self-absorption. Without any absorption, the total intensity does not depend on the shape of the line profile. Calcium on the other hand, has strong lines that are typically self-absorbed. Consequently, the propagated uncertainty form the Stark parameters is relatively large. Opposite to the Stark parameters, the propagated uncertainty from the Einstein coefficients have smaller affect on the total emission in the case of stronger self-absorption. This can be seen from the slope of the COG as in Figure 2.2.4 in Chapter 2, but also inferred by considering chromium in Figure 4.1.10. The emission lines from chromium were taken from the Kurucz database [83], which does not provide any uncertainties of Einstein coefficients. As a conservative estimate, I have set the uncertainty to 75 %, but still the propagated uncertainty is only 60 %.

Even though the uncertainties of the total emissions are less affected by uncertainties in the Stark parameters, the line profiles might be strongly affected. This can be significantly reduced by considering spectrally integrated intensities of the emission lines, that is independent of line shapes in the case of negligible absorption, or by spectral smoothing. Smoothing is naturally introduced by instrumental broadening effects. In Figure 4.1.11 a comparison of the Doppler, Stark, and instrumental broadening can be seen for two different sets of temperature and electron densities. Depending on the plasma properties it is seen that many of the emission lines with smaller Stark broadening have line profiles that, when measured with the setup of this thesis, will be dominated by the instrumental profile.

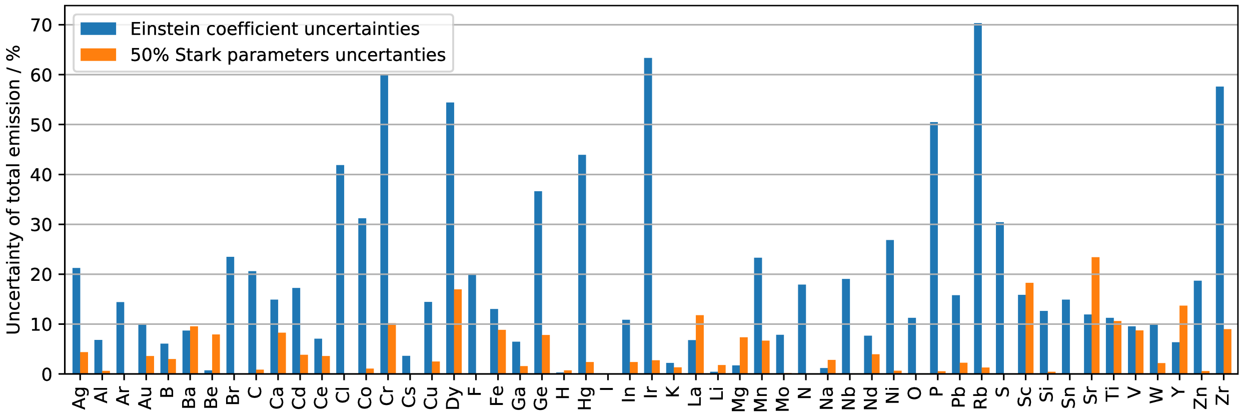

Figure 4.1.10: *Propagated uncertainty of the total emission from* 270 nm *to* 805 nm *from uncertainties of the Einstein coefficients and an assumed* 20 % *or* 50 % *uncertainty of Stark parameters with and without literature values, respectively. The radiated intensity was calculated element-wise and for a single LOS through a single homogeneous zone with the properties:* $\Delta x = 3\,\mathrm{mm}$, $T = 15\,000\,\mathrm{K}$, $n_e = 1 \times 10^{23}\,\mathrm{m}^{-3}$, $n_0 = 1 \times 10^{22}\,\mathrm{m}^{-3}$. *From the data it is seen that some elements have smaller uncertainties in the Einstein coefficients than others and that uncertainties in the Einstein coefficients dominates the projected uncertainties of the total intensities for most of the elements.*

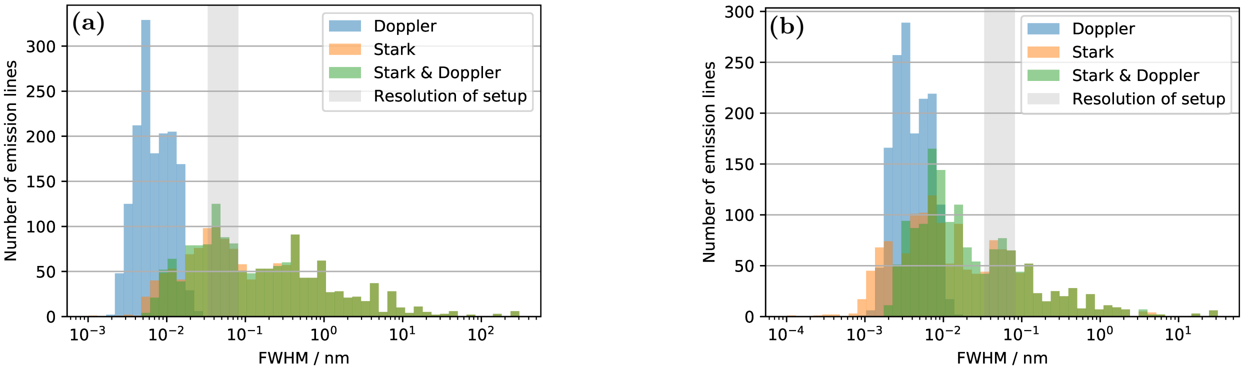

Figure 4.1.11: *Comparison of Doppler, Stark and the instrumental broadening for two different sets of plasma parameters corresponding approximately to an intermediate phase of the plasma lifetime and a later phase near the end of the lifetime of the plasma.* ***(a)*** *Temperature of* 15 000 K *and electron density of* $1 \times 10^{23}\,\mathrm{m}^{-3}$ *(intermediate phase).* ***(b)*** *Temperature of* 5000 K *and electron density of* $1 \times 10^{22}\,\mathrm{m}^{-3}$ *(late phase).*

4.1.4 Simulation of Spectra

The simulation of a spectrum is done by evaluating equation (4.1.7) and by providing the input parameters for the plasma properties of the zones, the elements inside the plasma, and a wavelength axis. The resolution of the wavelength axis should be sufficiently high to properly resolve the line profiles of the emission lines during the calculation of the LOS radiance, i.e. independent of wavelength resolution of the setup. The required wavelength resolution for the simulation is thereby limited by the emission line with the smallest width from the combined effect of Doppler and Stark broadening. From the histograms for the widths of the emission lines in Figure 4.1.11, it can be inferred that a wavelength axis with steps of 0.33 pm would be sufficient to sample the narrowest emission line five times along its FWHM for the late plasma phase (Figure 4.1.11b for $(T, n_e) = (5000\,\mathrm{K}, 1 \times 10^{22}\,\mathrm{m}^{-3})$). At the intermediate phase, wavelength steps of 1 pm would be sufficient (Figure 4.1.11a for $(T, n_e) = (15\,000\,\mathrm{K}, 1 \times 10^{23}\,\mathrm{m}^{-3})$). Unless anything else stated, simulations of the spectra of this thesis has been done with wavelength steps of 0.33 pm. After the LOS calculation, the emissions are convolution with the Gaussian for simulating the instrumental broadening effect. Finally, the simulated spectrum can be integrated to fewer bins corresponding to the pixel width in nm of the LIBS setup.

For convenience the equation governing the simulation of a spectrum is now repeated together with the parameters involved:

$$\tilde{I}_\lambda(\lambda; \vec{T}, \vec{n}_e, \vec{\tilde{n}}_0, \vec{\tilde{n}}_{\mathrm{rel}}, F) = I_\lambda(\lambda; \vec{T}, \vec{n}_e, \vec{\tilde{n}}_0, \vec{\tilde{n}}_{\mathrm{rel}}) \cdot F * b_{\mathrm{instr}}(\lambda) \ , \tag{4.1.11}$$

where λ is the wavelength defined by the wavelength axis. The input parameters are $\vec{T}$ which contains the temperature of the zones, $\vec{\tilde{n}}_0$ the effective path of the elements of the first zone (elemental densities in the first zone times the length of the first zone), $\vec{\tilde{n}}_{\mathrm{rel}}$ the relative effective path of the following zones, and F the experimental parameter that is a constant linked to the absolute value of the intensity response, the cross section of the LOS, and the integration time of a measurement.

The simulation of spectra has been implemented as a python script. An example of input parameters and the resulting simulated spectrum is shown in Figure 4.1.12. The composition of the plasma was similar to that of Martian regolith (JSC-1a [95], see table 4.1) and the discretized plasma properties, along the LOS, were similar to profiles obtained from numerical simulations of the plasma expansion (see Figure 2.1.2 in Chapter 2). A version of the python script with a graphical user interface (GUI) has also been implemented. The GUI allows for the simulation of spectra of plasmas with arbitrary composition and plasma properties and can be used as a tool for assisting the analysis of real measurements especially in terms of line identification, but also for planning measurements in terms of where to look for emission lines of specific elements. A screen shot of the GUI can be seen in Figure 4.1.13.

Element	Si	O	Al	Ti	Fe	Mn	Ca	Mg	K	Na	P
Concentration / a.t.%	15.85	60.85	10.00	1.04	5.69	0.09	2.42	1.85	0.28	1.70	0.22

Table 4.1: *Composition of the plasma used for the simulation of the spectrum shown in Figure 4.1.12. The composition is similar to that of a Martian regolith simulant [95].*

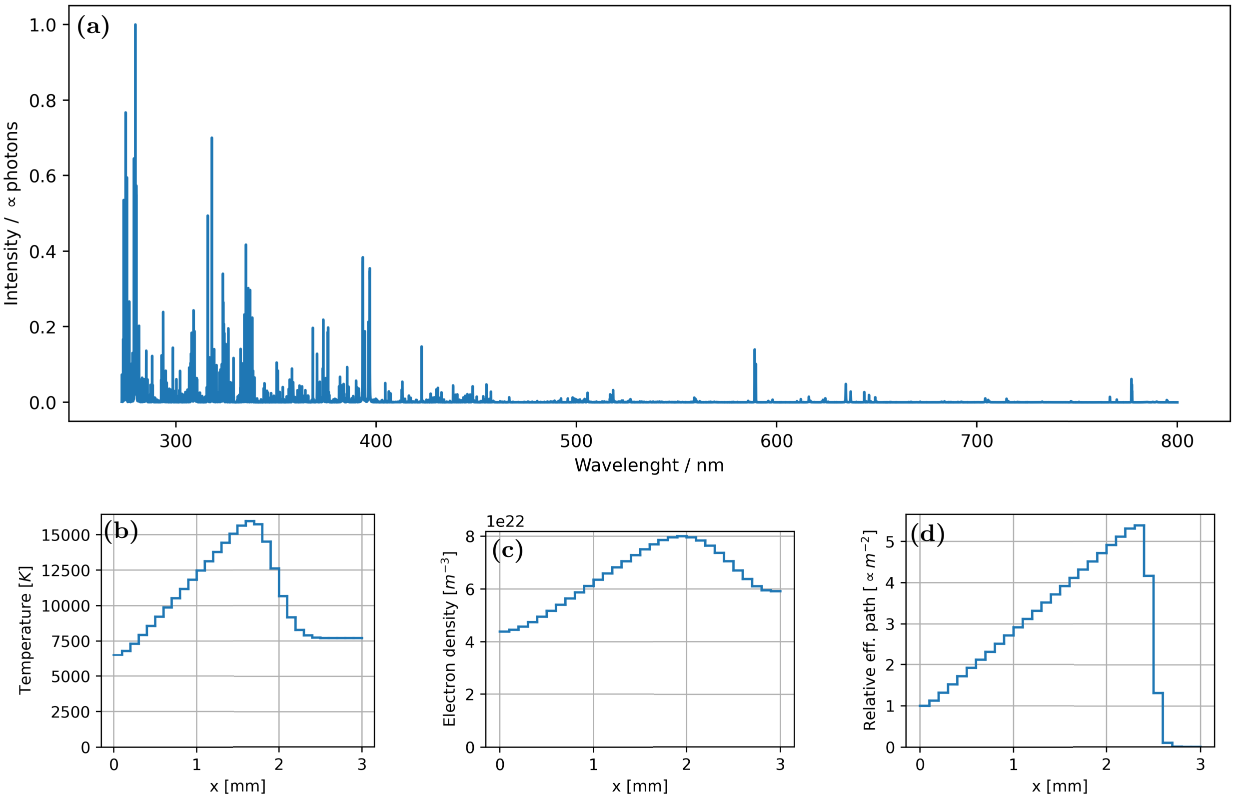

Figure 4.1.12: ***(a)*** *Example of simulated spectrum of a plasma divided into 30 homogeneous zones and with composition similar to that of Martian regolith (see Table 4.1). The total length of the LOS for the simulation is* 3 mm *and the experimental parameter was fixed such that the maximum intensity is one.* ***(b)*** *Temperature of the zones.* ***(c)*** *Electron density of the zones.* ***(d)*** *the relative effective path of the zones. The total density of the elements in the first zone is* $1.9 \times 10^{22}\,\mathrm{m}^{-3}$.

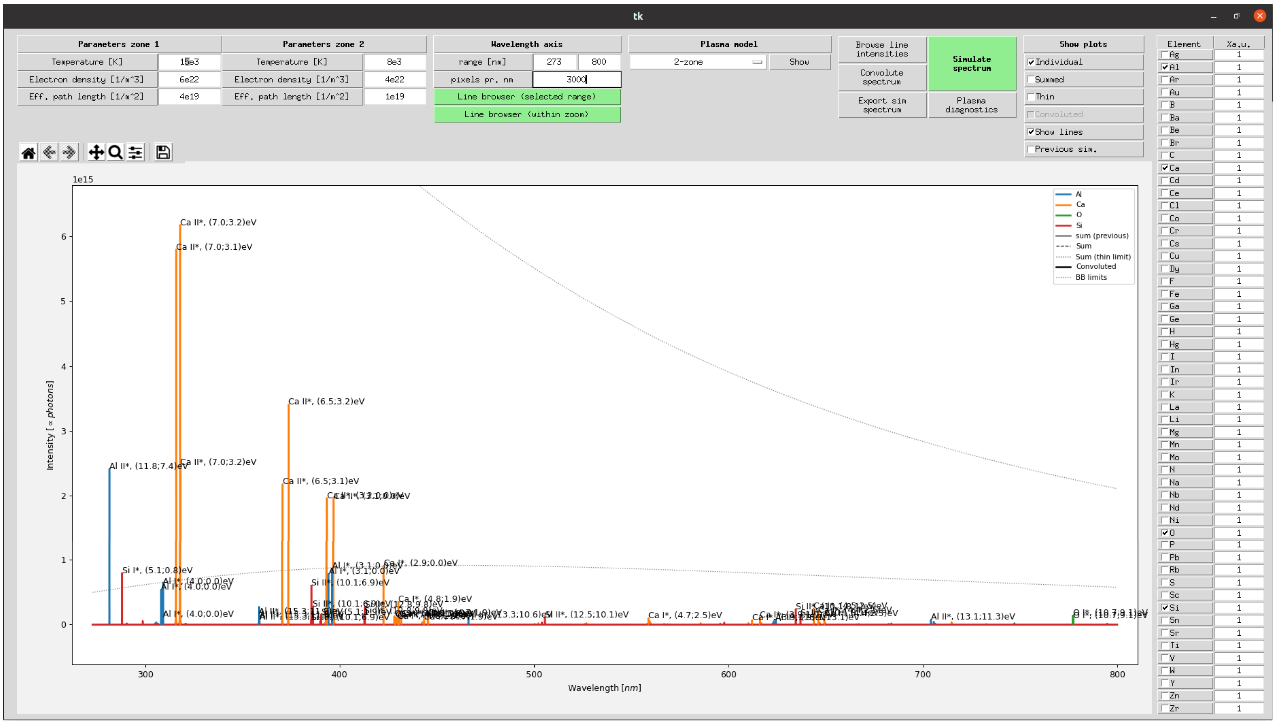

Parameters zone 1
Temperature [K]: 15e3
Electron density [1/m^3]: 6e22
Eff. path length [1/m^2]: 4e19

Parameters zone 2
Temperature [K]: 8e3
Electron density [1/m^3]: 4e22
Eff. path length [1/m^2]: 1e19

Wavelength axis
range [nm]: 273 800
pixels pr. nm: 3000

Plasma model: 2-zone

Show plots
☑ Individual
☐ Summed
☐ Thin
☐ Convoluted
☑ Show lines
☐ Previous sim.

Element	%a.u.
☐ Ag	1
☑ Al	1
☐ Ar	1
☐ Au	1
☐ B	1
☐ Ba	1
☐ Be	1
☐ Br	1
☐ C	1
☑ Ca	1
☐ Cd	1
☐ Ce	1
☐ Cl	1
☐ Co	1
☐ Cr	1
☐ Cs	1
☐ Cu	1
☐ Dy	1
☐ F	1
☐ Fe	1
☐ Ga	1
☐ Ge	1
☐ H	1
☐ Hg	1
☐ I	1
☐ In	1
☐ Ir	1
☐ K	1
☐ La	1
☐ Li	1
☐ Mg	1
☐ Mn	1
☐ Mo	1
☐ N	1
☐ Na	1
☐ Nb	1
☐ Nd	1
☐ Ni	1
☑ O	1
☐ P	1
☐ Pb	1
☐ Rb	1
☐ S	1
☐ Sc	1
☑ Si	1
☐ Sn	1
☐ Sr	1
☐ Ti	1
☐ V	1
☐ W	1
☐ Y	1
☐ Zn	1
☐ Zr	1

Figure 4.1.13: *Screen-shot from the GUI for the simulation of LIBS spectra. In the GUI, a plasma in a two-zone approximation containing the elements Al, Ca, O and Si can be seen to be chosen and simulated.*

4.2 Methods for Fits of Spectra

The goal of a fit to an input spectrum is to find the parameters of a simulated spectrum that minimize the difference between the simulated and the input spectrum. As introduced in the previous section, a simulated spectrum is written as

$$\tilde{I}_\lambda(\lambda;\vec{T},\vec{n}_e,\vec{\tilde{n}}_0,\vec{\tilde{n}}_{\text{rel}},F) \ , \tag{4.2.1}$$

where $F,\vec{T},\vec{n}_e,\vec{\tilde{n}}_0$, and $\vec{\tilde{n}}_{rel}$ are the input parameters to be fitted, i.e the fit parameters. The difference between the simulated and the input spectrum is quantified by the weighted squared residuals, r^2, defined as

$$r^2 = \sum_i \left(\left(\tilde{I}_\lambda(\lambda;\vec{T},\vec{n}_e,\vec{\tilde{n}}_0,\vec{\tilde{n}}_{rel},F)|_{\lambda=\lambda_i} - p_i\right) w_i\right)^2 \ , \tag{4.2.2}$$

where $\tilde{I}(\dots)|_{\lambda=\lambda_i}$ is the simulated spectrum evaluated at the wavelength λ_i corresponding to the wavelength of the i'th bin of the input spectrum and where p_i is the signal of the i'th bin of the input spectrum. The weight of the i'th residual is denoted by w_i. The weights are related to the uncertainties such that bins with signals of high uncertainties have lower weights. During a fit, the residuals are evaluated for different values of the input/fit parameters in a search for the set of parameters that minimizes r^2. There exist many choices for fit routines and the quality of the choice depends on how the model, in this case $\tilde{I}_\lambda$, depends on the fit parameters. Generally, $\tilde{I}_\lambda$ is a non-linear function of the input parameters. For example, if the temperature is increased, the intensity of different emission lines might either decrease or increase depending on the ionized states (see Figure 2.2.1 in Section 2.2.2). However, $\tilde{I}_\lambda$ increases monotonically with $\vec{\tilde{n}}_0$ (related to the elemental concentrations of the elements in the plasma) and in the optically thin limit it increases linearly and the square residual r^2 can be minimized analytically in $\vec{\tilde{n}}_0$ using the method of linear least squares. Even though the LIBS plasma is not optically thin at all wavelengths, the above considerations indicate that the residuals of r^2 can be minimized semi analytically in $\tilde{n}_0$ using non-linear least squares. To exploit this, a custom fit routine has been developed where the optimization of the fit parameters is split into two steps. The first step tunes the parameters $\vec{T},\vec{n}_e,\vec{\tilde{n}}_{rel}$ via a Monte Carlo approach whereas the second step optimizes $\vec{\tilde{n}}_0$ by non-linear least squares for different values of F. The fit routine is implemented in python and will be elaborated later in this section.

In order to reduce the problem, fits are done to spectrally integrated signals of peaks instead of the signal in the individual bins. Here, a peak is defined as a series of consecutive bins with signals higher than a certain threshold and extending to the background level. The definition of a peak will be elaborated in the following section where examples of peaks are shown in Figure 4.2.2. The residuals to be minimized thereby reduce to

$$r^2 = \sum_j \left(\left(\int\limits_{\lambda_{j,min}}^{\lambda_{j,max}} \tilde{I}_\lambda(\lambda;\vec{T},\vec{n}_e,\vec{\tilde{n}}_0,\vec{\tilde{n}}_{rel},F)d\lambda - P_j\right) W_j\right)^2 \ , \tag{4.2.3}$$

where P_j is the spectrally integrated signal of peak j, W_j the weight of peak j and $\lambda_{j,min}$ and $\lambda_{j,max}$ the wavelength span of peak j. By using integrated peak signals, the problem is reduced to a smaller number of features (thousands of bins versus a smaller number of peaks). Furthermore, the simulated intensities do not need to be convoluted with the instrumental broadening function b_λ which further decreases the computation time. The limitation of the approach is that the information contained in the shape of the line profiles is not directly utilized. This could otherwise help to confine the electron density via the Stark broadening or the Stark shift. On the other hand, the Stark parameters for many of the emission lines are unknown or uncertain and fitting to spectrally integrated peaks reduces the influences of such. An overview of the steps of the fit routine is illustrated in Figure 4.2.1 and the individual steps are explained in further detail below.

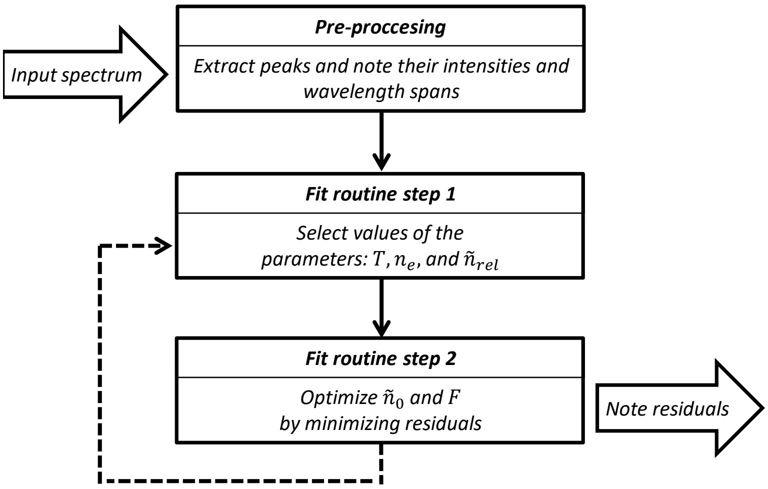

Figure 4.2.1: *Flow diagram showing the steps in the fit routine.* ***Pre-processing:*** *When given an input spectrum, peaks are identified and their wavelength spans and spectrally integrated intensities are noted and fed to the fit routine.* ***Fit routine step 1:*** *In the first step of the fit routine, a set of values for the parameters $\vec{T}, \vec{n}_e, \vec{\tilde{n}}_{rel}$ is selected and fed to the second step of the fit routine.* ***Fit routine step 2:*** *In the second step, $\vec{\tilde{n}}_0$ is optimized by minimizing the residuals by non-linear least squares for different values of F while keeping the parameters of step one fixed. The resulting minimized residuals are noted and used in the first step of the fit routine for assisting the selection of a new set of values for the parameters $\vec{T}, \vec{n}_e, \vec{\tilde{n}}_{rel}$. The process is repeated many times and the combined set of parameters, from both step 1 and step 2, resulting in the smallest residuals resembles the best fit.*

4.2.1 Pre-Processing of Input Spectrum

The pre-processing of the input spectrum consists in identifying and extracting the relevant information of the spectral peaks that is fed to the fit routine. The relevant information includes the spectrally integrated peak intensities and their uncertainties for evaluating the weights in the weighted residuals (W_i in equation 4.2.3).

For the identification of peaks, a threshold is estimated from the trend line of the background spectrum and its noise. The trend line of the background is estimated using a moving minima method applied to the intensities. The noise likewise, but applied to the standard deviation of the intensities calculated in smaller wavelength intervals. The algorithms for the noise and background level estimations were developed during my Master's thesis [96] in Matlab and now translated to Python. The threshold for identifying the peaks is chosen to be six times the spectral noise from the background. Peaks are then extracted by finding pixels with intensities above this threshold and tracing their neighbouring pixels until the level of the background. With this approach, no fitting of line profiles is required and a peak might consist of several emission lines. By setting the peak threshold to six times the spectral noise from the background, some spectral peaks will not be included in the fit. However, the probability of wrongly identifying a peak due to noise is simultaneously reduced. With the threshold of six times the zero'th level noise in a spectrum containing 25 000 bins, the probability of falsely identifying a peak is only

$$1 - (1 - 1.7 \cdot 10^{-6})^{25000} = 4\,\% \ ,$$

where $1.7 \cdot 10^{-6}$ is the probability of a random $\geq 6\sigma$ event. An example of the peak identification applied to a time-resolved LIBS spectrum can be seen in Figure 4.2.2.

After the identification of a peak, its intensity/signal is calculated as the sum of the intensities of the bins making up the peak minus the background level

$$P_j = \sum_{i,\ \lambda_i \in P_j} p_i - p_{(bg),i} \ , \tag{4.2.4}$$

where p_i is the intensity and $p_{(bg),i}$ the estimated background level at the i'th bin. The weight of a peak is

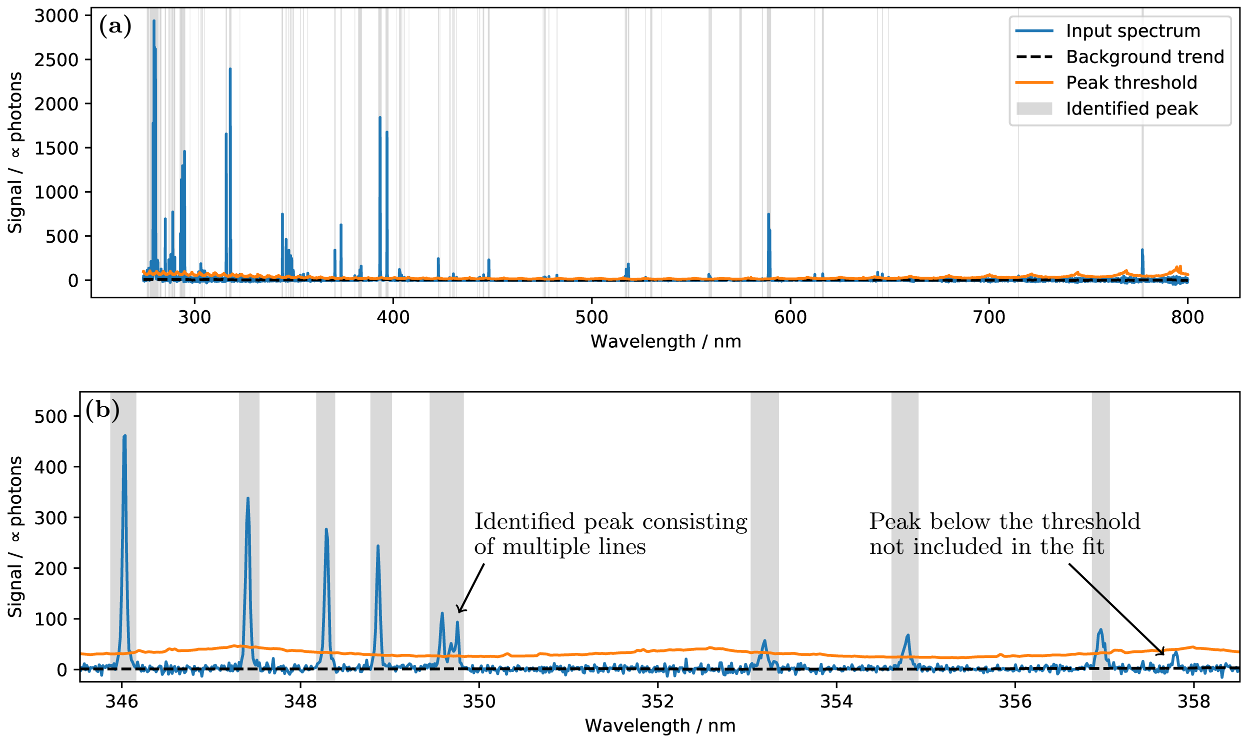

Figure 4.2.2: *Example of identified peaks of a time-resolved LIBS spectrum of a carbonate pellet.* ***(a)*** *The input spectrum shown together with the estimated trend of the background level, the peak threshold, and the areas containing identified peaks. The peak threshold is six times the noise from the background level. The shape of the peak threshold is the product of the noise as estimated from the raw counts and the intensity response function (see Chapter 3).* ***(b)*** *Close-up of (a) in a smaller wavelength range.*

related to the uncertainty of its intensity and it is calculated as

$$W_j = \left(|G \cdot P_j| + \left(\sum_{i,\ \lambda_i \in P_j} \sigma_i^2 \right) + (0.1 \cdot P_j)^2 + \left(\sum_{i,\ \lambda_i \in P_j} \sigma_i \right)^2 \right)^{-1/2} . \tag{4.2.5}$$

Here, the first term contains the uncertainty due to photon noise, where g is the detector gain in counts per photo-electron (see Section 3). The second term contains the uncertainty due to the estimated spectral noise at the background level σ. The third term is a 10% peak uncertainty. It can be considered as a model uncertainty covering discretizations and uncertainties in the atomic constants and intensity calibration. The last term is added to weight the smallest peaks less since they are more prone to systematic errors in the estimation of the background level.

4.2.2 Fit Routine

The optimization of the values for the parameters $\vec{T}$, $\vec{n}_e$ and $\vec{\tilde{n}}_{rel}$, during the first step of the fit routine (Figure 4.2.1), is done via the optimization method simulated annealing [97]. Simulated annealing is a type Monte Carlo optimization method. It can be described as an adaptive random sampling of the parameter space. Given a set of values for $\vec{T}$, $\vec{n}_e$ and $\vec{\tilde{n}}_{rel}$ from the simulated annealing, optimal values of F and $\vec{\tilde{n}}_0$ are obtained by minimizing the residuals, as given in eq. (4.2.3), by non-negative non-linear least squares. More specifically, this is done by arranging a system of equations between the spectrally integrated simulated intensities and the extracted peaks from the input spectrum:

$$\begin{aligned}
&\int_{C_1} \tilde{I}_\lambda\left(\lambda;\vec{T},\vec{n}_e,\vec{\tilde{n}}_0,\vec{\tilde{n}}_{rel},F\right)d\lambda\cdot W_1 = P_1\cdot W_1\\
&\int_{C_2} \tilde{I}_\lambda\left(\lambda;\vec{T},\vec{n}_e,\vec{\tilde{n}}_0,\vec{\tilde{n}}_{rel},F\right)d\lambda\cdot W_2 = P_2\cdot W_2\\
&\qquad\vdots\\
&\int_{C_k} \tilde{I}_\lambda\left(\lambda;\vec{T},\vec{n}_e,\vec{\tilde{n}}_0,\vec{\tilde{n}}_{rel},F\right)d\lambda\cdot W_k = P_k\cdot W_k \quad ,
\end{aligned} \tag{4.2.6}$$

where C_k are the wavelength span of the k'th peak (grey shaded areas in Figure 4.2.2). There exists one equation for each extracted peak. Setting up the equations requires no line identification: all emission lines from the spectral database with wavelengths within the wavelength spans of the peaks are included. In the optically thin limit, the simulated intensities are directly proportional to the product of $\vec{\tilde{n}}_0$ and F (see eq. (2.2.28) in Section 2.2.3). As a starting point, the equations are written in the optically thin limit and solved for $(\vec{\tilde{n}}_0\cdot F)$ using non-negative least squares. A first estimate of the instrumental factor F is then found from an initial guess of the sum of $\sum\vec{\tilde{n}}_0 = \tilde{N}_{\text{guess}}$ that are related to the product of the total atomic density of the plasma and the zone lengths

$$F_{\text{guess}} = \frac{\sum\left(\vec{\tilde{n}}_0\cdot F\right)_{\text{est.}}}{\tilde{N}_{\text{guess}}} \quad . \tag{4.2.7}$$

By setting F to F_{guess}, $\vec{\tilde{n}}_0$ is decoupled from F and the system of equations, in the non-optically thin limit, is linearised around the current values and an improved estimate of $\vec{\tilde{n}}_0$ is obtained by again solving the equation. This process is repeated iteratively until convergence in $\vec{\tilde{n}}_0$.

The experimental factor F was estimated from an initial guess of the total elemental density (eq. 4.2.7). The above process is therefore repeated for different values of F around the initial guessed value (grid search). The combination of F and $\tilde{n}_0$, that resulted in the lowest residual, is saved and fed back to the simulated annealing process (fit routine step 1) where it is used to assist the selection of a new set of values for the parameters $\vec{T},\vec{n}_e,\vec{\tilde{n}}_{rel}$ for which the process is repeated.

The simulated peaks (left hand side of equation (4.2.6)) are evaluated with wavelength steps of 0.33 pm and the derivatives in the linearization of the system of equations (eq. 4.2.6) are calculated numerically by the forward finite difference approximation. For solving the linearized system of equations the function lsq_linear from the Scipy Python library is used [98].

4.3 Verification of the Fit Routine and the Two-Zone Model

In principle plasma models of any number of zones can be fitted to an input spectrum, but due to the complexity of a fit, in terms of computation time, models with a maximum of two zones will be fitted. In a real LIBS experiment, the plasma properties change continuously throughout time and space and it is evident that the real LIBS plasma is not that of a two-zone plasma model. By acquiring the spectra with a sufficiently small exposure time, the plasma can in practice be considered stationary and the temporal variations/gradients can be ignored. However, the acquired spectra will still be a product from spatial gradients of the plasma parameters along the LOS of the LIBS instrument. In this section, the effect of such spatial gradients in a stationary plasma is studied. More specifically it is studied how synthetic spectra with spatial variations of plasma properties, are approximated in a discrete two-zone plasma model. It is done by fitting two-zone models to synthetic test spectra simulated from different spatial profiles of the plasma properties along the LOS. The spatial profiles for the simulation of the synthetic spectra are embedded in a 30-zone plasma model in order to simulate a continuous plasma. This ensures that the robustness of the simplified two-zone model can be easily evaluated. Furthermore, the results serve as a verification of the implementation of the fit routine. For the fits to the synthetic spectra in this section, the model uncertainty was set to 5 %, instead of 10 %, (see equation (4.2.5) in section 4.2.1) as uncertainties in the atomic constants are not considered when generating the test spectra.

4.3.1 Synthetic Test Spectra

Five different synthetic test spectra have been simulated with different spatial profiles of the plasma properties along a LOS of 3 mm. The composition of the plasma is the same for all spectra and similar to a carbonate sample from which real LIBS spectra have been obtained and that will be presented later in this chapter. The elemental composition for the test spectra is 3.57 at% of Ca, 5.44 at% of Mg, 3.38 at% of Mn, 12.68 at% of Na, 18.73 at% of C, and 56.20 at% of O. The profiles of the plasma properties are shown in Figure 4.3.1. The ”Homogeneous” spectrum has a homogeneous temperature along the LOS, whereas the temperature profile of the ”Gaussian” spectrum is that of a Gaussian. The ”Reversed Gaussian” spectrum shares the same profiles as the ”Gaussian” spectrum, but reversed. The temperature profile of the ”Shifted Gaussian” is that of a shifted Gaussian. For the afore mentioned spectra (”Homogeneous”, ”Gaussian”, ”Reversed Gaussian” and ”Shifted Gaussian”), the atomic density was chosen such as to be proportional to the reciprocal of the temperature and the electron density was then solved using the Saha-Equation and conservation of charge (see eq. (2.2.16) in Chapter 2). Finally, the ”Bogaerts” spectrum has profiles similar to those derived from numerical simulations of the plasma generation and expansion [52] (See Figure 2.1.2 in Chapter 2). In order not to consider the atmospheric component of the plasma, i.e. for the sake of simplicity, both the temperature, atomic density, and the electron density were given freely for this spectrum. The absolute values of the plasma properties of the synthetic spectra are of less interest compared to their gradients/shape along the LOS, but the absolute values have been chosen such as to be comparable to the results obtained from fits to real measured LIBS data that will be presented later in this chapter. The resulting simulated test spectra are shown in Figure 4.3.2. Again, for a better comparison to later results, the test spectra have been integrated to fewer bins, corresponding approximately to the bins of the LIBS setup of this thesis, and Gaussian zero’th level noise (see Chapter 3) has been added such that the SNR is similar to that of measured spectra.

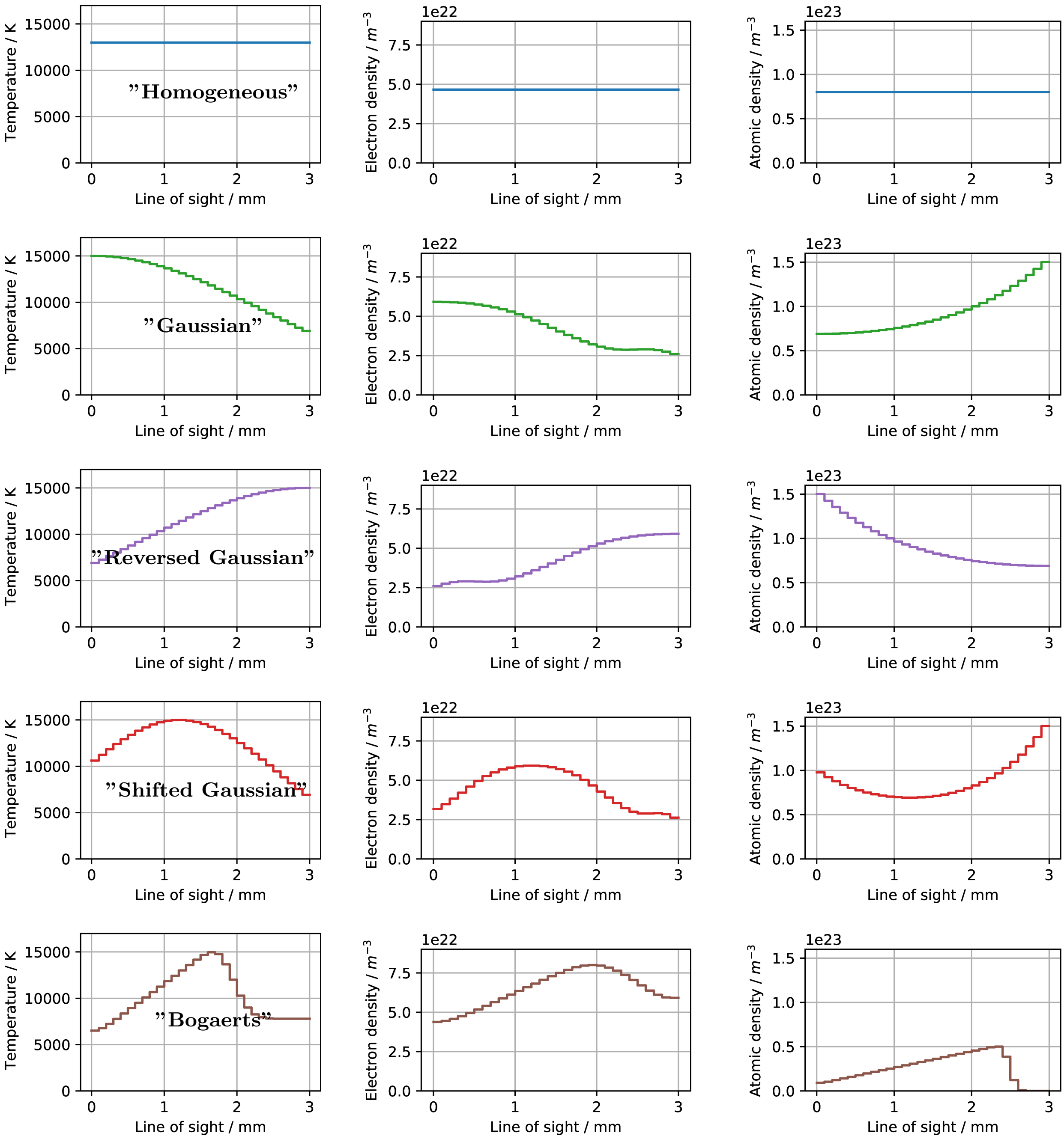

Figure 4.3.1: *Profiles of the plasma parameters along the LOS in the plasma model for the generation of four different synthetic test spectra. The test spectra/profiles are nicknamed after the temperature profiles (see annotation on figures). The resulting synthetic spectra are shown in Figure 4.3.2.*

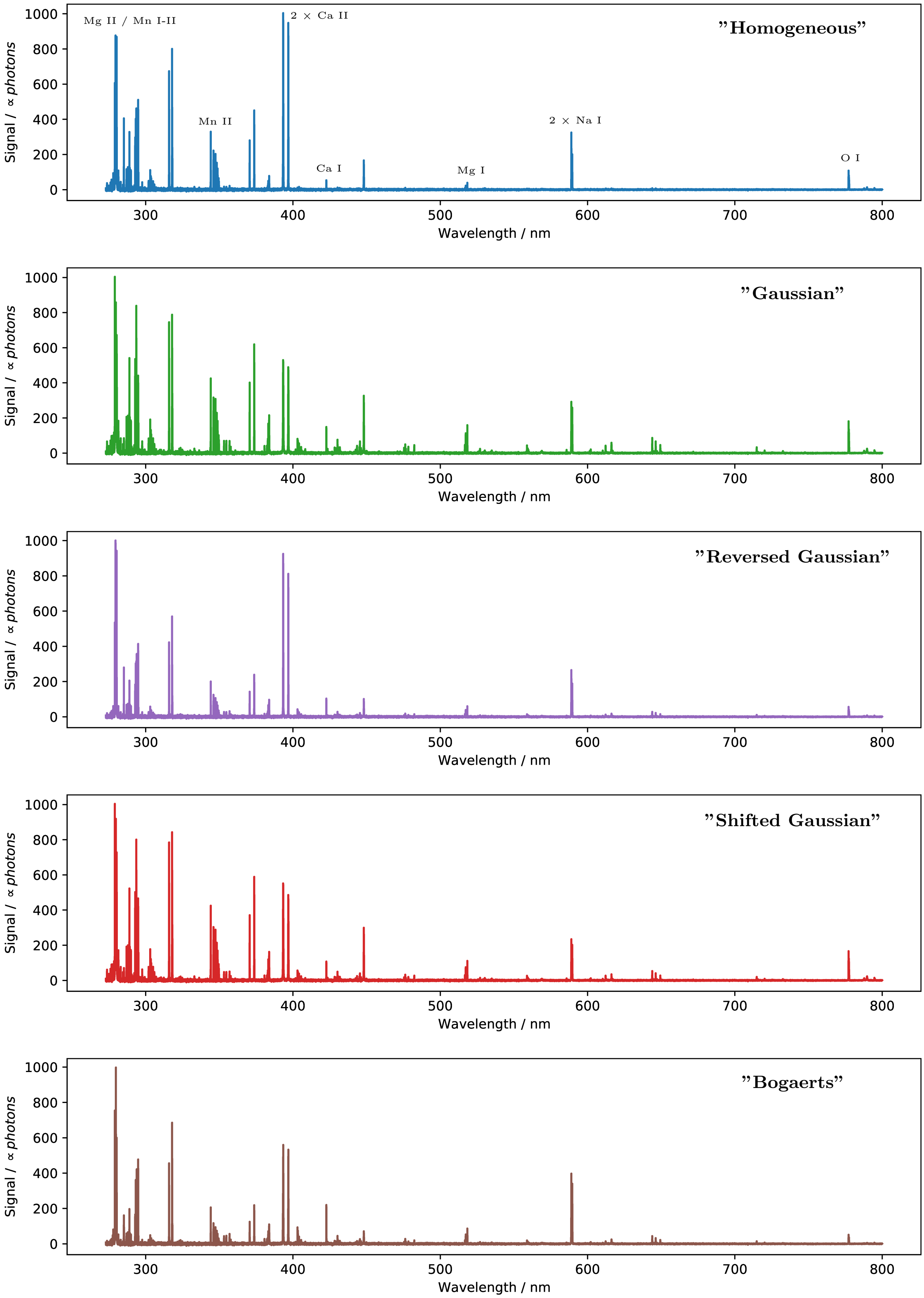

Figure 4.3.2: *Synthetic test spectra simulated from the profiles in Figure 4.3.1. The composition is similar to that of a Carbonate sample with the four major elements: Ca, Mg, Mn, Na. In order to resemble real measurements, the spectra have been integrated to fewer bins and Gaussian noise has been added.*

4.3.2 One-zone Fit to "Homogeneous" Spectrum

Fits of a one-zone plasma model has been performed to the "Homogeneous" spectrum. In Figure 4.3.3 the χ^2 for different values of the temperature and electron density of the one-zone model can be seen as a colormap. These are the parameters tuned during the first step of the fit routine via simulated annealing. The χ^2 values were obtained by normalizing the residuals (r^2 in equation 4.2.3) to the degrees of freedom (number of peaks included in the fit minus the number of parameters in the plasma model). The best fit is obtained for a temperature equal to the actual value used for simulating the test spectrum and for an electron density that is the closest within the discretization of the fit parameter search space (see Figure 4.3.1 for the reference profiles). In Figure 4.3.4, the convergence during the iterative solving and linearization of equation (4.2.6) can be seen. This is what takes place during the second step of fit routine. The convergence is shown exemplary for the set of temperature and electron density corresponding to the best fit. From the figure, it can be seen that the iterative solving and linearization converges within eight iterations.

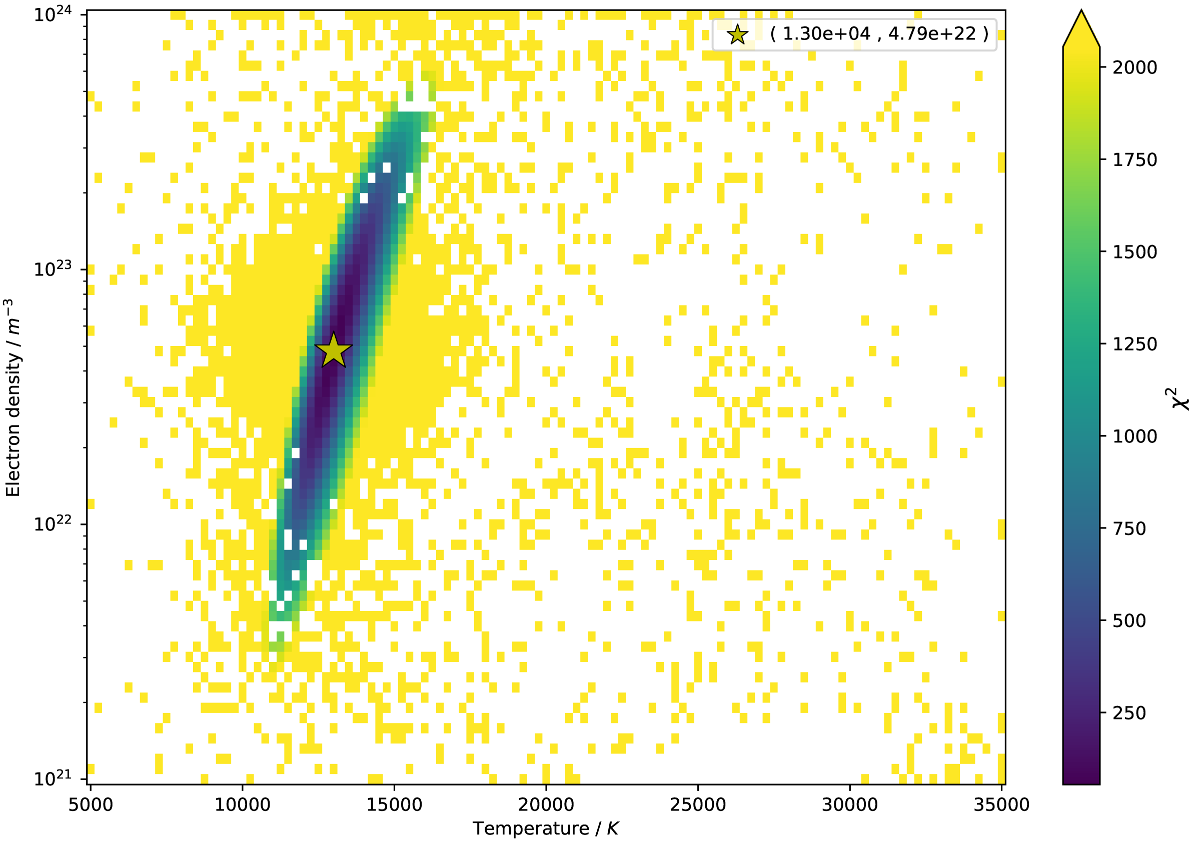

Figure 4.3.3: *χ^2 for different values of temperatures and electron densities. The best solution, which is the only minimum, is marked by the star. White areas are combinations of plasma parameters not visited during fit (see Fit routine step 1 in previous section). The best solution is found for a temperature equal to the actual temperature of the "Homogeneous" plasma and an electron density that is the closest within the discretization of the parameter space. The discretization of the parameters space can be inferred by the size of the data points. When considering the large span in χ^2 of 2000 values between blue and yellow points, the best solution can be seen to be very well confined.*

For the best solution/fitted parameters, a histogram of the relative residuals of the spectrally integrated peak intensities can be seen in Figure 4.3.5. The relative residuals are defined as the expected peak intensities (as obtained from the two-zone fit) minus the observed peak intensities and divided by the observed peak intensities. The residuals have a RMSE of 7.6 % and with a maximum residual of ~30 %. The derived relative elemental concentrations can be seen in Figure 4.3.6. The values were obtained by normalizing the fitted and the reference values to 100 %. For the four considered elements, the relative deviations from the reference values are within ±2 %. Using the best fitted parameters (set of plasma properties and elemental concentrations) the spectrum has been evaluated in the full spectral range of the input spectrum (the fit is only done to extracted and integrated peak intensities, i.e. a smaller part of the spectral full spectral range). This will be referred to as the reconstructed spectrum and it can be seen in Figure 4.3.7 together with the input spectrum as well as the residuals.

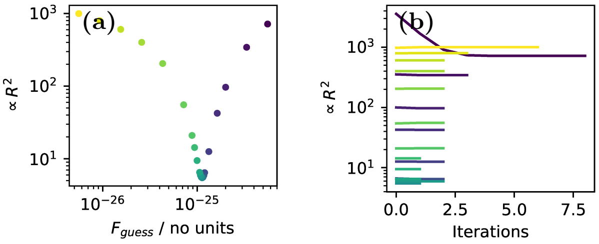

Figure 4.3.4: *The residuals, r^2, during the second step of the fit routine (iterative linearization and solving of eq. (4.2.6)) shown for the set of temperature and electron density corresponding to the best fit.* ***(a)*** *The converged residuals for different values of F_{guess}.* ***(b)*** *The residuals during the iterative solving for different values of F_{guess}. The points and lines in (a) and (b) are mapped to each other by the colors.*

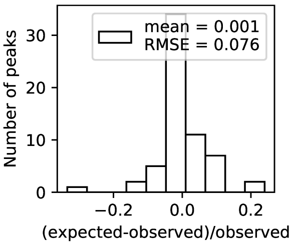

Figure 4.3.5: *The relative residuals of the integrated peak intensities for the best solution. The residuals have an RMSE of 7.6 %.*

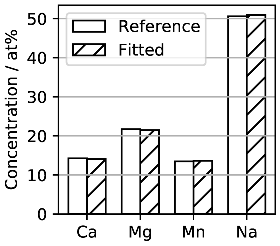

Figure 4.3.6: *The derived relative concentrations compared to the reference values. The relative deviations are within ±2 %.*

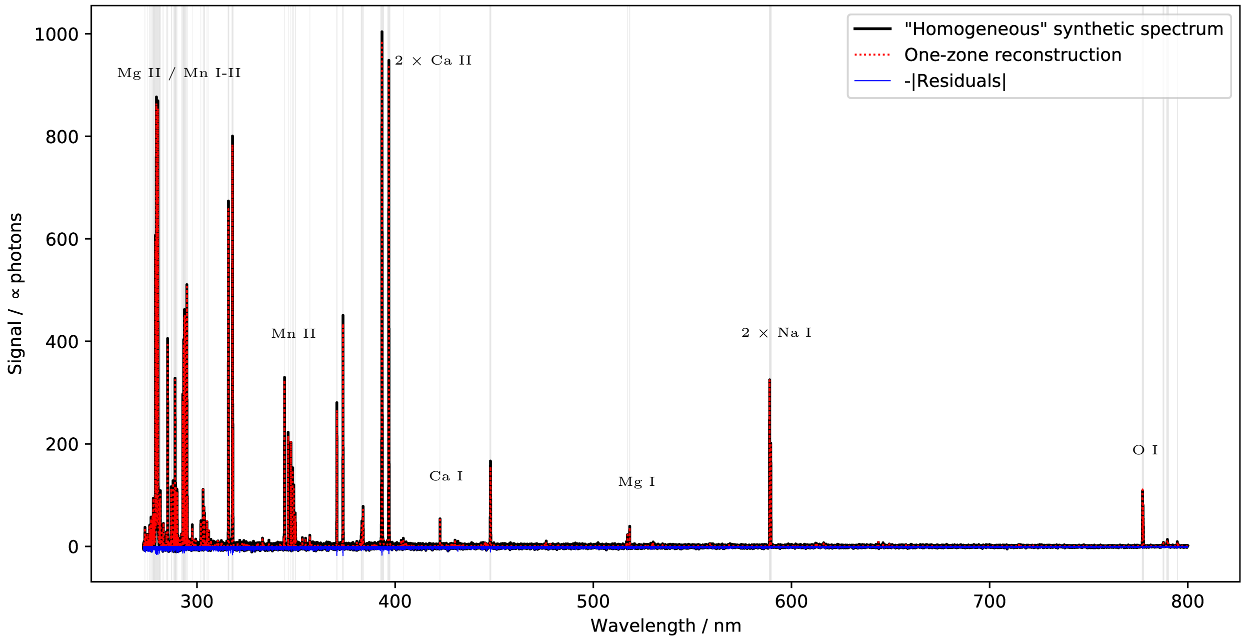

Figure 4.3.7: *Reconstructed spectrum (red dashed curve) calculated from the best fit shown together with the original data (black solid curve). The negation of the absolute residuals between the reconstructed and the original data is also shown (blue solid curve). The residuals can be seen to be very low.*

4.3.3 Two-zone Fits to Synthetic Spectra

Fits of the two-zone model have been performed to the "Gaussian", "Reversed Gaussian", "Shifted Gaussian", and the "Bogaerts" synthetic spectra. The χ^2 for different values of the plasma properties of the two zones are shown in Figure 4.3.8 and in 4.3.9 as colormaps with two different scalings. For a two-zone plasma model these χ^2 values are in a five dimensional space. The shown figures therefore correspond to different 2D projections using the *minimum intensity projection* [99]. From Figure 4.3.8, showing χ^2 values up to 100 from the best solutions, it can be seen that the best solutions are statistically very well confined. From Figure 4.3.8, showing χ^2 values up to 2250 from the best solutions, a symmetry in the exchange of the temperatures of the zones can be seen. This results in a second local minimum with fitted parameters similar to the best solutions but with the zones interchanged. Furthermore, a "cross" or "butterfly shape" of lower χ^2 values for the temperatures of the zones can be seen. It can be described as being is composed of two elongated regions of lower χ^2 values where one of the temperatures is constant and the other extends towards lower or higher temperatures. The two elongated regions intersects at $\mathrm{T}_{\mathrm{inner}} \sim \mathrm{T}_{\mathrm{outer}}$ which corresponds to the one-zone solution. The one-zone plasma model is naturally contained in the two-zone model when the plasma properties of the zones are equal or when the relative effective path of either of the zones is negligible compared to the other. The χ^2 values of the best, the symmetric, and the one-zone solutions are summarized in Table 4.2. For the "Gaussian" and "Shifted Gaussian" spectra the symmetric solution has a χ^2 value that is approximately 500 higher than the best solution, whereas the difference is half as big for the "Reversed Gaussian" and the "Bogaerts" spectrum. The difference between the best and the one-zone solution is at least 1600 for all the four spectra.

Two-zone fit to:	Gaussian	Reversed Gaussian	Shifted Gaussian	Bogaerts
χ^2 (best):	113	63	97	71
χ^2 (symmetric):	592	200	732	295
χ^2 (one-zone):	~ 1600	~ 1500	~ 2000	~ 1600

Table 4.2: *Table of χ^2 values for the best, symmetric, and one-zone solutions (see Figure 4.3.9). For the "Gaussian" and the "Shifted Gaussian" spectra, the symmetric solution has a χ^2 that is more than 500 higher than that of the best solution. For the "Reversed Gaussian" and the "Bogaerts" spectra, the χ^2 of the symmetric solution is around 150 higher than that of the best solution. For all the spectra, the χ^2 of the one-zone solution is at least 1300 values higher than that of the best solution.*

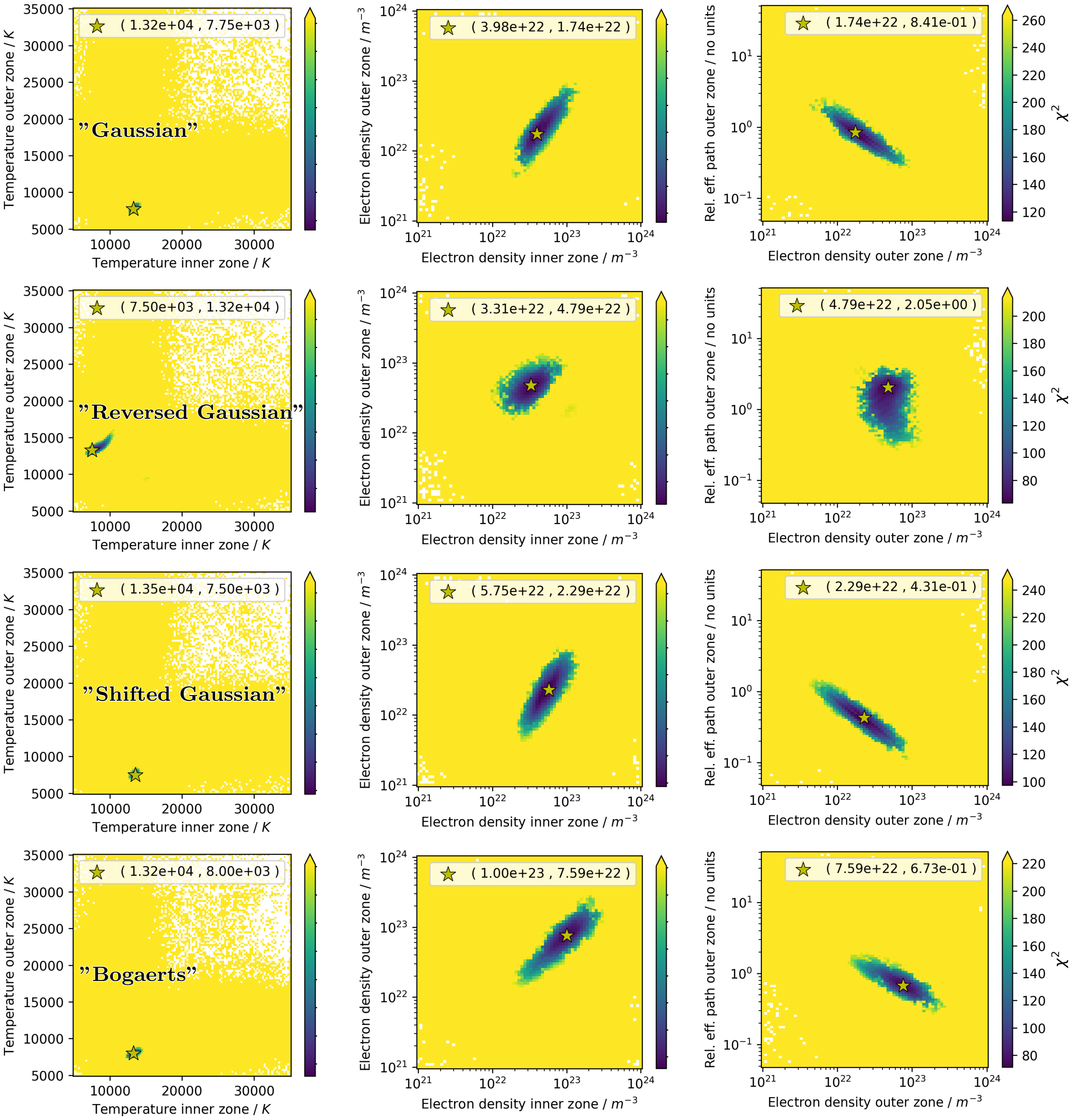

Figure 4.3.8: *χ^2 for different values of temperatures and electron densities and relative effective path of the outer zone when fitting a two-zone plasma model to four of the synthetic test spectra. Each row corresponds to results of the spectrum annotated on the left most figures. The χ^2 values are obtained by normalizing the residuals to the degrees of freedom of the fit and shown as colormaps spanning 100 χ^2 values. The best solution is marked by the star. Within the χ^2 span only one minimum is present for each of the test spectra and it can be seen that the temperatures are the best constrained parameters.*

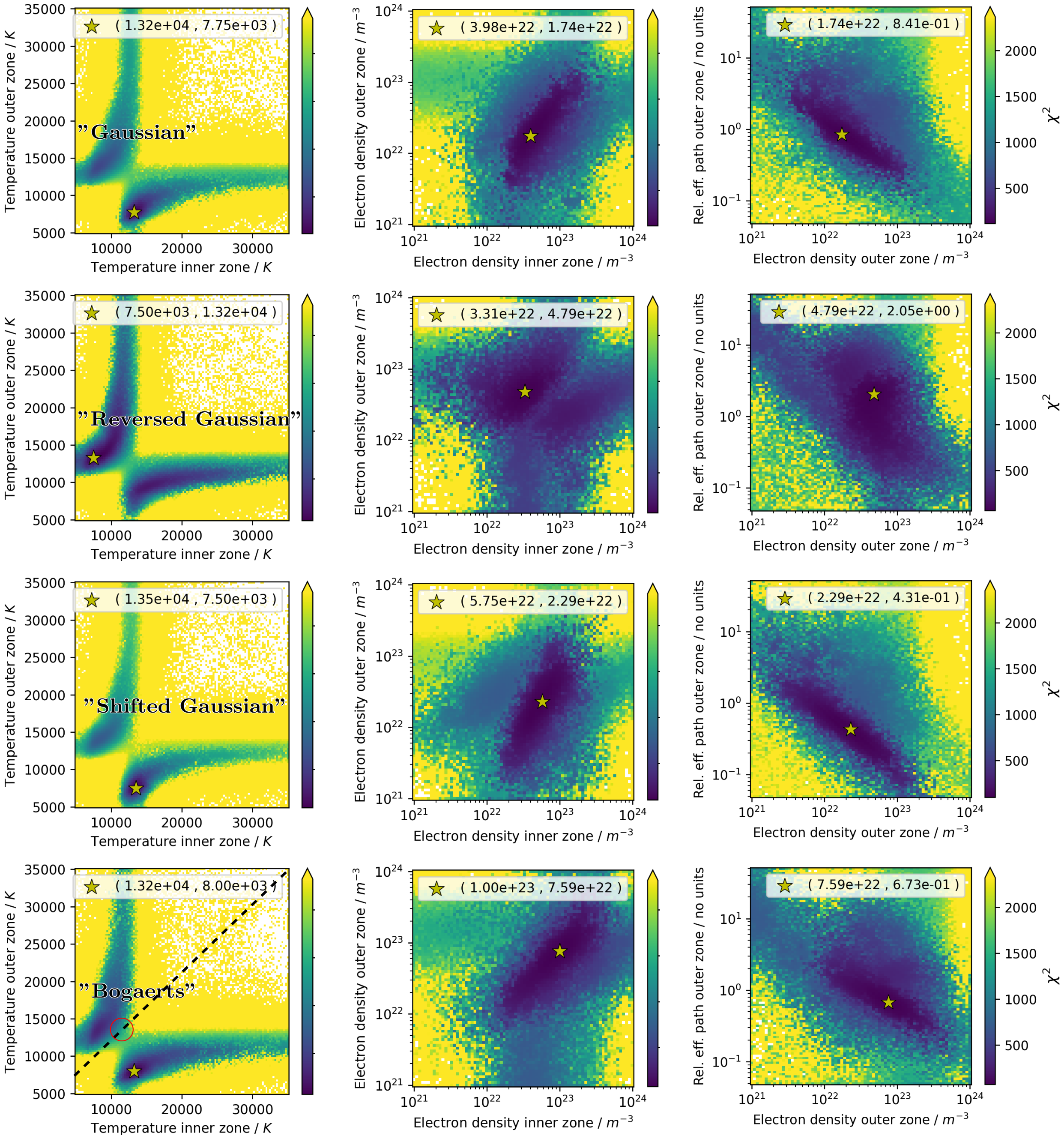

Figure 4.3.9: *Same as Figure 4.3.8, but for a χ^2 span of 2250 values. At such high χ^2 a symmetry in the interchange of the temperatures of the zones can be seen. Furthermore, the one-zone solutions at $T_{inner} \sim T_{outer}$ are visible. Exemplary, the symmetry axis and the one-zone solution have been annotated for the "Bogaerts" spectrum (bottom row of plots) by the black dashed line and the red circle, respectively.*

In Figure 4.3.10 the relative peak residuals for the best solutions can be seen. For the "Gaussian", "Reversed Gaussian", and the "Shifted Gaussian" test spectra, the relative residuals have a RMSE of ~8 %. The RMSE for the "Bogaerts" spectrum is a little higher and of 11 %. In Figure 4.3.11 the derived relative elemental concentrations of the four major elements are compared to the reference values. For all the four spectra, the relative deviations are similar and within 12 % for all the four considered elements.

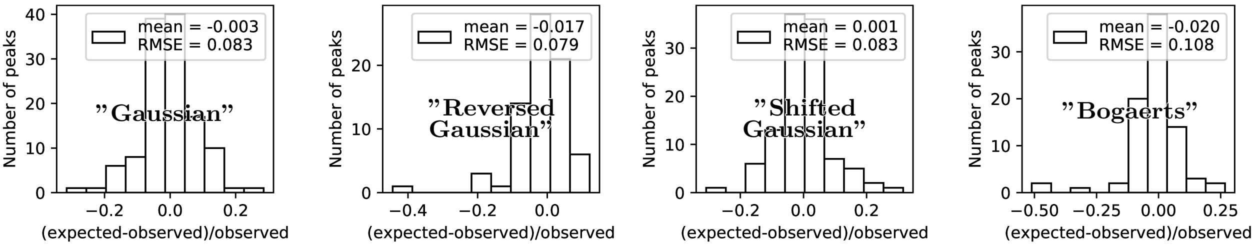

__Figure 4.3.10:__ Relative peak residuals for the best solution. As seen from the figure annotations the RMSE of the residuals is around 8 % for the "Gaussian", "Reversed Gaussian", and "Shifted Gaussian" spectra and 11 % for the "Bogaerts" spectrum.

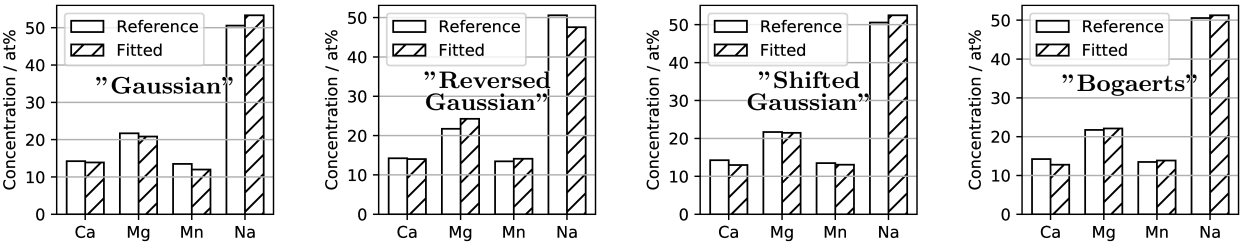

__Figure 4.3.11:__ Derived relative elemental concentrations of the four major elements in the plasma compared to the reference values. For all the four spectra the relative deviations are similar and within ±12 %.

The reconstructed spectra in the two-zone model approximation, using the best fitted parameters, are shown together with the original test spectra in Figure 4.3.12, 4.3.13, 4.3.14, and 4.3.15. From the figures it can be seen that the reconstructed spectra resemble the original well. In Figure 4.3.16 histograms of the reconstructed intensities are shown with and without the effect of absorption. It can be seen that the effect of absorption reduces the strongest intensities by a factor of ~100. For comparison, the histograms of the original test spectrum intensities, i.e. the intensities of the spectra as shown in Figure 4.3.2 before any two-zone discretization, are also shown in the same figure. The histograms of the two-zone reconstructed and the reference/original intensities are seen to have similar distributions.

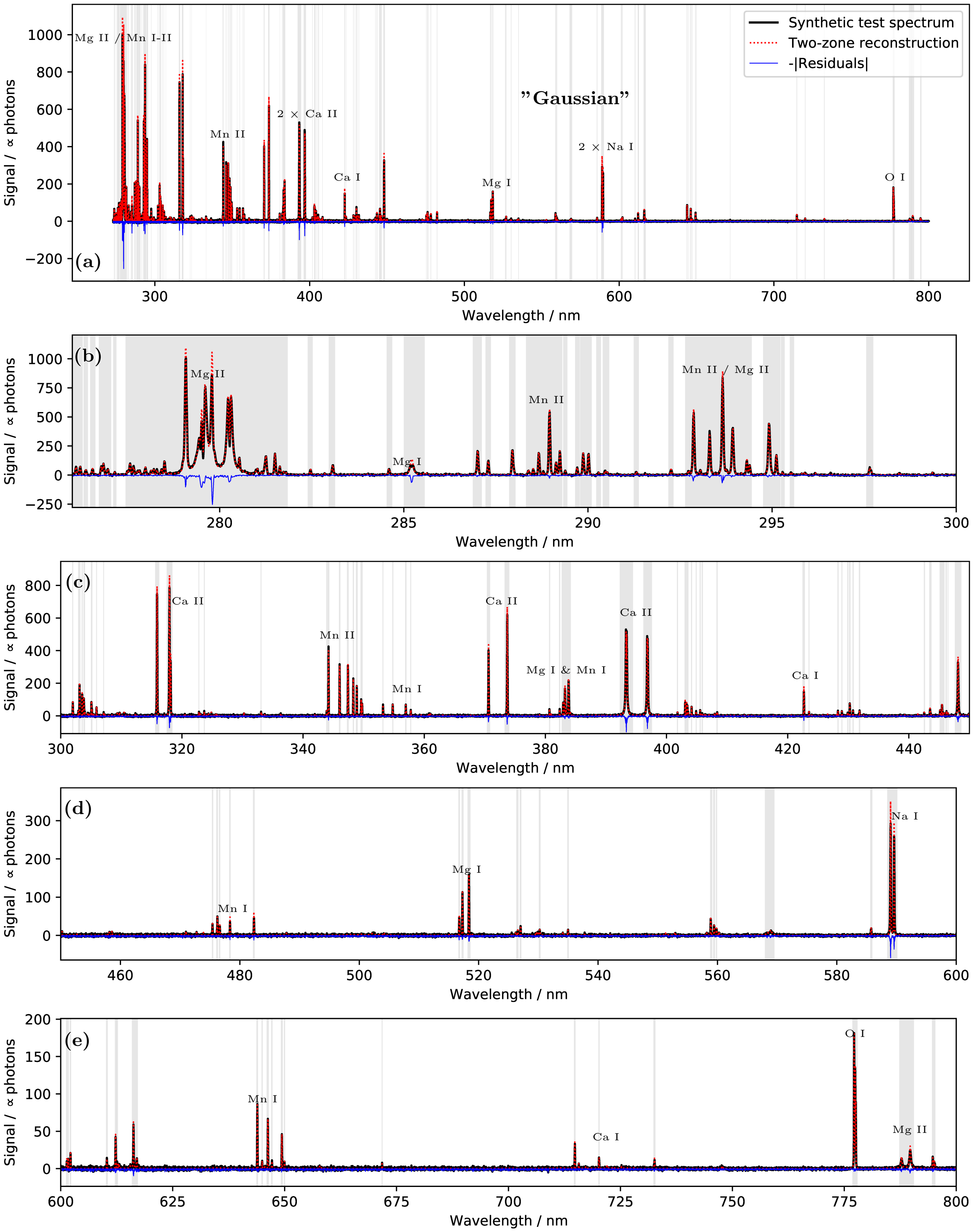

Figure 4.3.12: ***(a)*** *Reconstructed spectrum (red dotted curve) using the best fit of the two-zone model applied to the "Gaussian" synthetic test spectrum (black curve). The negation of the absolute residuals between the reconstructed and the test spectrum is also shown (blue curve). The spectral ranges that were included in the fit are marked by the vertical grey shades.* ***(b-e)*** *Close-ups of (a) in smaller wavelength ranges. The residuals can be seen to be low and the two-zone approximation provides a good description of the "Gaussian" test spectrum.*

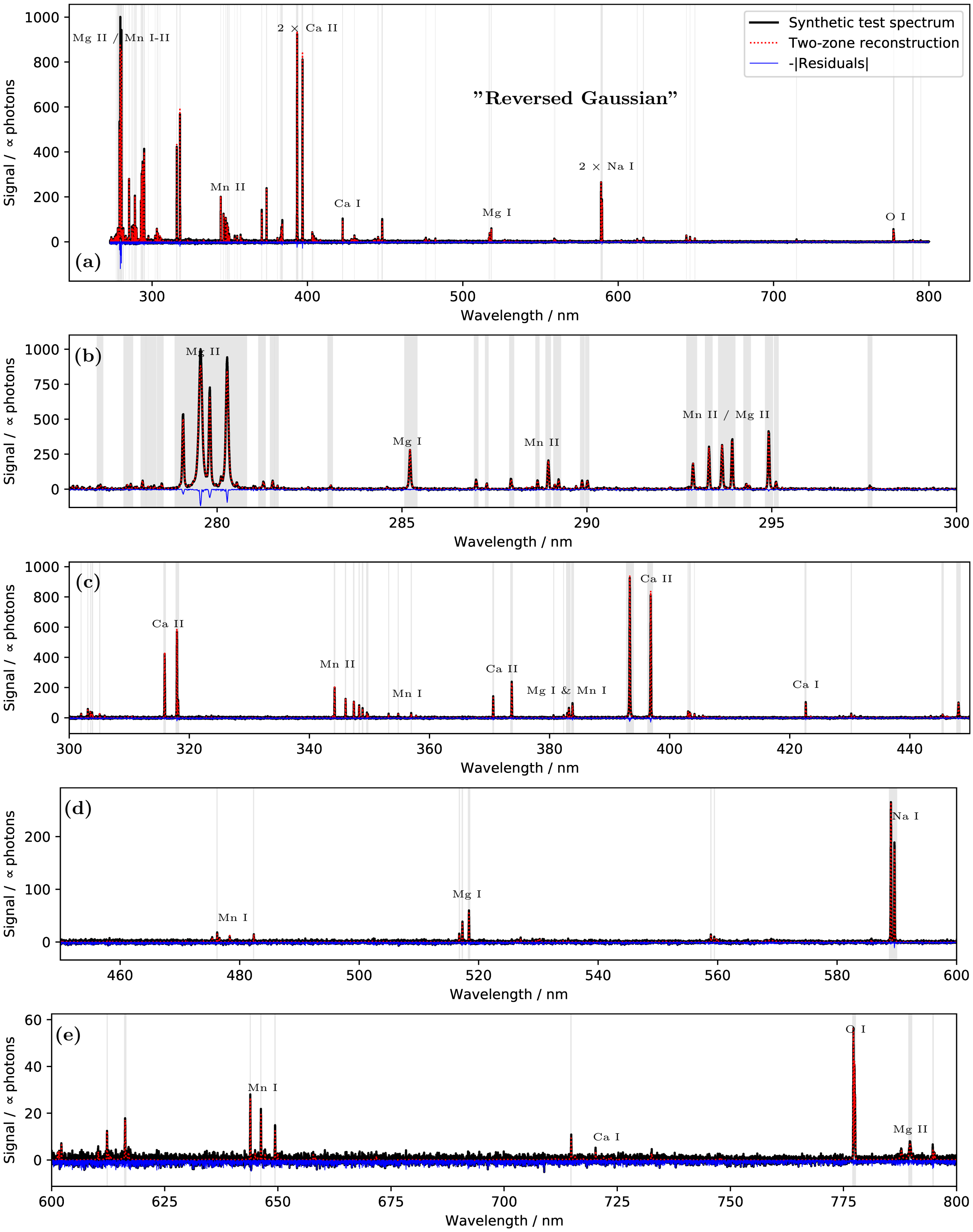

Figure 4.3.13: Same as 4.3.12 but for the "Reversed Gaussian" spectrum.

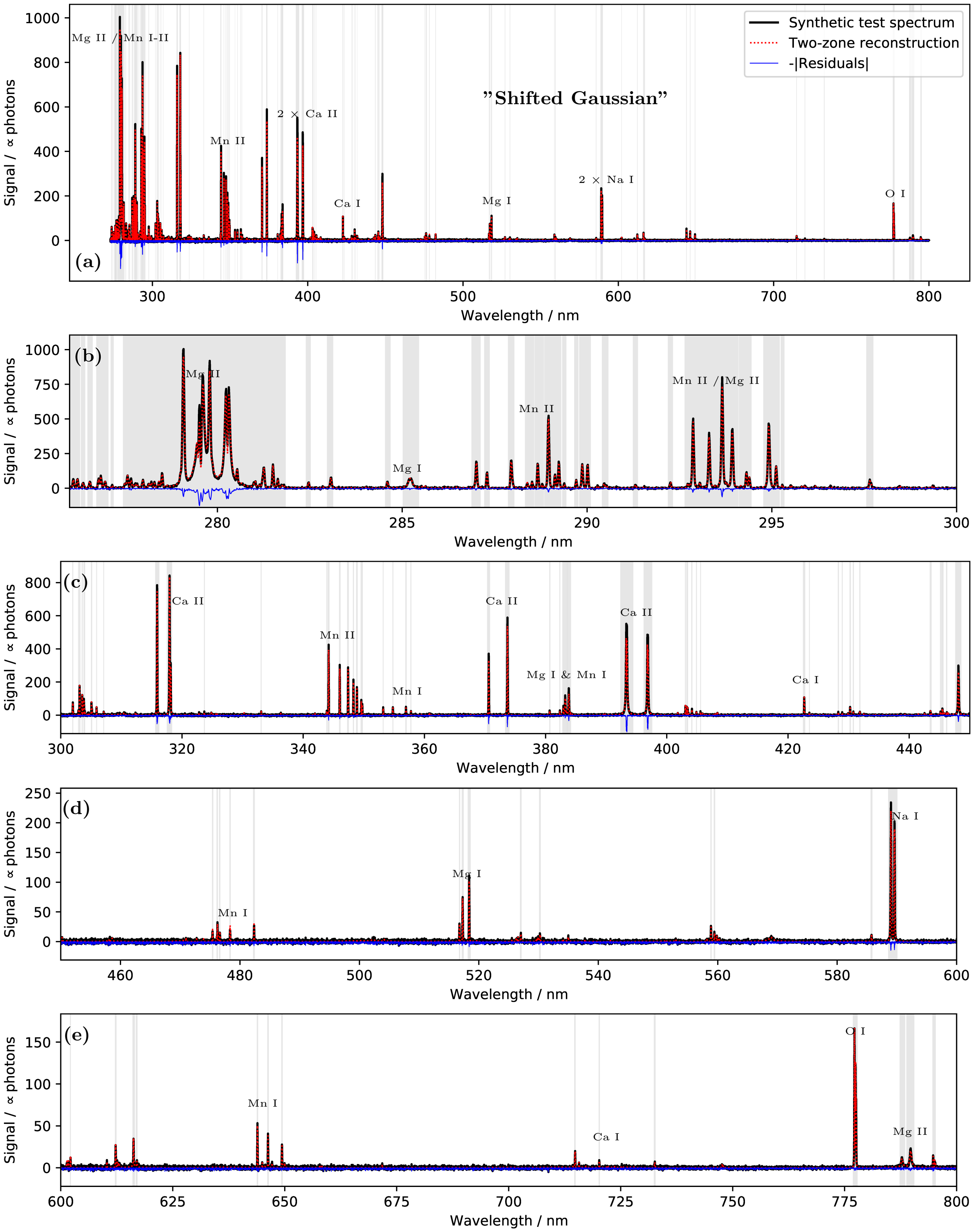

Figure 4.3.14: *Same as 4.3.12 but for the "Shifted Gaussian" spectrum.*

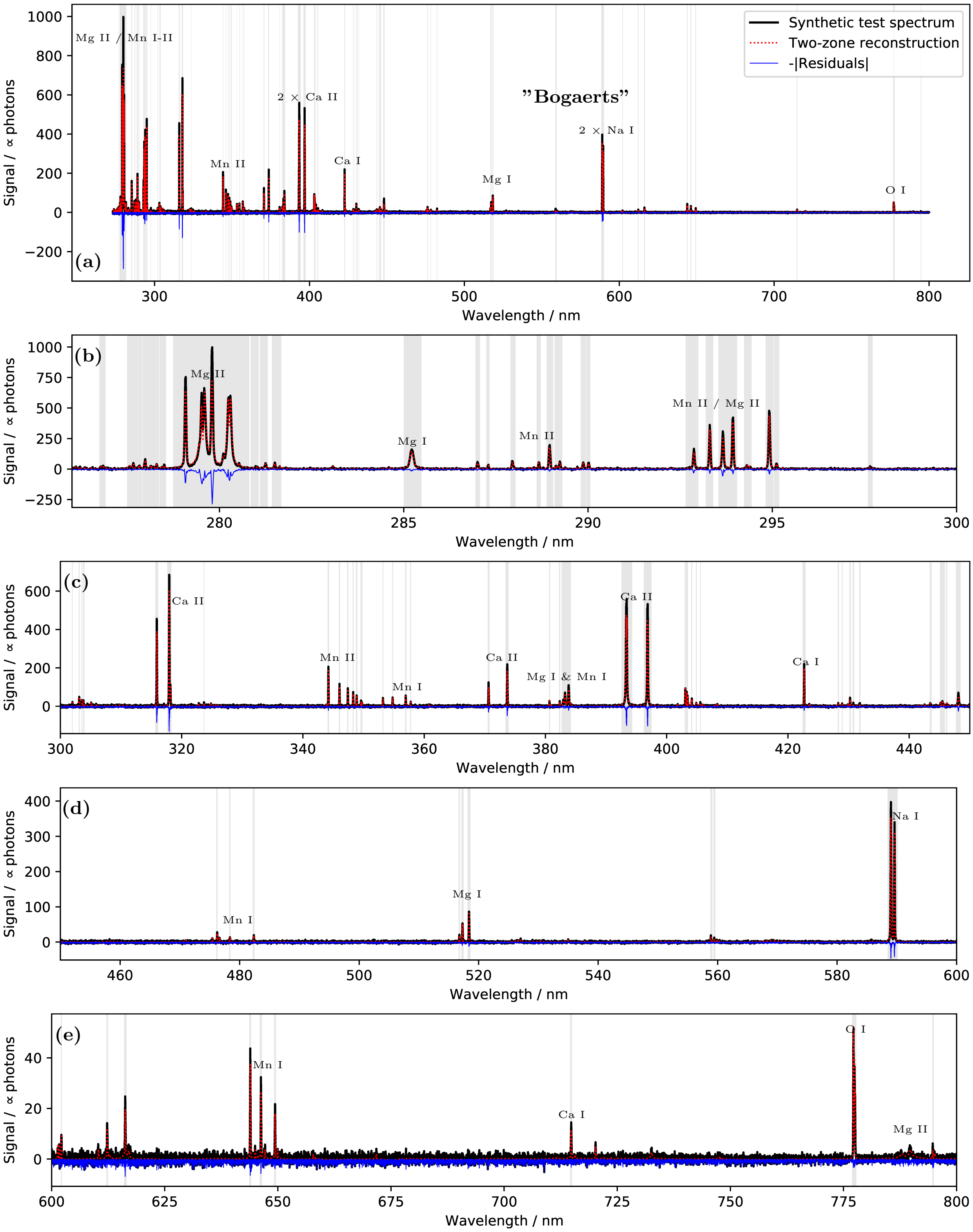

Figure 4.3.15: *Same as 4.3.12 but for the "Bogaerts" spectrum.*

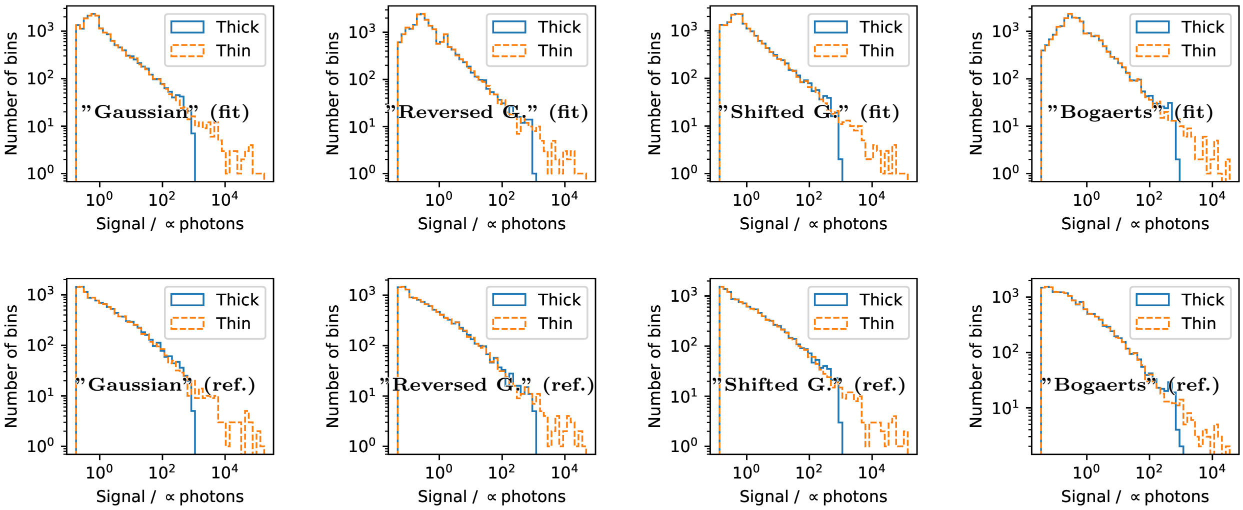

Figure 4.3.16: ***Top row:*** *Histograms of predicted pixel intensities as obtained from reconstruction of the spectra using the best fitted parameters with and without the effect of absorption.* ***Bottom row:*** *Pixel intensities as derived from the actual profiles of the synthetic test spectra (Figure 4.3.1) with and without the effect of absorption.*

In Figure 4.3.17 the derived profiles in the two-zone approximation are shown together with the true/reference profiles of the synthetic spectra. The derived profiles include the lengths of the zones and the elemental densities. These values have been derived from the best fitted plasma properties and the effective paths of the elements using conservation of charge and the Saha-equaiton ((2.2.16) Chapter 2). As the profiles of the ”Bogaerts” spectrum were chosen freely, this spectrum is not included. The profiles of the ”Homogeneous” spectrum, derived from the one-zone fit in the previous section, is also shown. The derived profiles for the ”Homogeneous” spectrum can be seen to match the reference profiles well. For the other synthetic spectra, larger discrepancies can be seen. For example the electron density of the outer zone of the ”Gaussian” and ”Shifted Gaussian” spectra can be seen to be fitted to a value below the minimum electron density along the LOS of the reference profiles. This is not the case for the ”Reversed Gaussian” spectrum. On the other hand, the fitted temperatures of the zones appear to be more systematic. For the temperature, one of the zones adapts to a value close to the minimum temperature along the LOS and the other zone adapts to a value approximately half way between the middle and the maximum value.

In Figure 4.3.18, the reconstructed spectra after passage of the inner zone and the outer zone are shown exemplary for the ”Gaussian” and ”Reversed Gaussian” spectra. From the figure it can be seen that the role of the second zone is different for the two spectra. For the ”Gaussian” spectrum many of the strong emission lines decrease in signal after passage of the outer zone (zone 2) which, for these lines, works as an absorbing slab of material pulling the signal down towards the black-body limit corresponding to the temperature of the outer zone. For the ”Reversed Gaussian” spectrum the signal of all emission lines increases after the passage of the outer zone.

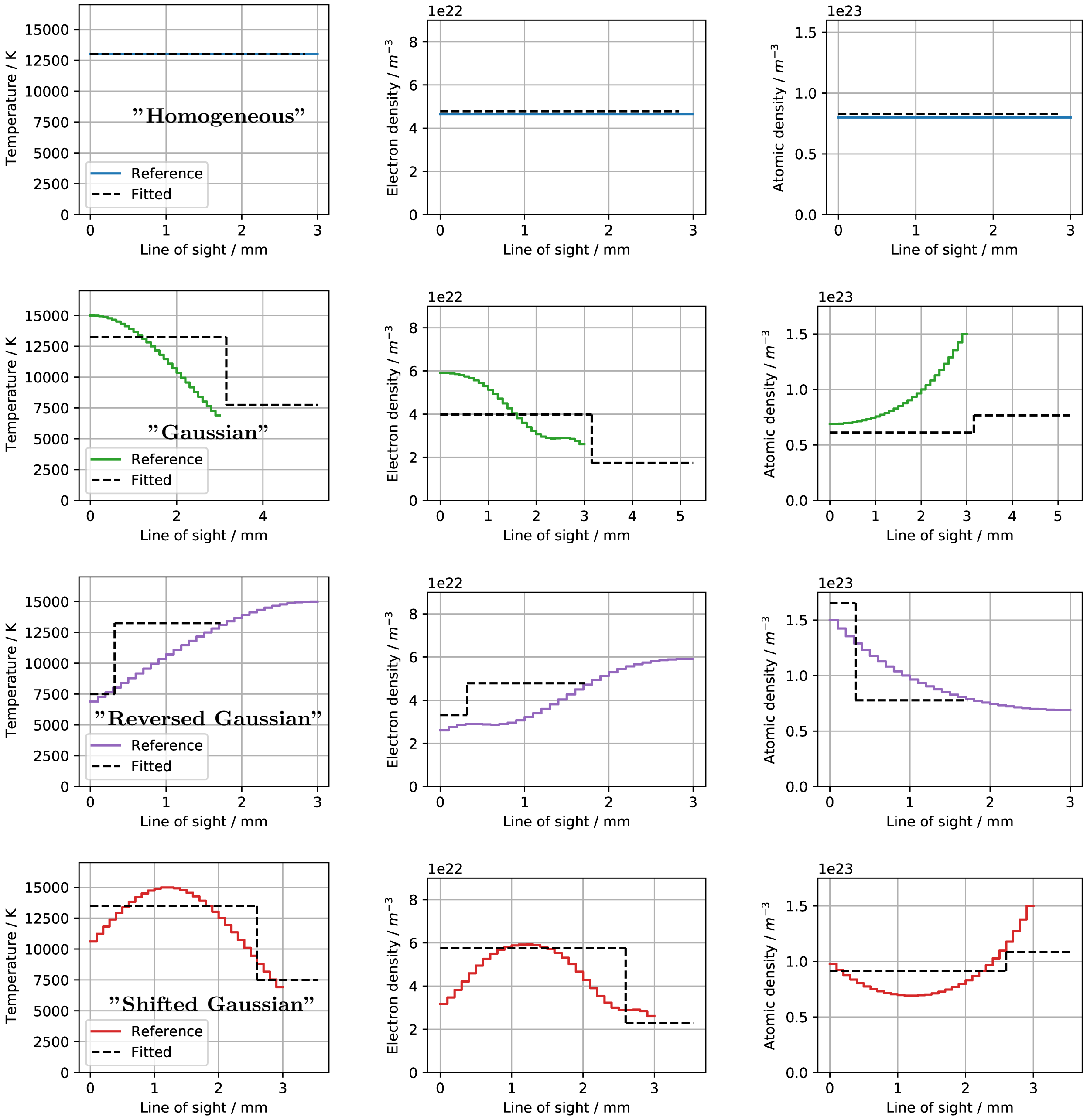

Figure 4.3.17: *Derived profiles in the two-zone approximation compared to the true profiles of the synthetic spectra. The profiles have been derived using conservation of charge and the best fitted plasma properties of the zones. For comparison the results for the one-zone plasma fit to the "Homogeneous" spectrum is also shown. The derived profiles for the "Homogeneous" spectrum can be seen to be in good agreement with the reference/actual profile. For the two-zone fits, the trends of the fitted plasma properties of the zones are in agreement with the reference profiles, but the absolute values for the plasma lengths and the atomic densities have larger discrepancies for the "Gaussian" and the "Reversed Gaussian" spectrum, whereas they are in reasonable agreement for the "Shifted Gaussian" spectrum. The fitted temperatures of the zones are for all the two-zone fits close to the minimum temperature along the LOS and the* ~80 % *percentile of the temperature span.*

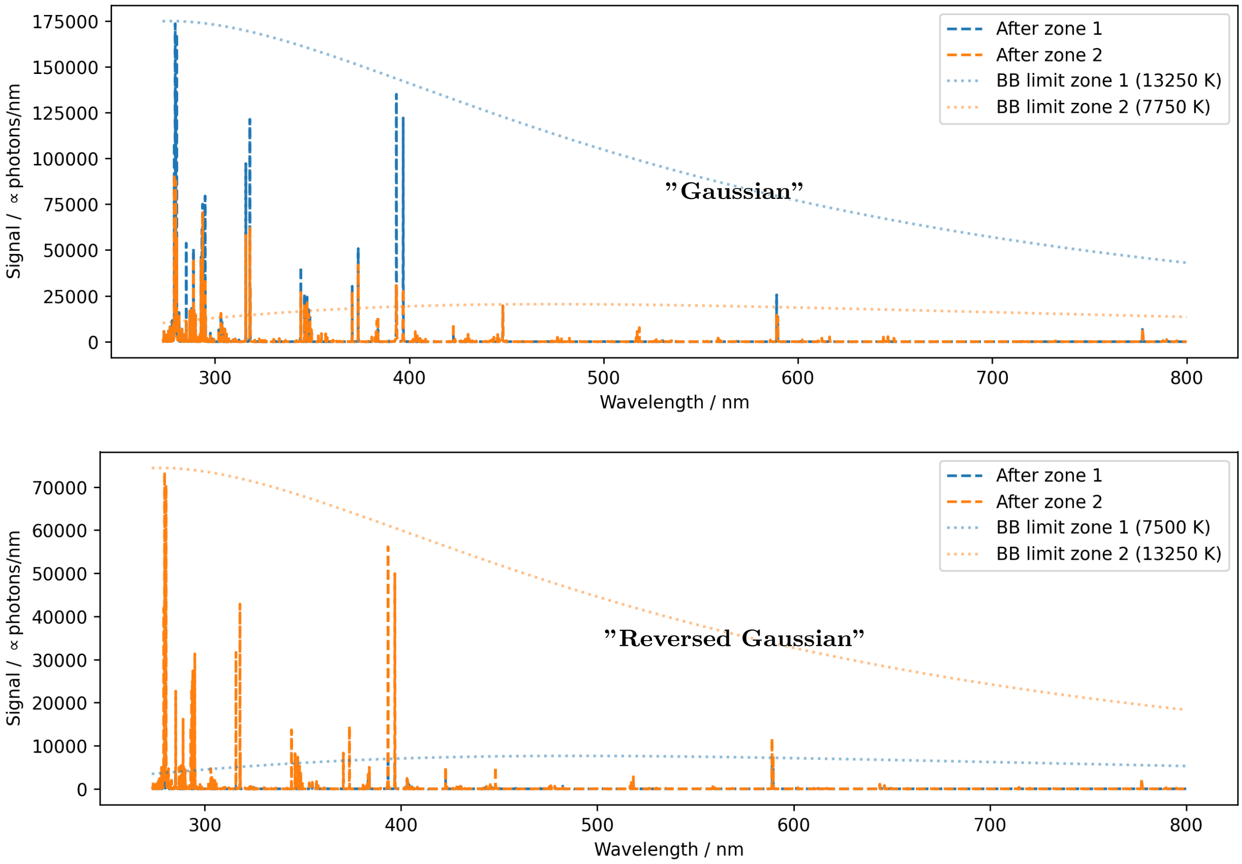

Figure 4.3.18: *Reconstructed spectra from the two-zone fits to the "Gaussian" and "Reversed Gaussian" spectra shown after the passage of the inner and the outer zones*

Reconstructed spectra from the fits to the "Gaussian" and "Reversed Gaussian" spectra shown after the passage of the inner and the outer zones (zone 1 and zone 2, respectively). The reconstructed spectra has not been integrated to fewer bins nor convoluted with the instrumental broadening function. For the "Gaussian" spectrum the outer zone can be seen to work as an absorbing zone for the strongest emission lines pulling their signals down towards the black-body limit (BB in the legends) corresponding to the temperature, whereas the outer zone for the "Reversed Gaussian" spectrum only adds to the signal of the emission lines.

4.3.4 Discussion of Fit Results

As the "Homogeneous" spectrum was created with constant plasma properties along the LOS, the fitted one-zone model should be able to describe the data very well. The results meet this expectation and verify the implementation of the fit-routine and the iterative solving and linearisation of the equations during the second step of the fit routine. As the fitted plasma properties almost exactly match the reference values (0 % and 3 % relative deviations for the temperature and the electron density, respectively), the smaller deviations among the peak intensities (RMSE of 7.6 %) and the relative concentration estimates (below ±2 % relative errors) are attributed to the noise in the spectrum.

The results from the two-zone fits to the "Gaussian", "Reversed Gaussian", "Shifted Gaussian", and the "Bogaerts" synthetic spectra confirm that spectra from plasmas with spatial variations of the plasma properties are well modelled by a two-zone plasma model. This can be inferred by the small deviations between the peak intensities (RMSEs below 11 %) and the relatively low residuals between the reconstructed and the original spectra (Figure 4.3.12, 4.3.13, 4.3.14, and 4.3.15). The RMSEs for the peak intensities for the two-zone fits are only around 3 % points larger than the RMSE for the one-zone fit to the "Homogeneous" spectrum. The contribution from the discretization of the plasmas into a two-zone model to the RMSEs therefore seems low. Adding an extra zone to the fit model, i.e. fitting a three-zone model to the spectra, would therefore likely not improve the results significantly. The synthetic spectra were simulated without considering uncertainties in the atomic constants. The signal variation expected from these uncertainties for many of the relevant emission lines (see Figure 4.1.10) are larger than the RMSEs of the peak residuals and a three-zone model might therefore lead to over-fitting when considering such uncertainties.

From the χ^2 colorplots for the different values of the plasma properties of the two-zone fits (Figure 4.3.8), it can be seen that the temperatures of the zones are the best confined and thereby the most important parameters in the thermodynamic description of the of the plasma. As only integrated intensities are considered, the information about the electron density from the line profiles is not directly utilized in the fits which otherwise could help further confine the electron density. Related to this, the temperature in the derived profiles compared to the reference/true profiles (Figure 4.3.17) is also the most systematic parameter. The electron densities, atomic densities, and the lengths of the zones are for some spectra underestimated and for others overestimated. The temperatures, however, are fitted to a value close to the minimum temperature along the LOS for one zone and for the other zone close to a value approximately half way between the median and the maximum value. When considering the χ^2 colorplots with colors spanning a larger interval of χ^2 values (Figure 4.3.9) a symmetry in the interchange of the properties of the inner and outer zone can be seen. This results in a second local minimum referred to as the symmetric solution. The physical effect distinguishing the best and the symmetric solution is the effect of absorption. In the case of negligible absorption, the order of the zones, i.e. which one is the hotter and which one is the colder, does not matter as all the emissions reaches the detector. In the case of non negligible absorption, the order of the zones becomes significant.

4.4 Analysis of Real Data in the Two-Zone Model Approximation

For the analysis of real data with the two-zone plasma model, a pellet of four mixed carbonates ($CaCO_3$, $MgCO_3$, $MnCO_3$, and Na_2CO_3) was prepared as described in Chapter 3. The elemental concentrations in the sample are 3.57 at % of Ca, 5.44 at % of Mg, 3.38 at % of Mn, 12.68 at % of Na, 18.73 at % of C, and 56.20 at % of O. This is the same composition as the synthetic test spectra from the previous section. The uncertainties of the concentrations due to weighing of the powders are below 0.05 at %. The simple composition of the sample allows for the fits to be achieved without too long computation times. Nonetheless, the elements of Ca, Mg and Mn contain many strong emission lines from both neutral and singly ionized species and furthermore from a relatively broad range of upper energy levels. The emissions from these elements therefore challenge the thermodynamic description of the data in the two-zone model approximation and also help confine the fit parameters. This has been the motivation for selection the sample composition.

4.4.1 Measurements

LIBS measurements of the carbonate pellet were performed in experimentally simulated Martian atmospheric conditions (see Chapter 3) with a fixed integration time of 50 ns at four different delay times: 500 ns, 750 ns, 1000 ns, and 1250 ns. For all measurements, the laser pulse energy was attenuated to be 35 mJ as measured at the sample surface and the laser was operated with a repetition rate of 10 Hz. The light from 30 subsequentially induced plasmas was integrated on the camera chip to obtain one measurements. For each delay time, measurements were obtained at eight different positions of the pellet and repeated five times at a single position (at five different "depths") leading to a total of 150 induced plasmas per position on the pellet. The many repetitions were done in order to later combine the measurements to obtain spectra with a high SNR and in order to average out potential heterogeneities in the pellet. However for each consecutive depth, the measurements were found to fluctuate. This can be seen from Figure 4.4.1 showing the spectra at 750 ns delay time at different depths. The fluctuations are due to the plasmas being induced in an already formed crater of a previous laser pulse/pulses, referred to as crater effects [100]. In a compromise between a high SNR and minimizing crater effects, measurements at depths from one to three (first and third repetition) at all positions of the pellet ($3 \times 8 = 24$ measurements) were used to calculate a median spectrum for each of the four considered delay times. The four resulting median spectra (one for each delay time) can be seen in Figure 4.4.2. These spectra are the ones used for the analysis throughout the rest of this chapter.

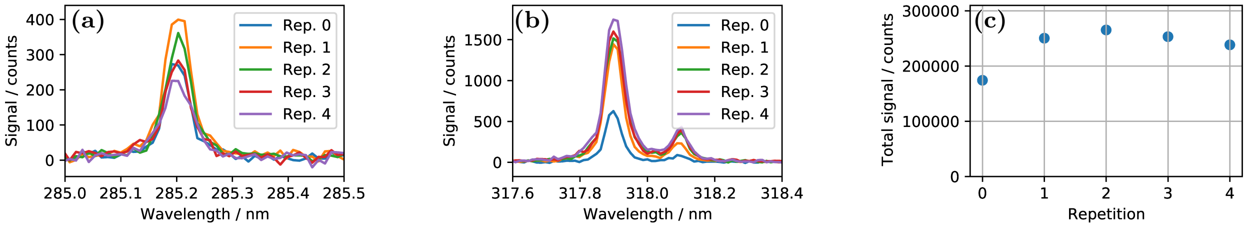

Figure 4.4.1: *The median spectra calculated over all positions at the pellet but different repetitions/depths shown exemplary for the spectrum at* 750 ns *delay.* ***(a)*** *Close-up of the Mg I groundstate transition.* ***(b)*** *Close-up of two Ca II lines.* ***(c)*** *The total signal (sum of all pixel intensities). From the figures it can be seen that the spectra varies from repetition to repetition. The variations are larger than expected from the photons noise (gain of 9 with the median from 8 positions). The largest fluctuation is between repetition 0 and 1.*

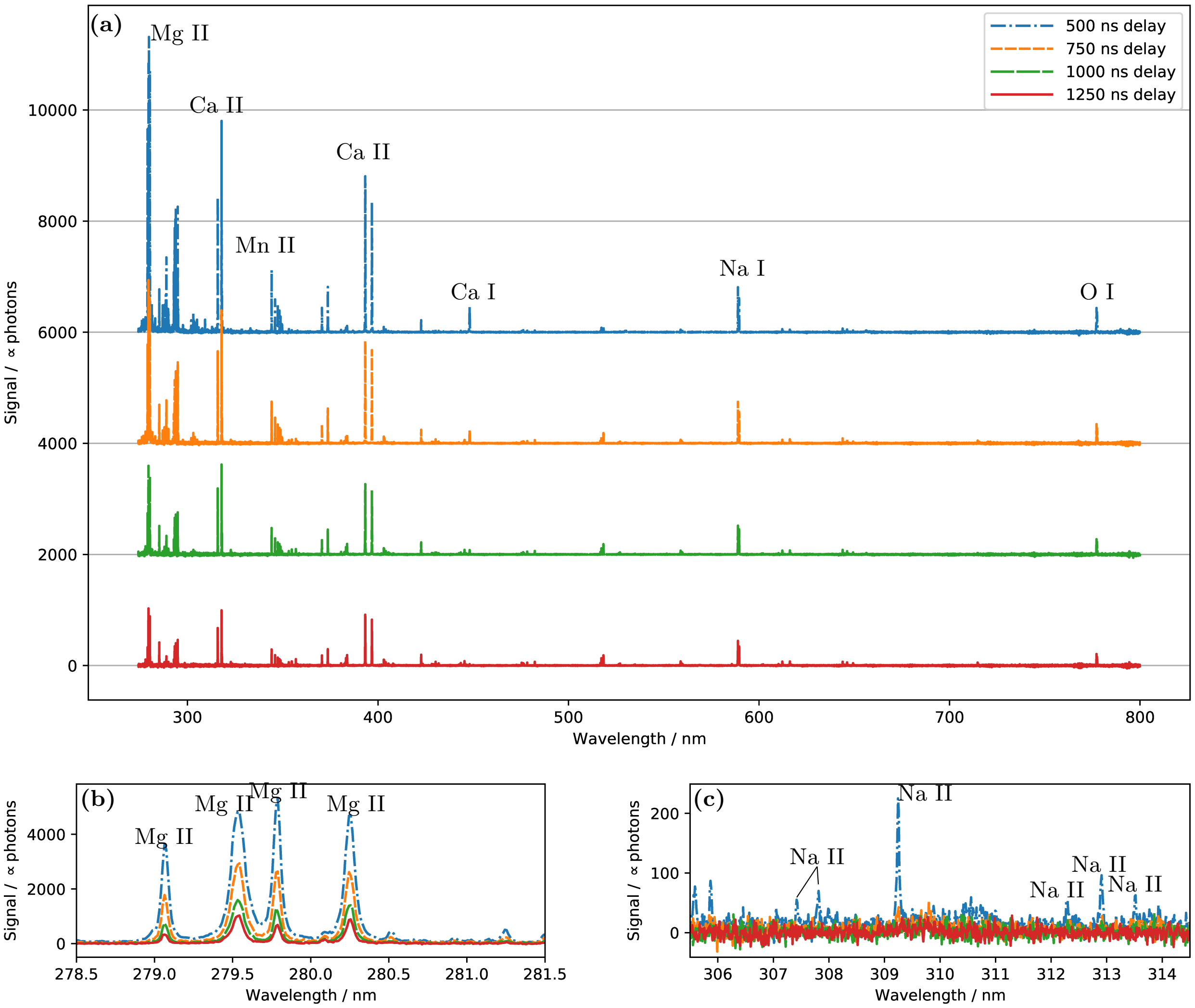

Figure 4.4.2: *The intensity calibrated median spectra of the carbonate mixture at the four different delay times.* ***(a)*** *full spectral range and shown with an offset,* ***(b)*** *close-up of the strong Mg II emission lines and* ***(c)*** *close-up of several Na II lines from highly excited states* ~ 37 *eV. As expected from a cooling of the plasma, the signal can be seen to decrease with increasing delay time.*

4.4.2 Pre-Analysis of Data

For the sake of comparison and in order to facilitate the discussion of the later results obtained from fits of the two-zone plasma model, the time-resolved spectra were analysed using the more conventional calibration-free LIBS methods. More specifically, the electron density has been determined via Stark broadening and the temperature and relative elemental concentrations have been determined by multi-element Saha-Boltzmann plots.

Although the carbonate sample was produced with nominally anhydrited reagent grade carbonate salts, a small peak originating from the Hydrogen-α emission line at 656 nm can be seen since there was some water being adsorbed at the surface of the pellet. This H emission line was used to determine the electron density. By fitting Voigt profiles, with a fixed Gaussian width corresponding to the combined effect of Doppler broadening at 10 000 K ($\mathrm{FWHM}_{\mathrm{Doppler}} = 0.047\,\mathrm{nm}$) and the instrumental broadening at the position of the line ($\mathrm{FWHM}_{\mathrm{instr.}} = 0.065\,\mathrm{nm}$), the FWHM_γ of the Lorenzian part has been extracted and linked to the electron density by [92]

$$H_\alpha : \mathrm{FWHM} = 0.549\,\mathrm{nm} \cdot \left(\frac{n_e}{1 \times 10^{23}\,\mathrm{m}^{-3}} \right)^{0.67965} . \tag{4.4.1}$$

Examples of the Voigt fits are shown in Figure 4.4.3 for the smallest and largest delay time. From the figure it can be seen that the Stark broadening dominates the widths of the line profiles and deviations from the Doppler broadening at 10 000 K are thereby relatively small. The derived electron density for the four different delay times are shown in Figure 4.4.4. From the figure it can be seen electron density decreases monotonically with the delay time starting at around $7 \times 10^{22}\,\mathrm{m}^{-3}$ at 500 ns and decreasing to $3 \times 10^{22}\,\mathrm{m}^{-3}$ at 1250 ns.

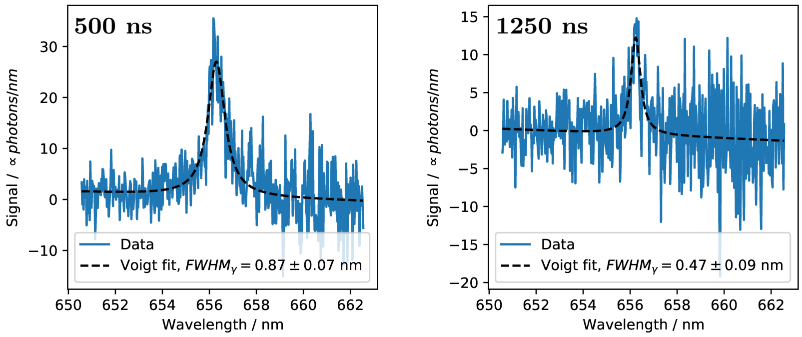

Figure 4.4.3: Voig fits to the Hydrogen-α emission line in the time-resolved measurements of the carbonate sample in experimentally simulated Martian atmospheric conditions (shown in Figure 4.4.2). The Voigt fits were done in order to extract the Lorentzian width ($FWHM_\gamma$) that can be linked to the electron density. ***(a)*** *The spectrum at the smallest delay time.* ***(b)*** *The spectrum at the largest delay time.*

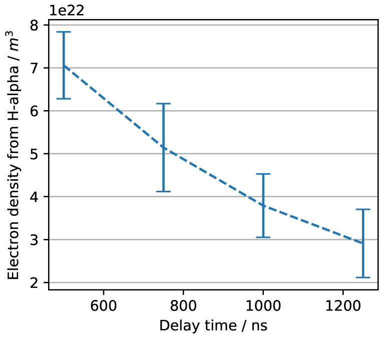

Figure 4.4.4: *The electron density obtained from the Stark broadening of the Hydrogen-α emission line. The vertical bars indicate the uncertainties as propagated from the uncertainties of the Stark widths.*

For the multi-element Saha-Boltzmann plots the emission lines in Figure 4.4.3, shown exemplary for the delay time of 500 ns, have been used together with the electron density derived from the Hydrogen-α Stark broadening. The intensities of the emission lines have been extracted via Voigt fits. The resulting Saha-Boltzmann plots for the four different delay times are shown in Figure 4.4.6. From the figure it can be seen that the temperature decreases monotonically from 12 800 K at the smallest delay time to 9600 K at the largest delay time. The statistical uncertainties of the temperature estimates are only around 200 K, but in reality the uncertainty is higher due to the assumption of a homogeneous plasma which is inherent to the the Saha-Boltzmann plot method. The resulting relative concentrations compared to the reference values are shown in Figure 4.4.7. The relative deviations for all the four considered elements (Ca, Mg, Mn, and Na) are within 55 % for all the delay times. The relative concentrations have been derived without corrections for self-absorption.

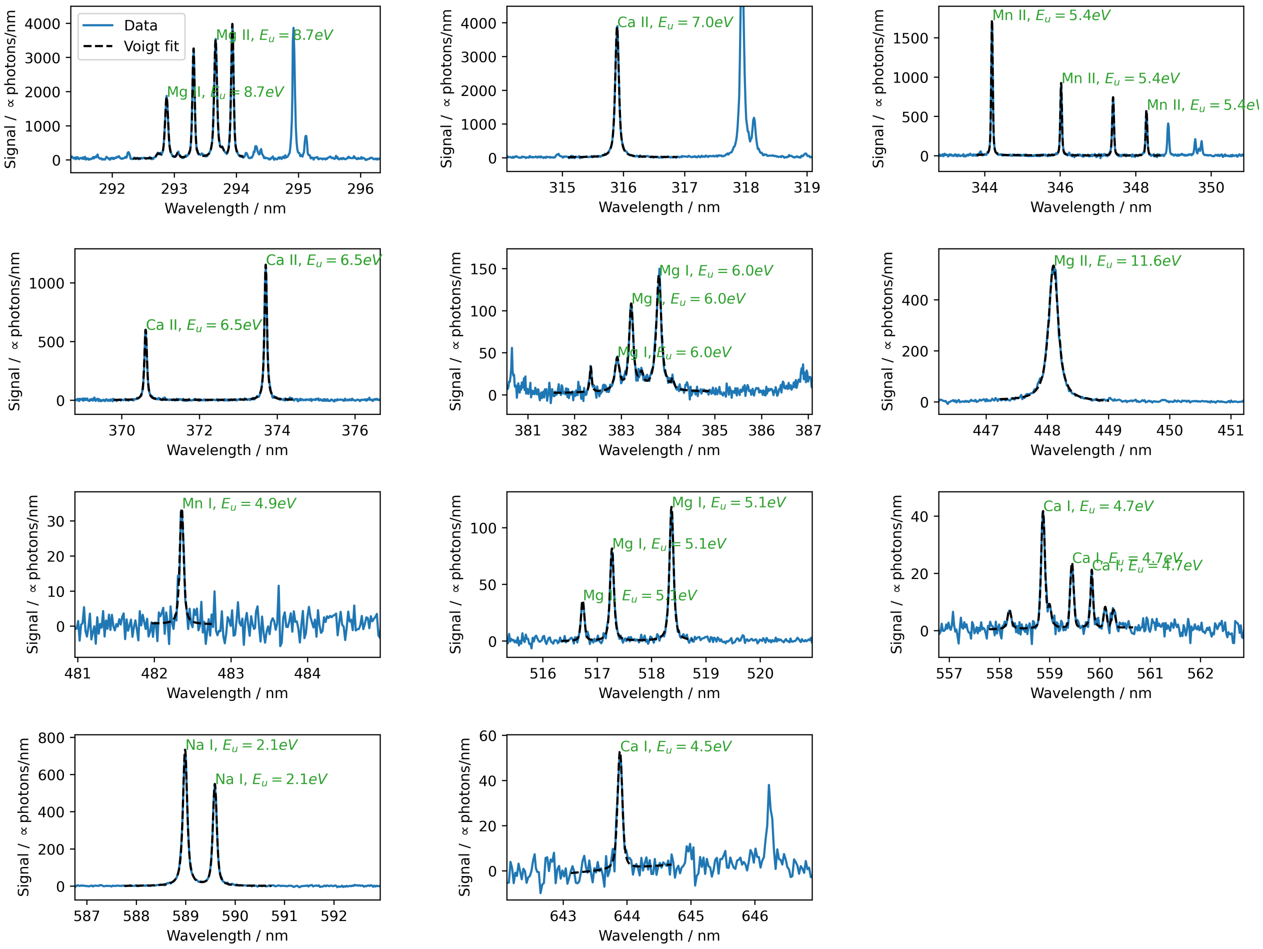

Figure 4.4.5: *Voigt fits to emission lines in the spectrum of the carbonate sample measured at a delay time of 500 ns. The lines marked in green are the ones used for the creation of multi-element Saha-Boltzmann plots.*

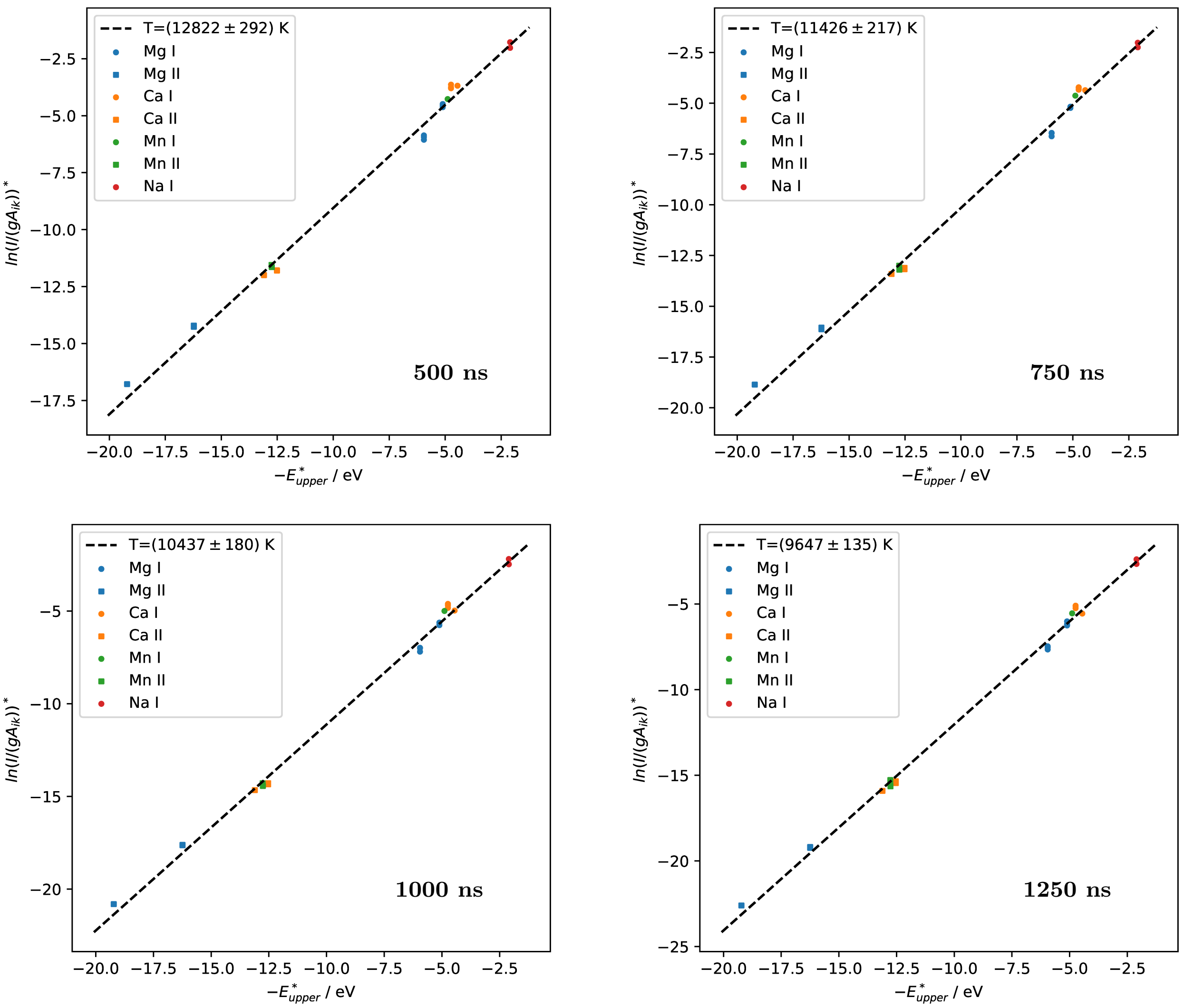

Figure 4.4.6: *Result from applying the method of multi-element Saha-Boltzmann plots to the spectra at the four different delay times using the emission lines in Figure 4.4.3 and the electron density in Figure 4.4.4. The derived temperatures are noted in the legend and the resulting relative concentration estimates are shown in Figure 4.4.7.*

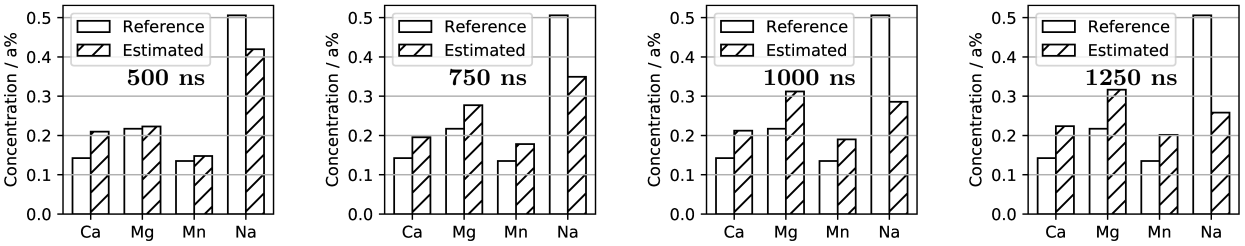

Figure 4.4.7: *Derived relative elemental concentrations via the multi-element Saha-Boltzmann plots (Figure 4.4.6) of the four major elements in to the reference values. For all the four delay times the relative deviations are within 55 %.*

4.4.3 Two-zone Fits to Real Spectra

Fits of the two-zone model have been performed to the time-resolved spectra of the carbonate sample. The χ^2 for different values of plasma properties of the two zones are shown in Figure 4.4.8 and in 4.4.9. Both as colormaps, but with different color scalings. From Figure 4.4.8, with a color scaling showing a χ^2 interval of five, it can be seen that the temperatures are well confined whereas the electron density and the relative effective path of the outer zone are only confined within an order of magnitude for a ± 5 χ^2 interval. From Figure 4.4.9, with a color scaling showing a χ^2 intervals of 100, the same symmetry as for the two-zone fits to synthetic spectra can be seen. The symmetry results in a second local minima with parameters similar to the

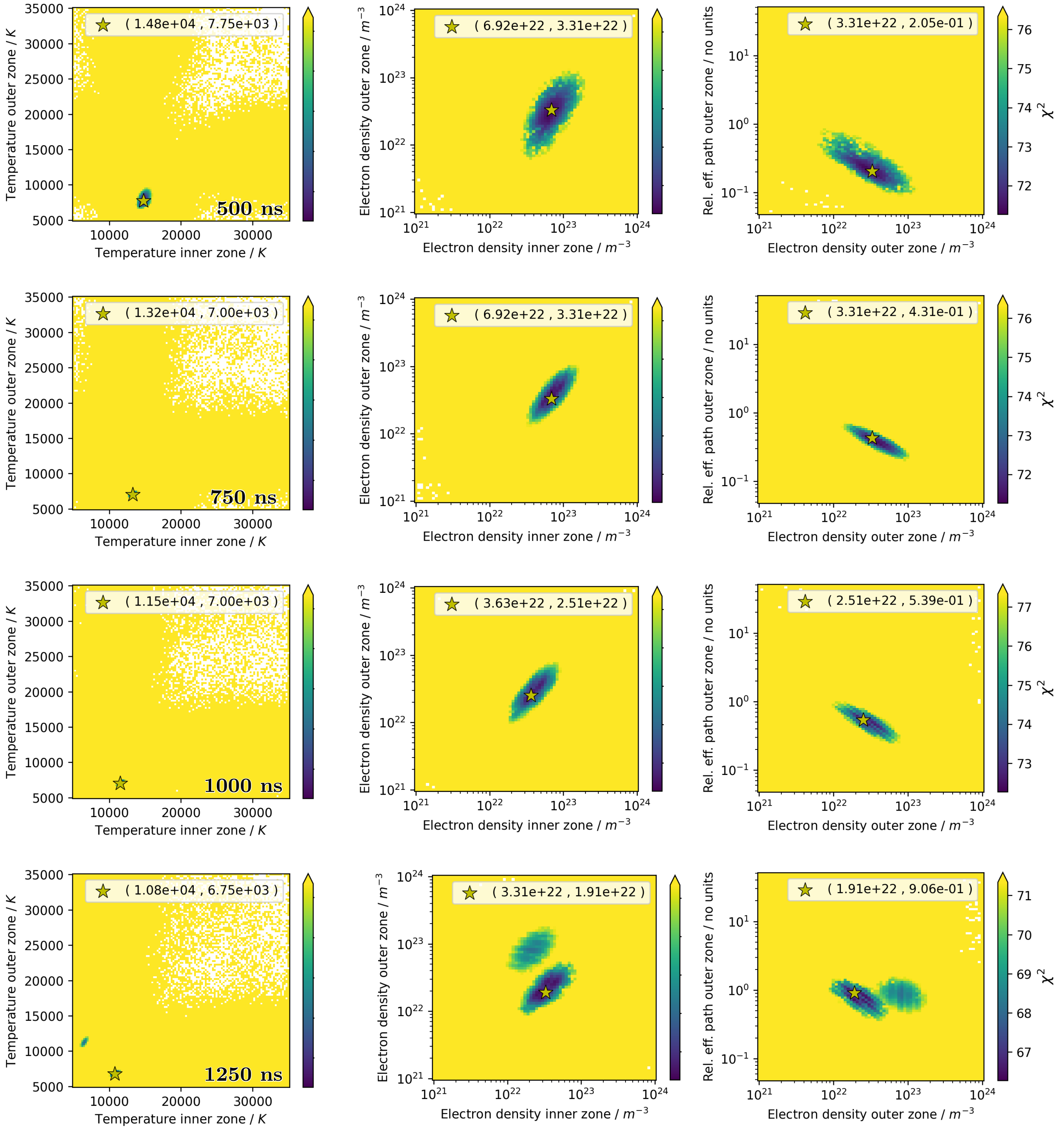

Figure 4.4.8: χ^2 *for different values of temperatures and electron densities and relative effective path of the outer zone when fitting a two-zone plasma model to the four time resolved spectra of the carbonate mixture. Each row corresponds to a different delay time. The colors span 5* χ^2 *values. Within five* χ^2 *values from the best solution (marked by the star) one minimum can be seen for the three earliest delay times whereas for the latest delay time (1250 ns) the local minimum corresponding to the symmetric solution is visible. Exemplary the symmetry axis in the exchange of the temperatures of the zones and the one-zone solution are marked by the dashed line and the red circle, respectively, for the delay time of 1250 ns.*

best solution but with the inner and outer zone interchanged. Furthermore, the one-zone solution can be seen. However, for the spectrum at 500 ns delay time two additional local minima at high temperatures of either of the zones can be seen. These solutions corresponds to the description of the Na II lines from the highly excited states (~37 eV) (See Figure 4.4.2c). The χ^2 values of the best, symmetric, and one-zone solution are summarized in Table 4.3. From the table it can be seen that the symmetric solution at 1500 ns has a χ^2 that is only two values higher than the best solution. At 1250 ns the difference is 26. For all the delay times, the one-zone solution has a χ^2 that is at least 40 values higher than that of the best solution.

In Figure 4.4.10 the relative peak residuals for the best solutions are shown. For the spectra at the three largest delay times, it can be seen that the RMSEs of the peak residuals are between 23 % and 25 %. For the

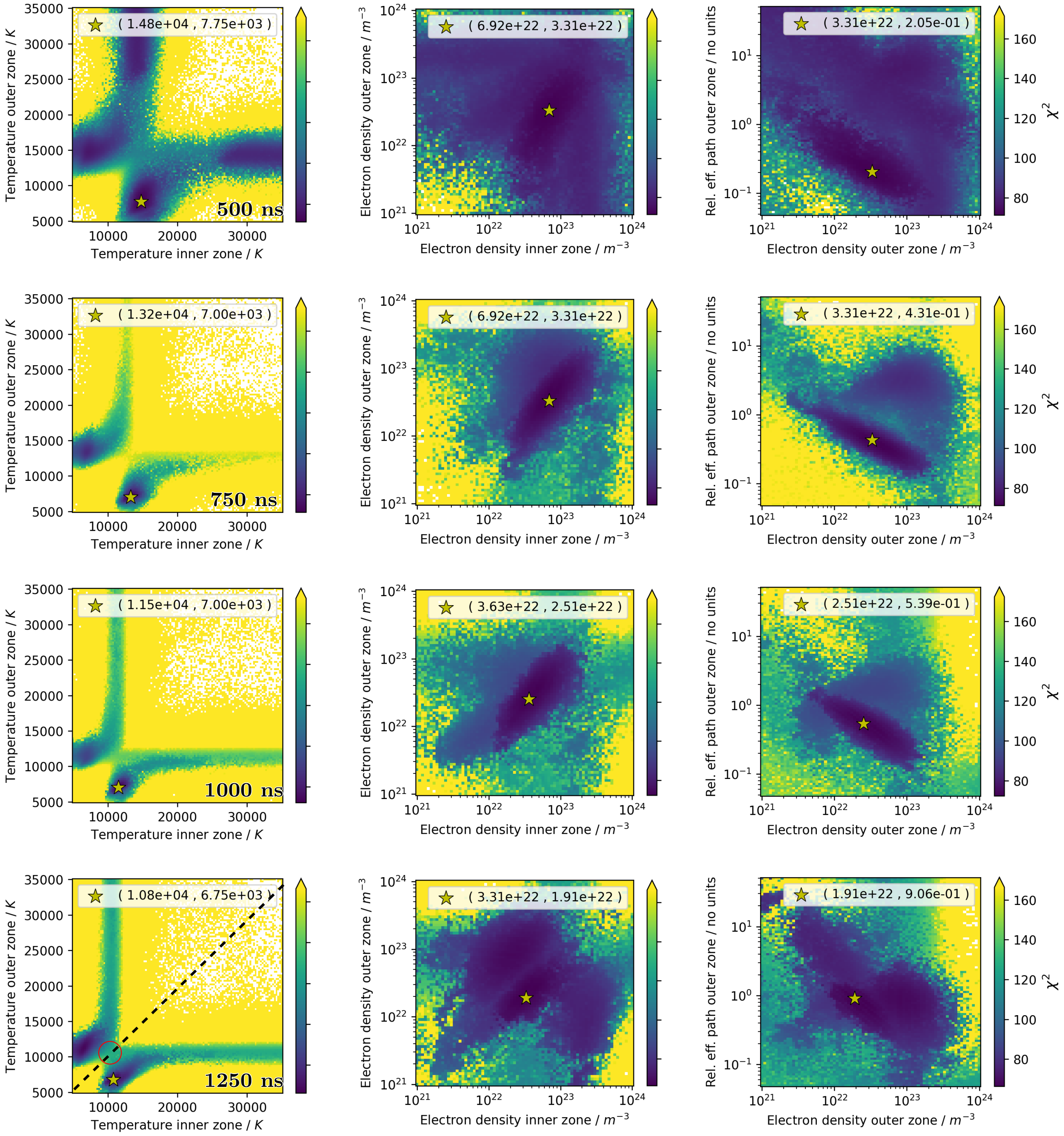

Figure 4.4.9: *Same as Figure 4.4.8, but for a* χ^2 *span of 100 values. For all the delay times, the local minimum corresponding to the symmetric solution (exchanging the order of the zones) can be seen as well as the one-zone solution at* $(T_{inner}) = T_{outer})$*. Besides these solution an extra set of symmetric local minima can be seen for the spectrum at* 500 ns *delay. These are located at temperatures around* 30 000 K *for either of the zones and are for the description of the Na II emission lines involving the highly excited states of* ~37 eV *(see Figure 4.4.2c.)*

Two-zone fit to spectrum at:	500 ns delay	750 ns delay	1000 ns delay	1250 ns delay
χ^2 **(best):**	71	71	72	66
χ^2 **(symmetric):**	77	83	92	68
χ^2 **(one-zone):**	~ 110	~ 175	~ 160	~ 130

Table 4.3: *χ^2 values for the best, symmetric, and one-zone solutions. The difference in χ^2 between the best and the symmetric solution varies between 2 at 1500 ns and 26 for the spectrum at 1250 ns. The χ^2 of the one-zone solution is around 40 values or higher for any of the delay times.*

delay of 500 ns, the RMSE is 38 %. This is due to the lack of the description of the highly excited Na II lines (left most bin of Figure 4.4.10a). Ignoring these peaks, the RMSE at 500 ns would be similar to those at the larger delay times. In Figure 4.4.11 the derived relative elemental concentrations of the four major elements in the plasma are compared to the reference values. For all the four spectra the relative deviations are similar and within 25 % for all the four considered elements

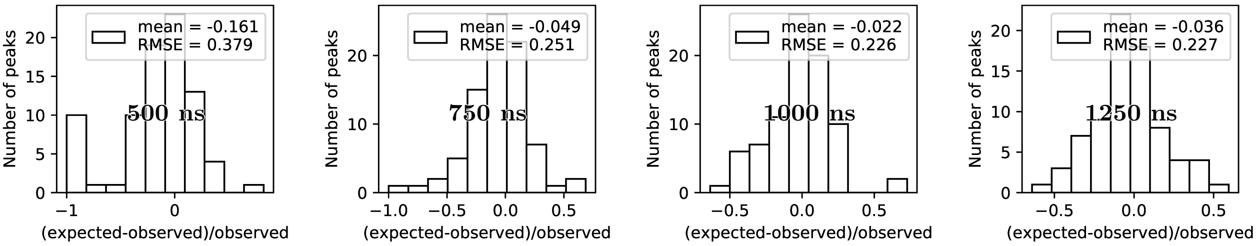

Figure 4.4.10: *Relative peak residuals for the best solution. For the three latest delay times the RMSEs are around 25 % and below. For the earliest delay time, the RMSE is 38 %. This higher value is due to the Na II lines not described in the best solution indicated by the left most bin in the histogram corresponding to peaks with zero predicted intensity.*

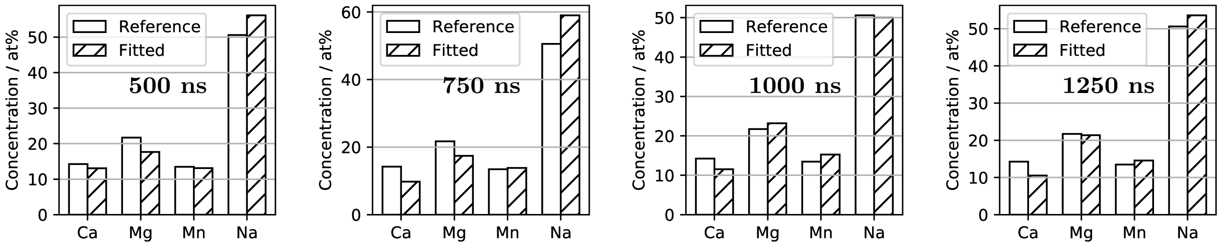

Figure 4.4.11: *Derived relative elemental concentrations of the four major elements in the plasma compared to the reference values. For all the four spectra the relative deviations are similar in size and within 25 % for all the considered elements.*

The reconstructed spectra, using the best fitted parameters, are shown in Figure 4.4.12, 4.4.13, 4.4.14, and 4.4.15 for the delay times of 500 ns, 750 ns, 1000 ns, and 1250 ns, respectively. For the spectrum at 500 ns delay time, it can be seen that the highly excited Na II lines are not described in the best fit (Figure 4.4.12c). These lines are not visible in the measured spectra at the larger delay times. For all the delay times, the Mg I ground state transition at 285.2 nm is systematically underestimated. For example, the deviation between its predicted integrated intensity and its observed integrated intensity is −54 % at 1250 ns. Aside from these deviations, there is a visually good match between the reconstructed and the measured spectra.

In Figure 4.4.16, histograms of the reconstructed intensities are shown with and without the effect of absorption. It can be seen that the effect of absorption reduces the strongest intensities by a factor of ∼100 for all the delay times.

In Figure 4.4.17 the temporal evolution of the fitted plasma model parameters can be seen together with the electron density as derived from the H-α and the temperature derived via Saha-Boltzmann plots (Figure 4.4.4 and 4.4.6, respectively). The vertical bars indicate the $\pm 3\sigma$ confidence intervals. The fitted temperatures of both zones are seen to decrease with increasing time. The electron densities of both zones remain constant from 500 ns to 750 ns from where they decrease monotonically. The relative effective path of the outer zone increases monotonically with time. The temperature via Saha-Boltzmann plots has values between the temperatures of the zones but closer to that of the inner zone. The electron density obtained from the H-α coincides very well with that of the inner zone. From the fitted plasma properties of the zones (Figure 4.4.17) the decay time ($T/(dT/dt)$, $n_e/(dn_e/dt)$) and the characteristic variation length ($T/(dT/dx)$, $n_e/(dn_e/dx)$) of the temperature and electron density have been calculated. The decay time was calculated by the best fitted plasma properties at the earliest and latest delay times. The characteristic length was calculated by averaging the properties of the inner and outer zone over the four different delay times assuming a total length of the plasma of 4 mm which is typical for the plasma in Martian atmospheric conditions [58]. The values are summarized in Table 4.4. For the possible existence of LTE, the decay time should be larger than the relaxation time for the excitation of the first excited states (eq. (2.2.5) Section 2.2) and the characteristic length should be larger than the particle diffusion length during the relaxation time (eq. (2.2.7) Section 2.2). Furthermore, the electron density should be higher than that of the McWhirter criterion (eq. (2.2.3) Section 2.2). The relaxation time, the diffusion length during the relaxation time, and the McWhirter criterion have been calculated for the elements used for the fit (Ca, Mg, Mn, and Na) and additionally for O. The values are summarized in Table 4.5. By comparing the values in the two tables it can be seen that the criteria for the assumption of LTE are not violated for Ca I-II, Mg I-II, Mn I-II, and Na I, whereas all the criteria in both inner and outer zone are violated for Na II and O I-II.

	Decay time inner zone / ns	Decay time outer zone / ns	Variation length / mm
Temperature	2400	5300	14
Electron density	1100	1500	13

Table 4.4: *Decay time and variation length calculated from the fitted plasma properties shown in Figure 4.4.17.*

	Inner zone			Outer zone		
	McWhirter criterion / m^{-3}	relaxation time / ns	Diffusion during relaxation time / mm	McWhirter criterion / m^{-3}	relaxation time / ns	Diffusion during relaxation time / mm
Ca I	4.5e21	0.5	0.09	3.4e21	5.9	0.3
Ca II	5.6e21	0.5	-	4.2e21	7	-
Mg I	1.5e22	2.8	0.68	1.1e22	85	2
Mg II	1.6e22	3	-	1.2e22	89	-
Na I	1.7e21	0.4	0.1	1.3e21	3.0	0.3
Na II	6.6e24	2.5e13	-	5.0e24	5.7e23	-
O I	1.6e23	26000	33	1.2e23	2.9e7	30
O II	5.9e23	6.4e5	-	4.4e22	3.2e10	-

Table 4.5: *McWhirter criterion, relaxation time and the diffusion during relaxation time calculated using the averaged fitted plasma properties of Figure 4.4.17 and the approximate formulas in [101] assuming a fully ionized plasma. The values can be compared to the fitted electron density, the plasma decay time and the characteristic length variation (Table 4.4) in order to assess the validation of the assumption of LTE. Missing numbers (”-”) are due to no available approximate formulas in [101].*

Finally, the reconstructed spectrum for the symmetric solution at the delay time of 750 ns can be seen in Figure 4.4.18. From the figure it can be seen that the Mg I resonance transition at 285 nm is favoured in the symmetric solution on behalf of other strong emission lines such as the Mg II lines around 278 nm and the Ca II doublet around 317 nm. For the symmetric solution, the relative deviations of the fitted relative concentrations and the reference values are 50 % for Mn and within 20 % for Ca, Mg, and Na.

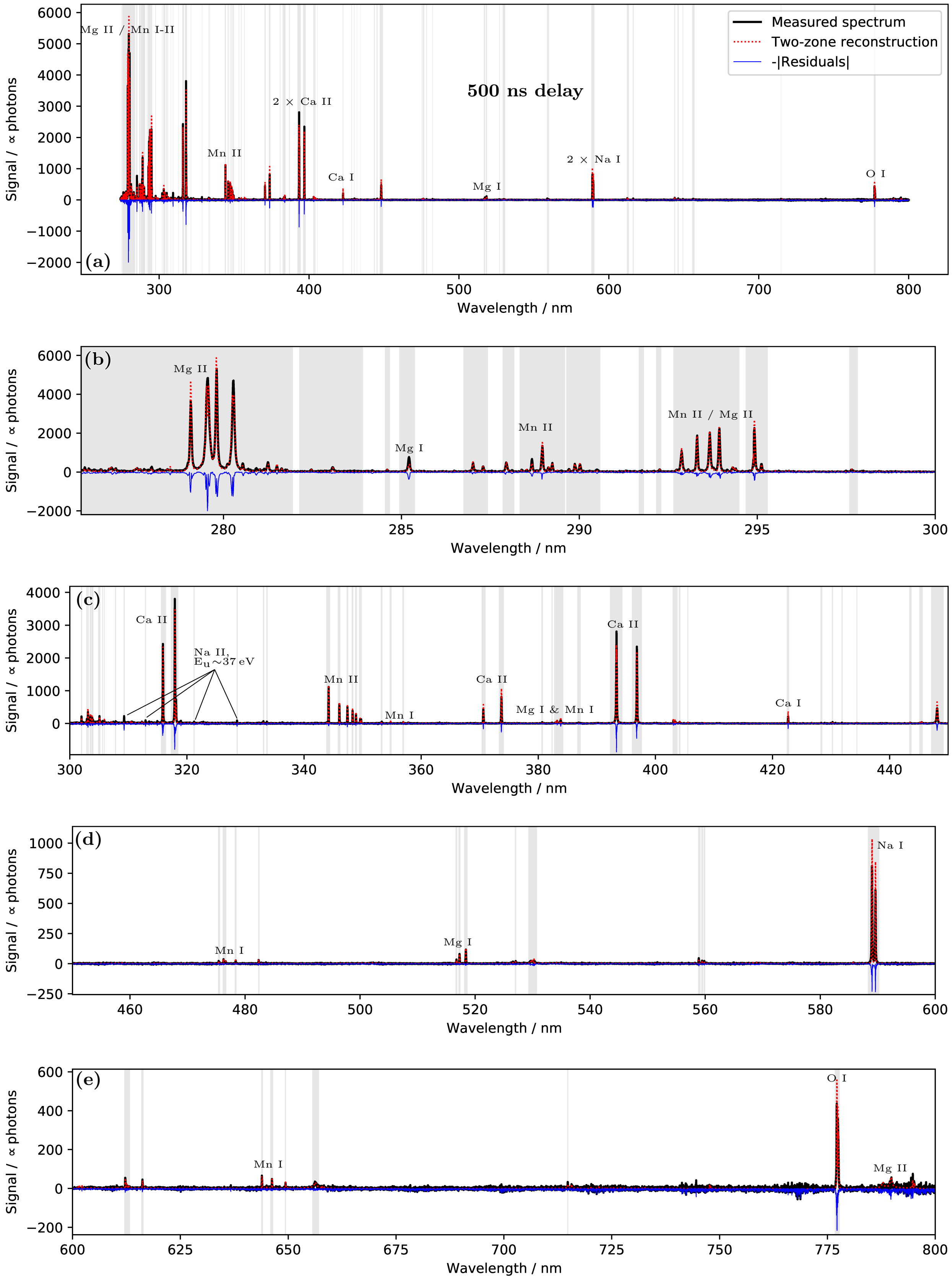

Figure 4.4.12: *Reconstructed spectrum (red dashed curve) calculated from the best fit of the two-zone model applied to the spectrum at* 500 ns *delay (black curve). Spectral ranges included in the fit are marked by the vertical grey shades. The negation of the absolute residuals are also shown (blue curve). Generally, these residuals are more prone to uncertainties in the Stark parameters and the wavelength calibration of the setup. They are therefore higher than the spectrally integrated peak intensities shown in Figure 4.4.10.* ***(a)*** *Full spectral range.* ***(b)-(e)*** *Close-ups of (a) in smaller wavelength ranges. Most emission lines are described well in the fit and within what expected from experimental and modelling uncertainties. However, there are some Na II lines involving highly excited states that are not described in the fit at all. A few of these lines are pointed out in (c).*

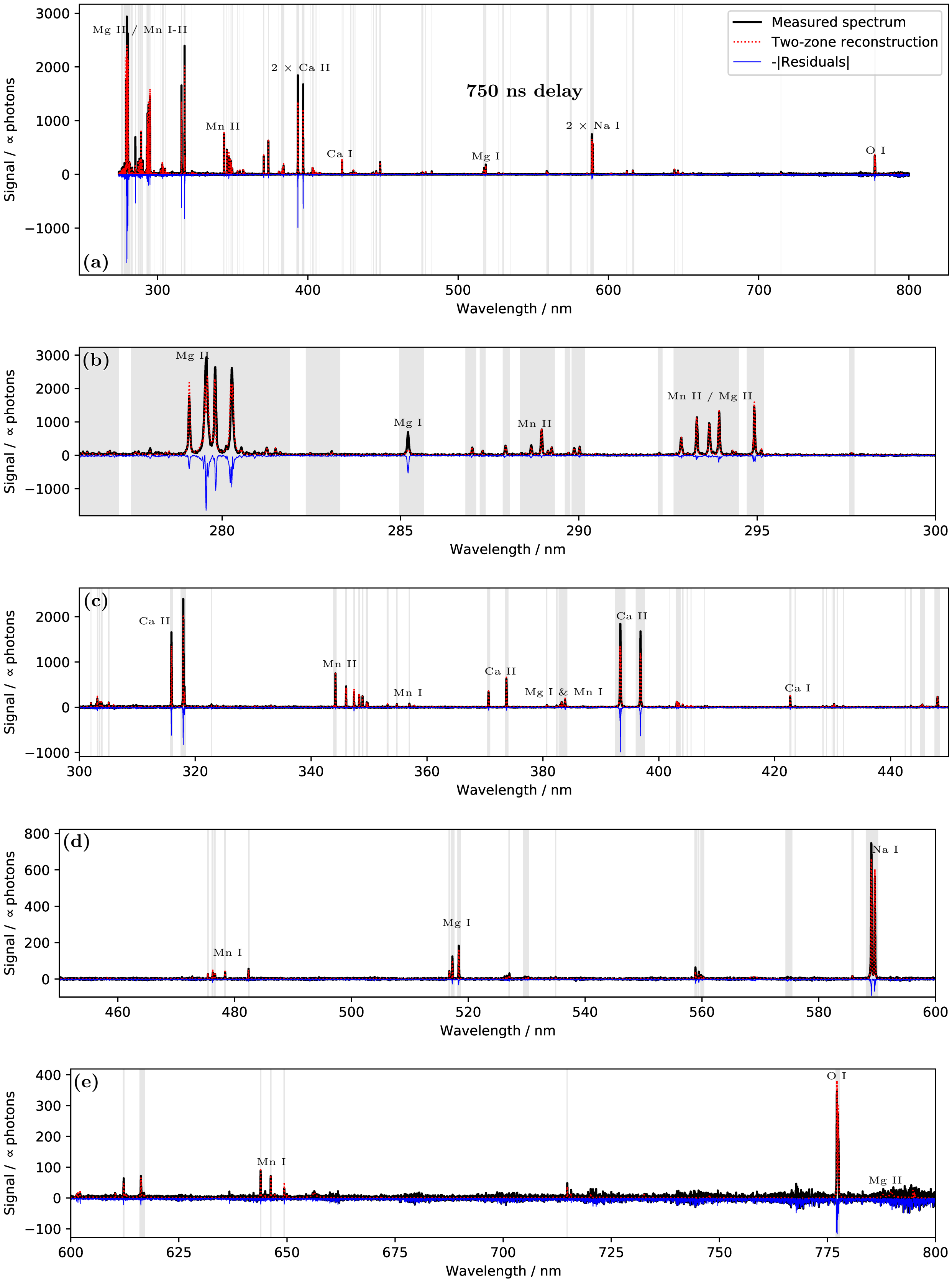

Figure 4.4.13: *Same as 4.4.12 but at a delay time of* 750 ns*. At this delay time the Na II lines, observable at* 500 ns *delay, are not visible in the spectrum. Aside from the Mg I line around* 285 nm *that is significantly underestimated, the two-zone reconstruction describes the data well.*

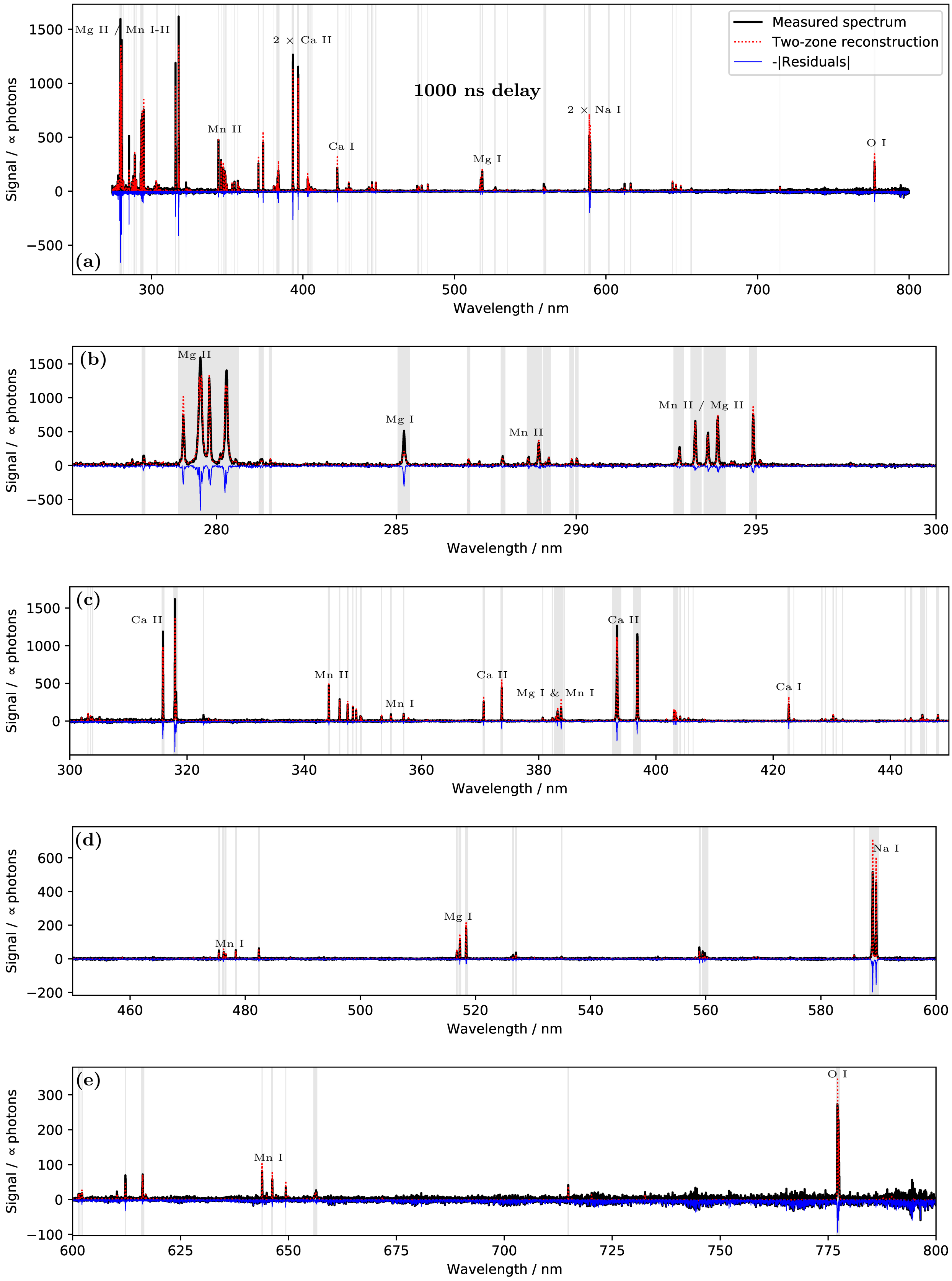

Figure 4.4.14: Same as 4.4.12 but at a delay time of 1000 ns. *Aside from the Mg I line around* 285 nm *that is significantly underestimated, the two-zone reconstruction describes the data well.*

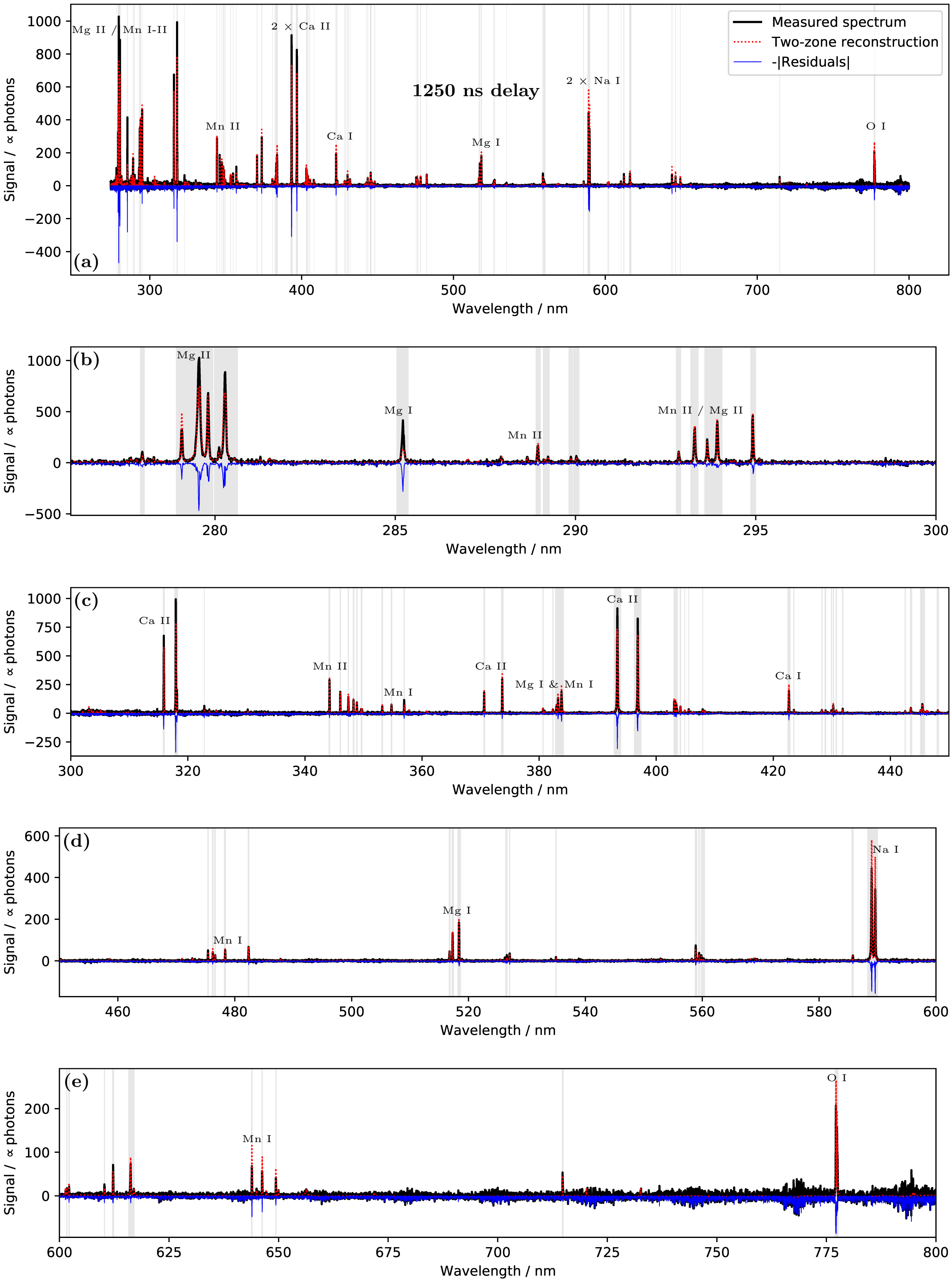

Figure 4.4.15: *Same as 4.4.12 but at a delay time of* 1250 ns. *Aside from the Mg I line around* 285 nm *that is significantly underestimated, the two-zone reconstruction describes the data well.*

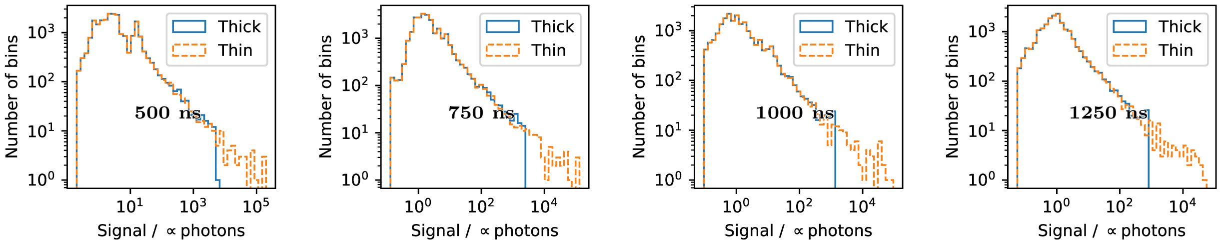

Figure 4.4.16: ***Top row:*** *Histograms of predicted pixel intensities as obtained from reconstruction of the spectra using the best fitted parameters with and without the effect of absorption. By comparing the distributions of the pixel intensities it can be seen that absorption is predicted to affect the pixel intensities strongly and around for the most extreme cases by a factor of 100.*

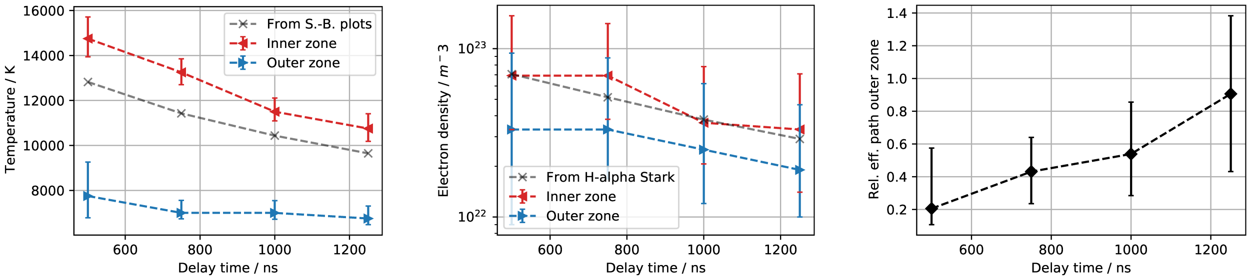

Figure 4.4.17: *Temporal evolution of the fitted plasma model parameters. The vertical bars indicate the* $\pm 3\sigma$ *confidence intervals. For comparison the electron density derived from the H-α emission lines (Figure 4.4.4) and the temperature derived from the Saha-Boltzmann plots (Figure 4.4.6 and "From S.-B. plots" in legend) are also shown. The fitted temperatures of both zones are seen to decrease with increasing time. The same is true for the electron density of the inner zone. The electron densities remain constant until 750 ns from where they decrease monotonically. The relative effective path of the outer zone increases monotonically with time.*

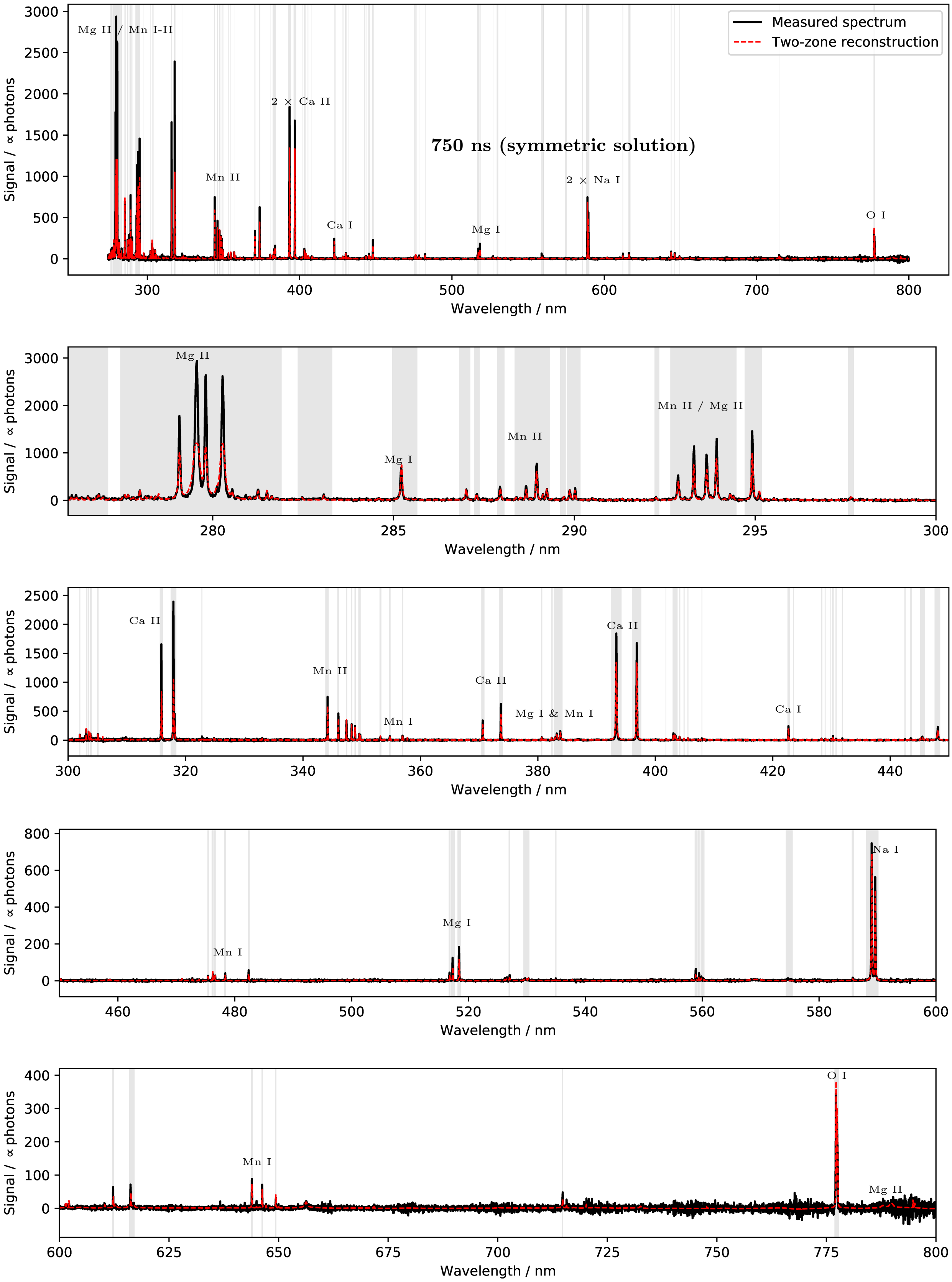

Figure 4.4.18: *Same as 4.4.13 but for the symmetric solution (see second row from the top of Figure 4.4.9).*

4.4.4 Discussion of Fit Results

As seen from the χ^2 plots for the different plasma model parameters (Figure 4.4.8 and 4.4.9), at least two local minima are observed for all times. The symmetric solution, i.e. the solution where the best fitted parameters of the zones are interchanged, is for all spectra a second local minimum and aside from the high temperature minima for the spectrum at 500 ns, the patterns are similar to what was obtained from the two-zone fits to the synthetic test spectra. However, compared to the the synthetic test spectra, the separation in χ^2 between the best and the symmetric solutions are much smaller. This was to be expected since the real data contain uncertainties not modelled in the synthetic test spectra. Furthermore, the χ^2 values for the real data are only approximate as uncertainties in the atomic constants have been averaged (model uncertainty of 10 % applied to all peaks). For example, the Mn emission lines generally have a higher uncertainty than those of Mg (see Figure 4.1.10). The χ^2 of the one-zone solution is a factor of ~ 2 higher than that of the best solution. This indicates that the peak residuals (Figure 4.4.10) in the one-zone approximation would be roughly twice as high. It is therefore evident that the two-zone description of the time-resolved data in Martian atmosphere is a great improvement over a one-zone approximation. The same conclusion can be reached from the relative concentration estimates from the two-zone fits (Figure 4.4.11) that have smaller deviations from the reference values than those obtained from the multi-element Saha-Boltzmann plots (Figure 4.4.7), which effectively corresponds to a one-zone plasma model.

The reconstructed spectra from the best solution (Figure 4.4.12,4.4.13,4.4.14, and 4.4.15) generally fit the measured spectra well and most discrepancies are within what expected due to spectral noise and uncertainties in the atomic parameters and calibration of the setup. However, there are two larger discrepancies. The first one in terms of the highly excited Na II emission lines around and above 300 nm that are observed in the spectrum at the smallest delay time and not described in the best solution/fit (see Figure 4.4.12c). In the thermodynamic description of the atomic states, a very high temperature is required to populate the upper levels involved in the transitions ($E_u = 37\,\mathrm{eV}$). This is indicated by the high temperature local minima in the χ^2 plot for the temperatures (top left of Figure 4.4.9). Such hotter zone would also cause other emission lines from the other elements to appear in the spectrum and the Na II emission lines are therefore likely better modelled by non-equilibrium effects rather than a third hotter zone. The nature of the non-equilibrium should not be attributed to the violation of the McWhirter criterion since no excited states of Na II are supposed to be populated at the temperatures corresponding to the best fitted values. For example, Ca III would also not satisfy any of the criteria of LTE (Table 4.5 and 4.4), but that is not a problem since no Ca III ions exist at the considered delay times. The observation of the Na II lines is therefore most likely due to a relatively long recombination rate of Na III. In the beginning of the plasma lifetime, Na III ions might exist due to the high temperatures. If the recombination rate of Na III in the plasma is around 500 ns or larger, the highly excited states of Na II could still appear after 500 ns due to recombination cascades. For comparison, the recombination time of Ti II was estimated in [102] to be between 1×10^{-7} s to 1×10^{-6} s, in a laser induced plasma in a low-pressure environment. However, the species out of equilibrium such as the Na II may have negligible abundance, and the LTE model can still provide an accurate description of all other species and results in good concentration estimates, even for sodium, which is the case for all the spectra. The second discrepancy is the underestimation of the intensity of the Mg I resonance line at 285 nm for especially the three later delay times (Figure 4.4.13, 4.4.14, and 4.4.15). According to Table 4.5 and 4.4 the criteria for LTE, obtained via the best fitted parameters, are far from being violated for Mg I or Mg II. The underestimation of the Mg I therefore cannot be ascribed to violations of LTE. One explanation could be that the two-zone model is insufficient for the simultaneous description of this line and the bulk of the observable emission lines. An indication of this is that the Mg I line is favoured in the symmetric solution with the inner and outer zones interchanged. This was only exemplified for the spectrum at 750 ns in Figure 4.4.18, but is also the case for the two later delay times. This could correspond to the real plasma having profiles such as the "Bogaerts" spectrum, i.e. an inner cold region, and outer cold region, and a hot region in between. This is supported by recently published results from spatially resolved temperature estimates of the plasma in experimentally simulated Martian atmospheric conditions [58]. However, the Mg I line is well described, as well as all other observable emission lines, in the two-zone approximation of the "Bogaerts" spectrum. To investigate the potential need of a three-zone model, further and more systematic applications to synthetic spectra would be useful. More specifically, by generating series of synthetic test spectra by gradually changing the behaviour of one of the plasma properties along the LOS and keeping the other fixed and see how, and how well, the spectra are approximated in the two-zone model and for which types of profiles, if any, a three-zone model is preferable. Another explanation of the underestimation of the Mg I line is simply uncertainties in the atomic constants or experimental uncertainties such as changes in the instrumental response or due to non-linear effects by obtaining the data from several induced plasmas at the same position/different "depths" (crater effects). As seen from Figure 4.4.1a,b, the Mg I line indeed has a larger shot-to-shot fluctuation compared to the Ca II lines around 318 nm (when regarding the first measurement, rep. 0, as a cleaning shot). Last but not least, it could be due to the approximations in the plasma model, i.e. the single LOS approximation or equal number density distributions of the elements in the plasma. However, from the consistency in the fitted relative concentrations with increasing delay time (Figure 4.4.11), the latter approximation seems to be less critical.

From the two-zone fits to the synthetic spectra with predominantly negative gradients in the temperature profile ("Gaussian","Shifted Gaussian", and "Bogaerts"), it was observed that the temperatures of the inner zone adapt to values between the median to the maximum temperature along the LOS. It wil also observed that the temperatures of the outer zone adapt to values close to temperature at the end of the LOS (see Figure 4.3.18). Therefore, this is likely also a good interpretation of the fitted temperatures of the inner and outer zones for the real data. This interpretation can be further supported by comparing the best fitted electron density value of the inner zone with the electron density as derived from the Stark broadening of the Hydrogen-α line at 656 nm whose values are in good agreement with each other (see Figure 4.4.17). Due to the high ionization potential of Hydrogen (13.6 eV) and the relatively high energy involved in the hydrogen transition (12.1 eV), the hydrogen emission will be dominated by the higher temperatures in the plasma. Given the high correlation between the fitted electron density and temperature of the inner zone (see Appendix C), the agreement of the fitted electron density and the value from the hydrogen line not only validates the fitted electron density, but also the interpretation of the temperature of the inner zone as obtained from the applications to the synthetic spectra.

In the study of Hermann et al. [6], it was found that the LIBS plasma induced in an argon atmosphere at a pressure of 50 kPa, at certain experimental conditions, produces an almost homogeneous plasma core containing target material and with all the temperature gradients in the ambient argon gas. It was argued to be due to the isolating properties of argon (mostly elastic collisions with elements from target materials due to large spacing between ground and first excited state of Ar I). The thinner Martian atmosphere at 0.7 kPa pressure of mainly CO_2 is likely to be less isolating, and indeed gradients in the plasma properties are evidenced by the differences of the fitted parameters of the inner and outer zone (Figure 4.4.17). The fitted electron density values of this study are furthermore relatively low compared to estimates from measurements in thicker atmospheres. Hermann et. al [103] found that the electron density in the laser plasma of an aluminium target in Earth's atmosphere at a delay time of ∼1000 ns is about $5 \times 10^{23}\,\mathrm{m}^{-3}$ whereas the electron density at 1000 ns was estimated to be $3.31 \times 10^{22}\,\mathrm{m}^{-3}$ in this study. The measurements in Earth's atmosphere of Hermann et al. were done with an UV laser with a 4 ns pulse length and 6 mJ pulse energy. The pulse energy used for the measurements in this study was 35 mJ, but still the electron density is approximately an order of magnitude lower. This is in agreement with the larger and faster expansion of the plasma at reduced pressures. Due to the larger expansion, the density is smaller which decreases the effect of self-absorption, however self-absorption is still predicted to affect the intensities strongly as seen from the histograms of the pixel intensities with and without the effect of absorption (Figure 4.4.16). Even though the plasma in Martian atmospheric conditions is decaying faster and less dense than plasmas induced in higher pressures, the plasma properties were found to be consistent with the approximation of the assumption of LTE for all the considered species except of Na II. When including non-metallic species, such as oxygen or carbon, the criteria for LTE would not be fulfilled (Table 4.5 and 4.4). In general LTE is favoured when the electron density is higher, and it might be that a higher laser energy could result in a sufficient increase. Another approach would be to go to even earlier delay times where the plasma would be denser, but as other non-equilibrium effects were discovered at the delay time of 500 ns in terms of the Na II emission lines, this is probably not favourable. As the considered criteria for LTE refers to the set of levels that are the most difficult to retain in or establish to equilibrium, i.e. usually the ground state and the first stable excited state, higher excited states of such non-metals will probably be in equilibrium (due to the decreasing spacing between higher excited levels). The plasma properties for describing the metals might therefore also provide a good description of the emissions of non-metals which could be included in the spectral modelling. The non-equilibrium effects would then be expressed by errors in the concentration estimates, due to the non-equilibrium of the ground state, but the emission might still be well modelled.

As shown via applications to synthetic spectra, the derived elemental concentrations and the effect of self-absorption, from the two-zone model fits, are in good agreement with the reference values (Figure 4.3.11 and 4.3.16). In other words, the discrete two-zone model contains the physical characteristics of the plasma well and better than the properties derived via Saha-Boltzmann plots. This was exemplified by the lower deviations in the concentration estimates using the two-zone model when compared to the estimates obtained from the Multi-element Saha-Boltzmann plots (Figure 4.4.11 versus Figure 4.4.7). Overall it can therefore be said that the two-zone model provides a good framework for analysing and obtaining insights into time-resolved LIBS data in Martian atmospheric conditions.

Chapter 5

Spectral Unmixing

In this chapter, a method for the qualitative calibration-free analysis of LIBS data is presented and tested. The method allows for automated line identification and can also be used to give rough estimates on the composition of the sample and the plasma properties. It is meant as an alternative to the fit method described in Chapter 4. It is less computationally heavy and it can therefore be applied to samples of complex compositions and also to time-integrated measurements without an increased computation times. The method is therefore more suitable to real mission LIBS data that, at the current state, are time-integrated and of geological targets.

5.1 Basic Principles

The presented method is a type of spectral unmixing. The goal of the unmixing is to resolve an input spectrum into individual spectra of pure components. In the unmixing it is assumed that an input spectrum can be written as

$$I_{input} = P_{Al} \cdot s_{Al} + P_{Ba} \cdot s_{Ba} + \ldots + P_{Fe} \cdot s_{Fe} \ , \tag{5.1.1}$$

where I_{input} is the input spectrum to be analysed/unmixed, P_{Al} is the pure spectrum of aluminium, and s_{Al} is its coefficient, i.e. a measure of how much of the input spectrum that can be attributed to emissions from aluminium. This will be referred to as the score. The spectra of the pure elements on the right side of the equation are fixed and do not depend on any parameters. They can therefore be said to be template spectra and they can be obtained from either measurements or simulations. The collection of template spectra forms the database for the unmixing. When given an input spectrum, the only unknowns are therefore the scores. As the unmixing equation is linear in the scores, they can be solved analytically, i.e. fast, by linear least squares. However, the unmixing as described by equation 5.1.1 is too simple for the application to LIBS data. First of all, the spectra of the elements will look different when measured in different sample matrices due to matrix effects. Secondly, the template spectra depend non-linearly on the elemental concentrations because of self-absorption. It therefore follows that a single fixed template spectra for each element can not be used on the right side of equation (5.1.1). One option is to use non-fixed template spectra, i.e. make the template spectra depend on some parameters. This would correspond more or less to the fit approach of Chapter 4. Another option, which is chosen here, is to expand the right-hand-side of equation (5.1.1) with template spectra corresponding to different sample matrices and elemental concentrations such that

$$\begin{aligned} I_{input} =& P_{Al,m_1,c_{low}} \cdot s_{Al,m_1,c_{low}} + P_{Al,m_1,c_{mid}} \cdot s_{Al,m_1,c_{mid}} + P_{Al,m_1,c_{high}} \cdot s_{Al,m_1,c_{high}} \\ &+ P_{Al,m_2,c_{low}} \cdot s_{Al,m_2,c_{low}} + P_{Al,m_2,c_{mid}} \cdot s_{Al,m_2,c_{mid}} + P_{Al,m_2,c_{high}} \cdot s_{Al,m_2,c_{high}} \\ &+ P_{Ba,m_1,c_{low}} \cdot s_{Ba,m_1,c_{low}} + P_{Ba,m_1,c_{mid}} \cdot s_{Ba,m_1,c_{mid}} + P_{Ba,m_1,c_{high}} \cdot s_{Ba,m_1,c_{high}} \\ &+ P_{Ba,m_2,c_{low}} \cdot s_{Ba,m_2,c_{low}} + P_{Ba,m_2,c_{mid}} \cdot s_{Ba,m_2,c_{mid}} + P_{Ba,m_2,c_{high}} \cdot s_{Ba,m_2,c_{high}} \\ &+ \ldots \ , \end{aligned} \tag{5.1.2}$$

where $P_{Al,m_1,c_{low}}$ is the pure spectrum of aluminium as measured in sample matrix number 1 (m_1) with a low concentration of aluminium (c_{low}). By doing so, the linearity of the unmixing is kept and it can still be quickly solved by linear least squares. The expansion of the template spectra can be said to provide many choices of template spectra. When solving the unmixing it is assumed that the correct choice is automatically obtained. For example, if an input spectrum was measured in a matrix similar to that of sample matrix 1 (m_1) the scores of the pure spectra corresponding to that matrix, e.g. $s_{Al,m_1,c_{low}}$ and $s_{Ba,m_1,c_{low}}$, would be solved with higher values than the scores corresponding to template spectra for the description of other sample matrices, e.g. $P_{Al,m_2,c_{low}}$ and $P_{Ba,m_2,c_{low}}$. The expansion of the template spectra increases the size of the unmixing database considerably. Building the database with solely measured LIBS data therefore seems unrealistic. Inspired by the good results from fits to time resolved spectra with the stationary LTE plasma model (Chapter 4), the database will mainly be built from synthetic spectra simulated as described in Chapter 4. For describing the spectra in different sample matrices, the spectra are simulated from various combinations of the plasma properties such that the sample matrix corresponding to a good coupling between the target surface and the laser can be described by the template spectrum simulated with a high temperature or density. That is, $P_{Al,m_1,c_{low}}$ in equation (5.1.2) is replaced by $P_{Al,T_1,n_{e,1},c_{low}}$. The same goes for other effects such as varying laser energies or chemical matrix effects. As time-integrated spectra can be described as a series of stationary spectra (see Chapter 2), usually with decreasing temperatures and densities, the variety of different temperatures and densities for describing different sample matrices simultaneously allows for the analysis of time-integrated data.

In summary, the spectral unmixing can be described by the matrix equation

$$\begin{pmatrix} I_1 \\ I_2 \\ I_3 \\ \vdots \\ I_n \end{pmatrix} = \begin{pmatrix} Al_1^{(1)} & Al_1^{(2)} & Al_1^{(3)} & \cdots & Ba_1^{(1)} & Ba_1^{(2)} & Ba_1^{(3)} & \cdots \\ Al_2^{(1)} & Al_2^{(2)} & Al_2^{(3)} & \cdots & Ba_2^{(1)} & Ba_2^{(2)} & Ba_2^{(3)} & \cdots \\ Al_3^{(1)} & Al_3^{(2)} & Al_3^{(3)} & \cdots & Ba_3^{(1)} & Ba_3^{(2)} & Ba_3^{(3)} & \cdots \\ Al_4^{(1)} & Al_4^{(2)} & Al_4^{(3)} & \cdots & Ba_4^{(1)} & Ba_4^{(2)} & Ba_4^{(3)} & \cdots \\ Al_5^{(1)} & Al_5^{(2)} & Al_5^{(3)} & \cdots & Ba_5^{(1)} & Ba_5^{(2)} & Ba_5^{(3)} & \cdots \\ \vdots & \vdots & \vdots & \ddots & \vdots & \vdots & \vdots & \ddots \\ Al_n^{(1)} & Al_n^{(2)} & Al_n^{(3)} & \cdots & Ba_n^{(1)} & Ba_n^{(2)} & Ba_n^{(3)} & \cdots \end{pmatrix} \begin{pmatrix} s_1 \\ s_2 \\ s_3 \\ \vdots \\ s_m \end{pmatrix} \tag{5.1.3}$$

where the vector on the left side of the equation contains the signals of the n pixels in the input spectrum. The matrix on the right side of the equation contains the template spectra and constitute the spectral unmixing database. It is an $n \times m$ matrix where each column contains a template spectrum resulting in m different template spectra. The vector on the right side of the equation contains the score of each of the m template spectra.

The unmixing is applied to the individual pixel intensities and not the integrated signal from series of pixels constituting peaks as in the fit routine. The unmixing thereby exploits more of the information in the spectra including pixels without any observable emission lines as well as the shapes of the emission lines. This is necessary due to the many template spectra and thereby the many unknowns, i.e. scores, to be solved. In order to make the results more robust to uncertainties in the wavelength calibration (Figure 3.3.9 in Chapter 3) and uncertain Stark parameters (Figure 4.1.9 in Chapter 4), both the input spectrum and the template spectra are smoothed by a Gaussian with a FWHM of 0.12 nm. For the template spectra in the unmixing database, this broadening comes on top of the instrumental broadening (Figure 3.3.5 Chapter 3). The value of 0.12 nm is small enough to preserve many of the finer spectral features of the input spectra and can at the same time compensate for some of the uncertainties in the wavelength calibration and Stark parameters. Finally, the unmixing is implemented in python and the unmixing (equation 5.1.3) will be solved using non-negative least squares (nnls). The non-negative constraint is imposed to avoid negative and thereby non-physical intensities.

5.2 Unmixing Database

The unmixing database contains spectra of pure elements simulated from the plasma model described in Chapter 4. As only the emissions from the atomic transitions are modelled, the continuum emission is described by linear parametric functions added as rows in the matrix of equation (5.1.3). Furthermore, template spectra for some of the most relevant molecules are added via features extracted from measured LIBS data. The unmixing database thereby consists of three distinct parts; spectra of simulated atomic emissions, parametric functions for describing the continuum emission, and molecular emissions extracted from laboratory LIBS data. Each of the parts are explained in detail in the following.

5.2.1 Atomic Emissions

The atomic emissions are simulated from a one-zone plasma model for various sets of plasma properties. As argued in Chapter 4, the LIBS plasma in Martian atmospheric conditions is not homogeneous and therefore better described by a two-zone model. For now, this seemingly contradiction will be ignored and addressed later after applying the unmixing. The span of the plasma properties, for calculating the various element templates, should be large enough to contain template spectra for the description of the early and the later stages of the plasma lifetime. A rough estimate of the plasma properties of the very early plasma can be obtained by considering the amount of ablated material and the amount of energy delivered by the laser pulse. This is now done exemplary for the case of an iron target. As the initial plasma must approximately coincide with the crater from the laser ablation, the initial plasma volume and number of atoms can be estimated from the density of the iron target and the weight of the ablated material. Assuming the typical value of ablated mass of 100 ng and a target density of 8000 kg/m^3, the ablated volume/crater size and the number of ablated iron atoms would be $8.56 \times 10^{28}\,\mathrm{m}^{-3}$ and $1.25 \times 10^{-14}\,\mathrm{m}^3$, respectively. As the plasma is formed on the scale of picoseconds and usually with lasers of nanosecond pulse lengths, the maximum plasma temperature will be reached near the end of the laser pulse, i.e. after some nanoseconds of expansion. The expansion velocity of a plasma induced from an iron target, in Martian atmospheric conditions, was measured in our research group by a colleague. The measurements are well described by the exponentially decaying function

$$v_{exp} = 4.39 \cdot 10^4 \cdot \exp(-2.32 \cdot 10^7 (t + 10^{-8})) \ , \tag{5.2.1}$$

where v_{exp} is the expansion velocity in m/s, and t the time in seconds after firing of the laser. Assuming that the plasma expands from the target surface as a half-sphere, the plasma volume and density at later times can be deduced using equation (5.2.1). As an approximation to the gradually deposition of the laser energy, it is assumed that all the energy is supplied instantaneously to the plasma after 3 ns of expansion. According to equation (5.2.1), the density and the volume after 3 ns of expansion are $3.03 \times 10^{26}\,\mathrm{m}^{-3}$ and $3.53 \times 10^{-12}\,\mathrm{m}^3$, respectively. Assuming a homogeneous plasma in thermodynamic equilibrium, the temperature and the supplied energy to the plasma can be linked by calculating the energies partitioned into photons, electronic excitations, ionizations and kinetic energies of free particles (electrons and atoms) for different temperatures, as

$$E_{rad} = \frac{8\pi^5 k_b^4}{15(hc)^3} V T^4 \tag{5.2.2}$$

$$E_{exc} = V \sum_z \sum_i E_i \cdot m_{Fe,z,i} \tag{5.2.3}$$

$$E_{ion} = V \sum_z \chi_{Fe,z} \cdot n_{Fe,z} \tag{5.2.4}$$

$$E_{kin} = V(n_{Fe} + n_e) \cdot k_b T, \tag{5.2.5}$$

where the population density of ionized and electronic states ($m_{Fe,z,i}$ and $n_{Fe,z}$, respectively) are evaluated using the standard equilibrium distributions as described in Chapter 2. Exemplary, the calculated population of ionized states and the electron density are shown in Figure 5.2.1 and the total partitioning of energy in the plasma as a function of temperature is shown in Figure 5.2.2. Both figures for densities corresponding to the iron plasma after 3 ns of expansion. Assuming that all the laser energy is supplied to the plasma, thereby neglecting the energy in the process of target melting, vaporizing and reflections of the laser beam by the plasma or target, Figure 5.2.2 gives a rough overview of the expected maximum plasma temperature for different laser energies. For example, it can be inferred that a laser energy of 26 mJ, instantaneously deposited after 3 ns of expansion, would result in a maximum temperature of 113 000 K. A temperature of ∼100 000 K could then be used as an upper limit for the range of temperatures used for the template spectra. The pulse energy of the laser of the ChemCam and SuperCam instrument is 35 mJ, but at the target surface it reduces to ∼14 mJ due to absorptions and reflections in the optical system [15]. The upper limit of ∼100 000 K would therefore also apply to data from the ChemCam and Supercam instruments.

However, 100 000 K is much higher than the value obtained by extrapolating the fitted temperature of the inner zone as obtained from the spectra oof the carbonate sample (Figure 4.4.17 Chapter 4). This indicates that the plasma temperature is decreasing much more rapidly in the beginning than at later times. This is in agreement with the general understanding of the evolution of the plasma [44]. Due to a fast decay at the beginning, the emissions from the initial high temperature plasma might therefore be negligible compared to the emission after some tens of nanoseconds. Element templates corresponding to these very high temperatures could therefore be neglected and the size of the unmixing database decreased. To verify this, hydrodynamic simulations of the plasma expansion would be preferable. However, a much simpler approach based on an adiabatic expansion [28, 44, 104] of the plasma is chosen here. During the adiabatic expansion, the plasma is assumed homogeneous and heat conduction, radiation losses and particles entering/leaving the plasma are assumed negligible. Finally, the plasma radius is assumed to follow from the expansion velocity as given by equation (5.2.1). The resulting energy loss can then be calculated by the second law of thermodynamics and translated into a temperature decrease by the heat capacity of the plasma. This is done for the iron plasma discussed above with the initial conditions corresponding to 3 ns of expansion and a laser energy of 26 mJ. The resulting temperature and density profiles from such adiabatic expansion are shown in Figure 5.2.3a,b,c. From Figure 5.2.3a it can be seen that the temperature indeed decreases very fast during the first tens of nanoseconds. Starting at 116 000 K at 3 ns it can be seen to drop to 40 000 K at 16 ns. The resulting simulated spectrum from 3 ns to 16 ns and the spectrum from 16 ns to 130 ns are shown together in Figure 5.2.4. From the figure it can be seen that the early spectrum mainly consists of very broad features due to the high electron density. Furthermore, many emission lines are suppressed due to a strong continuum lowering according to equation (2.2.14) in Chapter 2. In Figure 5.2.5 and Figure 5.2.6 similar plots but for the division in temperatures and electron density can be seen. From the figures it can be inferred that temperatures higher than 40 000 K and electron densities higher than $5 \times 10^{24}\,\mathrm{m}^{-3}$ mostly contribute with broad emission features. These broad features are of less spectroscopic interest compared to the features at lower temperatures and densities. Furthermore, they are so broad that they would be difficult to distinguish from the continuum emissions that are also expected at the early stage of the plasma. Consequently, element templates for the description of these very high temperature/density emissions will not be included in the unmixing database. Instead the unmixing database will be build from plasmas/spectra with maximum temperatures of 50 000 K, thereby adding a small buffer for higher laser energies or targets with different heat capacities, and maximum densities of $5 \times 10^{24}\,\mathrm{m}^{-3}$. The initial high temperature/density emissions will be modelled by the parametric functions also used for modelling/describing the continuum emissions. The initial atomic emissions are thereby defined as part of the background spectrum.

At the end of the plasma lifetime, the plasma has equilibrated with the ambient gas. The minimum temperature used for the element templates would therefore be equal to that of the ambient gas. At such low temperatures, however, excited states involved in transitions for emissions in the UV-VIS-NIR range will be negligible. Consequently no template spectra are needed for the latest stage of the plasma. To quantify this, the ground state transition of Na I doublet at ∼589 nm is considered. This is one of the most persistent lines in LIBS in the VIS-NIR range. The reason for this is its relatively low upper electronic level of 2.1 eV. According to the Boltzmann distribution, the population of this level at 4000 K is almost eight times higher than at

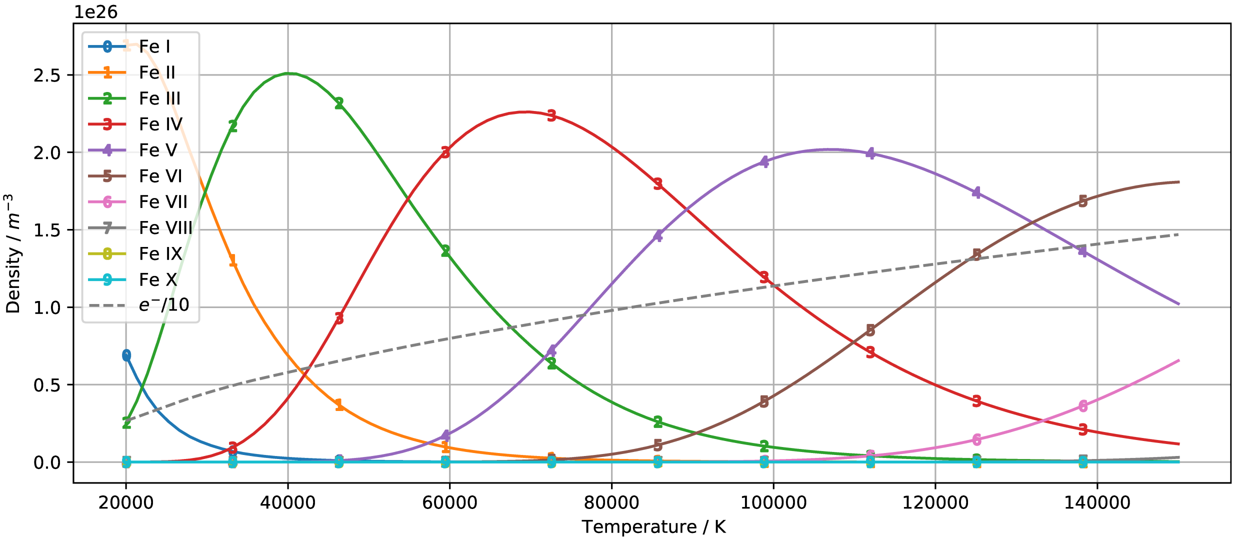

Figure 5.2.1: *Population of ionized states for an homogeneous Iron plasma with a density of* $3.03 \times 10^{26}\,\mathrm{m}^{-3}$*. The populations were evaluated using the Saha-equation and conservation of charge (see Chapter 2 equation* (2.2.16)*).*

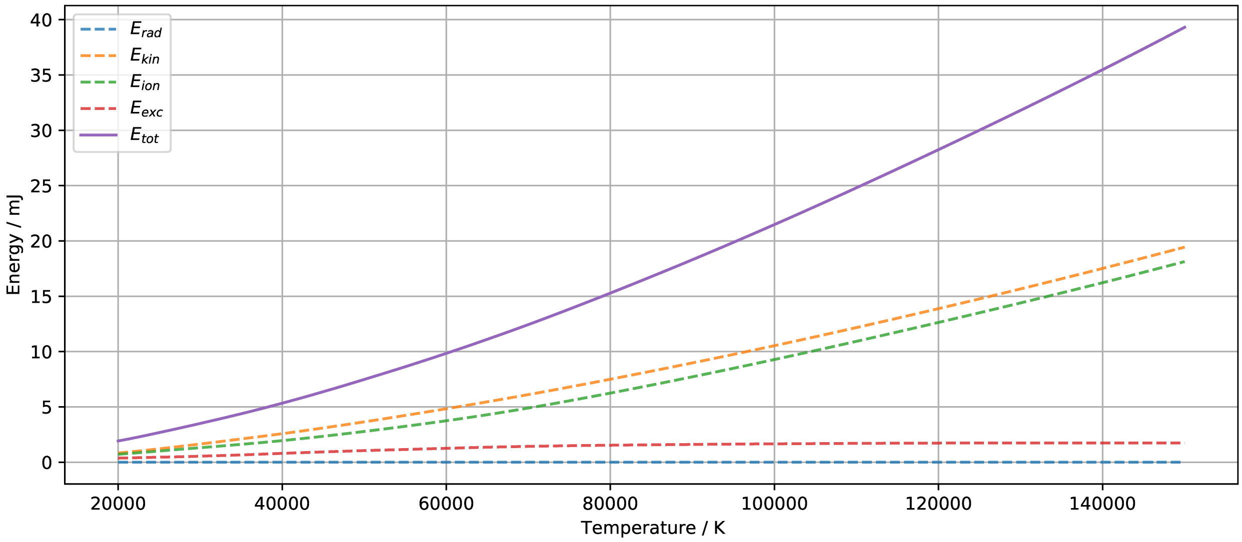

Figure 5.2.2: *Energy of the iron plasma for different temperatures after* 3 ns *of expansion. Most of the energy is partitioned into ionization and kinetic energy.*

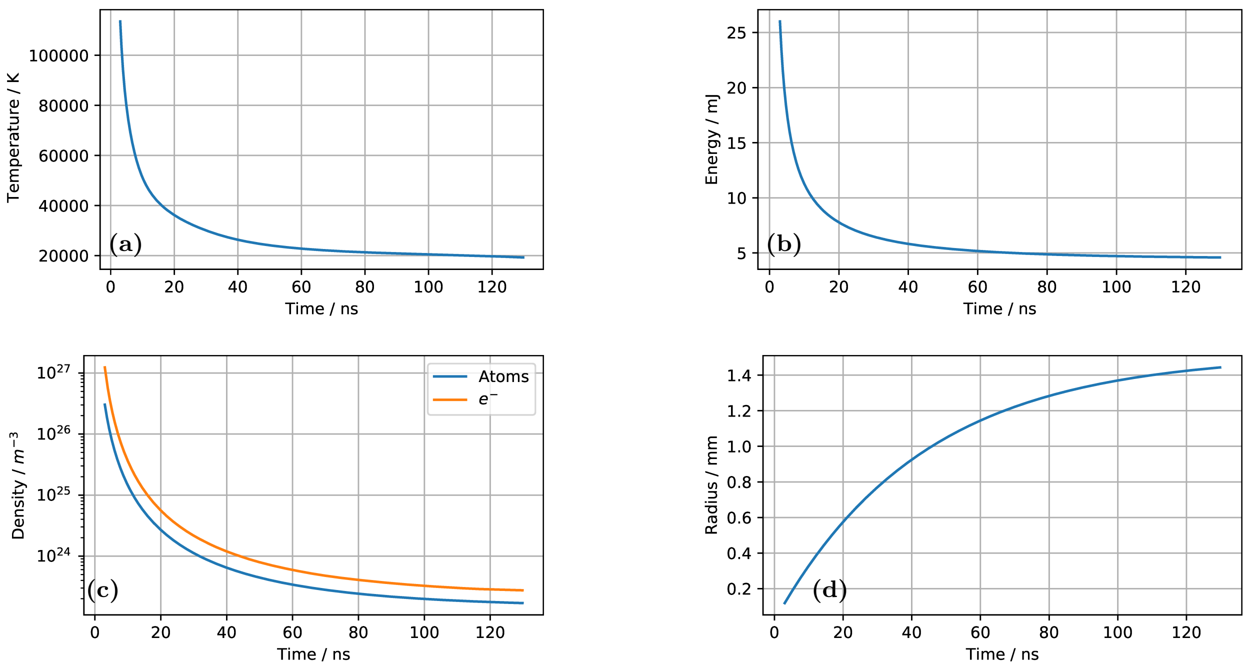

Figure 5.2.3: *Resulting profiles of* ***(a)*** *temperature,* ***(b)*** *internal energy,* ***(c)*** *density, and* ***(d)*** *radius for the adiabatic expansion of an iron plasma. From* ***(a)*** *it is seen that the temperature decreases faster at the earlier times.*

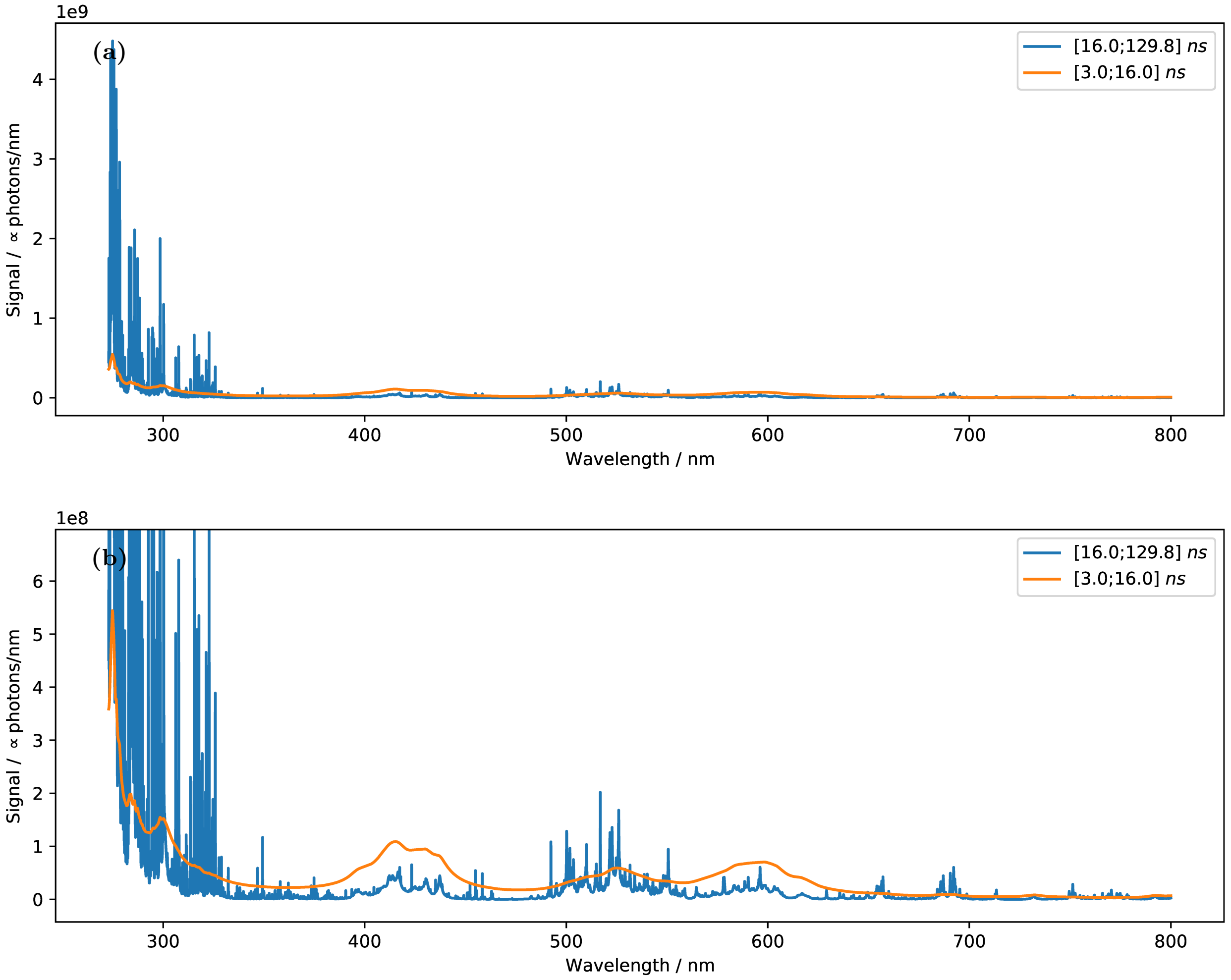

Figure 5.2.4: ***(a)*** *Iron spectrum simulated from the plasma parameters of the adiabatic expansion scheme (Figure 5.2.3). The orange curve is the spectrum from 3 ns to 10 ns. The blue curve is the spectrum from 10 ns to 130 ns. The spectrum for the earliest times is seen to be very broad, due to the high initial plasma density, and thereby containing spectral features of less spectroscopic interest.* ***(b)*** *Close up where the earliest spectrum is better seen.*

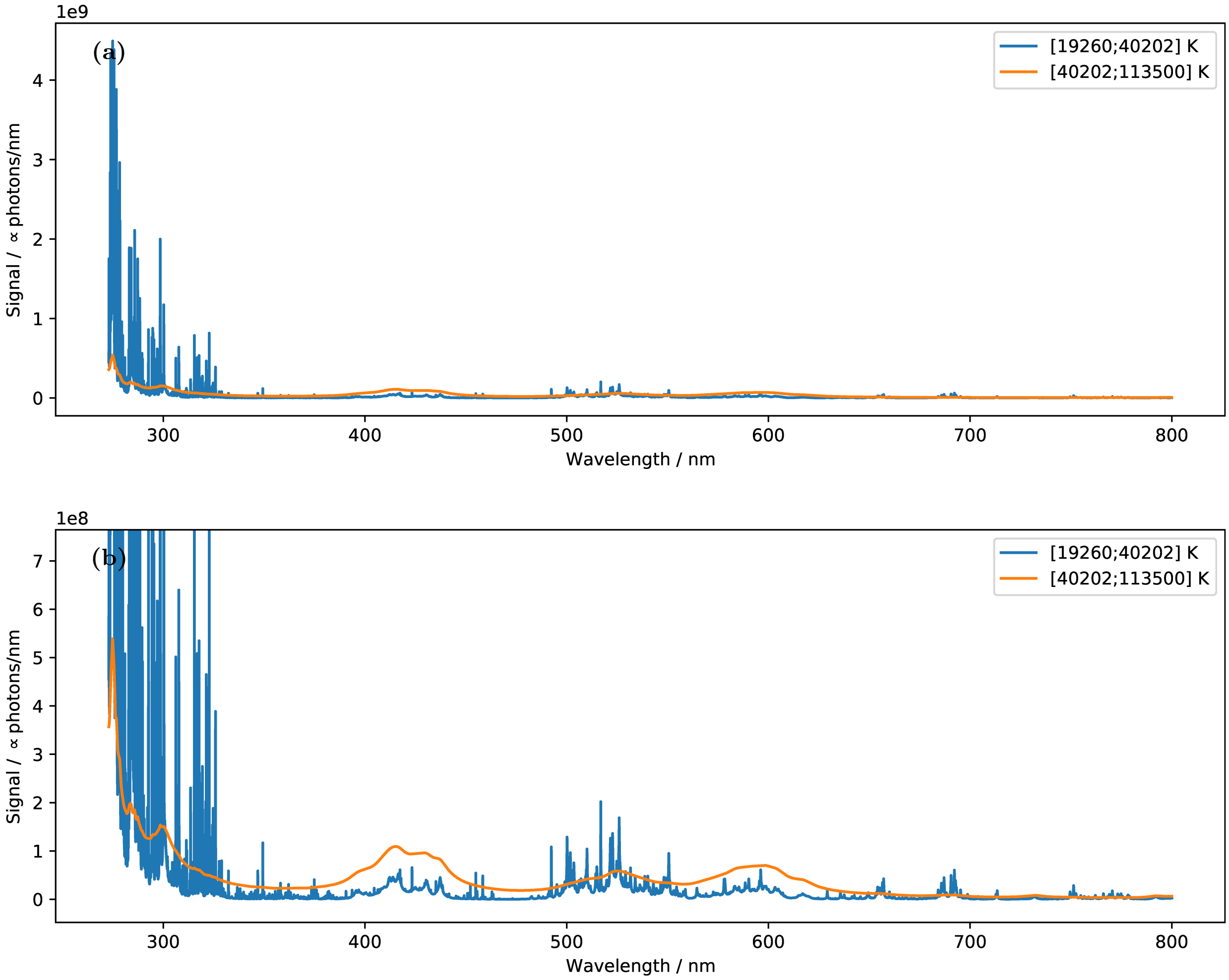

Figure 5.2.5: ***(a)*** *Iron spectrum simulated from the plasma parameters of the adiabatic expansion scheme (Figure 5.2.3). The orange curve is the spectrum for temperatures of* 116.400 K *to* 41 600 K*. The blue curve is the spectrum from* 41 600 K *to* 20 300 K*. The spectrum for the earliest times is seen to be very broad, due to the high initial plasma density, and thereby containing spectral features of less spectroscopic interest.* ***(b)*** *Close up of (a) where the higher temperature spectrum is better seen.*

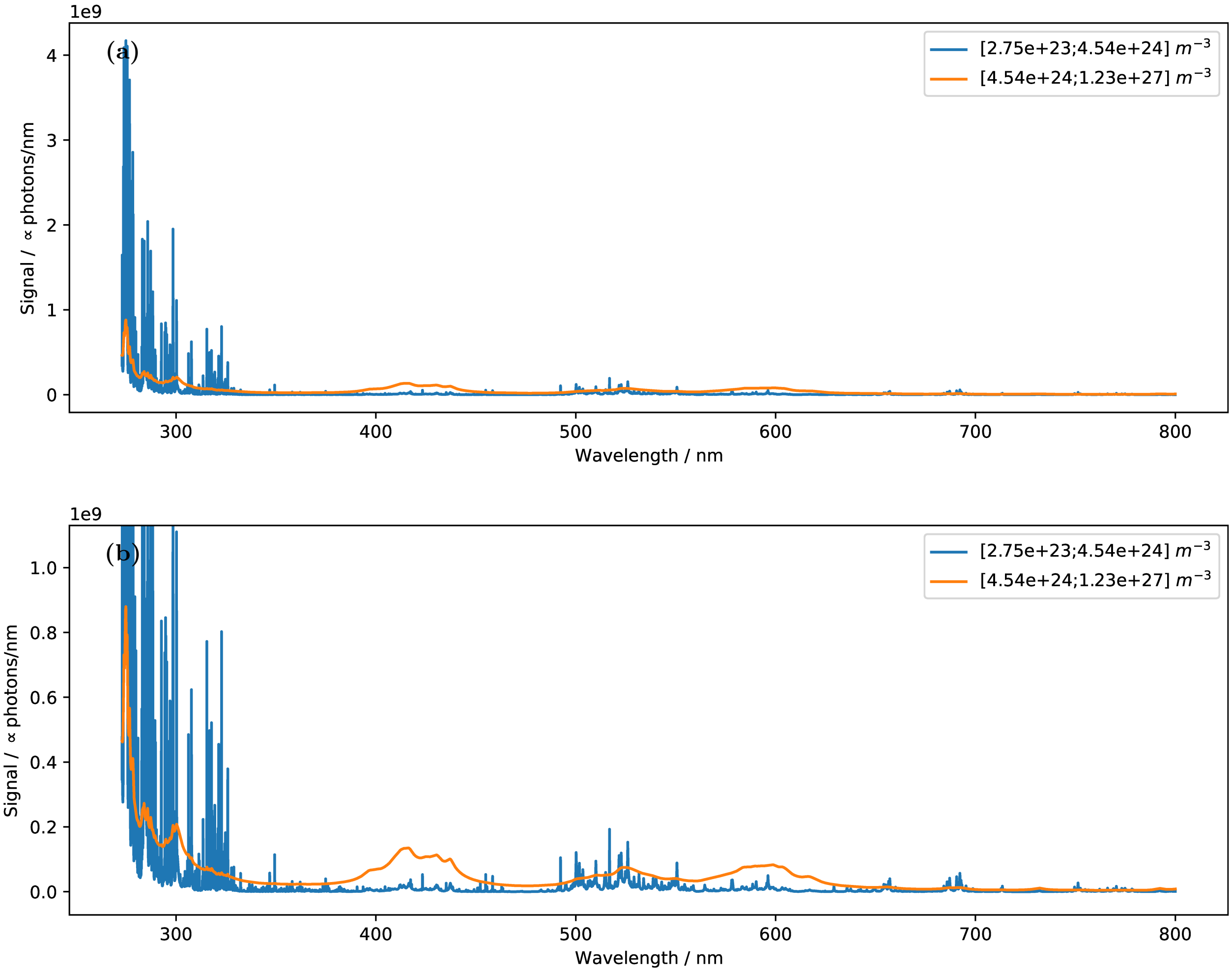

Figure 5.2.6: ***(a)*** *Iron spectrum simulated from the plasma parameters of the adiabatic expansion scheme (Figure 5.2.3). The orange curve is the spectrum for electron densities of* $1.25 \times 10^{27}\,\mathrm{m}^{-3}$ *to* $4.61 \times 10^{24}\,\mathrm{m}^{-3}$*. The blue curve is the spectrum from* $4.61 \times 10^{24}\,\mathrm{m}^{-3}$ *to* $2.79 \times 10^{23}\,\mathrm{m}^{-3}$*. The spectrum for the earliest times is seen to be very broad, due to the high initial plasma density, and thereby containing spectral features of less spectroscopic interest.* ***(b)*** *Close up showing where the earliest spectrum is better seen.*

3000 K. This is due to the exponential dependence on the temperature. To illustrate the effect of leaving out the lower temperature stages of the plasma, the spectrum of a homogeneous plasma of fixed Na density and electron density but with an exponentially decaying temporal temperature profile has been simulated. The spectrum for temperatures of 8000 K to 300 K is shown together with the spectrum from 4000 K to 300 K in Figure 5.2.7. From the figure it can be seen that the latter spectrum does not contribute significantly to the total spectrum. Consequently, template spectra of atomic emissions are only included for temperatures higher than 4000 K.

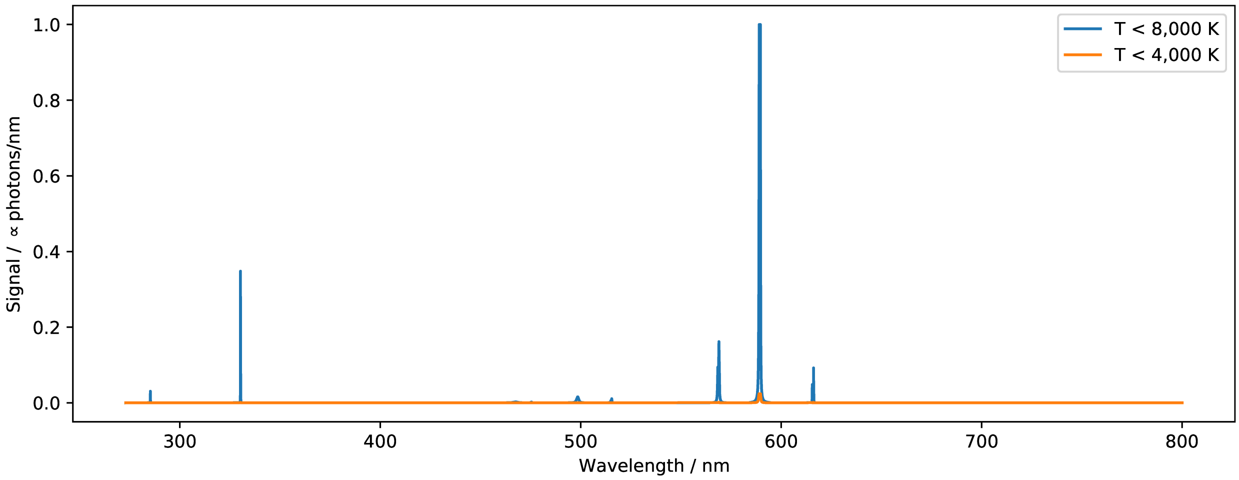

Figure 5.2.7: *Simulated spectra of homogeneous plasma of Na with an exponentially decaying temperature profile. Na density and electron density were kept constant at* $2 \times 10^{22}\,\mathrm{m}^{-3}$ *and the plasma size at* 3 mm. *The blue curve shows the spectrum for temperatures of* 8000 K *and towards* 0 K. *The orange curve shows the spectrum from* 4000 K *and towards* 0 K. *By comparing the curves, it can be seen that the temperatures of* 4000 K *and lower does not contribute much to the total spectrum compared to the higher temperatures.*

As the unmixing database must be comprised by a finite number of template spectra, some discretization of the plasma properties for the simulation of spectra must be done. Consequently, the interpolation between template spectra is investigated. For doing so, spectra simulated from a homogeneous plasma of the elements Ca, Mg, Mn, Na, C, and O are considered and the results are assumed representative for the rest of the elements contained in the database. This is motivated by the large variety of upper energy levels and ionized states for the stronger emission lines of Ca, Mg and Mn. Some selected results can be seen in Figure 5.2.8, 5.2.9, and 5.2.10 showing interpolations between spectra of different elemental concentrations, temperatures and electron densities, respectively. As indicated by Figure 5.2.8 and 5.2.9, interpolation can be done with good accuracy between relatively large spans of elemental concentrations and electron densities. As indicated by Figure 5.2.10 the accuracy of interpolation between different temperatures is not equally good and consequently the temperature discretization of the template spectra should be of higher resolution than for the electron density and the elemental concentrations. This is in agreement with the results obtained from fits of emission spectra in Chapter 4, where the temperature was found to be the best constrained plasma property and thereby concluded to be the most important parameter of the plasma model.

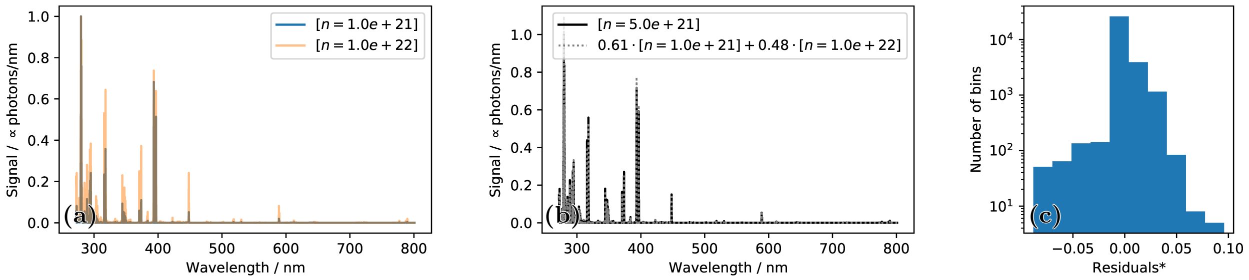

Figure 5.2.8: *Results from testing the interpolation between simulated spectra with different values of the atomic densities from a homogeneous plasma of length* 3 mm*, temperature of* 14 000 K*, electron density of* $5 \times 10^{22}\,\mathrm{m}^{-3}$*, and consisting of the elements Ca, Mg, Mn, Na, O, and C.* ***(a)*** *Spectra from two different values of the atomic densities in m*$^{-3}$ *as noted in the legend.* ***(b)*** *Spectrum resulting from an atomic density of* $5 \times 10^{21}\,\mathrm{m}^{-3}$ *(solid black curve) compared to the spectrum obtained from a linear combination of the spectra in (a) (dashed grey curve).* ***(c)*** *Histogram of the residuals between the curves in (b). The residuals are defined as* $(a - b)/(b + 0.005)$ *where a is the spectrum from interpolation and b is the exact spectrum. The value of 0.005 is to suppress the residuals among the pixels of lower intensities as these, when considered in a measured LIBS spectrum, usually will be dominated by spectral noise.*
From (b) and (c) it can be seen that the spectrum from atomic densities of $5 \times 10^{21}\,\mathrm{m}^{-3}$ *can be well described by interpolation of the spectra with lower and higher atomic densities in spite of a large influence of the atomic densities in the individual spectra as can be seen from (a).*

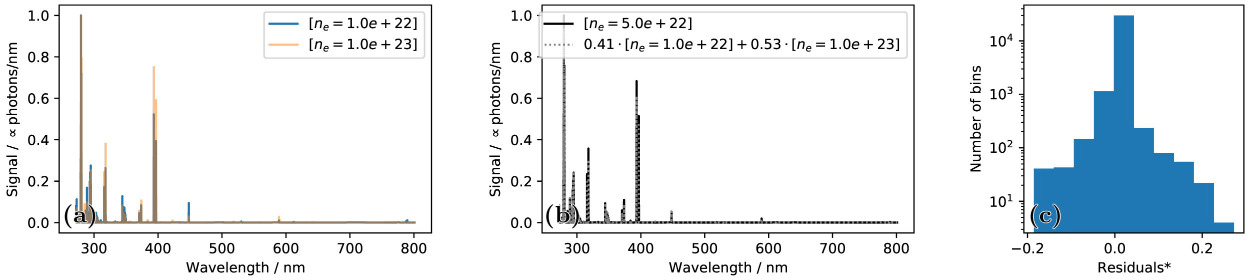

Figure 5.2.9: *Same as Figure 5.2.8 but for interpolation in electron density. From (b) and (c) it can be seen that the spectrum from an electron density of* $5 \times 10^{22}\,\mathrm{m}^{-3}$ *can be well described by interpolation of the spectra with lower and higher electron densities in spite of a large influence of the electron density in the individual spectra as can be seen from (a).*

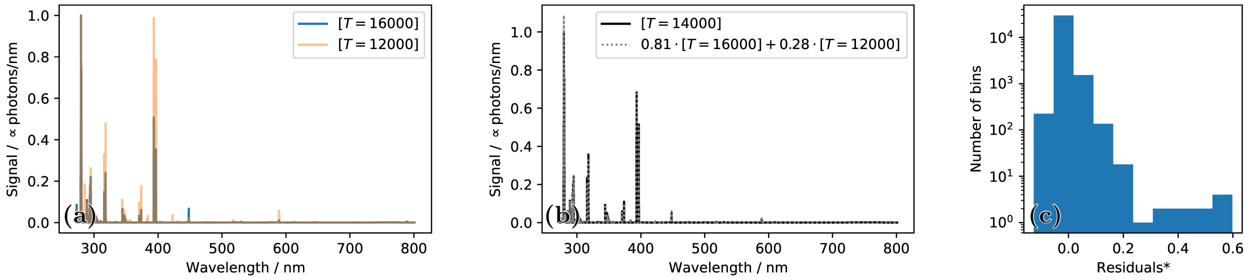

Figure 5.2.10: *Same as Figure 5.2.8 but for interpolation in temperature. From (b) and (c) it can be seen that the spectrum from temperature of* 14 000 K *can be relatively well described by interpolation of the spectra with lower and higher temperatures. The description is not equally good as for interpolation of atomic and electron densities (Figure 5.2.8 and 5.2.9), but only a few bins, corresponding to a few emission lines, are described by the interpolation with deviations of around* 60 %*.*

In summary the atomic emissions are described by spectra of pure elements, i.e. element templates, simulated from a homogeneous plasma model plasma of length 3 mm and with temperatures, elemental densities, and electron densities from different combinations of the values summarized in Table 5.1. This results in 186 template spectra per element obtained by iterating through all combinations, but with some constrains to exclude non-physical solutions. For example, combinations of high temperatures and low electron densities are excluded as well as combinations with high atomic densities and low electron densities. The number of template spectra in the unmixing database will later be reduced by removing redundant spectra. The reduction will be elaborated later in this chapter.

Temperature / K	Electron density m^{-3} / K	Atomic density / m^{-3}	No. of elements
4000, 8000, 12 000 16 000, 20 000, 25 000 30 000, 40 000, 50 000	5×10^{21}, 1×10^{22}, 5×10^{22} 1×10^{23}, 5×10^{23}, 1×10^{24} 5×10^{24}	1×10^{18}, 1×10^{20}, 1×10^{22} 1×10^{23}, 1×10^{24}	53

Table 5.1: *Summary of plasma properties used for creating the element templates for the unmixing database. There are 9 different values for the temperature, 7 values for the electron density, and 5 values for the atomic density. The ranges of the plasma properties follows from the previously described considerations involving the early and late phase of the plasma. The resolution (distance between values) are based on interpolation tests such as presented in Figure 5.2.8-5.2.10.*

5.2.2 Continuum Emissions

For describing the continuum emissions, a superposition of localized Gaussian functions is used. More specifically, the continuum is modelled by the superposition of Gaussians with fixed spacings and widths. By selecting the width of the Gaussians to be larger than the typical width of emission lines, it is ensured that the description of the continuum does not interfere with the description of the emission lines (except for the very early phase). As discussed in the previous section, the very early and broad emissions will be treated as part of the continuum. Therefore, the superposition of the localized Gaussians should be able to approximate the high temperature and density spectra of Figure 5.2.5 and 5.2.6. This has been tested and it was found that suitable parameters of the Gaussians are a width of 10 nm and a separation of 5 nm. The approximation of the high temperature spectrum as the superposition of Gaussians is shown in Figure 5.2.11. Further tests for synthetic functions are shown in Figure 5.2.12. From the Figures it can be seen that the superposition of Gaussians well approximates the early high temperature spectrum and both synthetic test functions.

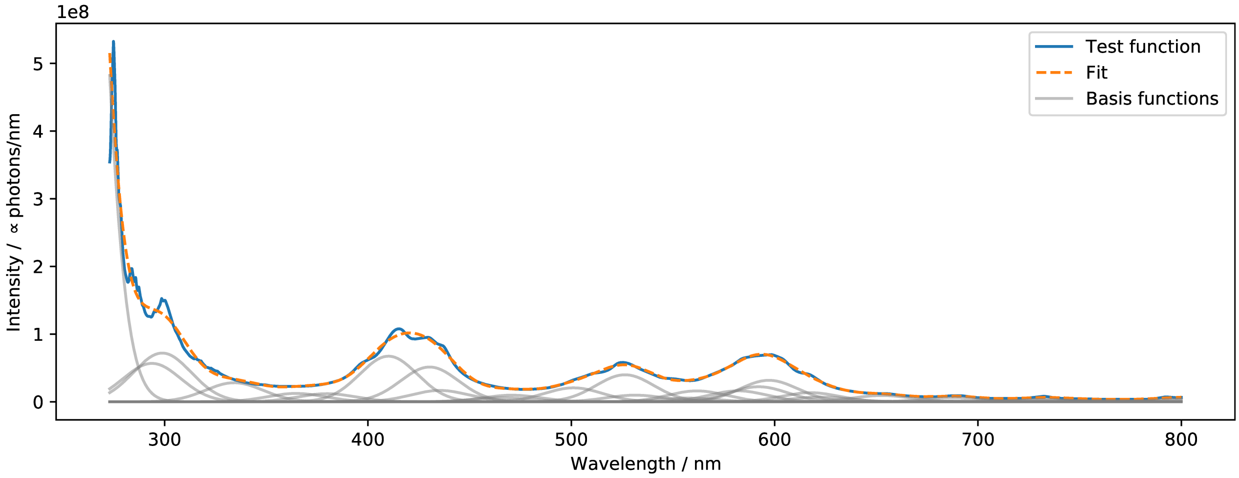

Figure 5.2.11: *The approximation of the high temperature spectrum (Figure 5.2.5) as the superposition of Gaussians functions with a widths of* 10 nm *and* 5 nm *apart.*

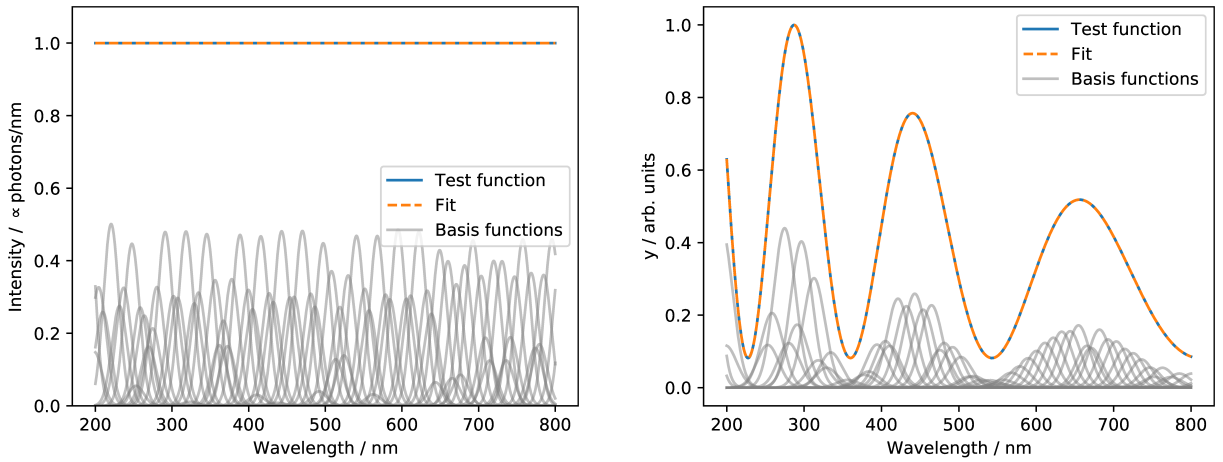

Figure 5.2.12: *The approximation of two test functions as the superposition of Gaussians functions with a width of* 10 nm *and* 5 nm *apart.* ***(left)*** *A constant function and* ***(right)*** *an arbitrary oscillating function.*

5.2.3 Molecular Emissions

As the plasma model does not include the formation of molecules, some of the more frequently encountered molecular emissions in the context of geomaterial analysis on Mars and elsewhere are added to the unmixing database via measured LIBS data. The data for this was obtained for the publication [105] by D. Vogt et al. and reused in this work. The data and the molecular features are summarized in Table 5.2. The molecular features have been extracted by filtering out atomic emissions by fits of Voigt profiles. Examples of extracted features are shown in Figure 5.2.13. Figure 5.2.13b and 5.2.13c show the same CaO band ($B^1\Pi - A'^1\Pi$) as measured in a $CaCO_3$ sample at a delay time of 5 us and 20 us, respectively. The shape of the CaO band can be seen to differ at the two delay times. This indicates the importance of having spectra for different delay times. For the unmixing database, each molecular feature is provided as a separate template. That means that the CaO feature centered around 550 nm can be described independently of the CaO feature centered around ∼610 nm. As only a limited number of molecular features has been considered, the description of molecular features should be considered as a work in progress. Nonetheless, the unmixing database contains the most important features, i.e. CaO, CaF and CaCl. CaO due to its frequent appearance in geological samples, and CaF and CaCl due to an improved detection of F and Cl compared to that from atomic emissions [105, 106].

Sample	Delay time / μs	Integration time / μs	Features extracted
$CaCO_3$	5	100	CaO
$CaCO_3$	10	100	CaO
$CaCO_3$	20	100	CaO
CaF_2	5	100	CaF
CaF_2	10	100	CaF
CaF_2	20	100	CaF
$Matrix_1+CaCO_3$	10	100	CaCl
$Matrix_2+CaCO_3$	20	100	CaCl
Paracetamol	5	100	C_2

Table 5.2: *Summary of the LIBS data from where the molecular features have been extracted. All measurements performed in experimentally simulated Martian atmospheric conditions using the setup described in Chapter 3 and with delay times of either* 5 us, 10 us *or* 20 us.

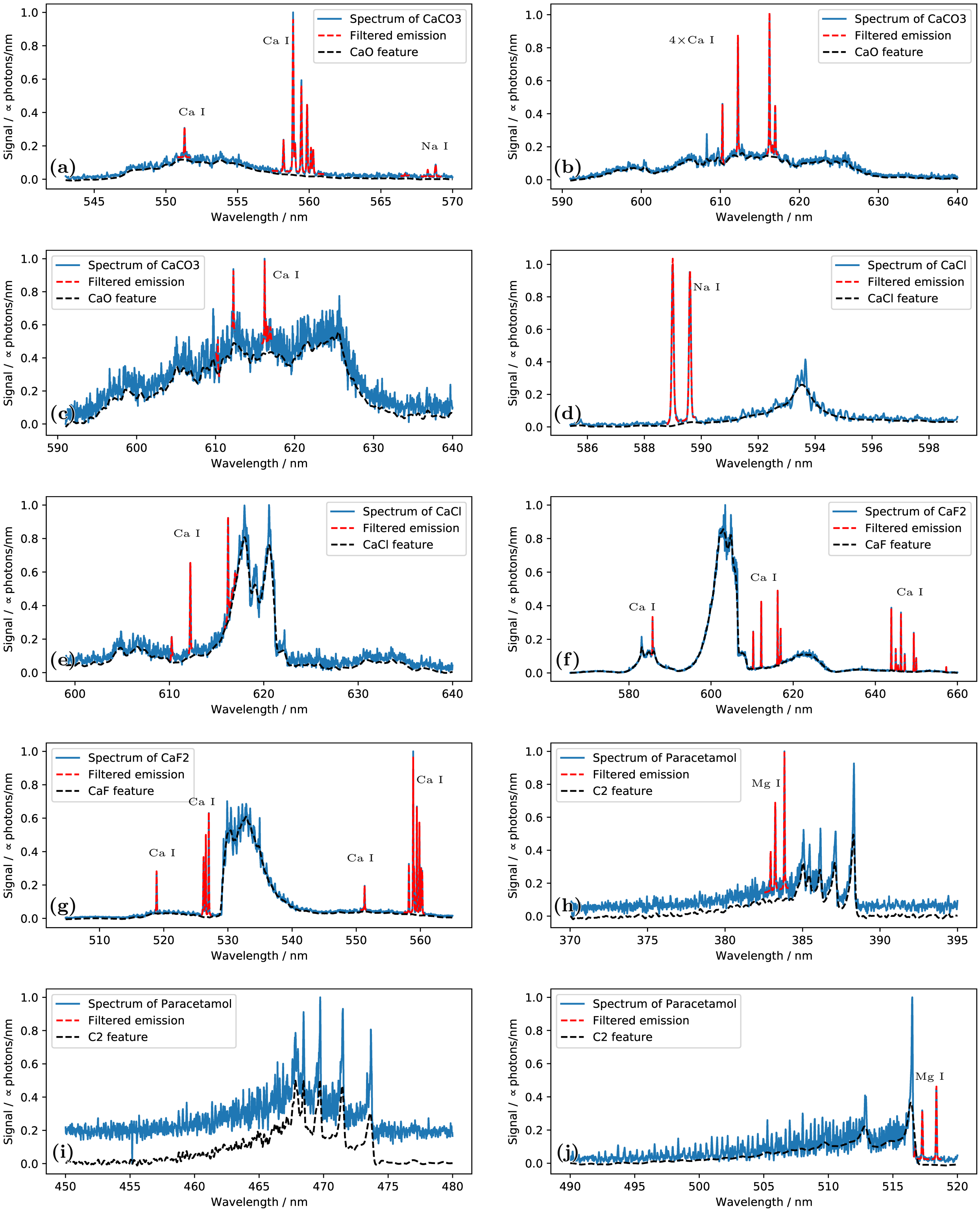

Figure 5.2.13: *Examples of molecular features extracted from the measured LIBS data summarized in Table 5.2. Atomic emissions are filtered out by fits of Voigt profiles before the molecular features are extracted. The features are shifted in intensity such that the intensity is zero at the ends and smoothed with the Gaussian function of a full width at half maximum of* 12 nm.

5.2.4 Reducing the Database

The unmixing database consists of 186 template spectra per element for the description of the atomic emissions. With a total of 52 elements (the element I does not have any lines with the necessary atomic constants in the considered spectral range, see Figure 4.1.8), this results in a total of 9858 template spectra. However, for many of the elements already a subset of the template spectra are enough to sufficiently describe their emissions. This concerns the elements with only few emissions in the considered spectral range or with emissions from a limited range of upper electronic or ionized species making their spectra less depending on the plasma properties. In order to decrease the computation time for applying the method, the unmixing database can therefore be reduced.

For reducing the database, a spectrum is removed if it can be described, within a certain threshold, using a linear combinations of the remaining template spectra in the unmixing database. As the template spectra are calculated from atomic constants with uncertainties (see Figure 4.1.10 in Chapter 4) a threshold of maximum 20 % relative deviations is chosen. Consequently, the i'th template spectrum of e.g. Al, $P_{Al,i}$, is removed if

$$\max\left(\left|\frac{P_{Al,i} - \sum_{j,j\neq i} c_j P_{Al,j}}{P_{Al,i} + 0.005}\right|\right) < 0.2 \ , \tag{5.2.6}$$

where $\sum_{j,j\neq i} c_j P_{Al,j}$ denotes the description of $P_{Al,i}$ via superposition of the other template spectra of Al. The coefficients of the superposition, c_j, are determined by nnls according to the constraint of non-negative intensities. In equation (5.2.6), the template spectra are assumed normalized to their maximum intensity and the value of 0.005 in the denominator is added to suppress differences among the pixels of lower signals as these will usually be dominated by the measurement noise of the input spectrum. After this reduction, the unmixing database is reduced to approximately one third of the original size. An overview of the number of template spectra can be seen in Figure 5.2.14. The number of template spectra can be seen to vary for each element. For example, the number of template spectra for H is reduced to 18 whereas the number of template spectra for Ca, Mg and Mn are reduced to 114, 107, and 88, respectively. This indicates that these spectra, compared to H, depend stronger on the plasma properties. It thereby verifies the use of these elements for testing the interpolations in the plasma properties (Figure 5.2.8, 5.2.9, and 5.2.10).

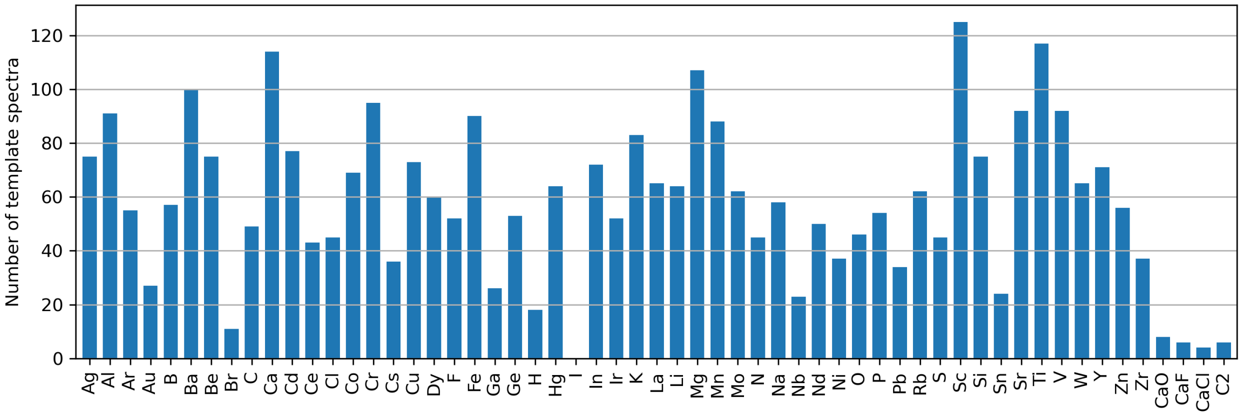

Figure 5.2.14: *Number of template spectra in the reduced unmixing database. No template spectra are obtained for Iodine (I) as no lines with the necessary atomic constants are contained in the database for the considered spectral range (see Figure 4.1.8 Chapter 4). No template spectra for the molecular emissions are removed in the reduction and their numbers of template spectra reflect the number of measured LIBS spectra (see Table 5.2).*

5.3 Solving and Visualizing the Unmixing

Before solving the unmixing equation, the input spectrum is smoothed by a Gaussian function of FWHM of 0.12 nm. After that, both the input spectrum and the individual template spectra of the unmixing database are normalized to a total signal of one. It therefore follows that a score equal to one, for a specific template spectrum, corresponds to all the signal of the input spectrum being explained by that specific template spectrum. For solving the unmixing, the algorithm of fast non-negative least squares is used (fnnls package in python [107]). In the equation each pixel is weighted similarly as in Chapter 4, but with a model uncertainty of 20 % instead of 10 %. The larger model uncertainty is chosen since the method is applied to the bins in the spectra and not spectrally integrated signals that are less dependent on the uncertainties in the shapes of the emission lines. After solving the scores, the coefficients in the non-reduced database are reconstructed using the coefficients in the linear combination obtained during the reduction of the database (equation 5.2.6). This is done to better interpret the scores. For example, if the template spectra of some element at 11 000 K and 16 000 K were similar within the threshold (equation 5.2.6), either one of them could be kept or removed from the unmixing database. To compensate such ambiguities, the scores of all the template spectra, including those removed during the reduction, are obtained in an approach of constrained minimization. The function to be minimized is the L^2-norm of the vector containing the reconstructed scores, i.e. $s_1^2 + s_2^2 + s_3^2 + \cdots + s_m^2$. By minimizing the L^2-norm, the scores of the template spectra at 11 000 K and 16 000 K, in the above mentioned example, would be equally distributed as $1^2 + 0^2$, corresponding to all of the score distributed in a single spectrum, is bigger than $0.5^2 + 0.5^2$, corresponding to the score distributed equally among the two spectra. The constraints in the minimization are given by demanding that each of the solved scores, i.e. the scores in the reduced database, are the same as when obtained from the reconstructed scores and the coefficients obtained when reducing the database. The latter is obtained using the coefficients in the superposition of the removed template spectra (equation (5.2.6)). Thereby, there exists one constraint for each spectrum in the reduced database. For example, the k'th constraint corresponding to the k'th template spectrum in the reduced database is given as

$$\tilde{s}_k = s_k + \sum_{j,j\neq k} c_{j,k} \cdot s_j \ , \tag{5.3.1}$$

where $\tilde{s}_k$ is the solved score of the k'th template spectrum in the reduced database, s_j is the reconstructed score of the j'th template spectrum, and $c_{j,k}$ is the amount of the k'th template spectrum in the superposition of the description of the j'th template spectrum. Using the method of *Lagrange multipliers* this minimization problem can be described as a system of linear equations that is solved for the scores using nnls.

After reconstructing the scores, the results are visualized in different ways. By summing the product of the scores, in the reduced database, and the template spectra for each element/molecular species, the total spectra of the different pure components are obtained and plotted together with the input spectrum. Due to the large number of pure spectra/components, only those with predicted signal, at some pixel, stronger than five times the zero'th level noise and not superseded by signals from other components, i.e. with spectral interferences below 50 %, are plotted (see Chapter 3 Figure 3.3.15 and 3.3.16 for the definition and classification of the zero level noise). Such pure spectra/components will be referred to as significant pure spectra/components. By only summing the scores, a score for each element/molecular species is obtained and due to the before mentioned normalization these scores correspond to the fractions of the total signal explained by the emissions from the different components (elements/molecules). As the templates for describing the atomic emissions are simulated, their solved scores can also be grouped for the plasma properties and a score for each temperature and density can be obtained. This is done to provide information about the temperature and density of the plasma. Similarly, as for the spectra of pure elements, the individual emission line intensities and line heights can be obtained and plotted giving a visualization of the line identification. This is done by also keeping track of the intensities and heights of the individual emission lines while simulating the spectra for generating the database. Finally, a routine for the automatic generation of a multi-element Saha-Boltzmann plot (see Chapter 2), using the line intensities as obtained from the solved scores, has been implemented and integrated in the implementation of the unmixing. As a standard, emission lines with a SNR of 10 or larger and with spectral interferences at the center wavelengths below 50 % are used. In order to compensate for self-absorption, a free parameter for the effective path are added and its value optimized for the best coefficient of determination (R^2) for the regression in the multi-element Saha-Boltzmann plot.

5.4 Results from Applications

The unmixing can be applied to spectra without any time gating and of complicated elemental compositions. Independent of the type of input spectra, the analysis of a spectrum takes less than one minute on a standard desktop computer. The analysis includes pre-processing, i.e. noise estimation etc., and plotting the results. The unmixing has been applied to both synthetic and measured LIBS data of different samples obtained in different experimental conditions. As for the fit routine in Chapter 4, the application to synthetic spectra is done to provide insight into the solutions and investigate limitations whereas the applications to measured data constitute the real test. Below some selected examples of applications are presented.

5.4.1 Synthetic "Homogeneous" Spectrum

The unmixing has been applied to the synthetic "Homogeneous" spectrum of the carbonate mixture introduced in Chapter 4. The spectra of the significant pure components are shown in Figure 5.4.1 together with the input spectrum. The residuals between the spectrum as predicted by the unmixing and the input spectrum are shown in Figure 5.4.2. From the figures it can be seen that the unmixing divides the input spectrum into its pure components without any predicted significant signals from elements not contained in the synthetic spectrum. From the close-up in Figure 5.4.1d showing the two strong Ca II ground state transitions, it can be seen that the line at 393 nm is a little over estimated by the unmixing. Such small discrepancies are due to the discretization of the plasma properties of the template spectra in the unmixing database. For example, the "Homogeneous" spectrum was simulated with a constant temperature of 13 000 K along the LOS, but the closest temperatures within the unmixing database are 11 000 K and 14 000 K (see Table 5.1. Nonetheless, the smaller discrepancies are not enough to cause over fitting by other elements. This is confirmed in Figure 5.4.3a where the 30 pure components with the highest scores are shown. From the figure it can be seen that the total score, i.e. the total signal, is dominated by Mg, Ca, Mn, Na and O which is in agreement with the composition of the "Homogeneous" spectrum. In Figure 5.4.3b-d the scores for the plasma properties are shown. From the figure it can be seen that the scores are obtained mainly from template spectra with temperatures of 11 000 K, 14 000 K and 19 000 K. The electron density scores can be seen mainly to be distributed among spectra of $1 \times 10^{22}\,\mathrm{m}^{-3}$, $5 \times 10^{22}\,\mathrm{m}^{-3}$, and $1 \times 10^{23}\,\mathrm{m}^{-3}$. These values closely resemble the reference plasma properties of the "Homogeneous" spectrum well (see Figure 4.3.1 in Chapter 4).

In Figure 5.4.4 the scores for the plasma parameters are shown individually for Ca and Na. From the figure it can be seen that the scores for Ca roughly resemble those of the total signal (Figure 5.4.3). This is not the case for Na where the scores can be seen to be distributed also among the lower temperatures. The results from the automatic generation of the multi-element Saha-Boltzann plot are shown in Figure 5.4.5. The electron density was fixed to $5 \times 10^{22}\,\mathrm{m}^{-3}$ according to the scores for the electron densities (Figure 5.4.3c). From the figure it can be seen that the derived temperature is only 5 K from the actual value and that the estimated relative concentrations are close to the actual values (within 7 % relative deviations).

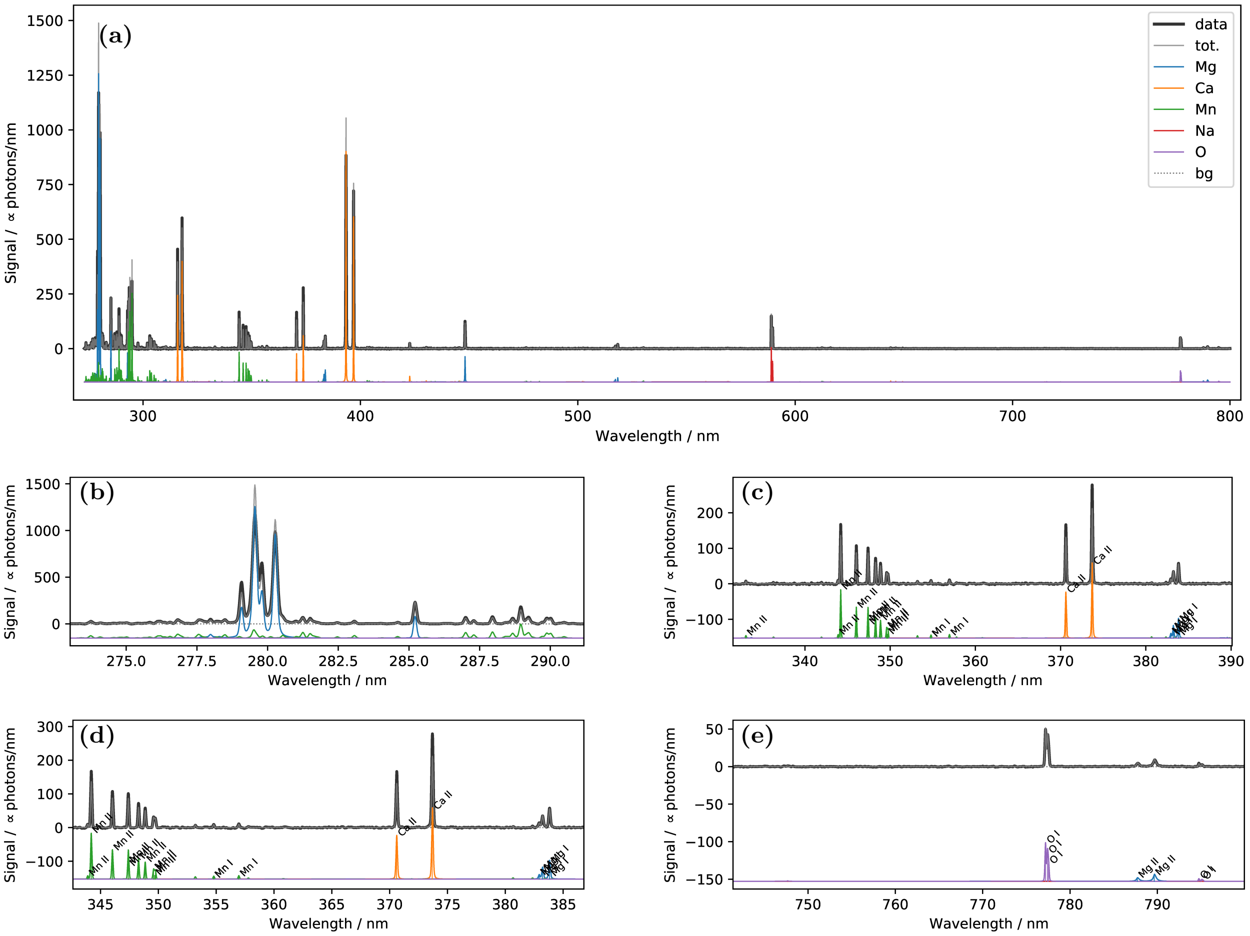

Figure 5.4.1: *Spectra of pure components obtained from applying the unmixing to the synthetic "Homogeneous" spectrum.* ***(a)*** *The input spectrum shown together with the pure spectra of the significant components. The pure spectra are shown with a negative y-offset. The curve marked by "bg" in the legend is the background spectrum obtained from the superposition of the localized Gaussians. The curve marked by "tot." is the sum of all the pure spectra. The strongest emission lines have been marked automatically according to their heights.* ***(b)-(e)*** *are close-ups of (a) in different wavelength ranges. Minor deviations, such as for the left Ca II line in (d) or the left most strong Mg II lines in (b), are due to the discretization of the unmixing database. The sum of the pure spectra ("tot." in legend) can be seen to match the input spectrum well and no over-fitting is observed.*

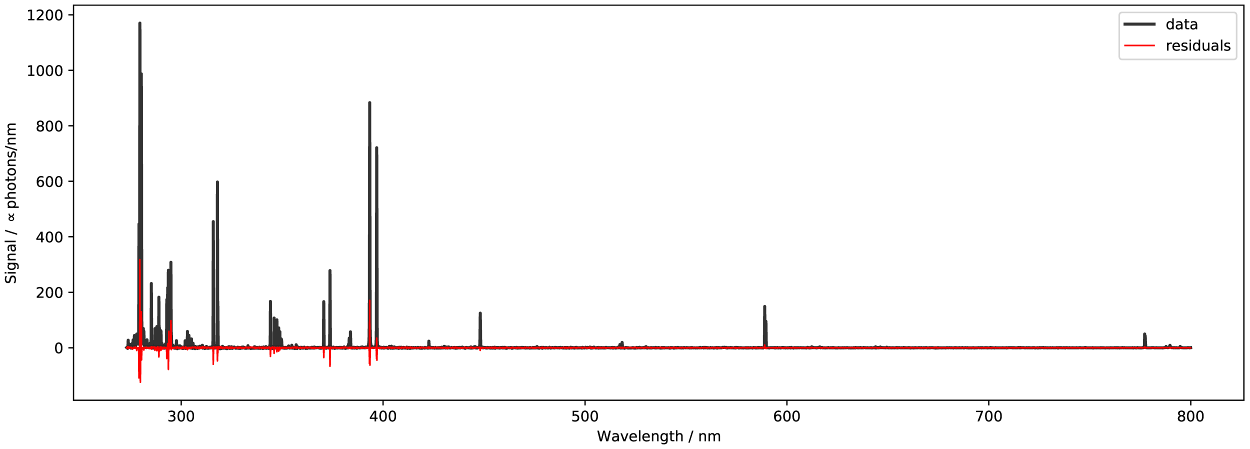

Figure 5.4.2: *Residuals between the spectrum as predicted by the unmixing ("tot." in Figure 5.4.1) and the "Homogeneous" synthetic spectrum. The residuals are relatively small and at the highest around 20 %.*

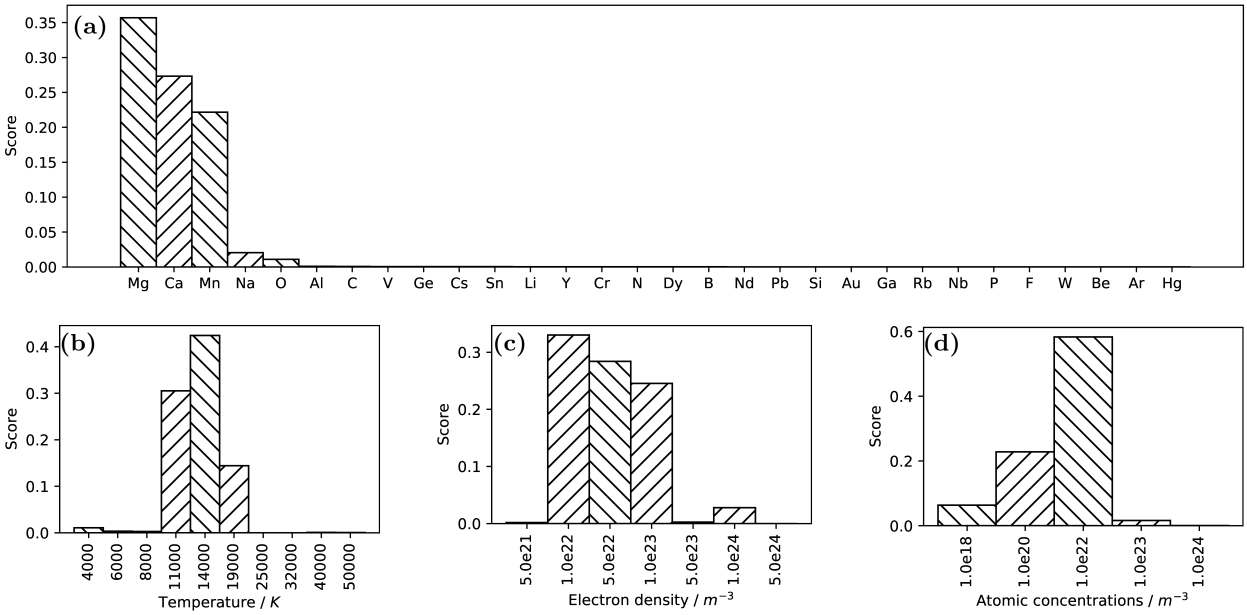

Figure 5.4.3: ***(a)*** *The scores for the 30 pure components with the highest values. Here it can be seen that Mg, Ca, Mn, Na and O are the elements with the highest score. This is in agreement with the composition of the "Homogeneous" spectrum.* ***(b)-(d)*** *Bar chart of the scores of the template spectra of the atomic emissions sorted according to the plasma properties. The "Homogeneous" spectrum was simulated with a temperature and electron density of* 13 000 K *and* $4.7 \times 10^{22}\,\mathrm{m}^{-3}$*, respectively. This is in good agreement with the distributions of the scores that are centred around values around* 14 000 K *and* $5 \times 10^{22}\,\mathrm{m}^{-3}$ *for the temperature and electron density, respectively.*

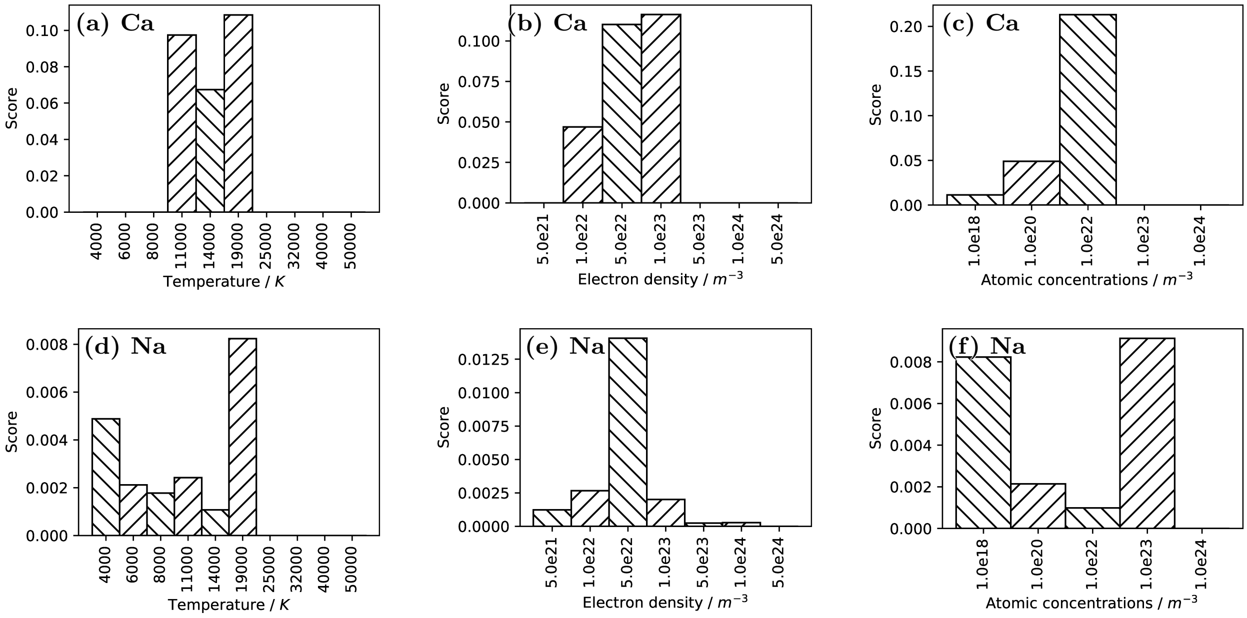

Figure 5.4.4: ***(a,b,c)*** *Bar charts for the scores of Ca template spectra sorted according to the plasma properties and* ***(d,e,f)*** *for Na. The scores of the plasma properties of Ca resemble the scores summed for all elements (Figure 5.4.3b,c,d) well. This is not true for the temperature scores of Na due to the low amount of information contained in the Na emission lines in the spectrum.*

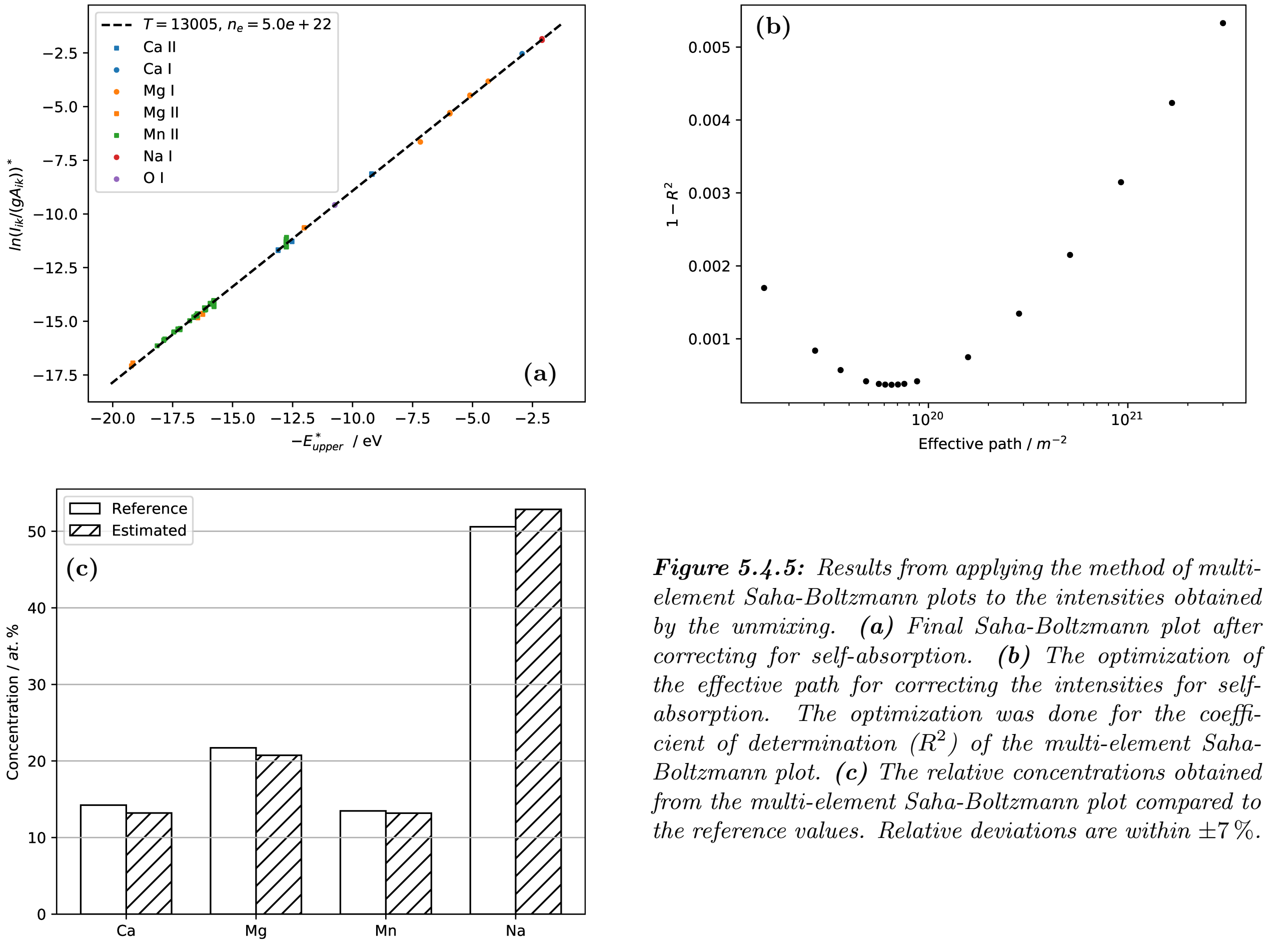

Figure 5.4.5: *Results from applying the method of multi-element Saha-Boltzmann plots to the intensities obtained by the unmixing.* ***(a)*** *Final Saha-Boltzmann plot after correcting for self-absorption.* ***(b)*** *The optimization of the effective path for correcting the intensities for self-absorption. The optimization was done for the coefficient of determination (R^2) of the multi-element Saha-Boltzmann plot.* ***(c)*** *The relative concentrations obtained from the multi-element Saha-Boltzmann plot compared to the reference values. Relative deviations are within ±7 %.*

5.4.2 Synthetic "Bogaerts" Spectrum

To test the unmixing database on a spectrum from a non-homogeneous plasmas, the unmixing has been applied to the "Bogaerts" synthetic spectrum introduced in Chapter 4. The spectra of the significant pure components are shown in Figure 5.4.6 together with the input spectrum. From the figure it can be seen that no significant pure components not contained in the Carbonate mixture are predicted. The majority of the peaks are described well (Figure 5.4.6a), but there are examples of deviations. The strongest deviation is found for the strong Mg II emission lines around 280 nm. The emission line can be seen in Figure 5.4.6b. An overview of the residuals between the total spectrum as predicted by the unmixing and the input spectrum can be seen in Figure 5.4.7.

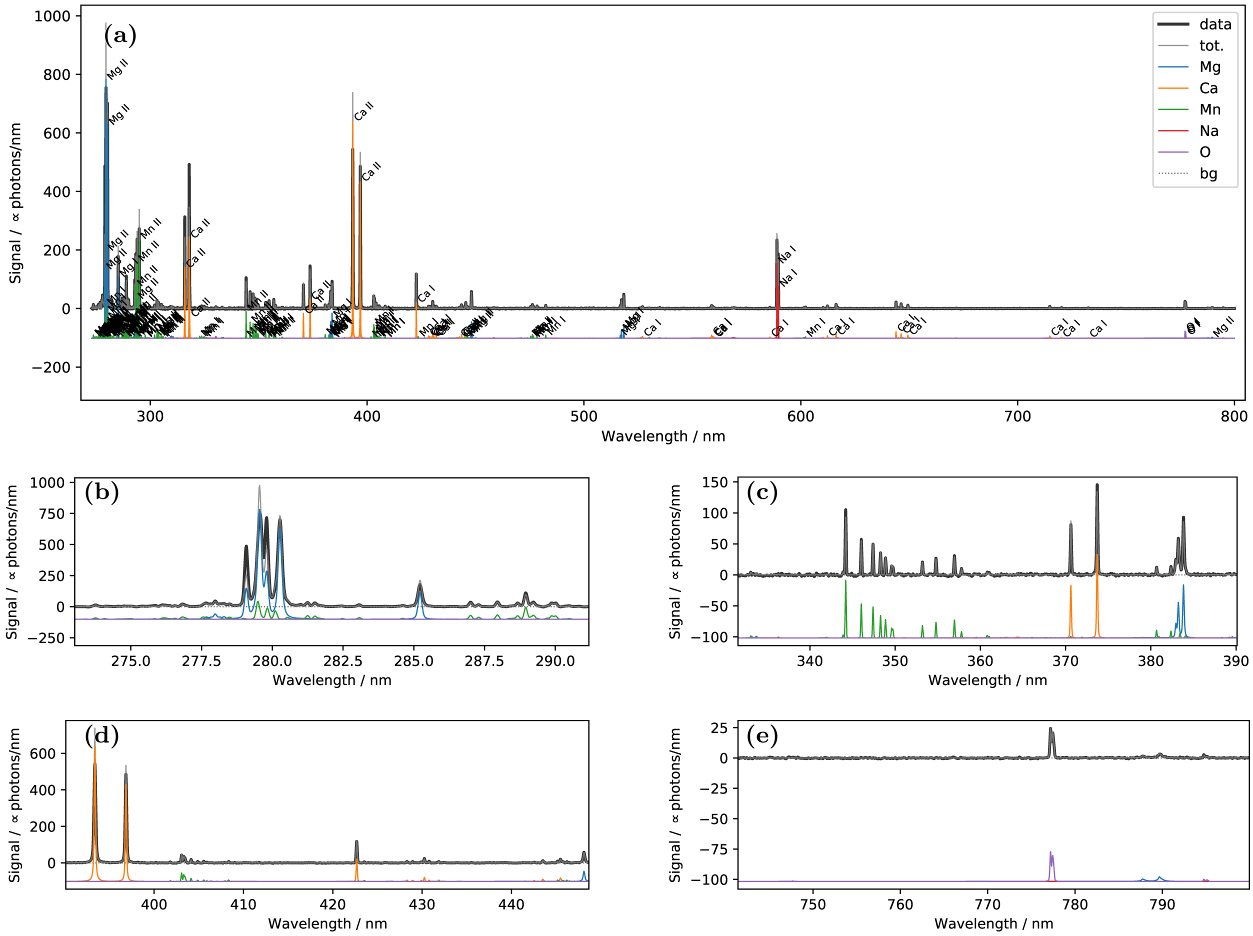

Figure 5.4.6: *Results from applying the unmixing to the synthetic "Bogaerts" spectrum.* ***(a)*** *The input spectrum shown together with the pure spectra of the predicted significant components. The pure spectra are shown with a negative y-offset. The strongest emission lines have been marked automatically according to the obtained line identification.* ***(b)-(e)*** *Close-ups of (a) with the line identification hidden. There are some smaller discrepancies between the pure components and the input spectrum, such as for the Mg II shown in (d), but generally the sum of the spectra of the pure components ("tot." in legend) resembles the input spectrum very well at most wavelengths and no signs of overfitting can be seen.*

The scores for the pure components and the plasma properties are shown in Figure 5.4.8. From the scores of the pure components, it can be confirmed that the elements and molecules not contained in the spectrum/plasma all have negligible or zero scores (Figure 5.4.8a). From the scores of the plasma properties (Figure 5.4.8b,c,d) the spatial gradients of the "Bogaerts" spectrum are evidenced by the spread in the values. For example, the scores for the temperatures of 8000 K and 6000 K both have non-negligible values (Figure 5.4.8b). The minimum temperature along the LOS of the "Bogaerts" plasma is around 7000 K.

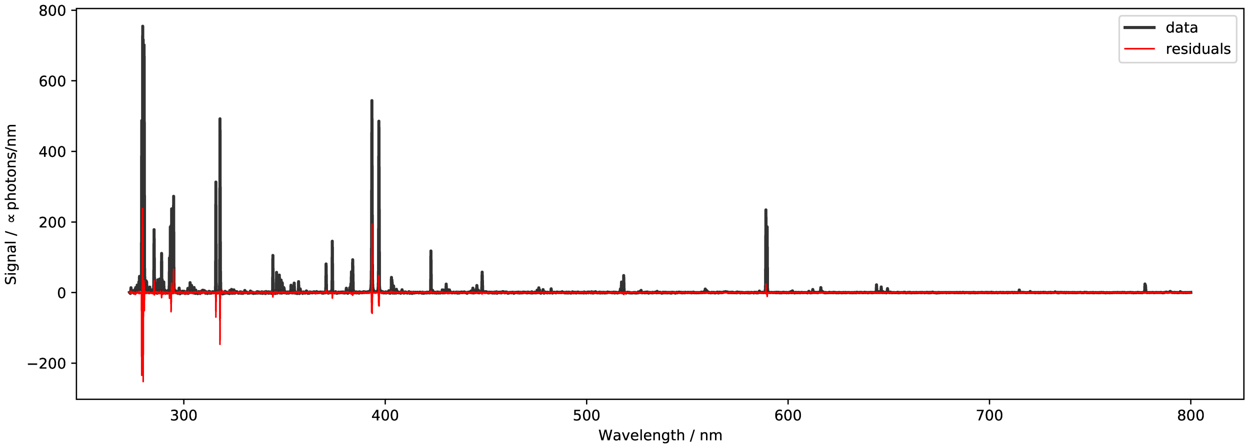

Figure 5.4.7: *Residuals between the spectrum as predicted by the unmixing ("tot." in Figure 5.4.6) and the "Bogaerts" synthetic spectrum. The residuals can be seen to be largest for the strongest signals, i.e. the Mg II lines around* 280 nm *and the Ca II lines around* 393 nm*.*

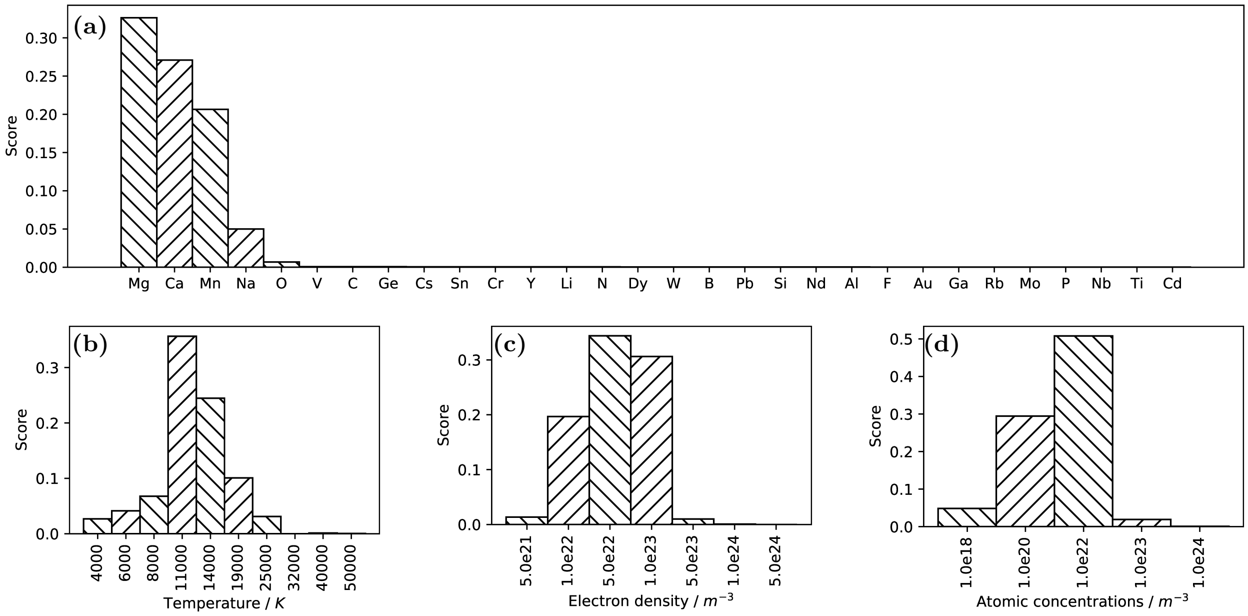

Figure 5.4.8: *More results from applying the unmixing to the synthetic "Bogaerts" spectrum.* ***(a)*** *The scores for the 30 pure components with the highest scores. From the figure it can be seen that Mg, Ca, Mn, Na and O dominates the scores. This is in agreement with the composition of the Carbonate mixture and indicates negligible overfitting.* ***(b)-(d)*** *Bar plots showing the scores of the plasma properties. The scores of the plasma properties extends towards lower temperatures in agreement with the presence of spatial gradients. The temperature with the highest score is* 11 000 K *which corresponds approximately to the average value of the temperature profile for the "Bogaerts" spectrum.*

The results from the multi-element Saha-Boltzmann plot analysis are shown in Figure 5.4.9. The Saha-Boltzmann plot is naturally affected by the gradients in the plasma properties of the "Bogaerts" spectrum. This is indicated by the convex shape of the data points (Figure 5.4.9a). Besides that, the data points in the plot lines up well and no errors in the line identification are indicated by outliers in the Saha-Boltzmann (Figure 5.4.9a) or in the relative concentration estimates (Figure 5.4.9c) whose deviations are within ±36 %.

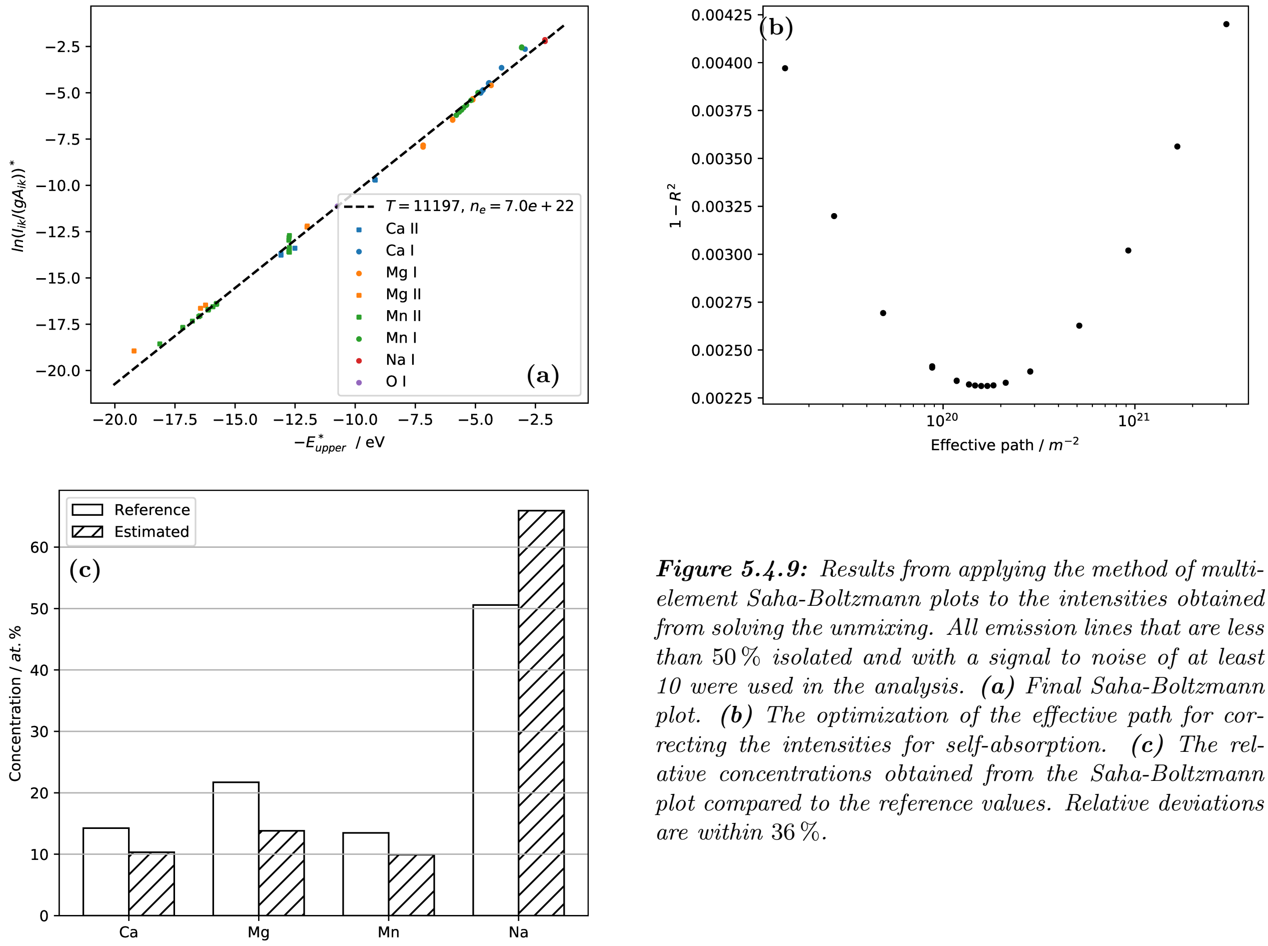

Figure 5.4.9: *Results from applying the method of multi-element Saha-Boltzmann plots to the intensities obtained from solving the unmixing. All emission lines that are less than 50 % isolated and with a signal to noise of at least 10 were used in the analysis.* ***(a)*** *Final Saha-Boltzmann plot.* ***(b)*** *The optimization of the effective path for correcting the intensities for self-absorption.* ***(c)*** *The relative concentrations obtained from the Saha-Boltzmann plot compared to the reference values. Relative deviations are within 36 %.*

5.4.3 Time-resolved Measurements of the Carbonate Mixture

For testing the unmixing on measured LIBS data, it has been applied to the time-resolved LIBS spectra of the Carbonate mixture measured in experimentally simulated Martian atmospheric conditions. These are the spectra introduced and fitted with a two-zone plasma model in Chapter 4. For the earliest delay time, 500 ns, the spectra of the significant pure components are shown in Figure 5.4.10 together with the input spectrum. From the figure it can be seen that emissions from Ca, Mg, Mn, Na, C and O are predicted to dominate the signal. This is in agreement with the composition of the sample. However, a weak but non negligible signal from Zr III is also predicted from the unmixing. This can be seen in Figure 5.4.10c showing two Zr III lines at 283.7 nm and 287.0 nm. However, the sample does not contain any Zr. The lower wavelength Zr line appear at the position of a small increase in the signal of the input spectrum. The width of the signal is broader than the Zr line and the signal is therefore probably due to a collection of several weaker emission lines not contained in the database or due to an experimental artefact. The other and higher wavelength Zr line appear inside a peak resulting from a stronger Mn II line. Due to uncertainties in the data or the model, the Zr III line helps the description of the Mn II peak. This is essentially possible for every peak in the spectrum, but as the spectra of the pure components are the product from many emission lines the probability of such over-fitting gets minimized. In Figure 5.4.10d, the Na II emission lines from the highly excited levels ($E_u \sim 37$ eV) can be seen. As argued in Chapter 4, these emission lines are due to non-equilibrium effects. Opposite to the solution of the two-zone fit (Chapter 4 Figure 4.4.12), these lines are described in the unmixing by the pure spectrum of Na. In Figure 5.4.11 the temperature scores for the emissions of Na and Ca are shown individually. From the figure it can be seen that the scores are differently distributed for the two elements and that Na has non-negligible scores for the highest temperatures. These high temperature scores correspond to the description of the highly excited Na II lines.

For the delay time of 750 ns the pure spectra from significant components are shown in Figure 5.4.12. At this delay time, neither the Zr III lines or the highly excited Na II lines are predicted in the unmixing. The pure spectra from applications to the spectra 1000 ns and 1250 ns delay are similar in quality as for 750 ns and are therefore not shown here. The residuals between the spectrum as predicted by the unmixing and the time-resolved spectra for all of the four considered delay times can be seen in Figure 5.4.13. The residuals can be seen to be relatively low and for most of the emission lines within 20 %, however the residuals are highest for the strongest emission lines.

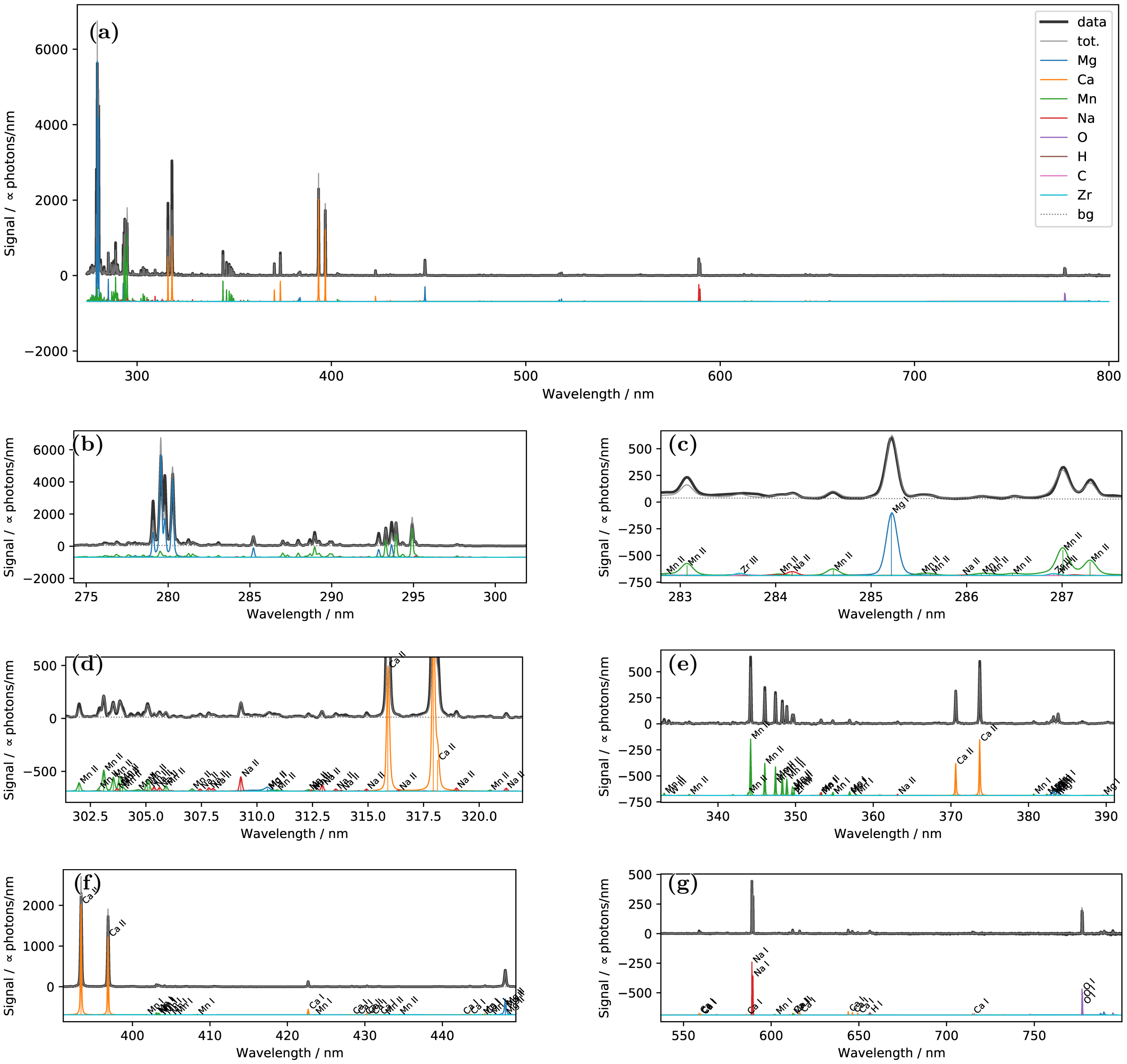

Figure 5.4.10: Results from applying the unmixing to the time-resolved LIBS spectrum of the carbonate mixture obtained in simulated Martian atmospheric conditions at a delay time of 500 ns. ***(a)*** *The input spectrum shown together with the significant pure spectra with the strongest lines marked. The pure spectra are shown with a negative y-offset.* ***(b)-(g)*** *Close ups of (a) showing smaller wavelength ranges where more details can be seen. In (c) two Zr III lines can be seen. As Zr is not present in the carbonate sample, the Zr signal is identified as overfitting. In (d) some Na II lines from highly excited levels (∼*37 eV*) can be seen. These lines are due to non-equilibrium effects (see Chapter 4). Still they are contained in the pure spectrum of Na by element templates of temperatures above* 30 000 K.

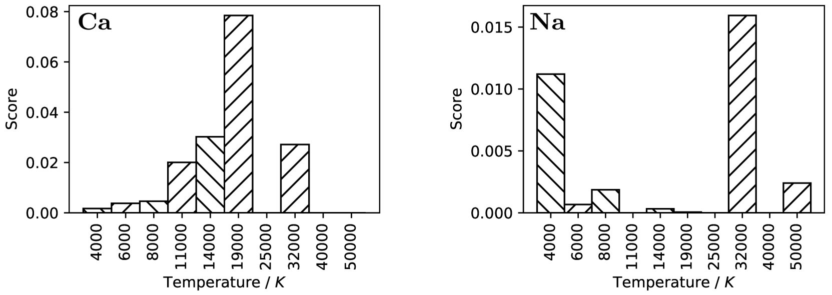

Figure 5.4.11: *Temperature scores for the spectrum at* 500 ns *delay shown individually for the Ca and Na the emissions. For Ca, the scores approximately resemble those of the total emissions (Figure 5.4.15). For Na, lower and higher temperatures are seen to have non-negligible scores. This is partly due to a low confinement of the plasma properties from Na emissions, but also due the highly excited Na II emissions that, although due to non-equilibrium effects, can be described by high temperature template spectra.*

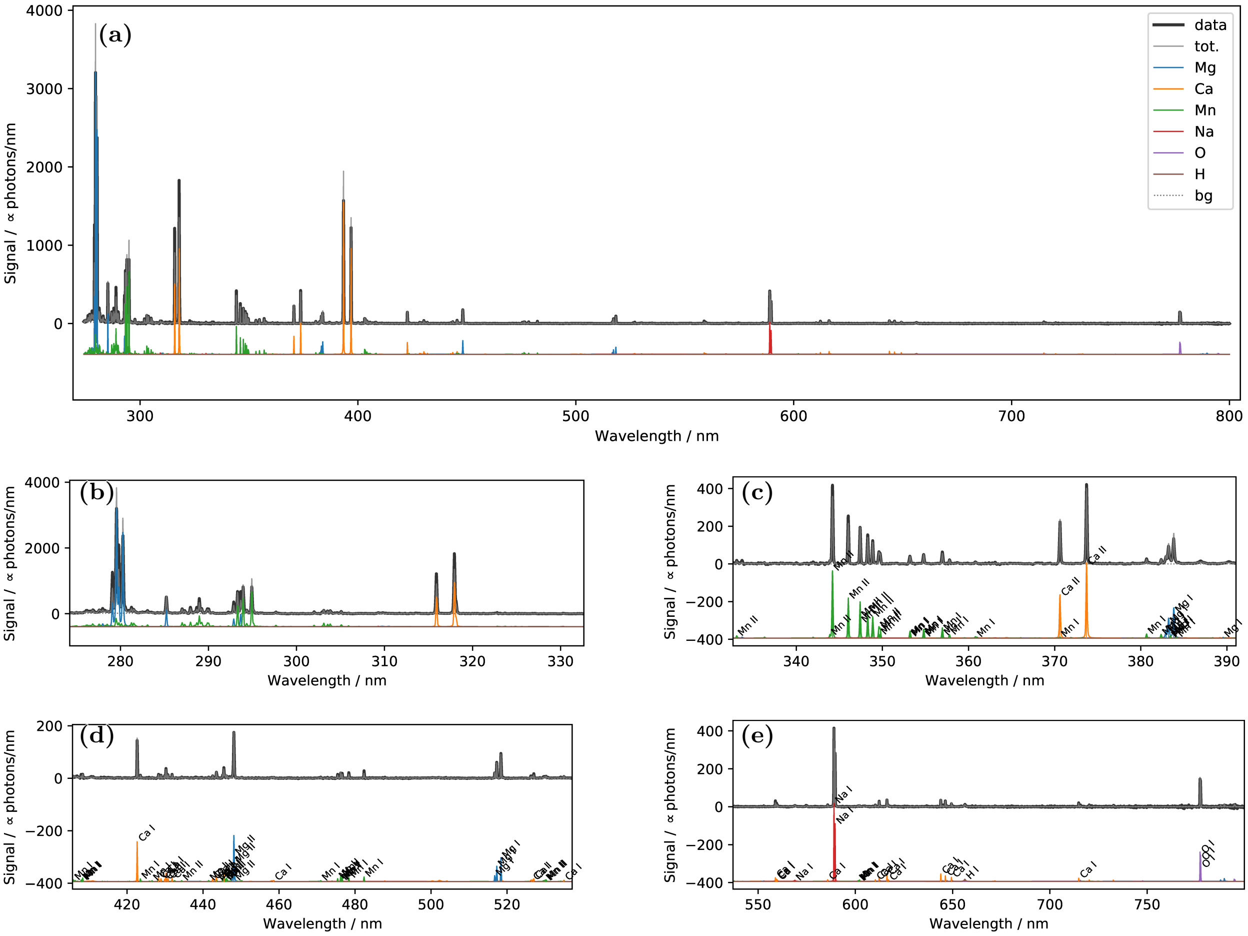

Figure 5.4.12: *Results from applying the unmixing to the time-resolved spectrum of the carbonate mixture measured at a delay time of* 750 ns *in experimentally simulated Martian atmospheric conditions.* ***(a)*** *The input spectrum shown together with the pure spectra with significant intensities. The pure spectra are shown with a negative y-offset.* ***(b-e)*** *Close-ups of (a) with the line labelling hidden. It can be seen that the predicted significant pure spectra resembles the input spectrum well.*

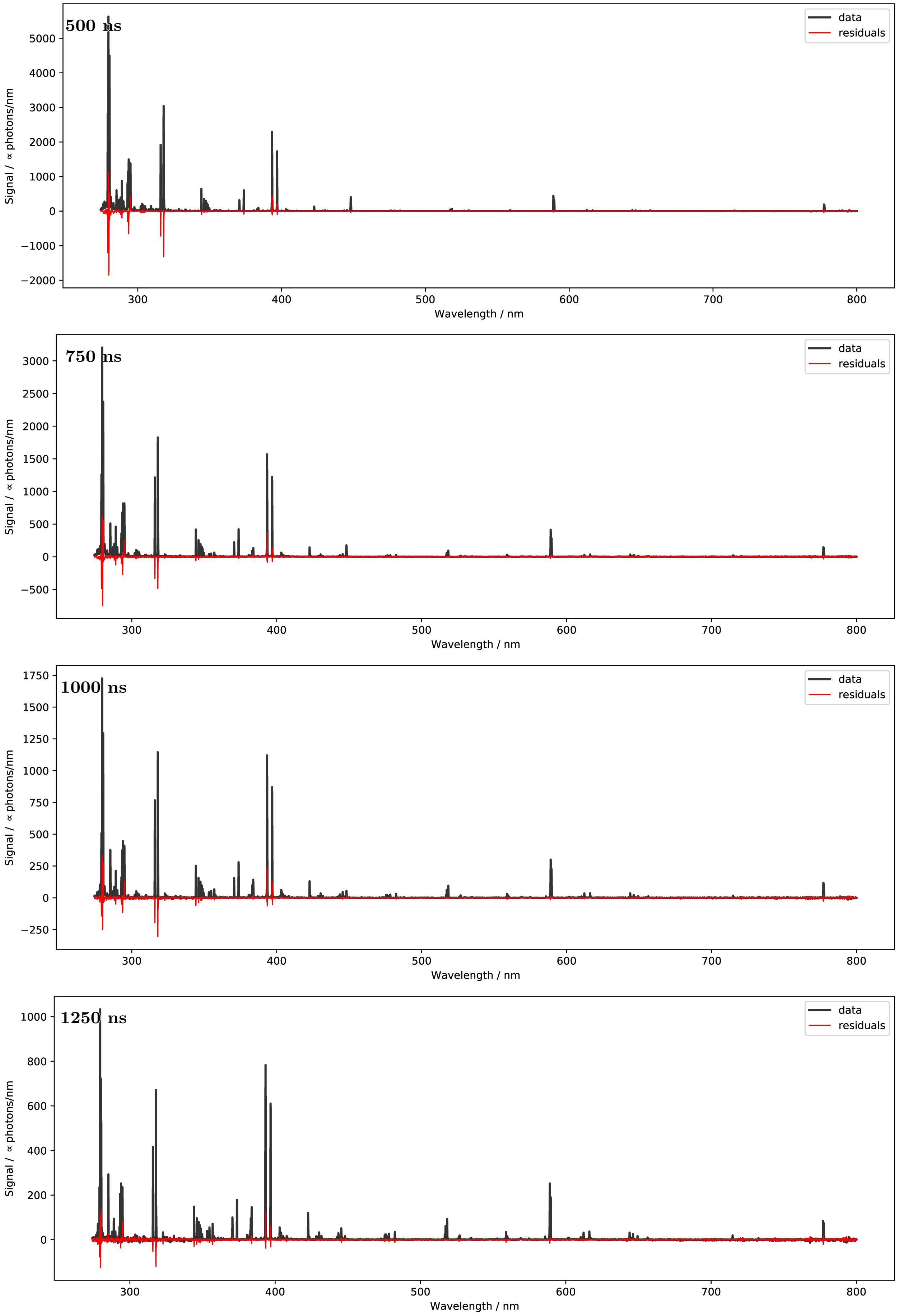

Figure 5.4.13: *Residuals between the spectrum as predicted by the unmixing and the time-resolved spectra of the Carbonate sample. The delay times are annotated in the figure. The residuals can be seen to be largest for the strongest signals, i.e. the Mg II lines around* 280 nm *and the Ca II doublet lines around* 317 nm *and* 393 nm*.*

In Figure 5.4.14, the pure components with the 30 highest scores are shown for the four considered delay times. Generally the scores are dominated by the elements contained in the sample. However other elements, not contained in the sample, are seen to be predicted with a non-zero score. For example, the score of Ir at a delay time of 1000 ns is seen to be relatively high. This is an example of overfitting. Although the predicted Ir signals in the individual pixels are not significant in terms of SNR, the signals of all the pixels add up resulting in an Ir score similar to that of O whose triplet at 777 nm contain pixels with signals of high SNRs.

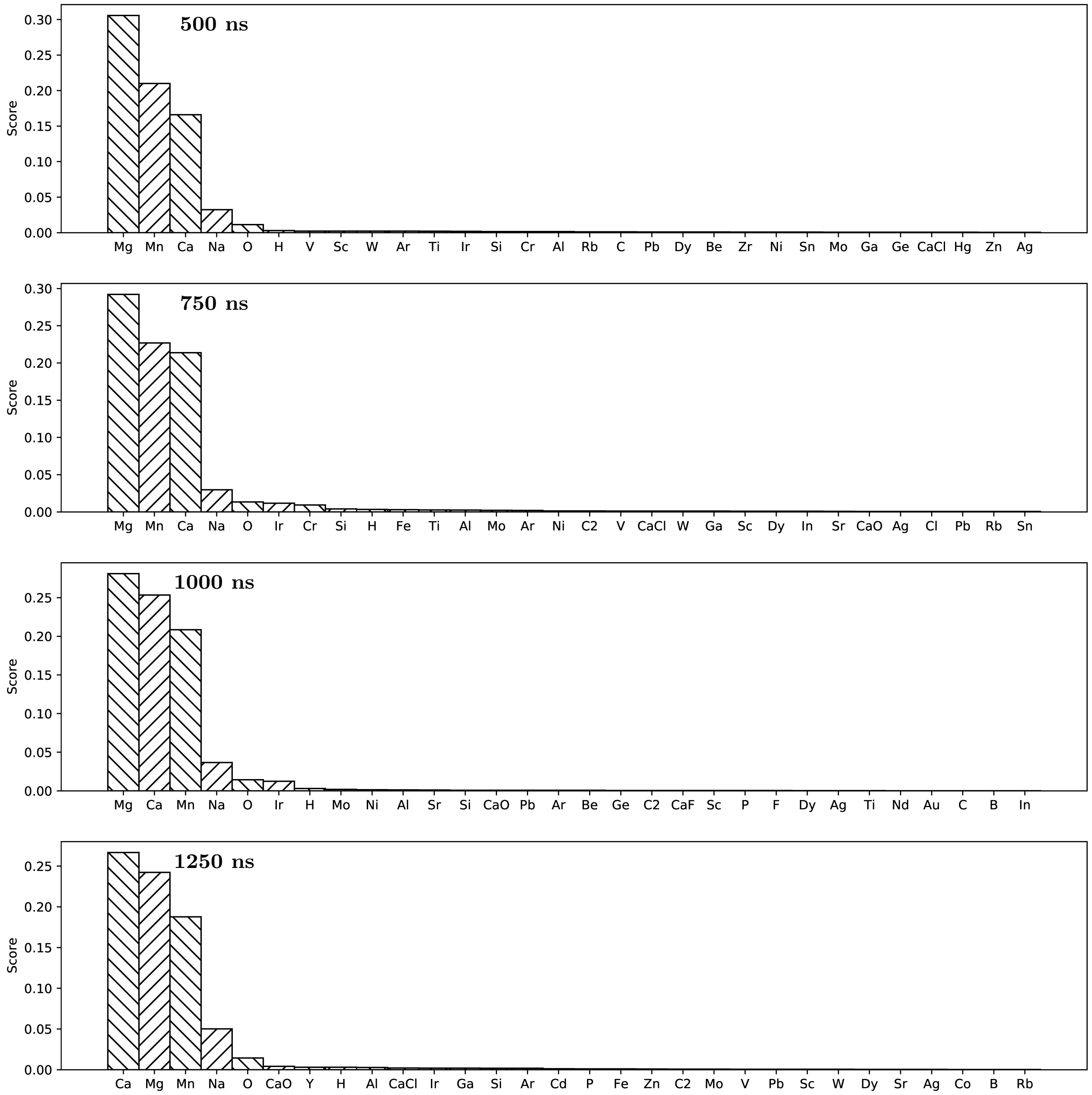

Figure 5.4.14: *Scores for the 30 most significant elements or molecules from applications to the time-resolved measurements of the carbonate mixture in experimentally simulated Martian atmospheric conditions. The scores are seen to be dominated by the elements present in the sample (Ca, Mg, Mn, Na, O, and C) but species not present in the sample are also seen to have non-zero scores. An example of that is the Ir score at* 750 ns.

In Figure 5.4.15 the scores of the plasma properties of the atomic emissions for the four different delay times are shown. The scores for the temperatures can be seen to shift towards lower values with increasing delay time. Furthermore, the values are centred around the values of the inner zones obtained from fits of the two-zone plasma model (see Figure 4.4.17 in Chapter 4). The trend of the electron densities scores with delay time is less clear and the values appear a little higher than those obtained from the two-zone fits. The scores of the atomic concentrations are seen to be approximately similar for all the delay times.

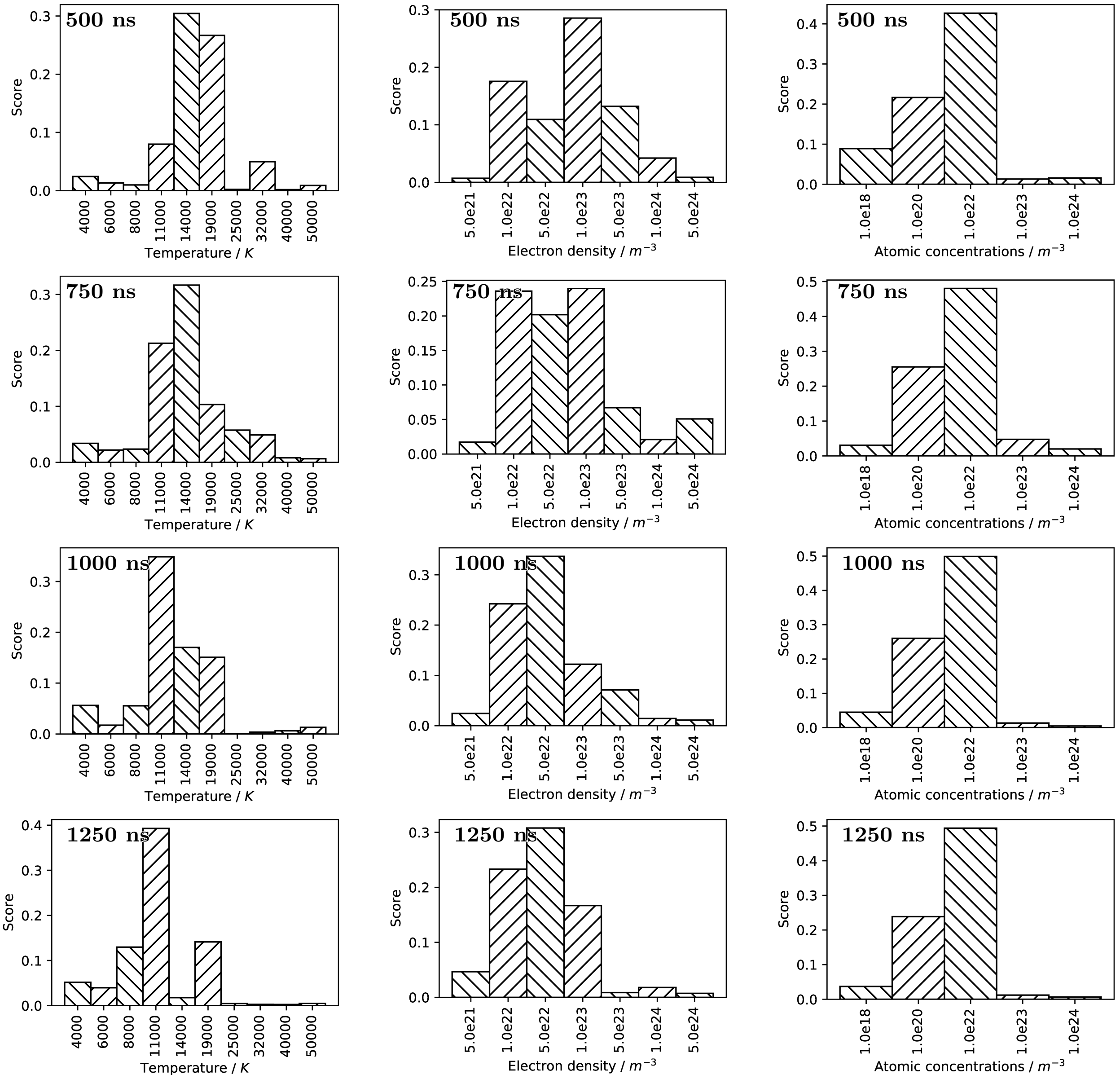

Figure 5.4.15: *Scores for the plasma properties of the atomic emissions from applications to the time-resolved measurements of the carbonate mixture. left to right: the scores of the temperatures, electron density and atomic concentrations. top to bottom: increasing delay time. The scores for the temperatures are seen to shift towards lower temperatures with increasing delay time. The same is true for the electron density although the trend is weaker. No trend is seen in the atomic concentrations where the distributions of the scores remain almost constant with increasing delay time.*

The results from applying the method of multi-element Saha-Boltzmann plot to the spectrum at 500 ns delay time are shown in Figure 5.4.16. Again, using line intensities with a predicted SNR of at least 10 and that are at least 50 % isolated. The results are distorted by the non-equilibrium Na II lines shown in Figure 5.4.10d. Excluding these from the analysis, the results are much improved. Together with the results from the other delay times, these results are shown in Figure 5.4.17 where the resulting Saha-Boltzmann plots can be seen after optimizing the effective path. The derived temperatures are noted in the legends and can be seen to decrease with increasing delay time. In Figure 5.4.18, the resulting concentration estimates can be seen. The relative deviations of the relative concentrations are within ±42 % for all the considered delay times.

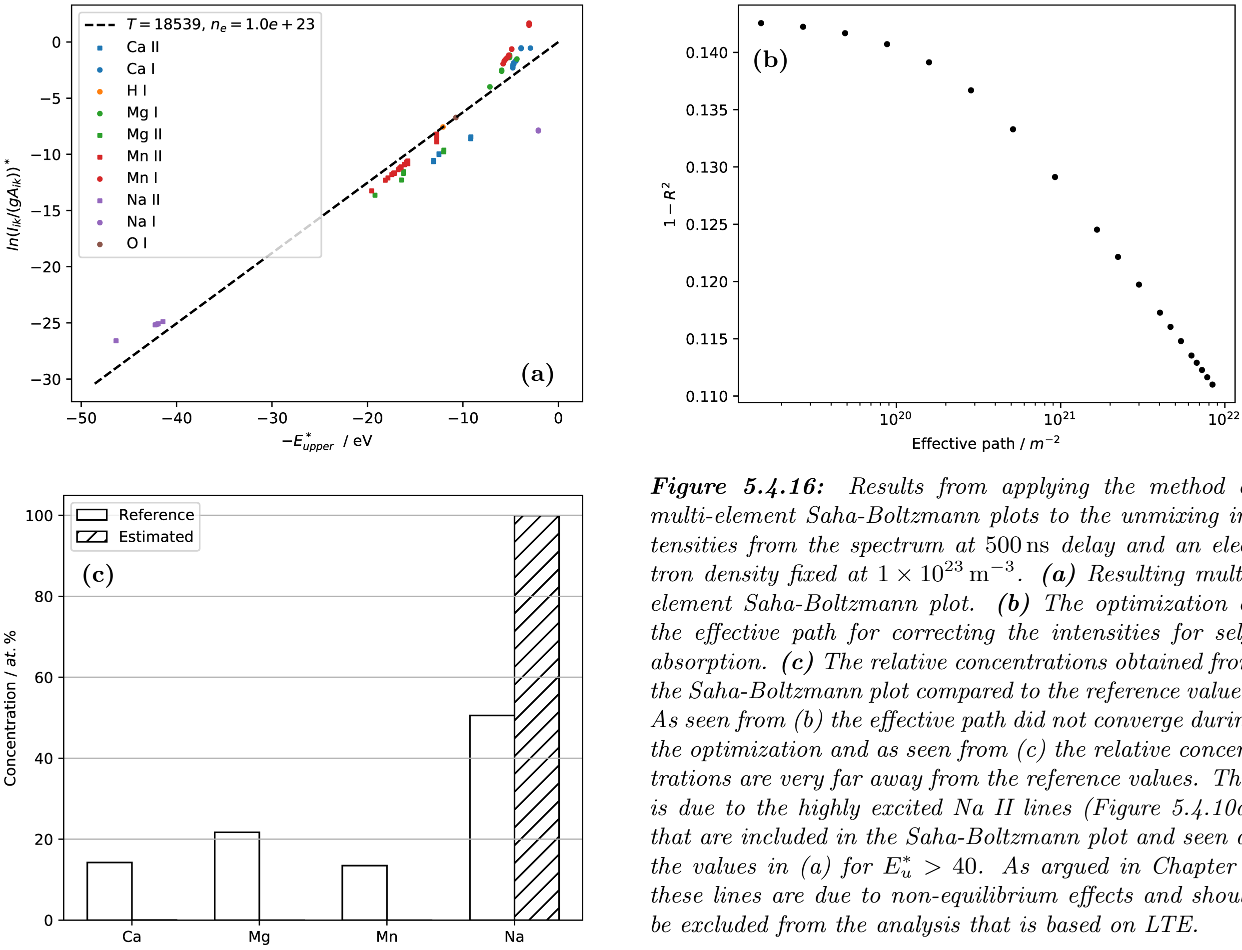

Figure 5.4.16: *Results from applying the method of multi-element Saha-Boltzmann plots to the unmixing intensities from the spectrum at* 500 ns *delay and an electron density fixed at* $1 \times 10^{23}\,\mathrm{m}^{-3}$*.* ***(a)*** *Resulting multi-element Saha-Boltzmann plot.* ***(b)*** *The optimization of the effective path for correcting the intensities for self-absorption.* ***(c)*** *The relative concentrations obtained from the Saha-Boltzmann plot compared to the reference values. As seen from (b) the effective path did not converge during the optimization and as seen from (c) the relative concentrations are very far away from the reference values. This is due to the highly excited Na II lines (Figure 5.4.10d) that are included in the Saha-Boltzmann plot and seen as the values in (a) for* $E^*_u > 40$*. As argued in Chapter 4 these lines are due to non-equilibrium effects and should be excluded from the analysis that is based on LTE.*

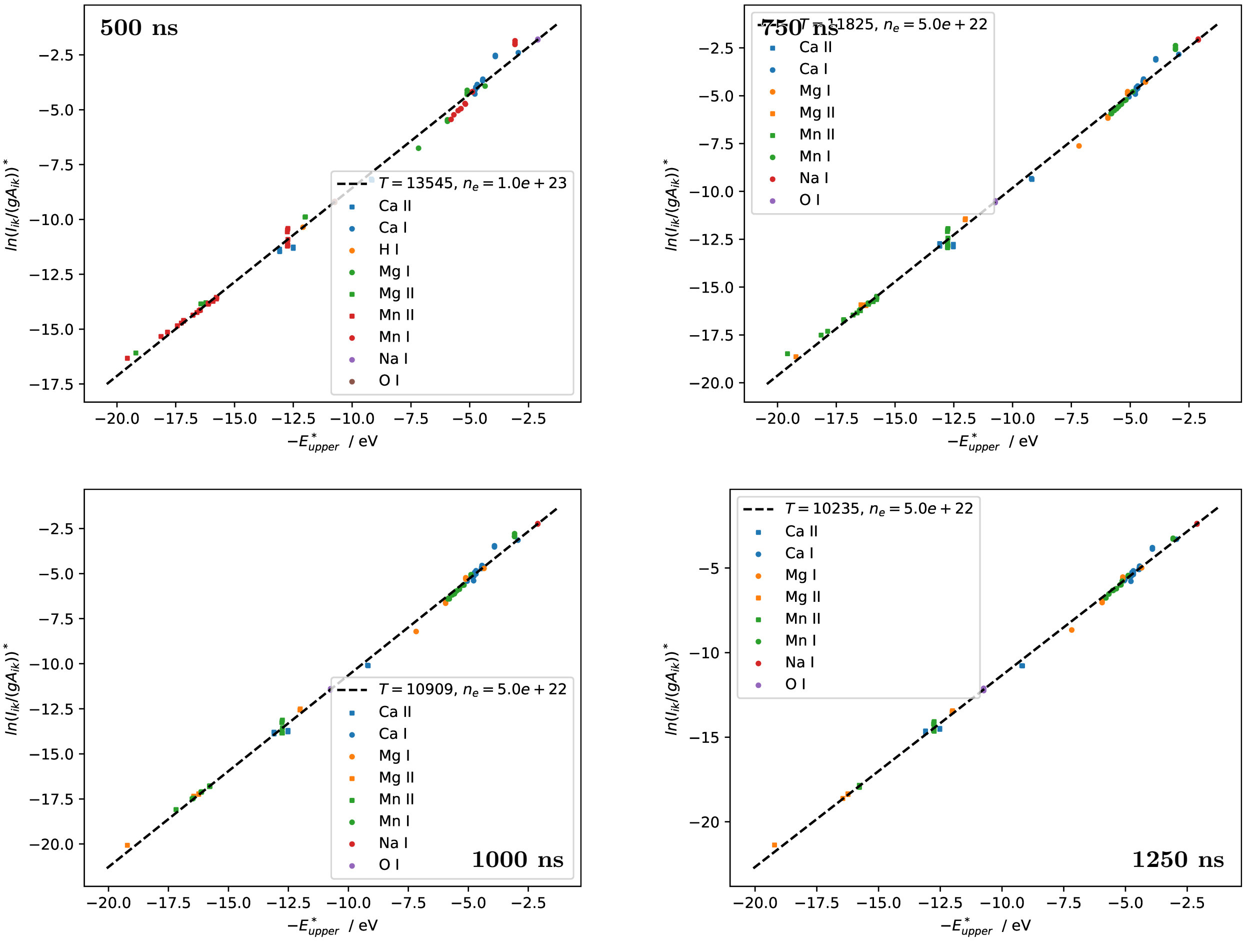

Figure 5.4.17: *Results from applying the method of multi-element Saha-Boltzmann plots to the unmixing intensities of the time-resolved spectra of the carbonate mixture. The delay time is noted in the figures. For the delay time of* 500 ns *a filter was applied to exclude the non-equilibrium Na II. Otherwise, all emission lines with a SNR greater than 10 and with interferences below* 50 % *were included. Corrections for self-absorption have been applied and the electron densities were fixed corresponding approximately to its scores (see Figure 5.4.15). The used electron densities and the derived temperatures are noted in the legends. The temperature can be seen to decrease with increasing delay time. The resulting relative concentration estimates are shown in Figure 5.4.18.*

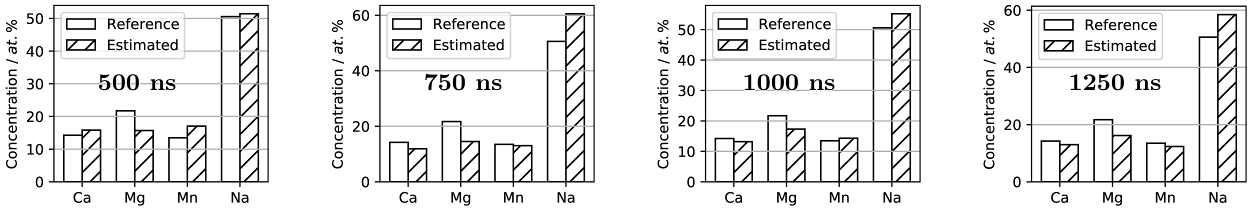

Figure 5.4.18: *The resulting concentration estimates from applying the method of multi-element Saha-Boltzmann plots to the unmixing intensities of the time-resolved spectra of the carbonate mixture (see Figure 5.4.17). The delay times are noted in the figures. The deviations of the relative concentrations are within* 33 % *for all the considered delay times and all the considered elements.*

5.4.4 Time-resolved Measurement of Martian Regolith Simulant

To test the unmixing on a geological sample, it has been applied to the time-resolved spectrum of a Martian regolith simulant (JSC [95]). The spectrum was measured with a delay time of 500 ns and an exposure time of 100 ns in experimentally simulated Martian atmospheric conditions. The spectra of the significant pure components are shown in Figure 5.4.19. From the figure it can be seen that the sum of the pure components (labelled "tot." in legend) adds up to the input spectrum without any visually significant discrepancies. This is also confirmed by the low residuals between the spectrum as described by the unmixing and the input spectrum that can be seen in Figure 5.4.20. The scores of the pure components and the plasma properties are shown in Figure 5.4.21. From Figure 5.4.21a it can be seen that the scores of the pure components are dominated by the pure components of significant signal (see legend in Figure 5.4.19). However, the element V is found to have a relatively large score even though its signal is not significant in terms of the SNR of the individual bins/pixels in the spectrum. The pure spectrum of V can be seen in Figure 5.4.22. For comparison, it is shown together with the pure spectrum of O whose triplet around 777 nm is clearly visible and with a high SNR. From the figure it can be seen that the spectrum of V is not predicted to have any significant signals, but as V contains many emission lines the sum of the signal adds up and results in the relatively high score. From the scores of the plasma properties (Figure 5.4.21b,c) it can be seen that the most significant temperatures are 11 000 K, 14 000 K, and 19 000 K. The most significant electron densities are 1×10^{22} , $1 \times 10^{23}\,\mathrm{m}^{-3}$, and $5 \times 10^{23}\,\mathrm{m}^{-3}$ which span one and a half order of magnitude.

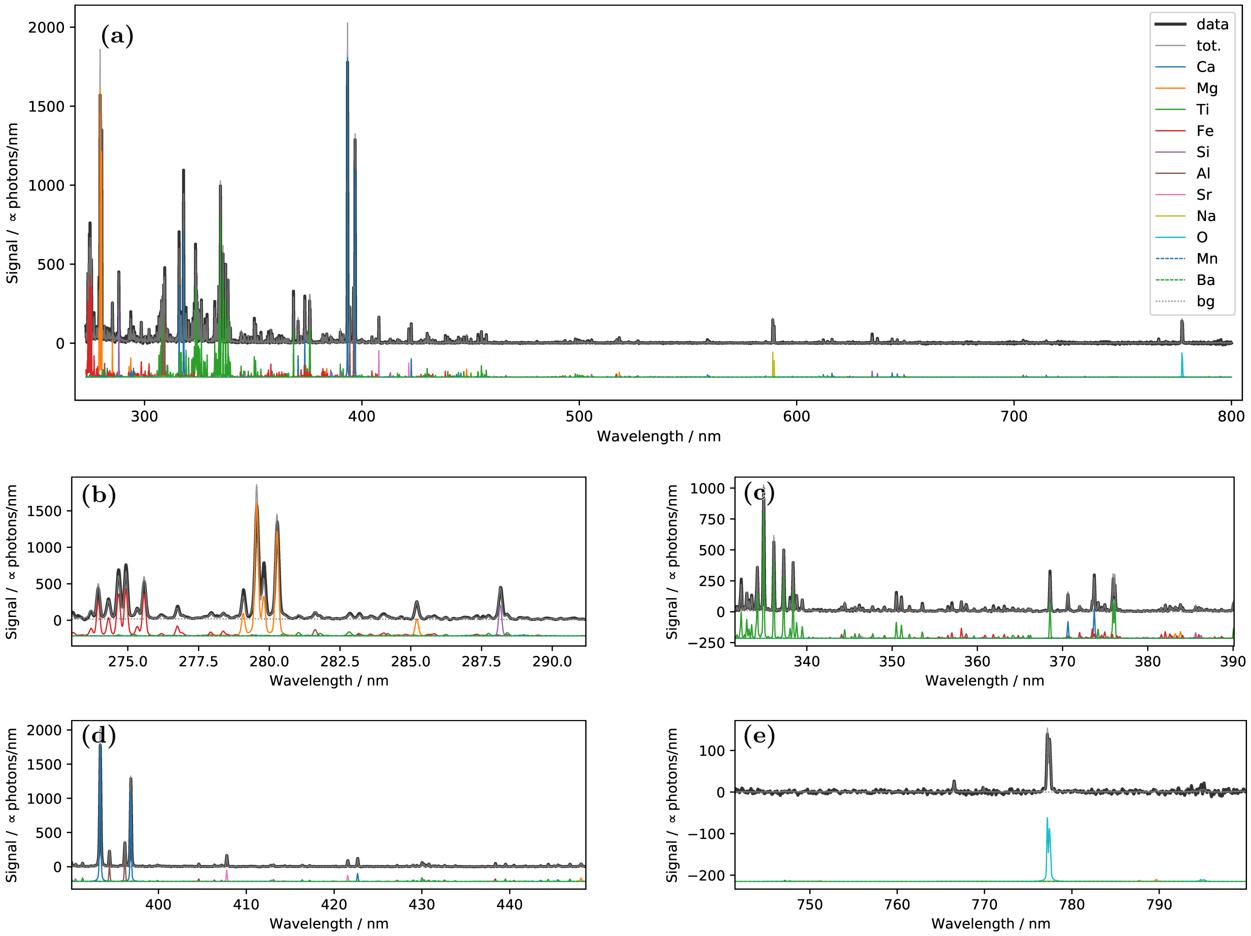

__Figure 5.4.19:__ Results from applying the unmixing to the time-resolved spectrum of a JSC sample measured at a delay time of 500 ns*, an integration time of* 100 ns*, and in experimentally simulated Martian atmospheric conditions. __(a)__ The input spectrum shown together with the significant pure spectra. The pure spectra are shown with a negative y-offset. __(b)-(e)__ Close-ups of (a) with the line labelling hidden. From the figures it can be seen that the predicted pure spectra describe the input spectrum well without any significant discrepancies.*

Results from the multi-element Saha-Boltzmann analysis are shown in Figure 5.4.23. The analysis were

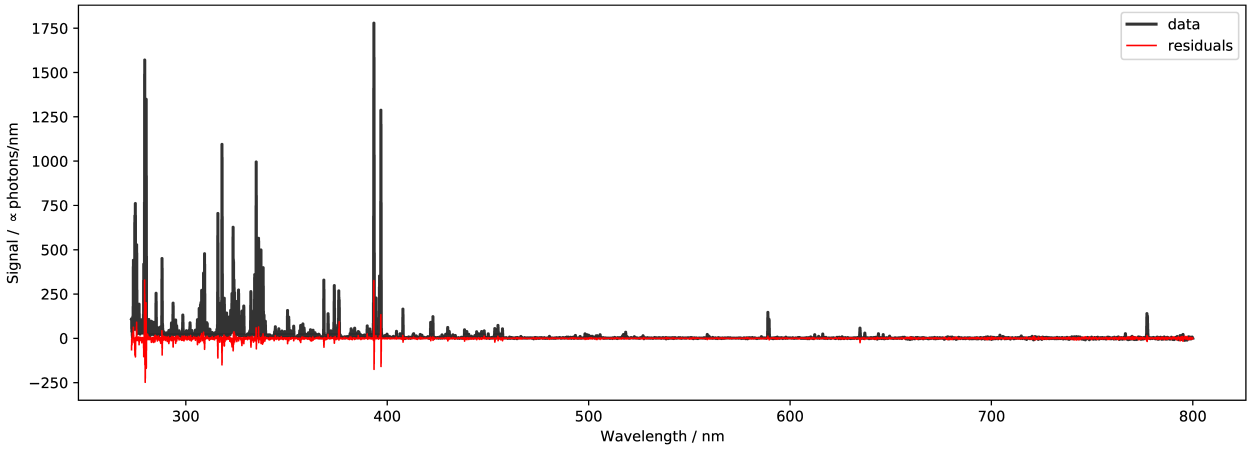

Figure 5.4.20: *Residuals between the spectrum as predicted by the unmixing and the time-resolved spectrum of a JSC sample measured at a delay time of* 500 ns*. The residuals can be seen to be relatively small.*

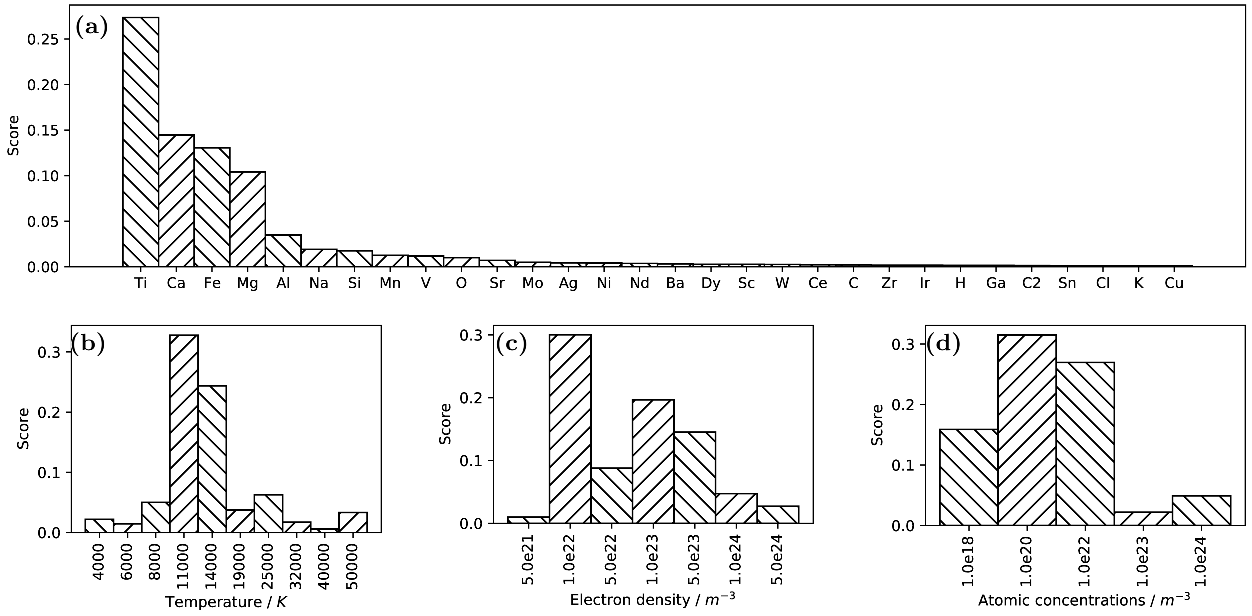

Figure 5.4.21: *More results from applying the unmixing to the time-resolved spectrum of JSC.* ***(a)*** *Scores of the 30 pure components with the highest scores.* ***(b)-(d)*** *Scores of the plasma properties. From (a) it can be seen that the significant pure spectra (see legend of Figure 5.4.19) dominate the scores. However, vanadium (V), which is not significant, has a relatively high score. This is due to the many emission lines of V that even though weak sums up to give a relatively high score (see Figure 5.4.22). From the scores of the plasma properties it can be seen that the most significant temperatures are* 11 000 K*,* 14 000 K*, and* 19 000 K *and that the most significant electron densities are* $1 \times 10^{22}\,\mathrm{m}^{-3}$*,* $1 \times 10^{23}\,\mathrm{m}^{-3}$*, and* $5 \times 10^{23}\,\mathrm{m}^{-3}$.

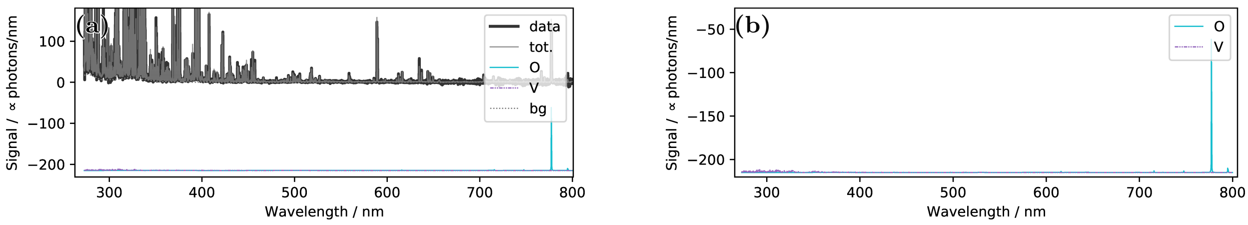

Figure 5.4.22: ***(a)*** *The pure spectrum of V compared to that of O as predicted by applying the unmixing to the time-resolved spectrum of JSC. The pure spectra are shown together with input data the estimated background and the total spectrum from the unmixing ("bg" and "tot." in legend, respectively).* ***(b)*** *Close-up of (a). V has a higher score of Oxygen meaning that the total intensity predicted of V is higher than that of O. However, the height of signal of the V emissions are all around the noise level and are likely to be describing part of the continuum emissions and random fluctuations due to noise and not actual V signatures from V being present in the sample.*

done using a fixed electron density of $1 \times 10^{23}\,\mathrm{m}^{-3}$ using all of the automatically selected emission lines. From the Saha-Boltzmann plot (Figure 5.4.23a) no obvious outliers can be seen and the derived temperature is 12 366 K which is in reasonable agreement with the scores of the temperatures (Figure 5.4.21b). The derived relative concentrations of the elements Al, Ca, Fe, Mg, Mn, Na, Si, and Ti are all within 34 % relative errors from the reference values [95].

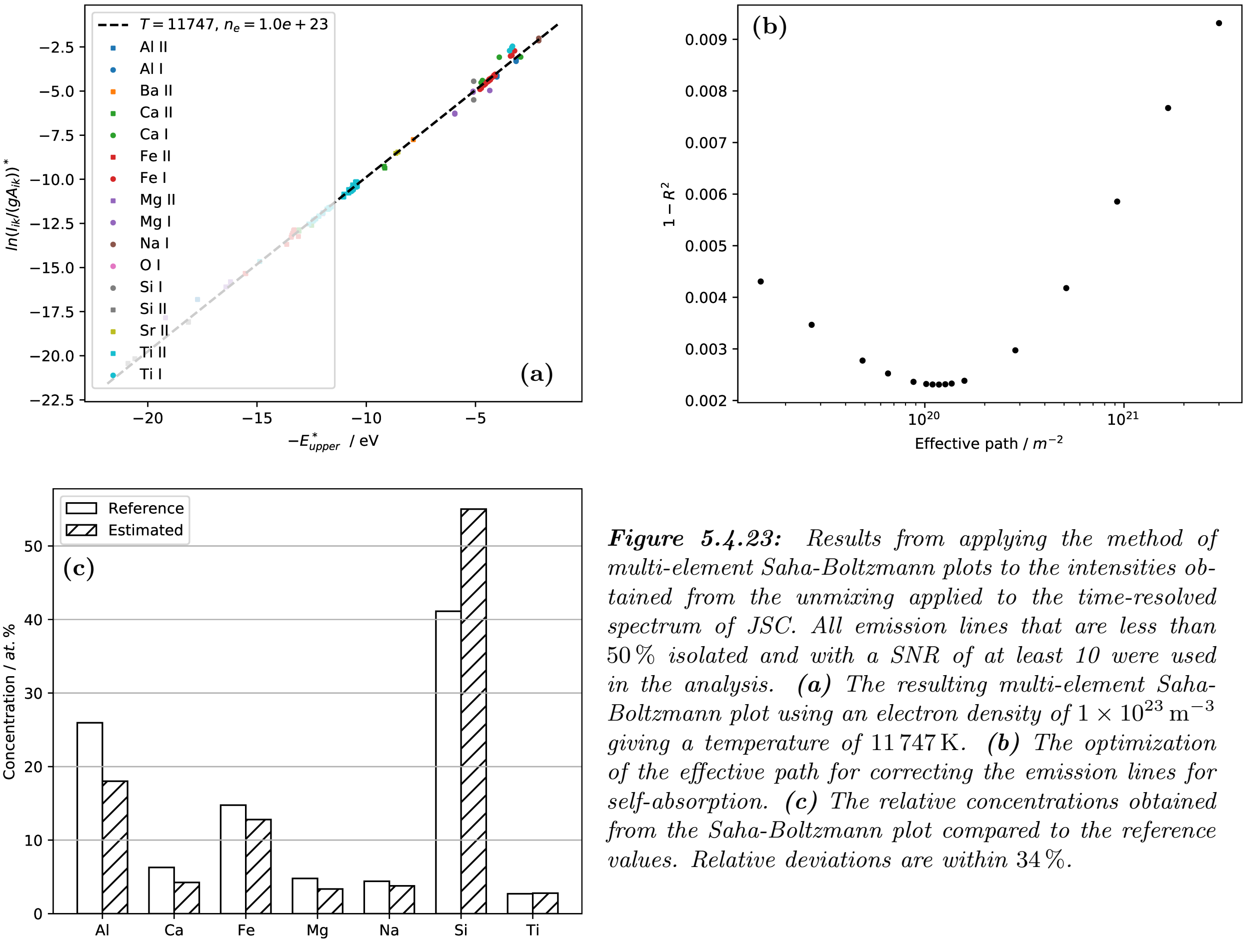

Figure 5.4.23: *Results from applying the method of multi-element Saha-Boltzmann plots to the intensities obtained from the unmixing applied to the time-resolved spectrum of JSC. All emission lines that are less than 50 % isolated and with a SNR of at least 10 were used in the analysis.* ***(a)*** *The resulting multi-element Saha-Boltzmann plot using an electron density of* $1 \times 10^{23}\,\mathrm{m}^{-3}$ *giving a temperature of 11 747 K.* ***(b)*** *The optimization of the effective path for correcting the emission lines for self-absorption.* ***(c)*** *The relative concentrations obtained from the Saha-Boltzmann plot compared to the reference values. Relative deviations are within 34 %.*

5.4.5 Time-integrated Measurement of Martian Regolith Simulant

The unmixing has also been applied to the Martian regolith simulant (JSC) measured with a zero delay time and an exposure time much greater than the lifetime of the plasma. That is a time-integrated measurement. The measurement was performed in experimentally simulated Martian atmospheric conditions. The spectra of the pure components with significant intensities are shown in Figure 5.4.24 and in Figure 5.4.25 in the full spectral range and as close-ups in different wavelength ranges, respectively. From Figure 5.4.25 it can be seen that the unmixing generally describes the input spectrum well with only a few and smaller discrepancies as exemplified in Figure 5.4.25f. Here, the resulting peak of multiple highly excited oxygen lines are seen to be overestimated. In Figure 5.4.26, the residuals between the unmixing spectrum and the input data can be seen.

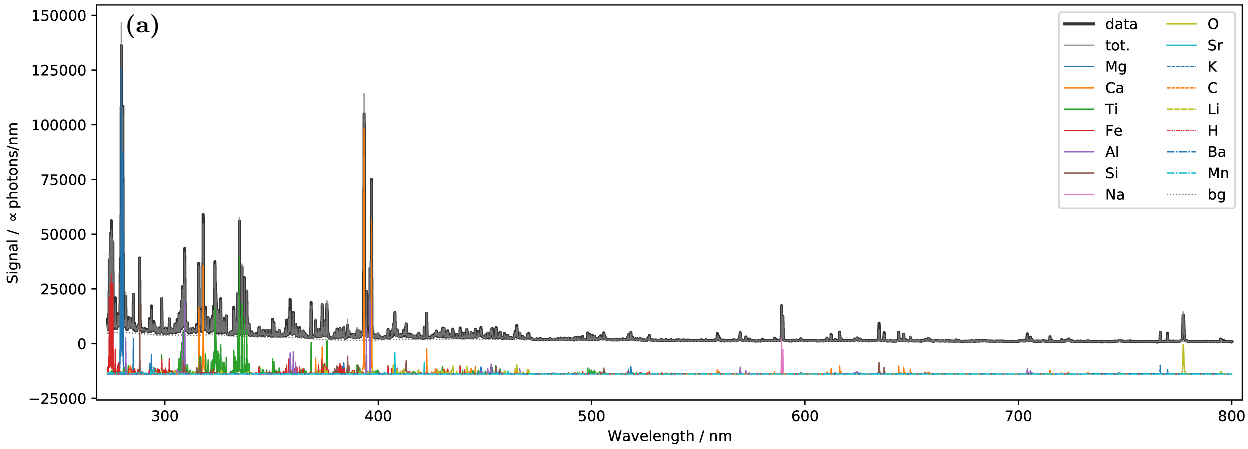

Figure 5.4.24: *Pure components obtained by applying the unmixing to the time-integrated spectrum of JSC measured in experimentally simulated Martian atmospheric conditions.* ***(a)*** *Pure components of significant intensity without line labelling.* ***(b)*** *With line labelling.*

The scores of the pure components are shown in Figure 5.4.27. From the scores of the pure components it can be seen that some components of non-significant elements (components not in the legend of Figure 5.4.24) have relatively high scores. Again, an example of that is V whose score is higher than that of Mn, Li and K that all have significant pure spectra. As for the previous example (JSC time-resolved spectrum), V is most likely describing part of the background spectrum and or random fluctuations of the noise in the input spectrum. To investigate the total effect from such components, the total spectrum of pure components with significant spectra has been plotted versus the non-significant pure components and also the background spectrum. This is shown in Figure 5.4.28. From the figure it can be seen that the spectrum from the non significant components lacks many of the clear and narrow peaks, as seen from the spectrum of the significant pure components. It is thereby more similar to the derived background spectrum. In Figure 5.4.29 the scores of the plasma properties are shown. Compared to the results from applications to time-resolved spectra (Figure 5.4.15 or 5.4.21b,c,d) the distributions of the scores appear broader and spans almost all the possible values. This is in agreement with the spectrum being time-resolved and therefore going through many different temperatures and densities as the plasma decays.

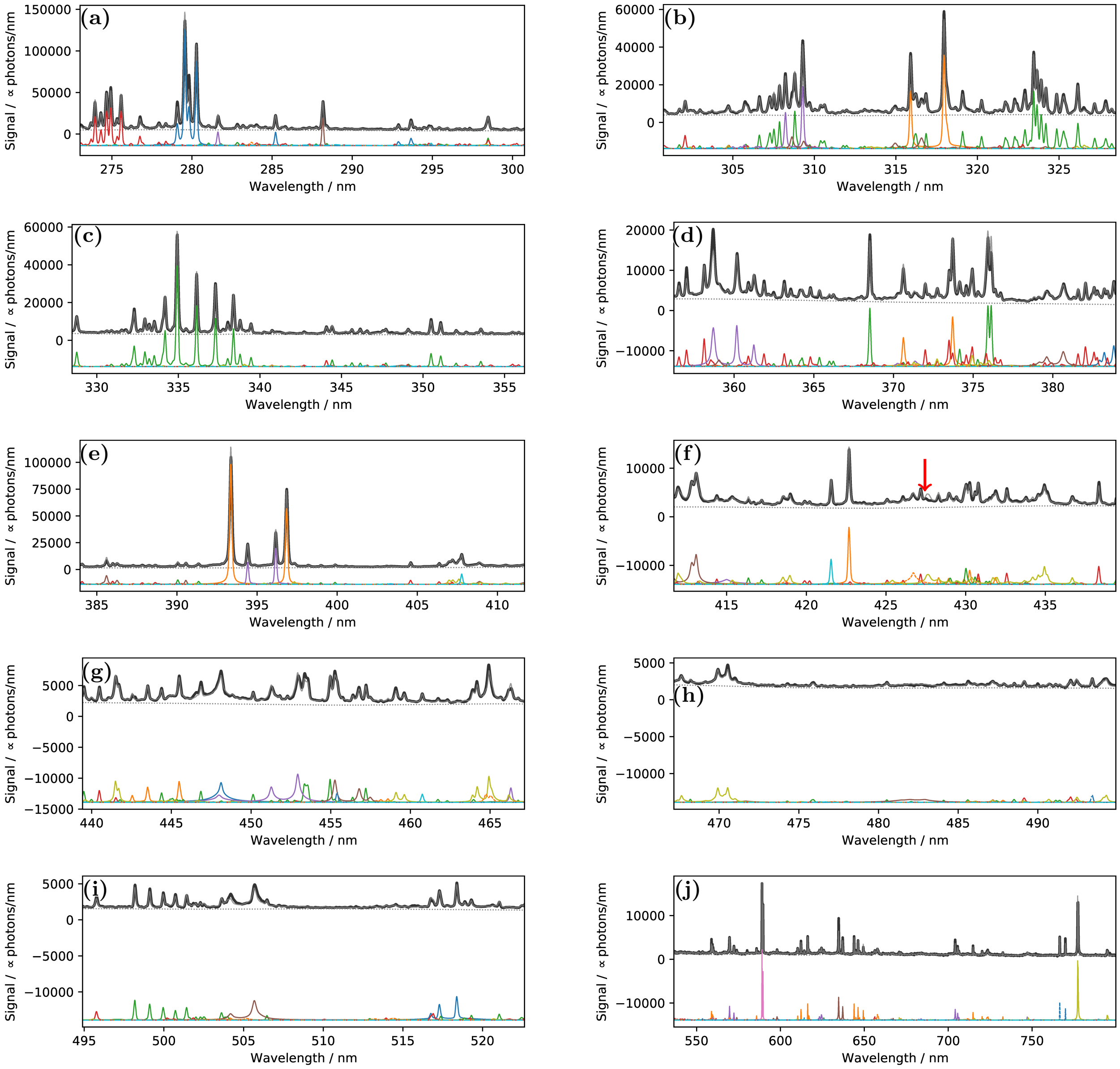

Figure 5.4.25: *Different close ups of Figure 5.4.24b (pure components of significant intensities from applications to time-integrated spectrum of JSC). The unmxing can be seen to generally describes the input spectrum well with only a few and smaller discrepancies such as the peak at ∼427 nm pointed out in (f). The peak results from multiple highly excited O II lines and is seen to be overestimated compared to the input spectrum/data.*

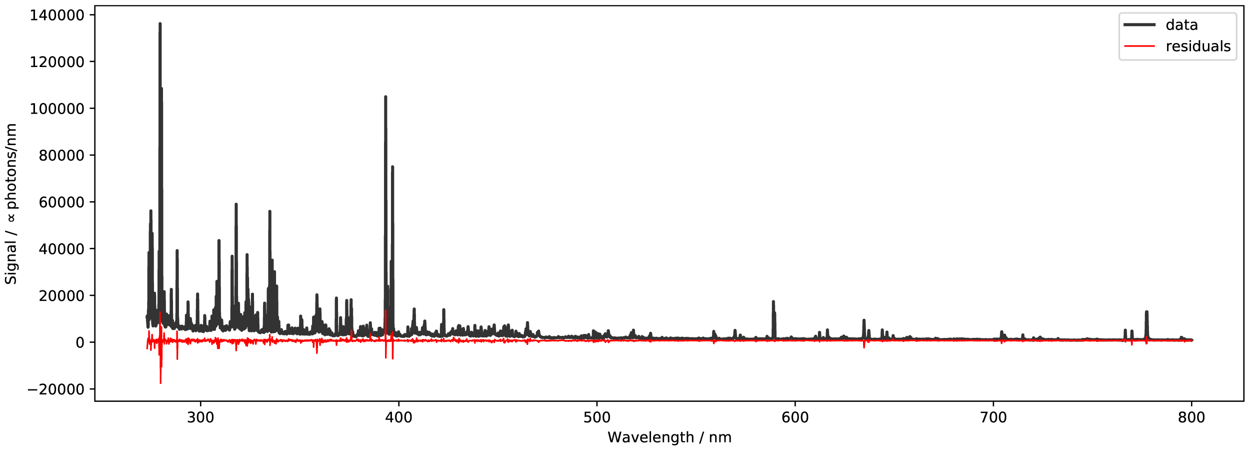

Figure 5.4.26: *Residuals between the spectrum as predicted by the unmixing and the time-integrated spectrum of a JSC sample. The residuals can be seen to be relatively small.*

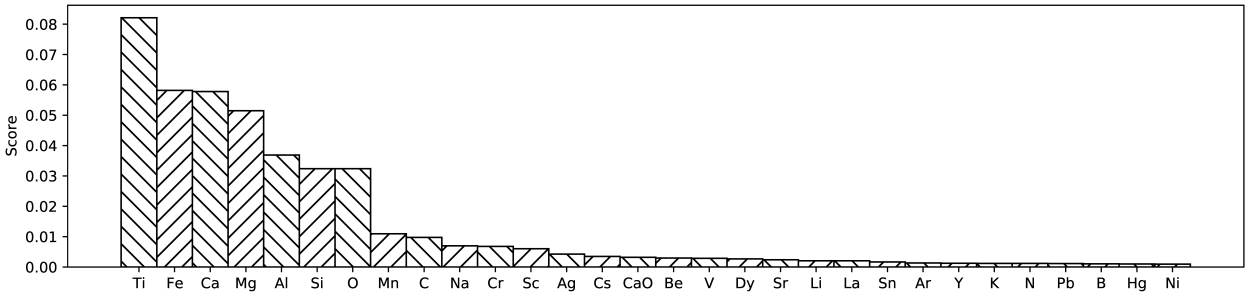

Figure 5.4.27: *Scores of the 30 pure components with the highest scores obtained by applying the unmixing to the time-integrated spectrum of a JSC sample. The scores can be seen to be dominated by the significant components (see legend in Figure 5.4.24), but some non-significant components, such as V, have relatively high scores. Such components are most likely describing part of the background spectrum and/or random fluctuations in the noise of the data.*

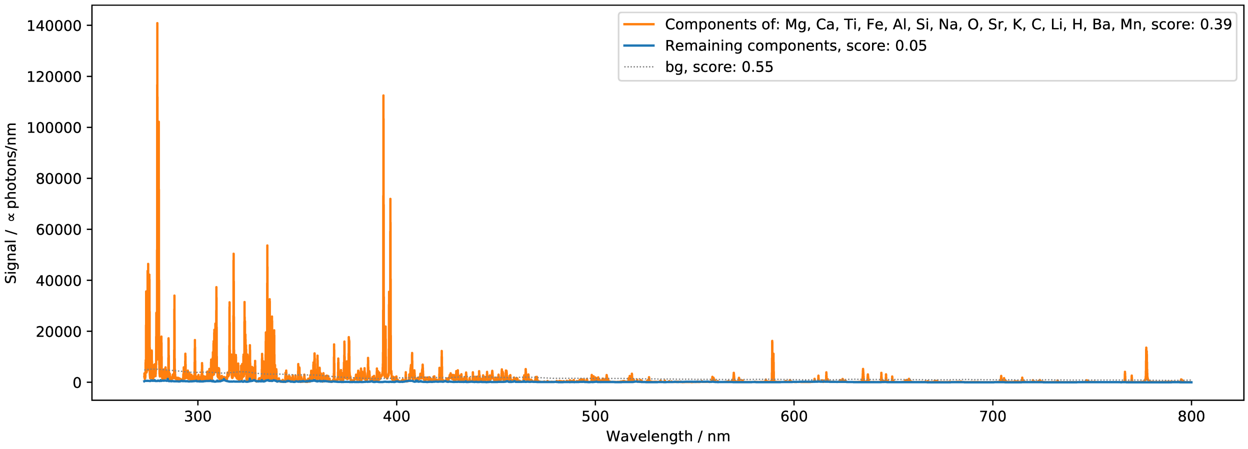

Figure 5.4.28: *The total spectrum from pure components of significant signal (orange curve) plotted versus the total spectrum of the remaining components (blue curve) and the background spectrum (grey dashed curve). The score of the remaining components adds up to 5 % of the total signal of the input spectrum (see legend), however shape of the signal is more similar to the derived background spectrum and the majority signal is therefore most likely describing part of the background/noise rather than actual emissions from elements in the sample.*

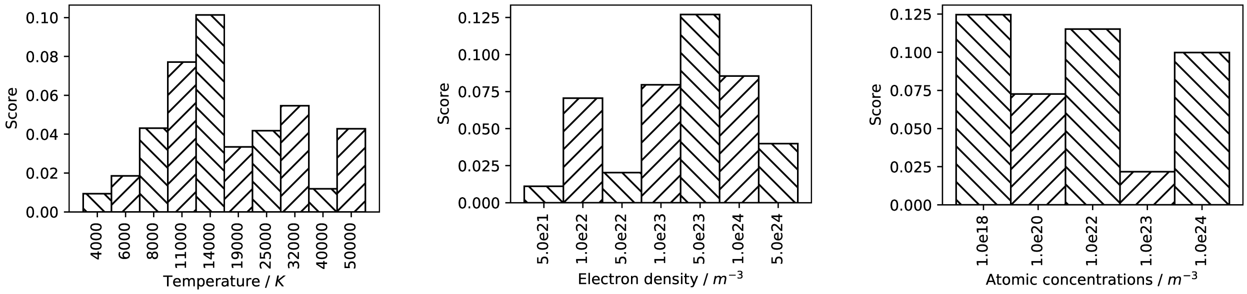

Figure 5.4.29: *Scores of the plasma properties obtained from applications to time-integrated spectrum of JSC. A large spread in the properties of significant scores can be seen. This is in agreement with the spectrum being time-integrated and therefore capturing the emissions from the early dense and hot stage and late cold and less dense.*

5.4.6 ChemCam data

For the application to ChemCam LIBS data, a separate unmixing database has been compiled. The procedure for this is exactly the same as for the setup of this thesis, but the values for the spectral range and for the simulation of the instrumental broadening differs. Furthermore, no extra broadening, for decreasing the influence of uncertainties in the wavelength calibration and Stark parameters, has been applied. This is because of the lower spectral resolution of the ChemCam LIBS instrument. According to the design of the ChemCam instrument, the unmixing database has been complied for the three spectral ranges: 244 nm to 340 nm, 383 nm to 467 nm, and 538 nm to 835 nm corresponding to the three spectrometers UV, VIO, and VISNIR of the ChemCam instrument [8]. For simulating the instrumental broadening, a Gaussian function with a FWHM fixed for each of the spectral ranges is used. The values of the FWHMs are obtained from the publication [8] and are

$$\begin{aligned}\textbf{UV} &: FWHM = 0.15\,\text{nm}\\ \textbf{VIO} &: FWHM = 0.20\,\text{nm}\\ \textbf{VISNIR} &: FWHM = 0.61\,\text{nm}\ .\end{aligned}$$

From an arbitrary spectrum downloaded from Martian solar day 15 [108], close-ups of some emission lines of Fe I and Ti II can be seen in Figure 5.4.30. From the figure it can be seen that the line profiles of the Ti II lines appear asymmetric. This is most likely due to a non Gaussian instrumental profile at the blue end of the UV spectral range. Elsewhere, the instrumental broadening profile seems fairly well described by a Gaussian as exemplified by the Gaussian fit to the Fe I line shown in Figure 5.4.30a. However, the FWHM of the instrumental broadening is likely to have a small wavelength dependence within each spectral range just as the spectrometer in the LIBS setup of this thesis.

The implementation of the unmixing for the ChemCam data works with data in the CSS = Clean Calibrated Spectra, level 1b pre-processing state [109]. This level includes dark spectrum subtraction, wavelength and intensity calibration, de-noising, and background subtraction. The algorithms for de-noising and background subtraction are based on the method of wavelet transformation as explained in [15]. As the spectra are de-noised, the weighting when solving the unmixing is also modified. Due to the de-noising, the combined effect from the zero'th level and photon noise in the input spectrum (see Chapter 3), should in principle be replaced by the uncertainty of the de-noising algorithm. However, a detailed understanding of this is outside the scope of this thesis and instead, obtained in a trial and error approach, a constant value throughout all wavelengths of 1/1000 of the maximum signal is used for the zero'th level noise, the photon noise is ignored, and the model uncertainty is kept as 20 %.

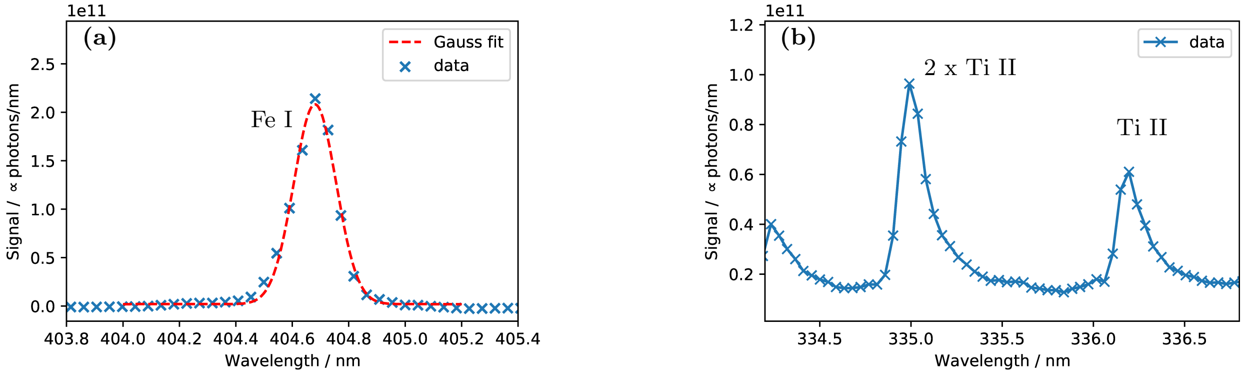

Figure 5.4.30: *Close-ups of the line-profiles of different emission lines in the spectrum of an arbitrary ChemCam target.* ***(a)*** *A Fe I emission line.* ***(b)*** *Two peaks from Ti II emission lines. From the figures it can be seen that the Fe I line is well described with a Gaussian profile. However, the Ti II lines appear asymmetric. This asymmetry is ascribed to the instrumental profile of the ChemCam instrument and is only observed in the blue end of the UV spectrometer. Elsewhere, the instrumental broadening appear to be fairly well described by a Gaussian profile.*

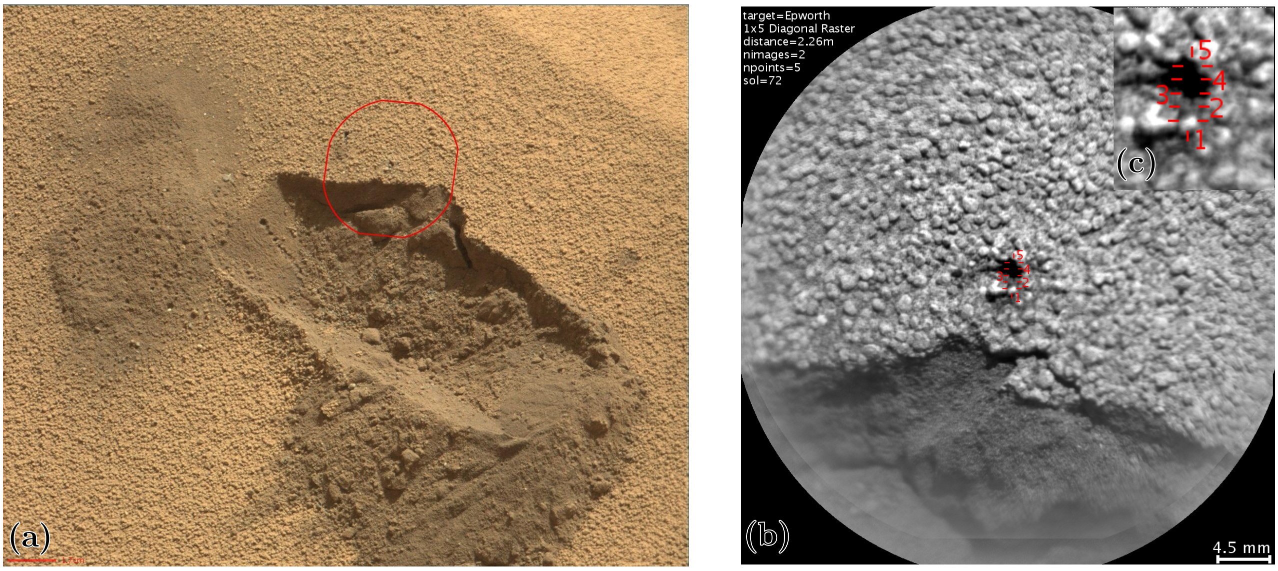

Figure 5.4.31: *Images from the Curiosity rover of the Epworth target.* ***(a)*** *Context image of the target area marked by the red circle.* ***(b)*** *RMI image of the target area also showing the five positions where LIBS measurements have been performed.* ***(c)*** *Close-up of (b) showing the LIBS spots. Data downloaded via the online tool Curiosity (MSL) Analyst's Notebook [108].*

For an example of applications to ChemCam data, a single spectum from the of Epworth soil target has been selected [110]. The spectrum was taken on the 72th Martian solar day after rover landing and downloaded via [111]. Context and close-ups of the target can be seen in Figure 5.4.31. More specifically, the spectrum at point 5 was selected for the application of the unmixing (see Figure 5.4.31c). The predicted significant pure spectra are shown in Figure 5.4.32 together with the input spectrum. From the figure it can be seen that the predicted pure components describe the input spectrum reasonably well. This can also be inferred from the residuals shown in Figure 5.4.33. The sum of the significant pure spectra are shown versus the sum of the remaining pure spectra in Figure 5.4.34a. From the figure it can be seen that the strongest signals of the remaining/non-significant pure spectra are in the UV range. These signals origin mainly from Hg, V, Nb, B, and Zr. This is highlighted in Figure 5.4.34b. The signal of B consists of the B I resonance doublet. The signal appear very broad and is therefore most likely due to over fitting. The remaining signals, are probably also examples of over fitting, but further investigations would be needed in order to be certain. Finally, close-up of the significant components together with the line identification can be seen in Figure 5.4.35, shown exemplary for the UV range.

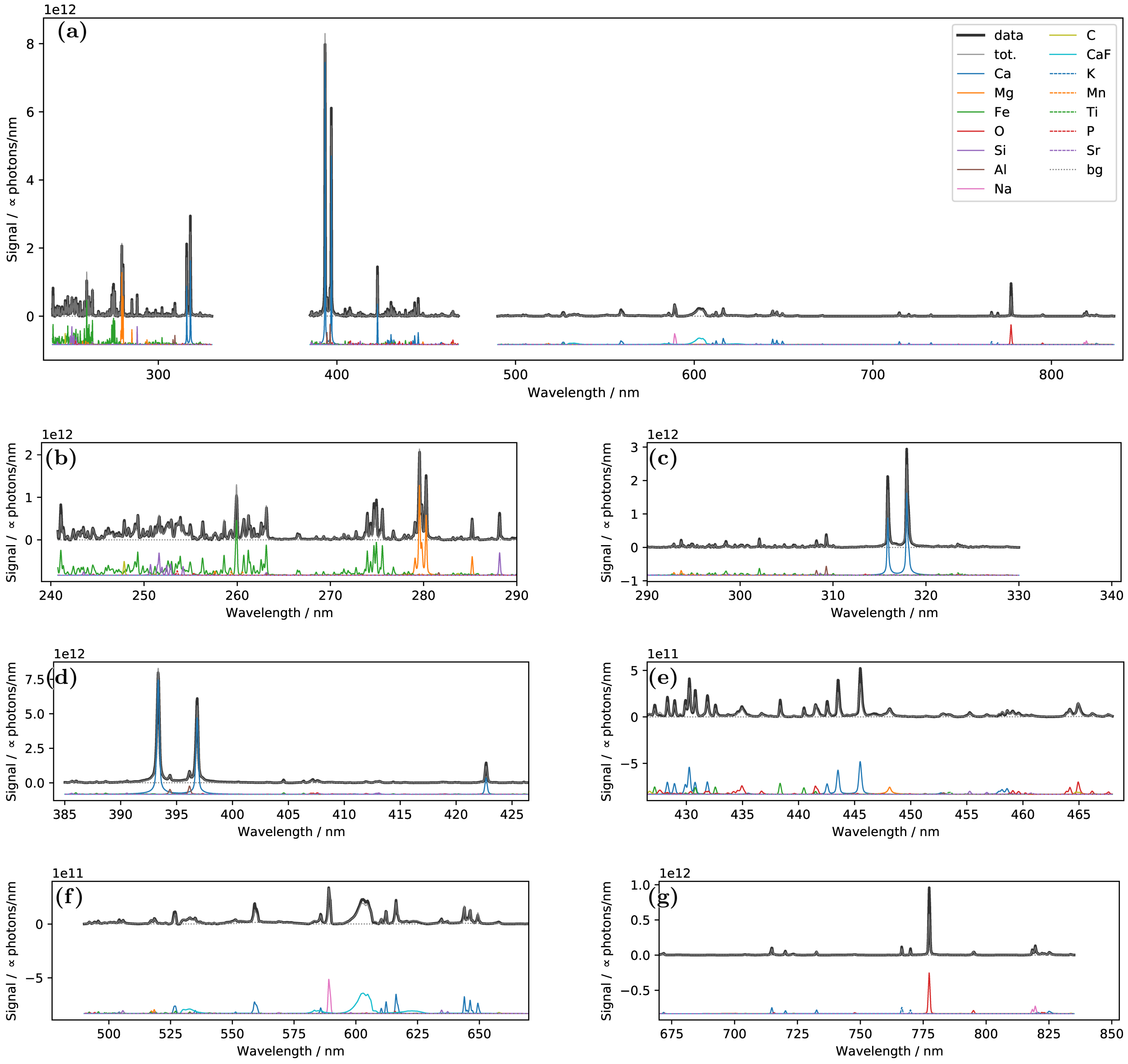

Figure 5.4.32: *Results from applying the unmixing to the ChemCam spectrum of Epworth position 5 (See Figure 5.4.31.* ***(a)*** *The predicted significant pure spectra shown in the full spectral range together with the input spectrum.* ***(b)-(g)*** *Close-ups of (a).*

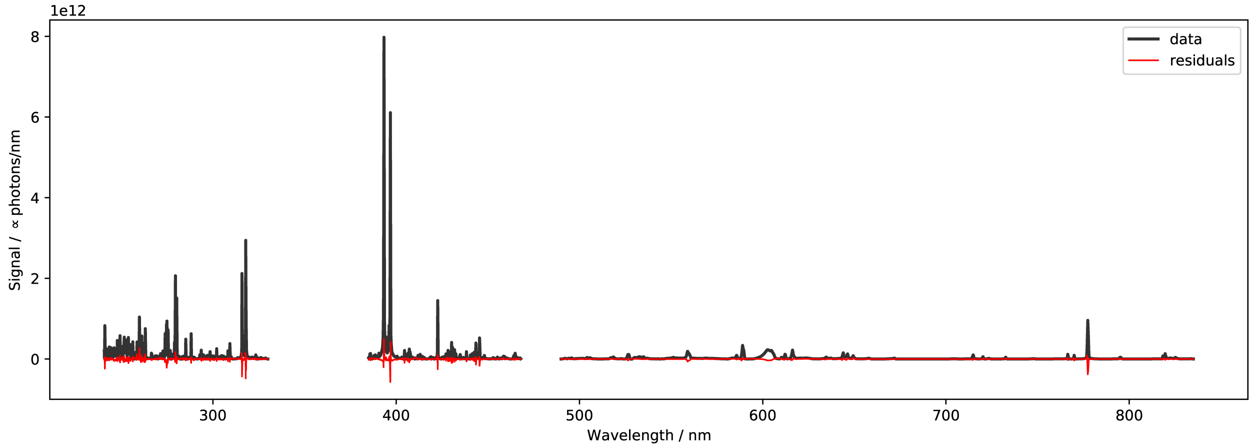

Figure 5.4.33: *Residuals between the spectrum as predicted by the unmixing and the ChemCam spectrum of Epworth position 5. The residuals can be seen to be relatively small.*

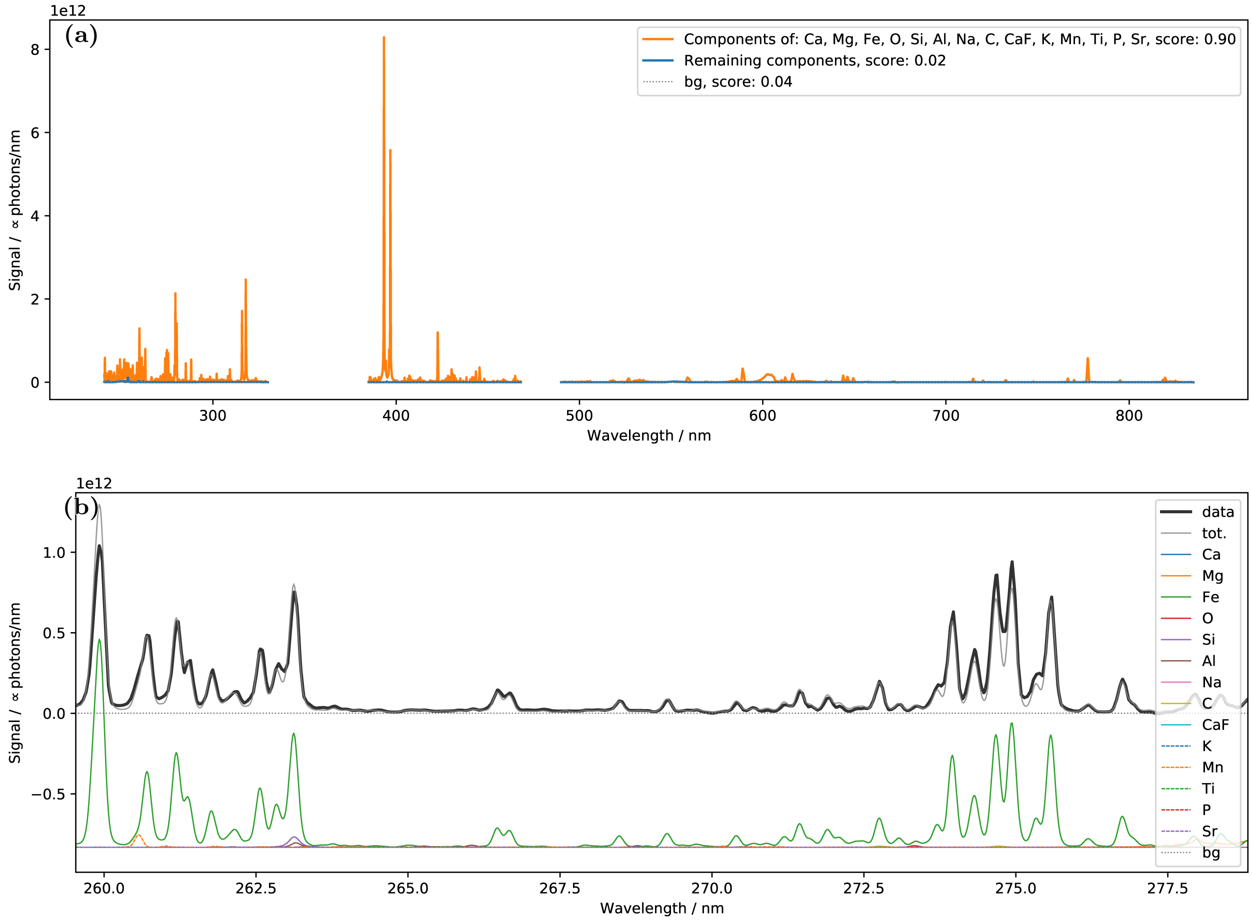

Figure 5.4.34: ***(a)*** *The sum of the significant pure spectra plotted versus the sum of the remaining/non-significant pure spectra. The strongest signals of the remaining/non-significant spectrum are in the UV range. These signals origin mainly from Hg, V, Nb, B, and Zr as shown in* ***(b)****. The signal of B appear very broad and is therefore most likely due to over fitting. The remaining signals, are probably also examples of over fitting, but further investigations would be needed in order to be certain.*

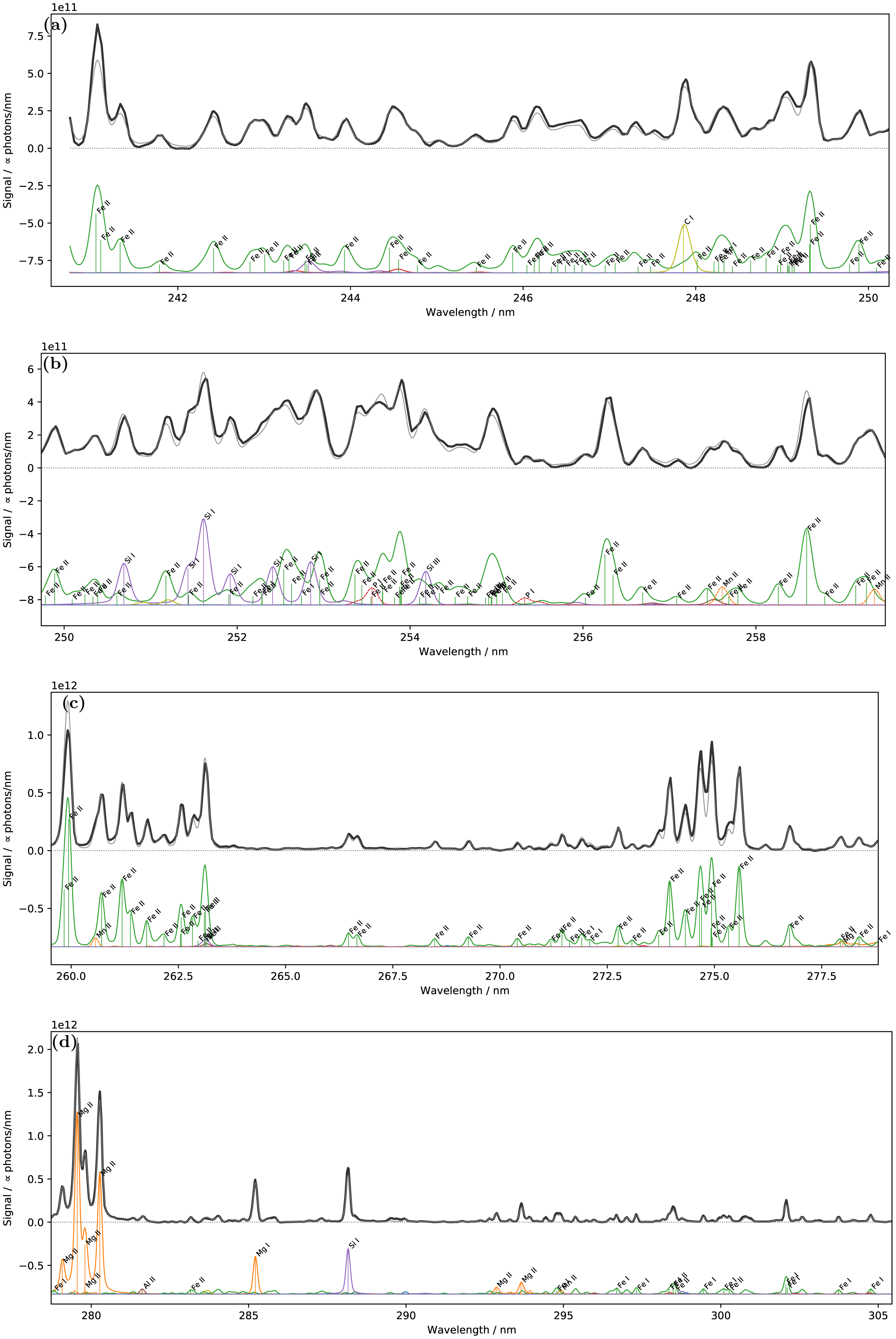

Figure 5.4.35: *Results from applying the unmixing to the ChemCam spectrum of Epworth position 4 shown in smaller spectral ranges for the UV spectrometer. The line identification is also shown providing information about spectral interferences.*

5.4.7 GUI Implementation

The unmixing algorithm has been wrapped with a graphical user interface (GUI) also written in python. The GUI implementation was used for all the shown examples of applications and for generating the included plots. A screen shot of the GUI during the analysis of the ChemCam spectrum can be seen in Figure 5.4.36.

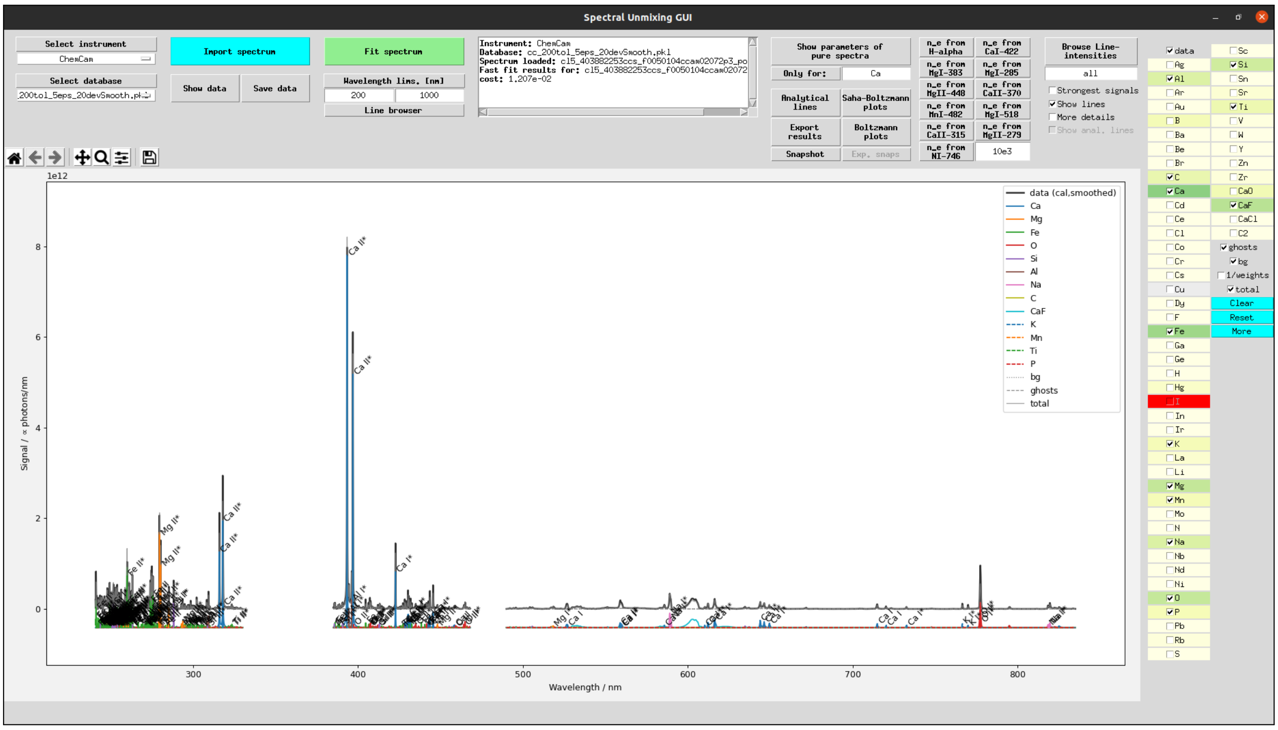

```
Instrument: ChemCam
Database: cc_200tol_5eps_20devSmooth.pkl
Spectrum loaded: c15_403882253ccs_f0050104ccam02072p3_po
Fast fit results for: c15_403882253ccs_f0050104ccam02072
cost: 1.207e-02
```

Figure 5.4.36: *Screenshot of the GUI for the unmixing during the analysis of the ChemCam spectrum of the Epworth target.*

The main feature of the GUI is the interactive plot window. By the check-buttons on the right side of the GUI, the pure spectra of the different components can be hidden or shown. The check-buttons are color-coded according to the scores of the pure components. As default, only significant pure components are checked and shown in the plot window. Using the ”Shown lines” check-button, the line identification can be shown. The properties of the identified lines can also be browsed using the ”Browse Line-intensities” button. The identified emission lines are thereby shown in a table also listing their predicted intensities and atomic parameters such as the involved energy levels, Einstein coefficients, and Stark parameters. Other features are the automatic generation of multi-element Saha-Boltzmann plots or simply Boltzmann plots using the line intensities as predicted by the unmixing. The GUI also allows for fits of Voigt profiles to the identified emission lines. This is initiated using the button ”Analytical lines”. The intensities as obtained from the Voigt fits, rather than those obtained from the unmixing, can then also be used for the generation of multi element Saha-Boltzmann/Boltzmann plots. Furthermore, the Lorentzian widths obtained from the Voigt fits can be used for the estimation of the Stark broadening of lines and thereby the electron density of the plasma. This has been hard-coded for some selected lines and resembles the buttons left to the ”Browse Line-intensities” button.

5.5 Discussion of Results

The results from the application to the "Homogeneous" synthetic test spectrum show that the spectrum can be divided into spectra of pure components without any over-fitting. That is, no significant signals were predicted from elements or molecules not present in the spectrum/plasma. This was achieved even though a total of $\sim$ 3000 template spectra from 56 different elements and molecular species are included in the unmixing and their scores solved for simultaneously. The distributions of the scores of the plasma properties (Figure 5.4.3) are also mainly centred around the reference values along the LOS used when generating the spectrum (Figure 4.3.1, Chapter 4). This indicates that the scores of the plasma properties can be used for a first assessment of the plasma properties and thereby as an alternative to Saha-Boltzmann or Boltzmann plots. However, the scores of the plasma properties for the individual elements should be interpreted with care. It was seen that the scores of the Ca emissions resembled those of the total emission well. However, this was not true for the scores of the Na emissions (Figure 5.4.4). This is because different elements are allowed to be described with different element templates/plasma properties. As the only Na emission lines above the spectral noise are the Na I doublet at 589 nm, the plasma properties are poorly constrained for Na and largely determined by random fluctuations due to the spectral noise. The unmixing allowing for the different species to be described by different plasma properties, is opposite to the fit method that was described in the previous chapter. In the fit approach the emissions from all elements are constrained to the same plasma properties. Not using this constraint in the unmixing is what allows it to be solved fast (see Section 5.1 in this chapter). On the other hand, it is also the reason why the unmixing does not directly allow for quantitative analysis. For example, if the predicted Na emissions were translated into concentrations using the equations for the LOS radiance (eq. (2.2.23), Chapter 2), the results would be very different if using the plasma properties corresponding to the scores of the Na emissions or the plasma properties corresponding to the scores of the total emission. Quantitative results might be obtained by imposing some regularization on the choices of template spectra/plasma properties when solving the unmixing. But this is not straight forward and could probably only be achieved by solving the unmixing iteratively which would increase the computation time. During the regression in the method of multi-element Saha-Boltzmann plots, the emission lines are forced to be described by the same homogeneous temperature. The method of multi-element Saha-Boltzmann plots, applied to the intensities as obtained from the unmixing, can therefore be considered as a kind of post regularization. By enforcing a single homogeneous temperature and total plasma density (for the correction of self-absorption), quantitative results are obtained in terms of relative concentration estimates. For the "Homogeneous" spectrum these are within ±7 % relative deviations (Figure 5.4.5).

When applying the unmixing to the "Bogaerts" synthetic spectrum the deviations are a little larger than for the "Homogeneous" spectrum. This is due to the spatial gradients of the plasma properties. As optically thin emissions from LOS with gradients can be well modelled by a superposition of several one-zone models (see eq. 2.2.28, Chapter 2), which essentially corresponds to the unmixing database, non-optically thin emissions are better modelled by a two-zone plasma model for describing the emission and absorption in the plasma at two different temperatures (see discussions in Chapter 4). This is in agreement with the strongly self-absorbed Mg II lines around 280 nm being among the emissions showing the largest discrepancies. Such lines would therefore be better described by an unmixing database calculated from a two-zone plasma model. On the other hand, a two-zone database would be larger and more insights for constraining the properties of the zones, e.g. by fluid dynamical simulations, would be needed as well as an improved method for reducing the database. However, the deviations between the total spectrum predicted by the unmixing and the "Bogaerts" synthetic spectrum are still small enough not to cause any significant over-fitting. Furthermore, no outliers due to false line identification are observed when applying the multi-element Saha-Boltzmann where also the relative concentration are obtained within ±36 % relative deviations (Figure 5.4.9). These higher deviations, compared to the "Homogeneous" spectrum, are mainly caused by the single temperature description (inherent to the method of Saha-Boltzmann plots) of the "Bogaerts" spectrum rather than uncertainties in the intensities of the emission lines as obtained from the unmixing [112].

From the applications to the time-resolved spectra of the carbonate target measured in Martian atmospheric conditions, i.e. real LIBS data, the results are very promising. Besides the Zr III lines at a delay time of 500 ns, no signs of over-fitting are observed by the derived significant components. Furthermore, the highly excited Na II emission lines, present due to non-equilibrium effects, are described in the unmixing. This is opposite to the two-zone fits presented in the previous chapter, where the Na II lines were not described. The description of the Na II lines are due to the allowance of different temperature for the different elements. Whether the successful description of such non-equilibrium is a coincidence or whether non-equilibrium effects generally can be modelled by high temperature plasma components would be interesting to investigate in a follow up study. At the spectrum taken at 500 ns delay time, the predicted Zr III lines are too weak to be included in the multi-element Saha-Boltzmann plot. However, the Na II lines are included and disturbs the analysis (see Figure 5.4.16). Nonetheless, due to a successful line identification, non-equilibrium lines like these can easily be removed by automatically filtering out emission from highly ionized or excited electronic states resulting in fair relative concentration estimates (see Figure 5.4.17a). However, as for the "Bogaerts" spectrum, the spatial gradients affects the concentration estimates obtained from the Saha-Boltzmann plots and the derived concentrations have deviations larger than when obtained from the fits of a two-zone plasma model (see previous chapter). But, instead of feeding the filtered emission line intensities to the method of Saha-Boltzmann plots, they could be fed to more sophisticated machine learning algorithms. This option would also be interesting to investigate in a follow up study.

The results from the application to the time-resolved spectrum of the Martian regolith simulant (JSC) are generally similar in quality as the results from the time-resolved spectra of the carbonate sample. No significant elements, not present in the sample, are predicted and the results from the multi-element Saha-Boltzmann method are reasonable and are not indicating any errors in the line identification. However, the scores of the pure components are less convincing and not representative for the composition of the sample. This was exemplified in Figure 5.4.22 showing the predicted signals from V and O. The score of V was seen to be higher than that of O, but the V signal is most likely describing part of the continuum emission and random fluctuations due to spectral noise. This interpretation is motivated as the effect seems to become larger with increasing continuum in the input spectra. This can be seen from the scores of the pure components obtained for the time-integrated spectrum of the JSC target where the continuum is stronger and where more and also exotic elements such as Dy have relatively high scores (see Figure 5.4.27). However, even for the time-integrated measurement the unmixing still divides the spectrum nicely into its pure components and no errors in the line identification among the lines with reasonable signal-to-noise ratios are observed (see Figure 5.4.25).

From the application to the ChemCam spectrum, the largest discrepancies between the spectrum as predicted from the unmixing and the input data are observed (Figure 5.4.32 and 5.4.35). Furthermore, the strongest over-fitting is observed in terms of the predicted emissions from B and most likely also Hg, V, Nb, and Zr (Figure 5.4.34). The larger discrepancies for the ChemCam data could have been expected since this application relies on assumptions about the spectral noise and instrumental broadening as this information is not publicly available with the sufficient level of detail. Getting the access to the detailed characterization of the ChemCam instrument, such as described in Chapter 3 for the setup of this thesis, would therefore likely improve the results. Furthermore, the atomic database for simulating spectra (Chapter 4 was optimized for the spectral range of the setup of this thesis. Since ChemCam extends further towards the UV, there are many lines that are only fitted with estimated Stark broadening parameters (see Chapter 4). For a full implementation of the spectral unmixing model for the ChemCam or SuperCam instruments, these parameters should be updated to improve the accuracy of the results. Finally, the lower resolution of the ChemCam setup decreases the information in the spectra and thereby allows for more over-fitting. In spite of this, the results are promising and still provide useful insights into the line identification and spectral interferences.

On a general note, the simultaneously fitting of a total of $\sim$ 3000 template spectra from 56 different elements and molecular species, with only a limited amount over-fitting, is only possible due to the large amount of information contained in the LIBS spectra. Together with the obvious experimental advantages (e.g. no sample preparation and remote sensing), this is one of the biggest strengths of LIBS. However, for geological samples with limited prior information about the composition, the amount of information, in terms of peaks from emission lines, can sometimes be overwhelming. The method of spectral unmixing is a powerful tool to overcome this by providing a quick overview of the elemental contributions to the LIBS plasma, the line identification, and also the plasma properties as well as improved temperature estimates by the method of multi-element Saha-Boltzmann plots. The implementation of the unmixing with the GUI is therefore currently being used in the LIBS and Raman spectroscopy research group for assisting the analysis of our own laboratory LIBS data but also by my colleagues for ChemCam and SuperCam spectra.

Chapter 6

Summary and Conclusion

The focus of this thesis was to investigate modelling and simulations of LIBS spectra for the application to LIBS data in Martian atmospheric conditions. In Chapter 2, the basics of the LIBS plasma were described as well as the theoretical framework for modelling and simulating LIBS spectra. For this thesis, the theoretical framework of LTE was chosen. Although involving idealizations of the plasma, LTE was chosen over the alternative, i.e. a complete kinetic description, due to its simplicity and thereby reduced computational costs.

In order to apply and test the later described modelling and simulation efforts, a high resolution LIBS setup was used to acquire LIBS spectra of reference samples in experimentally simulated Martian atmospheric conditions. As part of this thesis, this LIBS setup was calibrated and characterized in chapter 3.

In Chapter 4, it was described how LIBS spectra are simulated from a simplified one-dimensional model of the plasma. The model was that of a non-reactive stationary plasma in LTE comprised of a finite number of homogeneous zones. To enable the simulation of LIBS spectra, an atomic database was build from the NIST and the STARK-B databases. For emission lines without any Stark broadening parameters from the literature, parameters were assigned by interpolation and extrapolation of the literature values using a heuristic function. For emission lines without any Stark shift parameters, the shift was assumed negligible. After having established the methodology for the simulation of spectra, a custom made routine for the fits of spectra/plasma models was described and implemented as a Python script. Thereafter, fits of the plasma model, containing one or two zones, were applied to synthetic test data. The fits were done in order to test the implementation of the fit-routine but also to test the two-zone discretization of spectra simulated from plasma models with many more zones. The outputs from the fits show that LIBS spectra from plasmas with spatial variations in the temperature and densities can be well described by a two-zone plasma model. Furthermore, the two-zone model was shown to also contain the physical characteristics of the original data. For example, the self-absorption characteristics and the derived concentrations were shown to be similar to the original/non-discretized values. After this verification of the two-zone model, fits of the two-zone model were performed to measured time-resolved LIBS data of a carbonate sample acquired in experimentally simulated Martian atmospheric conditions. Generally, the two-zone model was found to describe the data well and the predicted concentration estimates were found to be in good agreement with the reference values. Furthermore it was shown that the two-zone model is a significant improvement from the one-zone model. This is due to spatial gradients in the plasma properties in Martian atmospheric conditions. However, two larger discrepancies in the two-zone discretization of the time-resolved data were observed. The first one is the underestimation of the ground-state Mg I emission line at 285 nm. This was hypothesised to either originate from discretization into a two-zone model or from the accumulation of uncertainties related to the atomic constants, light collection approximations, and/or characterizations of the setup. The first hypothesis was contrary to the two-zone discretization of the synthetic test spectra, that did not contain this discrepancy. Therefore further and more systematic applications to synthetic test data were proposed to clarify this. The second larger discrepancy was the lack of the description of the highly excited Na II emission lines at the smallest delay time (500 ns). In the thermodynamic description of the plasma, these lines require a very high temperature to exist without a non-negligible population. This was indicated by the observed high temperature local minima around 35 000 K for either of the zones. Nonetheless, the Na II lines were concluded to originate from non-equilibrium effects. Overall, the results indicate that the two-zone plasma model is a good framework for analysing and improving the understanding of time-resolved LIBS data in Martian atmospheric conditions. However, attention to non-equilibrium effects should be given at delay times around 500 ns and earlier due to the recombining character of the LIBS plasma. Furthermore, attention should be given to the ground-state populations of non-metallic elements for which the electron density does not seem to be sufficiently high to sustain LTE. Nonetheless, due to equilibrium of excited states, for which a lower electron density is required, LTE models might still provide a good description of their emissions and only the concentration estimates might be affected by deviations from LTE.

In Chapter 5, a method of spectral unmixing for the calibration-free analysis of LIBS data was developed and presented. The method of unmixing consists in setting up and solving a system of equations between the pixels of an input spectrum and a linear combination of so called template spectra. The unmixing equation is solved for the coefficients/scores in the linear combination of the template spectra. The collection of template spectra, i.e. the unmixing database, was based on a large number of synthetic spectra simulated for each of the elements contained in the atomic database and using a one-zone plasma model. For the description of continuum emissions, the database was expanded by localized Gaussian functions. For the description of molecular emissions, the unmxing database was expanded by a subset of the most important molecular features that were extracted from laboratory LIBS data. After applying the unmixing to a spectrum, the scores (coefficients of the linear combination of the template spectra) were grouped in order to obtain pure spectra of the individual elements, as well as their individual emission line intensities. Furthermore, the scores were grouped for the different plasma properties, also providing a quick overview of the important temperatures and densities in describing the spectrum. As a post processing step, a routine for the automatic generation of multi-element Saha-Boltzmann was implemented as part of the unmxing. Other than a value of the electron density, this routine uses only the outputs of the unmixing. For time-integrated measurements it can be used for concentration estimates in the approximation of a homogeneous and stationary plasma. More generally, it can be used as a sanity check of the unmixing outputs and especially for the line-identification.

By applications to synthetic test spectra, the implementation of the unmxing was verified. Furthermore, it was confirmed that the unmixing database, although based on a one-zone plasma model, can be fairly well used for the description of spectra from plasmas with spatial inhomogeneities. From applications to time-resolved LIBS data acquired in experimentally simulated Martian atmospheric conditions, it was seen that the unmixing was able to describe the data well and with only a limited amount of over-fitting. Furthermore, the non-equilibrium Na II emission, not contained in the two-zone fits presented in the previous chapter, were described in the predicted pure spectrum of Na. However, when including them in the multi-element Saha-Boltzmann plot analysis, they disturbed the results and obscured the concentration estimates. When excluded from the analysis, by automatically filtering lines from highly excited states, the analysis yielded reasonable concentration estimates. By applying the unmixing to the time-integrated spectrum of a Martian regolith simulant (JSC) in Martian atmospheric conditions, it was confirmed that the unmixing database also can be used for the description of time-integrated measurements. This was not an obvious result since non-equilibrium effects were expected at the earliest and later stages of the plasma. Finally, the unmixing was applied to real mission data in terms of a LIBS spectrum from the ChemCam instrument on board the Curiosity rover. Although containing many emission lines with extrapolated Stark-broadening parameters and a simplified description of the instrumental broadening for this specific instrument, the unmixing were able to describe the ChemCam spectrum well and with only a few examples of over-fitting.

In the Introduction the three following key questions were stated:

1. How can LIBS spectra acquired in Martian atmospheric conditions be modelled by simplified models of the plasma?
2. What can be learned from the models and what are the implications for the analysis of real mission

data?

3. How can spectral modelling be used as a tool for assisting the analysis of real mission data?

Concerning key question number 1, it is concluded that time-resolved LIBS data in Martian atmospheric conditions can be well modelled by a stationary two-zone LTE plasma model. Applications to synthetic test spectra indicate that values close to the average plasma properties should be used for the inner zone and that the plasma properties at the end of the LOS, i.e. the values around the boundary between the plasma core and the shocked atmospheric gas, should be used for the parameters of the outer zone. Thus, the inner zone describes the average plasma emissions whereas the outer zone mostly describes the absorption of the already emitted light. However, non-equilibrium effects seems to be significant at the earliest and later stages of the plasma. Although non-equilibrium emissions might be modelled by certain and perhaps exotic combinations of the plasma properties, the physical properties, such as concentration estimates, will probably be prone to large uncertainties. Consequently, these plasma stages are preferably modelled by kinetic descriptions of the plasma state.

Related to key question number 2, it is concluded that the two-zone model is a good framework for obtaining insights into LIBS in Martian atmospheric conditions. This was concluded because the two-zone model seems to contain the physical characteristics of the real plasma. Consequently, the effect of absorption, concentration estimates, and most likely other properties such as detection limits, as obtained in the two-zone discretization, are closely related to those of the real plasma. Furthermore, by comparing deviations between the measured spectra and the two-zone reconstructions, insights into the physics of the plasma can be obtained. This was exemplified with the lack of the description of the Na II emission lines in the two-zone reconstructions. These lines were thereby classified as non-equilibrium emissions and argued to originate from recombination cascades populating the involved highly excited electronic states. Predicting the existence of the Na II emission lines using kinetic descriptions would have required a much larger computational effort.

Related to key question number 3, two methods based on spectral modelling were investigated for the analysis of LIBS data in Martian atmospheric conditions. The first method in terms of the fits of the two-zone model and the second method in terms of the spectral unmixing. At present, real mission LIBS data from the Martian surface are all time-integrated. Adapting the two-zone plasma model for the application to such data would require additional model/fit parameters for describing the temporal decay of the plasma. The performed two-zone fits already need several hours of computation time on a standard desktop computer. Adding additional parameters will further and significantly increase the computation time and therefore does not seem beneficial. Contrary, the method of spectral unmixing was shown to be applicable to real mission data. However, for time-integrated measurements the method of multi-element Saha-Boltzmann plots cannot be used in order to obtain quantitative estimates. Nonetheless, the implementation with the GUI is at the moment being used by colleagues in the LIBS and Raman spectroscopy research group for assisting the analysis of ChemCam and SuperCam spectra.

Based on the results of this thesis a number of follow-up studies can be performed. For example, the discretization of synthetic test spectra into the two-zone plasma model could be further investigated. This would be done in order to asses if certain profiles of the plasma parameters, different from those studied in this thesis (”Gaussian”, ”Reversed Gaussian”, ”Shifted Gaussian”, and ”Bogaerts”), produce larger discrepancies when discretized in the two-zone. This would help clarify when a three-zone model becomes preferable and how this could be observed in terms of discrepancies for specific emission lines. Thereby, it would also help asses the origin of the underestimation of the signal of the Mg I emission line at 285 nm in the time-resolved spectrum of the carbonate sample.

Furthermore, the deviations from LTE for the ground-state of non-metallic elements should be studied. This could be done by fits of two-zone models to spectra from samples also containing N or Cl for which the critera of LTE seem difficult to satisfy for the Martian LIBS plasma [101]. The deviations from LTE would then correlate positively with the deviations between the fitted concentrations and the reference values. Also, it would be interesting to study the effect of laser energy, wavelength, and focus on the spatial distribution of the temperature and densities. These effects could be quantified by changes in the fitted properties of the inner and the outer zone in the two-zone model. This could help to find optimal laser parameters for which the plasma in Martian atmospheric conditions may be more homogeneous. A more homogeneous plasma would improve the concentration estimates as derived from the two-zone model and also improve the results obtained from the spectral unmixing that is based on a one-zone model, i.e. a homogeneous plasma.

For the method of spectral unmixing, there are some parts of the implementation that could be improved with the goal of reducing over-fitting. Firstly, the amount of over-fitting seems to be increasing with increasing signal of the continuum emission in the input spectra. It would therefore be interesting to explore different algorithms for removing the continuum in a pre-processing step, i.e. before applying the spectral unmxixing. Secondly, the over-fitting usually appears in terms of atomic/ionic emissions for combinations of plasma parameters where only a few emission lines make up the signal. For example, this could be template spectra from either a very low or a very high temperature corresponding to emission only involving the first excited states or emissions only involving ionized species due to a fully ionized plasma, respectively. Such over-fittings could be reduced by adding a temporal decay to the one-zone model such that template spectra for high temperature emissions inherently also contain lower temperature emissions. Due to the temporal decay, such unmixing database spectra would only be applicable to time-integrated spectra.

Furthermore, it would be interesting to compile a database with spectra simulated from a two-zone model. This would improve the description of the emission lines with strong self-absorption such as the Mg II and Ca II lines around 278 nm and 393 nm, respectively. However, the two-zone model contains more parameters than the one-zone model and the unmixing database would be much larger. In order to keep the database at a size not resulting in too long computation times, the lower and higher temperatures should be cut off making the database specific for time-integrated spectra. Alternatively, improvements to the reduction of the database should be investigated. Last but not least, it would be preferable to base the considerations on maximum temperatures and densities on fluid dynamical simulations of the plasma expansion rather than the adiabatic expansion model used in this thesis. Generally this could help further confine the size of the unmxing database but it would especially be helpful for the implementation of a two-zone spectral unmixing database.

Bibliography

[1] D. A. Cremers and L. J. Radziemski, *Handbook of Laser-Induced Breakdown Spectroscopy.* Chichester, UK: John Wiley & Sons, Ltd, apr 2006. [Online]. Available: http://doi.wiley.com/10.1002/0470093013

[2] A. W. Miziolek, V. Palleschi, I. Schecheter, A. W. Miziolek, V. Palleschi, I. Schechter, B. Welz, H. Becker-ross, S. Florek, U. Heitmann, S. S. Analysis, and W. P. Limited, *Laser-Induced Breakdown Spectroscopy (LIBS).* Cambridge University Press, 2006, no. 1.

[3] K. Stelmaszczyk, P. Rohwetter, G. Méjean, J. Yu, E. Salmon, J. Kasparian, R. Ackermann, J. P. Wolf, and L. Wöste, "Long-distance remote laser-induced breakdown spectroscopy using filamentation in air," *Appl. Phys. Lett.*, vol. 85, no. 18, pp. 3977–3979, 2004.

[4] J. D. Winefordner, I. B. Gornushkin, T. Correll, E. Gibb, B. W. Smith, and N. Omenetto, "Comparing several atomic spectrometric methods to the super stars: special emphasis on laser induced breakdown spectrometry, LIBS, a future super star," *J. Anal. At. Spectrom.*, vol. 19, no. 9, pp. 1061–1083, 2004. [Online]. Available: http://dx.doi.org/10.1039/B400355C

[5] A. M. Popov, S. M. Zaytsev, I. V. Seliverstova, A. S. Zakuskin, and T. A. Labutin, "Matrix effects on laser-induced plasma parameters for soils and ores," *Spectrochim. Acta Part B At. Spectrosc.*, vol. 148, pp. 205–210, 2018. [Online]. Available: https://www.sciencedirect.com/science/article/pii/S0584854718300776

[6] J. Hermann, D. Grojo, E. Axente, C. Gerhard, M. Burger, and V. Craciun, "Ideal radiation source for plasma spectroscopy generated by laser ablation," *Phys. Rev. E*, vol. 96, no. 5, p. 53210, nov 2017. [Online]. Available: https://link.aps.org/doi/10.1103/PhysRevE.96.053210

[7] M. Dong, X. Mao, J. J. Gonzalez, J. Lu, and R. E. Russo, "Time-resolved LIBS of atomic and molecular carbon from coal in air, argon and helium," *J. Anal. At. Spectrom.*, vol. 27, no. 12, pp. 2066–2075, 2012. [Online]. Available: http://dx.doi.org/10.1039/C2JA30222E

[8] R. C. Wiens, S. Maurice, B. Barraclough, M. Saccoccio, W. C. Barkley, J. F. Bell, S. Bender, J. Bernardin, D. Blaney, J. Blank, M. Bouyé, N. Bridges, N. Bultman, P. Caïs, R. C. Clanton, B. Clark, S. Clegg, A. Cousin, D. Cremers, A. Cros, L. DeFlores, D. Delapp, R. Dingler, C. D'Uston, M. Darby Dyar, T. Elliott, D. Enemark, C. Fabre, M. Flores, O. Forni, O. Gasnault, T. Hale, C. Hays, K. Herkenhoff, E. Kan, L. Kirkland, D. Kouach, D. Landis, Y. Langevin, N. Lanza, F. LaRocca, J. Lasue, J. Latino, D. Limonadi, C. Lindensmith, C. Little, N. Mangold, G. Manhes, P. Mauchien, C. McKay, E. Miller, J. Mooney, R. V. Morris, L. Morrison, T. Nelson, H. Newsom, A. Ollila, M. Ott, L. Pares, R. Perez, F. Poitrasson, C. Provost, J. W. Reiter, T. Roberts, F. Romero, V. Sautter, S. Salazar, J. J. Simmonds, R. Stiglich, S. Storms, N. Striebig, J.-J. Thocaven, T. Trujillo, M. Ulibarri, D. Vaniman, N. Warner, R. Waterbury, R. Whitaker, J. Witt, and B. Wong-Swanson, "The ChemCam Instrument Suite on the Mars Science Laboratory (MSL) Rover: Body Unit and Combined System Tests," *Space Sci. Rev.*, vol. 170, no. 1, pp. 167–227, 2012. [Online]. Available: https://doi.org/10.1007/s11214-012-9902-4

[9] “ChemCam’s laser is back to firing,” 2021. [Online]. Available: https://www.lanl.gov/discover/science-briefs/2021/May/0528-chemcam-laser-firing.shtml

[10] R. C. Wiens, S. Maurice, and F. R. Perez, “The SuperCam remote sensing instrument suite for the Mars 2020 rover mission: A preview,” *Spectroscopy*, vol. 32, no. 5, pp. 50–55, 2017.

[11] W. Xu, X. Liu, Z. Yan, L. Li, Z. Zhang, Y. Kuang, H. Jiang, H. Yu, F. Yang, C. Liu, T. Wang, C. Li, Y. Jin, J. Shen, B. Wang, W. Wan, J. Chen, S. Ni, Y. Ruan, R. Xu, C. Zhang, Z. Yuan, X. Wan, Y. Yang, Z. Li, Y. Shen, D. Liu, B. Wang, R. Yuan, T. Bao, and R. Shu, “The MarSCoDe Instrument Suite on the Mars Rover of China’s Tianwen-1 Mission,” *Space Sci. Rev.*, vol. 217, no. 5, p. 64, 2021. [Online]. Available: https://doi.org/10.1007/s11214-021-00836-5

[12] J. El Haddad, M. Villot-Kadri, A. Ismaël, G. Gallou, K. Michel, D. Bruyère, V. Laperche, L. Canioni, and B. Bousquet, “Artificial neural network for on-site quantitative analysis of soils using laser induced breakdown spectroscopy,” *Spectrochim. Acta Part B At. Spectrosc.*, vol. 79-80, pp. 51–57, 2013. [Online]. Available: https://www.sciencedirect.com/science/article/pii/S0584854712003679

[13] K. E. Eseller, M. M. Tripathi, F.-Y. Yueh, and J. P. Singh, “Elemental analysis of slurry samples with laser induced breakdown spectroscopy,” *Appl. Opt.*, vol. 49, no. 13, pp. C21—-C26, may 2010. [Online]. Available: http://www.osapublishing.org/ao/abstract.cfm?URI=ao-49-13-C21

[14] F. Barbieri Gonzaga and C. Pasquini, “A compact and low cost laser induced breakdown spectroscopic system: Application for simultaneous determination of chromium and nickel in steel using multivariate calibration,” *Spectrochim. Acta Part B At. Spectrosc.*, vol. 69, pp. 20–24, 2012. [Online]. Available: https://www.sciencedirect.com/science/article/pii/S0584854712000511

[15] R. Wiens, S. Maurice, J. Lasue, O. Forni, R. Anderson, S. Clegg, S. Bender, D. Blaney, B. Barraclough, A. Cousin, L. Deflores, D. Delapp, M. Dyar, C. Fabre, O. Gasnault, N. Lanza, J. Mazoyer, N. Melikechi, P.-Y. Meslin, H. Newsom, A. Ollila, R. Perez, R. Tokar, and D. Vaniman, “Pre-flight calibration and initial data processing for the ChemCam laser-induced breakdown spectroscopy instrument on the Mars Science Laboratory rover,” *Spectrochim. Acta Part B At. Spectrosc.*, vol. 82, pp. 1–27, apr 2013. [Online]. Available: https://linkinghub.elsevier.com/retrieve/pii/S0584854713000505

[16] S. M. Clegg, R. C. Wiens, R. Anderson, O. Forni, J. Frydenvang, J. Lasue, A. Cousin, V. Payré, T. Boucher, M. D. Dyar, S. M. McLennan, R. V. Morris, T. G. Graff, S. A. Mertzman, B. L. Ehlmann, I. Belgacem, H. Newsom, B. C. Clark, N. Melikechi, A. Mezzacappa, R. E. McInroy, R. Martinez, P. Gasda, O. Gasnault, and S. Maurice, “Recalibration of the Mars Science Laboratory ChemCam instrument with an expanded geochemical database,” *Spectrochim. Acta Part B At. Spectrosc.*, vol. 129, pp. 64–85, 2017. [Online]. Available: http://www.sciencedirect.com/science/article/pii/S0584854716303913

[17] E. Tognoni, G. Cristoforetti, S. Legnaioli, and V. Palleschi, “Calibration-Free Laser-Induced Breakdown Spectroscopy: State of the art,” *Spectrochim. Acta - Part B At. Spectrosc.*, vol. 65, no. 1, pp. 1–14, 2010.

[18] A. Ciucci, M. Corsi, V. Palleschi, S. Rastelli, A. Salvetti, and E. Tognoni, “New Procedure for Quantitative Elemental Analysis by Laser-Induced Plasma Spectroscopy,” *Appl. Spectrosc.*, vol. 53, no. 8, pp. 960–964, 1999. [Online]. Available: https://doi.org/10.1366/0003702991947612

[19] J. Aguilera and C. Aragón, “Multi-element Saha–Boltzmann and Boltzmann plots in laser-induced plasmas,” *Spectrochim. Acta Part B At. Spectrosc.*, vol. 62, no. 4, pp. 378–385, apr 2007. [Online]. Available: https://linkinghub.elsevier.com/retrieve/pii/S0584854707000924

[20] D. Bulajic, M. Corsi, G. Cristoforetti, S. Legnaioli, V. Palleschi, A. Salvetti, and E. Tognoni, “A procedure for correcting self-absorption in calibration free-laser induced breakdown spectroscopy,” *Spectrochim. Acta Part B At. Spectrosc.*, vol. 57, no. 2, pp. 339–353, feb 2002. [Online]. Available: https://linkinghub.elsevier.com/retrieve/pii/S0584854701003986

[21] L. Sun and H. Yu, "Correction of self-absorption effect in calibration-free laser-induced breakdown spectroscopy by an internal reference method," *Talanta*, vol. 79, no. 2, pp. 388–395, jul 2009. [Online]. Available: https://www.sciencedirect.com/science/article/pii/S0039914009002719https://linkinghub.elsevier.com/retrieve/pii/S0039914009002719

[22] Y. Yang, X. Hao, and L. Ren, "Correction of self-absorption effect in calibration-free laser-induced breakdown spectroscopy(CF-LIBS) by considering plasma temperature and electron density," *Optik (Stuttg).*, vol. 208, p. 163702, 2020. [Online]. Available: https://www.sciencedirect.com/science/article/pii/S0030402619316006

[23] R. Wester and R. Noll, "Heuristic modeling of spectral plasma emission for laser-induced breakdown spectroscopy," *J. Appl. Phys.*, vol. 106, no. 12, p. 123302, 2009. [Online]. Available: https://doi.org/10.1063/1.3259402

[24] C. Gerhard, J. Hermann, L. Mercadier, L. Loewenthal, E. Axente, C. Luculescu, T. Sarnet, M. Sentis, and W. Viöl, "Quantitative analyses of glass via laser-induced breakdown spectroscopy in argon," *Spectrochim. Acta Part B At. Spectrosc.*, vol. 101, pp. 32–45, nov 2014. [Online]. Available: https://linkinghub.elsevier.com/retrieve/pii/S0584854714001542

[25] A. Y. Kazakov, I. B. Gornushkin, N. Omenetto, B. W. Smith, and J. D. Winefordner, "Radiative model of post-breakdown laser-induced plasma expanding into ambient gas," *Appl. Opt.*, vol. 45, no. 12, pp. 2810–2820, apr 2006. [Online]. Available: http://www.osapublishing.org/ao/abstract.cfm?URI=ao-45-12-2810

[26] I. B. Gornushkin, A. Kazakov, N. Omenetto, B. W. Smith, and J. D. Winefordner, "Experimental verification of a radiative model of laser-induced plasma expanding into vacuum," *Spectrochim. Acta Part B At. Spectrosc.*, vol. 60, no. 2, pp. 215–230, 2005. [Online]. Available: https://www.sciencedirect.com/science/article/pii/S0584854704003155

[27] S. M. Zaytsev, A. M. Popov, and T. A. Labutin, "Stationary model of laser-induced plasma: Critical evaluation and applications," *Spectrochim. Acta Part B At. Spectrosc.*, vol. 158, p. 105632, aug 2019. [Online]. Available: http://www.sciencedirect.com/science/article/pii/S0584854719301740https://linkinghub.elsevier.com/retrieve/pii/S0584854719301740

[28] R. Noll, *Laser-Induced Breakdown Spectroscopy.* Berlin, Heidelberg: Springer Berlin Heidelberg, 2012. [Online]. Available: http://link.springer.com/10.1007/978-3-642-20668-9

[29] S. S. Mao, X. Mao, R. Greif, and R. E. Russo, "Initiation of an early-stage plasma during picosecond laser ablation of solids," *Appl. Phys. Lett.*, vol. 77, no. 16, pp. 2464–2466, 2000. [Online]. Available: https://doi.org/10.1063/1.1318239

[30] R. E. Russo, X. Mao, and S. S. Mao, "Peer Reviewed: The Physics of Laser Ablation in Microchemical Analysis," *Anal. Chem.*, vol. 74, no. 3, pp. 70 A–77 A, feb 2002. [Online]. Available: https://doi.org/10.1021/ac0219445

[31] D. Figg and M. S. Kahr, "Elemental Fractionation of Glass Using Laser Ablation Inductively Coupled Plasma Mass Spectrometry," *Appl. Spectrosc.*, vol. 51, no. 8, pp. 1185–1192, 1997. [Online]. Available: https://doi.org/10.1366/0003702971941728

[32] X. Mao, A. Ciocan, O. Borisov, and R. Russo, "Laser ablation processes investigated using inductively coupled plasma–atomic emission spectroscopy (ICP–AES)," *Appl. Surf. Sci.*, vol. 127-129, pp. 262–268, may 1998. [Online]. Available: https://linkinghub.elsevier.com/retrieve/pii/S0169433297007873

[33] O. V. Borisov, X. Mao, and R. E. Russo, "Effects of crater development on fractionation and signal intensity during laser ablation inductively coupled plasma mass spectrometry," *Spectrochim. Acta Part B At. Spectrosc.*, vol. 55, no. 11, pp. 1693–1704, 2000. [Online]. Available: https://www.sciencedirect.com/science/article/pii/S058485470000272X

[34] R. Multari and D. Cremers, “A time-resolved imaging study of Cr (I) emissions from a laser plasma formed on a sample at nonnormal incidence,” *IEEE Trans. Plasma Sci.*, vol. 24, no. 1, pp. 39–40, 1996. [Online]. Available: http://ieeexplore.ieee.org/document/491680/

[35] K. H. Lepore, C. I. Fassett, E. A. Breves, S. Byrne, S. Giguere, T. Boucher, J. M. Rhodes, M. Vollinger, C. H. Anderson, R. W. Murray, and M. D. Dyar, “Matrix Effects in Quantitative Analysis of Laser-Induced Breakdown Spectroscopy (LIBS) of Rock Powders Doped with Cr, Mn, Ni, Zn, and Co,” *Appl. Spectrosc.*, vol. 71, no. 4, pp. 600–626, 2017. [Online]. Available: https://doi.org/10.1177/0003702816685095

[36] S. Zhang, M. He, Z. Yin, E. Zhu, W. Hang, and B. Huang, “Elemental fractionation and matrix effects in laser sampling based spectrometry,” *J. Anal. At. Spectrom.*, vol. 31, no. 2, pp. 358–382, 2016. [Online]. Available: http://dx.doi.org/10.1039/C5JA00273G

[37] A. De Giacomo, R. Gaudiuso, C. Koral, M. Dell’Aglio, and O. De Pascale, “Nanoparticle-Enhanced Laser-Induced Breakdown Spectroscopy of Metallic Samples,” *Anal. Chem.*, vol. 85, no. 21, pp. 10 180–10 187, nov 2013. [Online]. Available: https://pubs.acs.org/doi/10.1021/ac4016165

[38] S. S. Harilal, B. E. Brumfield, and M. C. Phillips, “An evaluation of equilibrium conditions and temperature-dependent speciation in a laser-produced air plasma,” *Phys. Plasmas*, vol. 25, no. 8, p. 83303, 2018. [Online]. Available: https://doi.org/10.1063/1.5041987

[39] D. H. Zhang, X. X. Yuan, M. G. Su, Q. Min, C. Z. Dong, and D. X. Sun, “Shielding and diagnostics of laser-induced air plasmas generated in collinear double pulse configuration,” *Phys. Plasmas*, vol. 25, no. 6, p. 63112, 2018. [Online]. Available: https://aip.scitation.org/doi/abs/10.1063/1.5024734

[40] S. Nammi, N. J. Vasa, B. Gurusamy, and A. C. Mathur, “Single laser based pump-probe technique to study plasma shielding during nanosecond laser ablation of copper thin films,” *J. Phys. D. Appl. Phys.*, vol. 50, no. 35, p. 355204, aug 2017. [Online]. Available: https://doi.org/10.1088/1361-6463/aa7c4d

[41] J. Hermann, E. Axente, V. Craciun, A. Taleb, and F. Pelascini, “Evaluation of pressure in a plasma produced by laser ablation of steel,” *Spectrochim. Acta Part B At. Spectrosc.*, vol. 143, pp. 63–70, may 2018. [Online]. Available: https://hal.archives-ouvertes.fr/hal-02114127https://linkinghub.elsevier.com/retrieve/pii/S058485471730616X

[42] N. Farid, S. S. Harilal, H. Ding, and A. Hassanein, “Emission features and expansion dynamics of nanosecond laser ablation plumes at different ambient pressures,” *J. Appl. Phys.*, vol. 115, no. 3, p. 033107, jan 2014. [Online]. Available: http://aip.scitation.org/doi/10.1063/1.4862167

[43] B. Chide, S. Maurice, N. Murdoch, J. Lasue, B. Bousquet, X. Jacob, A. Cousin, O. Forni, O. Gasnault, P.-Y. Meslin, J.-F. Fronton, M. Bassas-Portús, A. Cadu, A. Sournac, D. Mimoun, and R. C. Wiens, “Listening to laser sparks: a link between Laser-Induced Breakdown Spectroscopy, acoustic measurements and crater morphology,” *Spectrochim. Acta Part B At. Spectrosc.*, vol. 153, pp. 50–60, 2019. [Online]. Available: https://www.sciencedirect.com/science/article/pii/S0584854718305081

[44] S. S. Harilal, C. V. Bindhu, M. S. Tillack, F. Najmabadi, and A. C. Gaeris, “Internal structure and expansion dynamics of laser ablation plumes into ambient gases,” *J. Appl. Phys.*, vol. 93, no. 5, pp. 2380–2388, mar 2003. [Online]. Available: http://aip.scitation.org/doi/10.1063/1.1544070

[45] P. J. Skrodzki, N. P. Shah, N. Taylor, K. C. Hartig, N. L. LaHaye, B. E. Brumfield, I. Jovanovic, M. C. Phillips, and S. S. Harilal, “Significance of ambient conditions in uranium absorption and emission features of laser ablation plasmas,” *Spectrochim. Acta Part B At. Spectrosc.*, vol. 125, pp. 112–119, 2016. [Online]. Available: https://www.sciencedirect.com/science/article/pii/S0584854716302221

[46] L. Mercadier, J. Hermann, C. Grisolia, and A. Semerok, "Plume segregation observed in hydrogen and deuterium containing plasmas produced by laser ablation of carbon fiber tiles from a fusion reactor," *Spectrochim. Acta Part B At. Spectrosc.*, vol. 65, no. 8, pp. 715–720, aug 2010. [Online]. Available: https://linkinghub.elsevier.com/retrieve/pii/S0584854710001229

[47] S. Zhang, X. Wang, M. He, Y. Jiang, B. Zhang, W. Hang, and B. Huang, "Laser-induced plasma temperature," *Spectrochim. Acta Part B At. Spectrosc.*, vol. 97, pp. 13–33, jul 2014. [Online]. Available: https://linkinghub.elsevier.com/retrieve/pii/S0584854714000615

[48] J. Lasue, R. C. Wiens, S. M. Clegg, D. T. Vaniman, K. H. Joy, S. Humphries, A. Mezzacappa, N. Melikechi, R. E. McInroy, and S. Bender, "Remote laser-induced breakdown spectroscopy (LIBS) for lunar exploration," *J. Geophys. Res. Planets*, vol. 117, no. E1, jan 2012. [Online]. Available: http://doi.wiley.com/10.1029/2011JE003898

[49] J. Yu, Q. Ma, V. Motto-Ros, W. Lei, X. Wang, and X. Bai, "Generation and expansion of laser-induced plasma as a spectroscopic emission source," *Front. Phys.*, vol. 7, no. 6, pp. 649–669, 2012. [Online]. Available: https://doi.org/10.1007/s11467-012-0251-2

[50] J. A. Aguilera and C. Aragón, "Characterization of laser-induced plasma during its expansion in air by optical emission spectroscopy: Observation of strong explosion self-similar behavior," *Spectrochim. Acta Part B At. Spectrosc.*, vol. 97, pp. 86–93, 2014. [Online]. Available: https://www.sciencedirect.com/science/article/pii/S0584854714000652

[51] S. Shabanov and I. Gornushkin, "Two-dimensional axisymmetric models of laser induced plasmas relevant to laser induced breakdown spectroscopy," *Spectrochim. Acta Part B At. Spectrosc.*, vol. 100, pp. 147–172, oct 2014. [Online]. Available: https://linkinghub.elsevier.com/retrieve/pii/S0584854714002018

[52] Z. Chen and A. Bogaerts, "Laser ablation of Cu and plume expansion into 1atm ambient gas," *J. Appl. Phys.*, vol. 97, no. 6, p. 63305, 2005. [Online]. Available: https://doi.org/10.1063/1.1863419

[53] S. Merk, A. Demidov, D. Shelby, I. B. Gornushkin, U. Panne, B. W. Smith, and N. Omenetto, "Diagnostic of Laser-Induced Plasma Using Abel Inversion and Radiation Modeling," *Appl. Spectrosc.*, vol. 67, no. 8, pp. 851–859, aug 2013. [Online]. Available: http://journals.sagepub.com/doi/10.1366/12-06929

[54] J. A. Aguilera, C. Aragón, and J. Bengoechea, "Spatial characterization of laser-induced plasmas by deconvolution of spatially resolved spectra," *Appl. Opt.*, vol. 42, no. 30, p. 5938, oct 2003. [Online]. Available: https://opg.optica.org/abstract.cfm?URI=ao-42-30-5938

[55] C. Aragón, F. Peñalba, and J. Aguilera, "Spatial characterization of laser-induced plasmas: distributions of neutral atom and ion densities," *Appl. Phys. A*, vol. 79, no. 4-6, pp. 1145–1148, sep 2004. [Online]. Available: http://link.springer.com/10.1007/s00339-004-2689-8

[56] Q. Ma, V. Motto-Ros, F. Laye, J. Yu, W. Lei, X. Bai, L. Zheng, and H. Zeng, "Ultraviolet versus infrared: Effects of ablation laser wavelength on the expansion of laser-induced plasma into one-atmosphere argon gas," *J. Appl. Phys.*, vol. 111, no. 5, p. 053301, mar 2012. [Online]. Available: http://aip.scitation.org/doi/10.1063/1.3689300

[57] A. Bogaerts, Z. Chen, R. Gijbels, and A. Vertes, "Laser ablation for analytical sampling: what can we learn from modeling?" *Spectrochim. Acta Part B At. Spectrosc.*, vol. 58, no. 11, pp. 1867–1893, nov 2003. [Online]. Available: https://linkinghub.elsevier.com/retrieve/pii/S0584854703001666

[58] D. S. Vogt, S. Schröder, S. Frohmann, P. B. Hansen, F. Seel, M. Gensch, and H.-W. Hübers, "Spatiotemporal characterization of the laser-induced plasma plume in simulated Martian conditions," *Spectrochim. Acta Part B At. Spectrosc.*, vol. 187, p. 106326, 2022. [Online]. Available: https://www.sciencedirect.com/science/article/pii/S0584854721002834

[59] P. Yaroshchyk and J. E. Eberhardt, “Automatic correction of continuum background in Laser-induced Breakdown Spectroscopy using a model-free algorithm,” *Spectrochim. Acta Part B At. Spectrosc.*, vol. 99, pp. 138–149, 2014. [Online]. Available: https://www.sciencedirect.com/science/article/pii/S0584854714001244

[60] A. Einstein, “On the Quantum Theory of Radiation,” *Phys. Zeitschrift*, vol. 18, pp. 121–128, 1917.

[61] H. Griem, *Spectral line broadening by plasmas.* ACADEMIC PRESS, INC., 1974.

[62] “Stark broadening parameters for neutral and singly charged ions: Helium through Calcium, and Cesium.” [Online]. Available: https://griem.obspm.fr/index.php?page=accueil.php

[63] “STARK-B: Database for ”Stark” broadening of isolated lines of atoms and ions in the impact approximation.” [Online]. Available: https://stark-b.obspm.fr/index.php/home

[64] M. Burger and J. Hermann, “Stark broadening measurements in plasmas produced by laser ablation of hydrogen containing compounds,” *Spectrochim. Acta Part B At. Spectrosc.*, vol. 122, pp. 118–126, aug 2016. [Online]. Available: https://linkinghub.elsevier.com/retrieve/pii/S0584854716300908

[65] G. Cristoforetti, A. De Giacomo, M. Dell’Aglio, S. Legnaioli, E. Tognoni, V. Palleschi, and N. Omenetto, “Local Thermodynamic Equilibrium in Laser-Induced Breakdown Spectroscopy: Beyond the McWhirter criterion,” *Spectrochim. Acta Part B At. Spectrosc.*, vol. 65, no. 1, pp. 86–95, jan 2010. [Online]. Available: https://linkinghub.elsevier.com/retrieve/pii/S0584854709003541

[66] A. Bogaerts, “Modeling plasmas in analytical chemistry—an example of cross-fertilization,” *Anal. Bioanal. Chem.*, vol. 412, no. 24, pp. 6059–6083, 2020. [Online]. Available: https://doi.org/10.1007/s00216-020-02587-8

[67] T. Fujimoto and R. W. P. McWhirter, “Validity criteria for local thermodynamic equilibrium in plasma spectroscopy,” *Phys. Rev. A*, vol. 42, no. 11, pp. 6588–6601, 1990. [Online]. Available: https://link.aps.org/doi/10.1103/PhysRevA.42.6588

[68] L. D. Pietanza, G. Colonna, A. De Giacomo, and M. Capitelli, “Kinetic processes for laser induced plasma diagnostic: A collisional-radiative model approach,” *Spectrochim. Acta Part B At. Spectrosc.*, vol. 65, no. 8, pp. 616–626, 2010. [Online]. Available: https://www.sciencedirect.com/science/article/pii/S0584854710000625

[69] V. Morel, A. Bultel, I. Schneider, and C. Grisolia, “State-to-state modeling of ultrashort laser-induced plasmas,” *Spectrochim. Acta Part B At. Spectrosc.*, vol. 127, pp. 7–19, 2017. [Online]. Available: https://www.sciencedirect.com/science/article/pii/S0584854716303329

[70] S. V. Shabanov and I. B. Gornushkin, “Anions in laser-induced plasmas,” *Appl. Phys. A*, vol. 122, no. 7, p. 676, jul 2016. [Online]. Available: http://link.springer.com/10.1007/s00339-016-0175-8

[71] H. R. Griem, “High-Density Corrections in Plasma Spectroscopy,” *Phys. Rev.*, vol. 128, no. 3, pp. 997–1003, 1962.

[72] S. J. Strickler, “Electronic partition function paradox,” *J. Chem. Educ.*, vol. 43, no. 7, p. 364, 1966. [Online]. Available: http://dx.doi.org/10.1021/ed043p364

[73] J. Hermann, C. Boulmer-Leborgne, and D. Hong, “Diagnostics of the early phase of an ultraviolet laser induced plasma by spectral line analysis considering self-absorption,” *J. Appl. Phys.*, vol. 83, no. 2, pp. 691–696, 1998. [Online]. Available: https://doi.org/10.1063/1.366639

[74] A. Kramida, Y. Ralchenko, J. Reader, and NIST Atomic Spectra Database Team, “NIST Atomic Spectra Database (version 5.3),” p. Available: http://physics.nist.gov/asd, 2015. [Online]. Available: http://physics.nist.gov/asd

[75] I. B. Gornushkin, J. M. Anzano, L. A. King, B. W. Smith, N. Omenetto, and J. D. Winefordner, "Curve of growth methodology applied to laser-induced plasma emission spectroscopy," *Spectrochim. Acta Part B At. Spectrosc.*, vol. 54, no. 3, pp. 491–503, 1999. [Online]. Available: https://www.sciencedirect.com/science/article/pii/S058485479900004X

[76] J. Aguilera and C. Aragón, "Characterization of a laser-induced plasma by spatially resolved spectroscopy of neutral atom and ion emissions." *Spectrochim. Acta Part B At. Spectrosc.*, vol. 59, no. 12, pp. 1861–1876, dec 2004. [Online]. Available: https://linkinghub.elsevier.com/retrieve/pii/S0584854704002514

[77] D. S. Vogt, "Laser-Induced Breakdown Spectroscopy for the Exploration of Mars: Analysis of Molecular Emissions and Spatial Characterization of the Plasma," Ph.D. dissertation, Humboldt-Universität zu Berlin, Mathematisch-Naturwissenschaftliche Fakultät, 2020.

[78] D. J. Schroeder and R. L. Hilliard, "Echelle efficiencies: theory and experiment," *Appl. Opt.*, vol. 19, no. 16, pp. 2833–2841, aug 1980. [Online]. Available: http://ao.osa.org/abstract.cfm?URI=ao-19-16-2833

[79] "ARYELLE Butterfly." [Online]. Available: http://www.ltb-berlin.de/produkte/spektrometer/aryelle-butterfly/

[80] P. B. Hansen, S. Schröder, S. Kubitza, K. Rammelkamp, D. S. Vogt, and H.-W. Hübers, "Modeling of time-resolved LIBS spectra obtained in Martian atmospheric conditions with a stationary plasma approach," *Spectrochim. Acta Part B At. Spectrosc.*, vol. 178, p. 106115, 2021. [Online]. Available: https://www.sciencedirect.com/science/article/pii/S0584854721000628

[81] M. Burger, P. J. Skrodzki, L. A. Finney, J. Hermann, J. Nees, and I. Jovanovic, "Isotopic analysis of deuterated water via single- and double-pulse laser-induced breakdown spectroscopy," *Phys. Plasmas*, vol. 25, no. 8, p. 083115, aug 2018. [Online]. Available: https://doi.org/10.1063/1.5042665http://aip.scitation.org/doi/10.1063/1.5042665

[82] C. Aragón, F. Peñalba, and J. A. Aguilera, "Spatial distributions of the number densities of neutral atoms and ions for the different elements in a laser induced plasma generated with a Ni-Fe-Al alloy," *Anal. Bioanal. Chem.*, vol. 385, no. 2, pp. 295–302, 2006. [Online]. Available: https://doi.org/10.1007/s00216-006-0301-0

[83] R. L. Kurucz, "The Kurucz (Smithsonian) Atomic and Molecular Database," *Highlights Astron.*, vol. 10, pp. 579–579, mar 1995. [Online]. Available: https://www.cambridge.org/core/product/identifier/S1539299600012119/type/journal{_}article

[84] I. Ahmed, R. Ahmed, J. Yang, A. W. L. Law, Y. Zhang, and C. Lau, "Elemental analysis of the thyroid by laser induced breakdown spectroscopy," *Biomed. Opt. Express*, vol. 8, no. 11, pp. 4865–4871, nov 2017. [Online]. Available: http://www.osapublishing.org/boe/abstract.cfm?URI=boe-8-11-4865

[85] S. Zielinska, S. Pellerin, K. Dzierzega, F. Valensi, K. Musiol, and F. Briand, "Measurement of atomic Stark parameters of many MnI and Fe I spectral lines using GMAW process," *J. Phys. D. Appl. Phys.*, vol. 43, 2010.

[86] F. Bredice, F. O. Borges, H. Sobral, M. Villagran-Muniz, H. O. Di Rocco, G. Cristoforetti, S. Legnaioli, V. Palleschi, A. Salvetti, and E. Tognoni, "Measurement of Stark broadening of Mn I and Mn II spectral lines in plasmas used for Laser-Induced Breakdown Spectroscopy," *Spectrochim. Acta Part B At. Spectrosc.*, vol. 62, no. 11, pp. 1237–1245, 2007. [Online]. Available: https://www.sciencedirect.com/science/article/pii/S0584854707003369

[87] M. Cirisan, M. Cvejić, M. R. Gavrilović, S. Jovićević, N. Konjević, and J. Hermann, "Stark broadening measurement of Al II lines in a laser-induced plasma," *J. Quant. Spectrosc. Radiat. Transf.*,

vol. 133, pp. 652–662, 2014. [Online]. Available: https://www.sciencedirect.com/science/article/pii/S002240731300424X

[88] C. Fleurier, S. Sahal-Brechot, and J. Chapelle, “Stark profiles of Al I and Al {II} lines,” *J. Phys. B At. Mol. Phys.*, vol. 10, no. 17, pp. 3435–3441, 1977. [Online]. Available: https://doi.org/10.1088/0022-3700/10/17/018

[89] D. Dojić, M. Skočić, S. Bukvić, and S. Djeniže, “Stark broadening measurements of Al II, Al III and He I 388.86 nm spectral lines at high electron densities,” *Spectrochim. Acta Part B At. Spectrosc.*, vol. 166, p. 105816, apr 2020. [Online]. Available: https://linkinghub.elsevier.com/retrieve/pii/S0584854720300227

[90] M. Dimitrijevic, “Stark broadening of SI II and SI III spectral lines,” *Astron. Astrophys.*, vol. 127, no. 1, pp. 68–72, 1983.

[91] M. S. Dimitrijević and S. Sahal-Bréchot, “Stark broadening of neutral sodium lines,” *J. Quant. Spectrosc. Radiat. Transf.*, vol. 34, no. 2, pp. 149–161, 1985. [Online]. Available: https://www.sciencedirect.com/science/article/pii/002240738590041X

[92] M. A. Gigosos, M. Á. González, and V. Cardeñoso, “Computer simulated Balmer-alpha, -beta and -gamma Stark line profiles for non-equilibrium plasmas diagnostics,” *Spectrochim. Acta Part B At. Spectrosc.*, vol. 58, no. 8, pp. 1489–1504, 2003. [Online]. Available: https://www.sciencedirect.com/science/article/pii/S0584854703000971

[93] E. V. Sarandaev and M. Salakhov, “Regularities in the Stark widths and shifts of spectral lines of singly-ionized aluminium,” *J. Quant. Spectrosc. Radiat. Transf.*, vol. 56, no. 3, pp. 399–407, 1996. [Online]. Available: https://www.sciencedirect.com/science/article/pii/0022407396845298

[94] I. Tapalaga, I. P. Dojčinović, and J. Purić, “Stark width regularities within magnesium spectral series,” *Mon. Not. R. Astron. Soc.*, vol. 415, no. 1, pp. 503–512, 2011. [Online]. Available: https://doi.org/10.1111/j.1365-2966.2011.18719.x

[95] C. C. Allen, R. V. Morris, M. J. Karen, D. C. Golden, M. M. Lindstrom, and J. P. Lockwood, “Martian Regolith Simulant JSC Mars-1,” in *Lunar Planet. Sci. Conf. XXIX*, 1998.

[96] P. B. Hansen, “Laser-Induced Breakdown Spectroscopy: An Implementation of Calibration-Free LIBS,” pp. 29–49. [Online]. Available: https://drive.google.com/file/d/16rkJhOG8Opgeb9h3XooVmgDk45LfHkNt/view?usp=sharing

[97] S. Kirkpatrick, C. D. Gelatt, and M. P. Vecchi, “Optimization by Simulated Annealing,” *Science (80-.).*, vol. 220, no. 4598, pp. 671–680, 1983. [Online]. Available: http://www.sciencemag.org/cgi/doi/10.1126/science.220.4598.671

[98] “scipy.optimize.lsq_linear.” [Online]. Available: https://docs.scipy.org/doc/scipy/reference/generated/scipy.optimize.lsq{_}linear.html

[99] Wikipedia, “Minimum intensity projection - Wikipedia, The Free Encyclopedia,” http://en.wikipedia.org/w/index.php?title=Minimum\%20intensity\%20projection&oldid=915050986, 2021.

[100] D. W. Hahn and N. Omenetto, “Laser-Induced Breakdown Spectroscopy (LIBS), Part II: Review of Instrumental and Methodological Approaches to Material Analysis and Applications to Different Fields,” *Appl. Spectrosc.*, vol. 66, no. 4, pp. 347–419, apr 2012. [Online]. Available: http://www.osapublishing.org/as/abstract.cfm?URI=as-66-4-347

[101] Y. Zhang, Z. Zhao, T. Xu, G. Niu, Y. Liu, and Y. Duan, “Characterization of local thermodynamic equilibrium in a laser-induced aluminum alloy plasma,” *Appl. Opt.*, vol. 55, no. 10, p. 2741, 2016. [Online]. Available: https://www.osapublishing.org/abstract.cfm?URI=ao-55-10-2741

[102] A. De Giacomo, "Experimental characterization of metallic titanium-laser induced plasma by time and space resolved optical emission spectroscopy," *Spectrochim. Acta Part B At. Spectrosc.*, vol. 58, no. 1, pp. 71–83, jan 2003. [Online]. Available: https://linkinghub.elsevier.com/retrieve/pii/S0584854702002343

[103] J. Hermann, A. Lorusso, A. Perrone, F. Strafella, C. Dutouquet, and B. Torralba, "Simulation of emission spectra from nonuniform reactive laser-induced plasmas," *Phys. Rev. E*, vol. 92, no. 5, p. 053103, nov 2015. [Online]. Available: https://link.aps.org/doi/10.1103/PhysRevE.92.053103

[104] P. E. Dyer, A. Issa, and P. H. Key, "Dynamics of excimer laser ablation of superconductors in an oxygen environment," *Appl. Phys. Lett.*, vol. 57, no. 2, pp. 186–188, 1990. [Online]. Available: https://doi.org/10.1063/1.103979

[105] D. Vogt, K. Rammelkamp, S. Schröder, and H. Hübers, "Molecular emission in laser-induced breakdown spectroscopy: An investigation of its suitability for chlorine quantification on Mars," *Icarus*, vol. 302, pp. 470–482, mar 2018. [Online]. Available: https://linkinghub.elsevier.com/retrieve/pii/S0019103517305389

[106] O. Forni, M. Gaft, M. J. Toplis, S. M. Clegg, S. Maurice, R. C. Wiens, N. Mangold, O. Gasnault, V. Sautter, S. Le Mouélic, P.-Y. Meslin, M. Nachon, R. E. McInroy, A. M. Ollila, A. Cousin, J. C. Bridges, N. L. Lanza, and M. D. Dyar, "First detection of fluorine on Mars: Implications for Gale Crater's geochemistry," *Geophys. Res. Lett.*, vol. 42, no. 4, pp. 1020–1028, 2015. [Online]. Available: https://agupubs.onlinelibrary.wiley.com/doi/abs/10.1002/2014GL062742

[107] R. Bro and S. Jong, "A Fast Non-negativity-constrained Least Squares Algorithm," *J. Chemom.*, vol. 11, pp. 393–401, 1997.

[108] "Curiosity (MSL) Analyst's Notebook." [Online]. Available: https://an.rsl.wustl.edu/msl/mslbrowser/an3.aspx

[109] "OpenPlanetary." [Online]. Available: https://openplanetary.github.io/blog/tools/chemcam.html

[110] A. Cousin, P. Y. Meslin, R. C. Wiens, W. Rapin, N. Mangold, C. Fabre, O. Gasnault, O. Forni, R. Tokar, A. Ollila, S. Schröder, J. Lasue, S. Maurice, V. Sautter, H. Newsom, D. Vaniman, S. Le Mouélic, D. Dyar, G. Berger, D. Blaney, M. Nachon, G. Dromart, N. Lanza, B. Clark, S. Clegg, W. Goetz, J. Berger, B. Barraclough, and D. Delapp, "Compositions of coarse and fine particles in martian soils at gale: A window into the production of soils," *Icarus*, vol. 249, pp. 22–42, 2015. [Online]. Available: https://www.sciencedirect.com/science/article/pii/S0019103514002449

[111] "PDS Geosciences Node." [Online]. Available: https://pds-geosciences.wustl.edu/msl/msl-m-chemcam-libs-4{_}5-rdr-v1/mslccm{_}1xxx/data/

[112] I. B. Gornushkin, S. V. Shabanov, S. Merk, E. Tognoni, and U. Panne, "Effects of non-uniformity of laser induced plasma on plasma temperature and concentrations determined by the Boltzmann plot method: implications from plasma modeling," *J. Anal. At. Spectrom.*, vol. 25, no. 10, pp. 1643–1653, 2010. [Online]. Available: http://dx.doi.org/10.1039/C0JA00016G

List of Figures

List of Tables

Appendix A

Stark Parameter Fits for More Species

In Figure A.0.1 and A.0.1 fits of equation (4.1.10) from Chapter 4 to different atomic species can be seen. The fits are done in order to assign Stark broadening parameters to emission lines where no values have been found in the literature. For Ba I, the span in upper energy is small, and consequently a constant function is fitted instead. For K II, Sr II, and Ti I, no data for any lines have been found in the literature and consequently no fits have been performed.

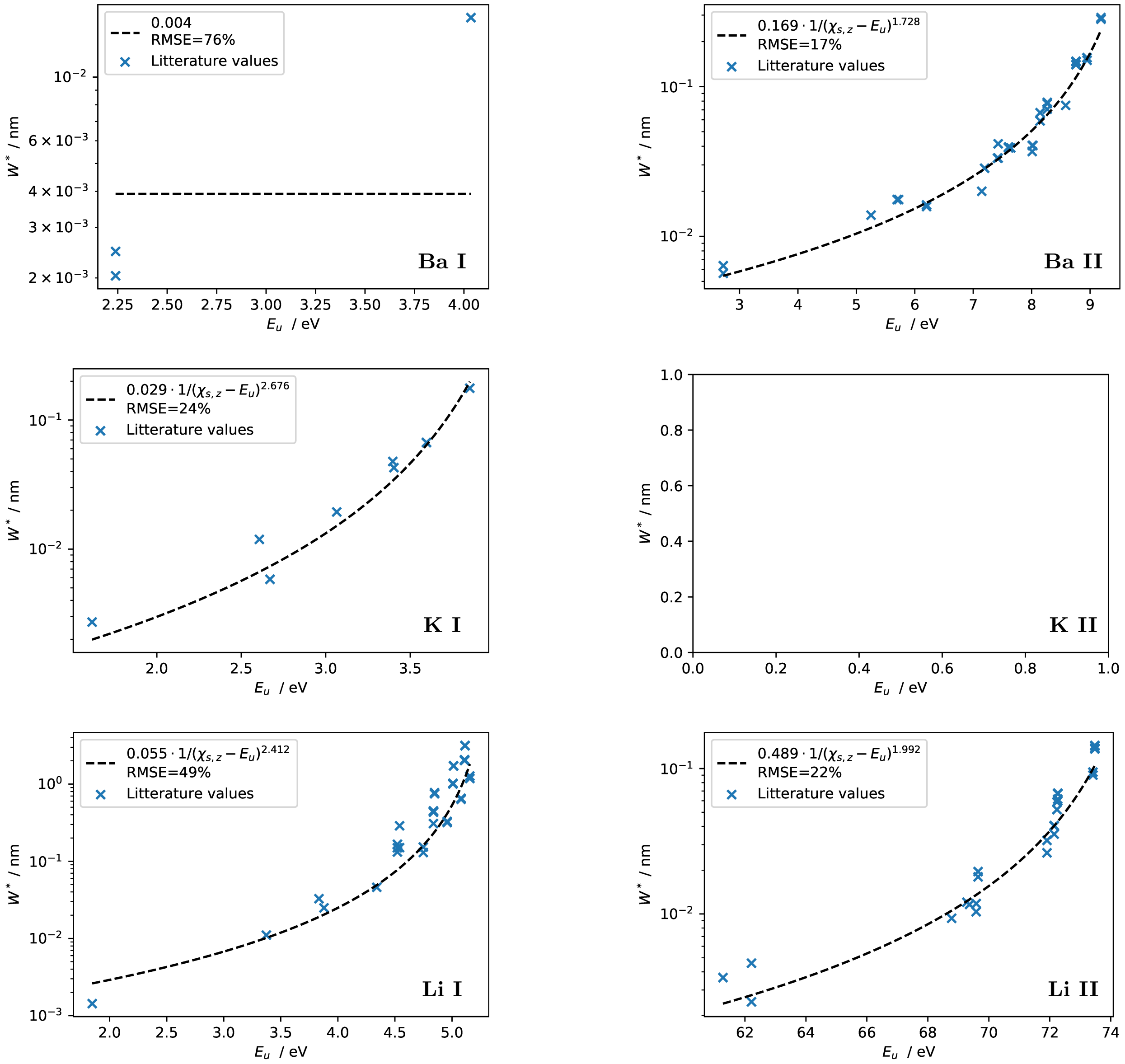

Figure A.0.1: *Fits of heuristic function to the literature values of the Stark broadening parameters of different atomic species*

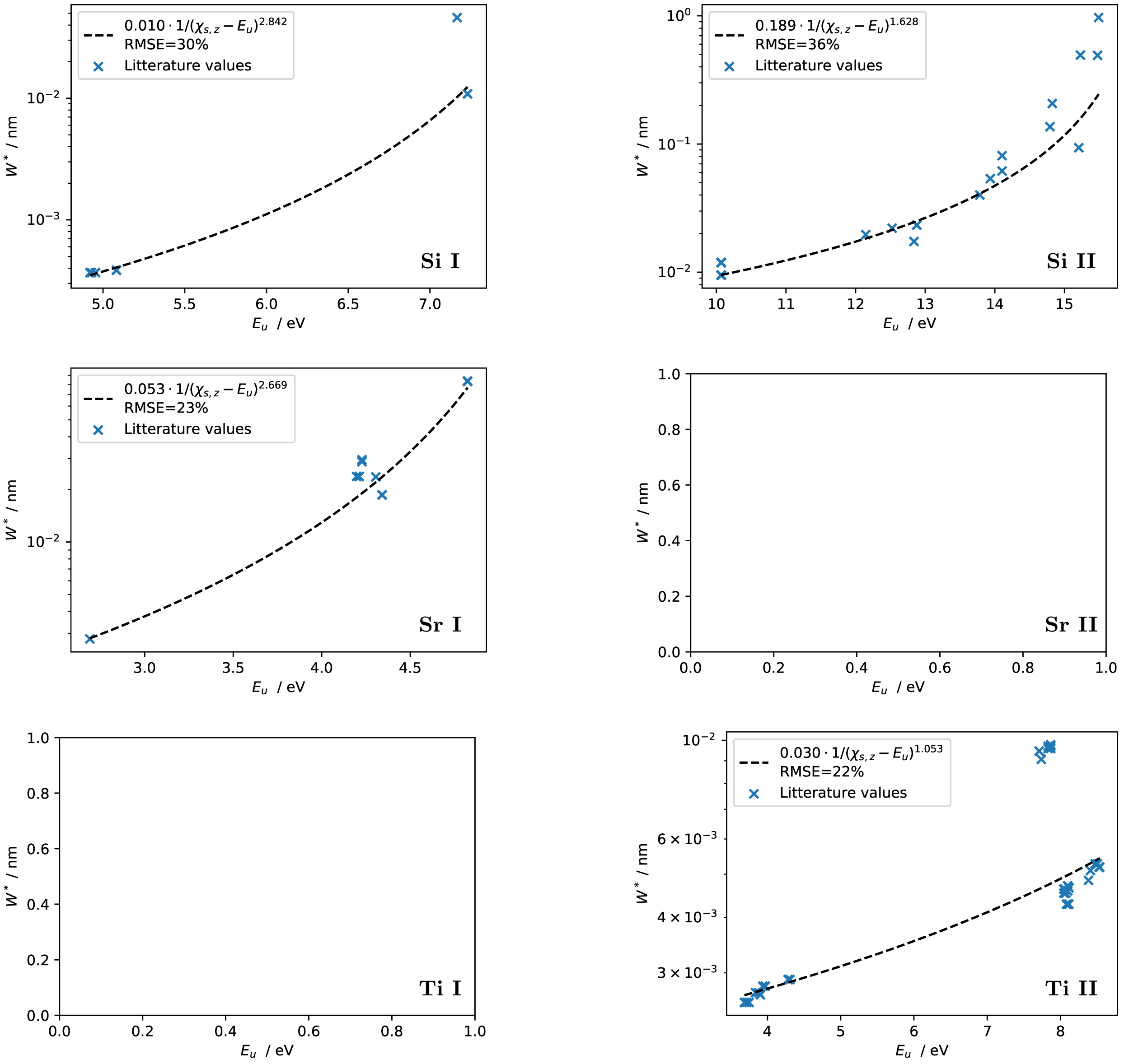

Figure A.0.2: *Fits of heuristic function to the literature values of the Stark broadening parameters of different atomic species*

Appendix B

Manually Added Lines to the Spectral Database

Table B.1: *Emission lines added to the spectral database of this thesis via data from the Kurucz database (Kurucz CD-ROM No. 23) [83]. For most of the lines, the NIST database contained the data for the upper (u) and lower (l) levels and only the Einstein coefficients from the Kurucz database were used.*

Element	Ion	Wavelength / nm	A_{ul} / s^{-1}	E_u / eV	E_l / eV	g_u	g_l	Conf$_\mathrm{u}$	Term$_\mathrm{u}$	Conf$_\mathrm{l}$	Term$_\mathrm{l}$
Ag	1	405.54755	2.31e+07	6.720	3.664	4	2	4d10.6d	2D	4d10.5p	2P*
Ag	1	421.09571	2.61e+07	6.722	3.778	6	4	4d10.6d	2D	4d10.5p	2P*
Ag	1	421.28109	4.36e+06	6.720	3.778	4	4	4d10.6d	2D	4d10.5p	2P*
Ag	1	447.60402	5.26e+06	6.433	3.664	2	2	4d10.7s	2S	4d10.5p	2P*
Ag	1	466.84735	9.36e+06	6.433	3.778	2	4	4d10.7s	2S	4d10.5p	2P*
Ag	1	768.77723	1.77e+07	5.276	3.664	2	2	4d10.6s	2S	4d10.5p	2P*
Al	3	290.69750	1.08e+08	25.045	20.781	8	6	2p6.6g	2G	2p6.4f	2F*
Al	3	290.70015	1.11e+08	25.045	20.781	10	8	2p6.6g	2G	2p6.4f	2F*
Al	3	290.70015	4.02e+06	25.045	20.781	8	8	2p6.6g	2G	2p6.4f	2F*
Al	1	305.00725	3.21e+07	7.668	3.604	6	4	3s.3p.(3P*).4s	4P*	3s.3p2	4P
Al	1	305.46790	4.49e+07	7.656	3.598	4	2	3s.3p.(3P*).4s	4P*	3s.3p2	4P
Al	1	305.71440	7.50e+07	7.668	3.613	6	6	3s.3p.(3P*).4s	4P*	3s.3p2	4P
Al	1	305.90295	1.42e+07	7.656	3.604	4	4	3s.3p.(3P*).4s	4P*	3s.3p2	4P
Al	1	305.99240	1.83e+07	7.649	3.598	2	2	3s.3p.(3P*).4s	4P*	3s.3p2	4P
Al	1	306.42900	8.92e+07	7.649	3.604	2	4	3s.3p.(3P*).4s	4P*	3s.3p2	4P
Al	1	306.61445	4.77e+07	7.656	3.613	4	6	3s.3p.(3P*).4s	4P*	3s.3p2	4P
Al	3	447.98910	3.30e+08	23.548	20.781	8	6	2p6.5g	2G	2p6.4f	2F*
Al	3	447.99690	1.22e+07	23.548	20.781	10	8	2p6.5g	2G	2p6.4f	2F*
C	1	752.34000	3.26e+06	10.419	8.771	3	3	p4d	1P	p3p	3S
Ca	1	386.61560	9.14e+05	8.255	5.049	3	5	4p.5d	1P	4p2	1D
Ca	1	387.02210	1.51e+05	9.035	5.832	3	5	4p.9d	1P	4s.8d	3D
Ca	1	387.29990	6.85e+06	5.909	2.709	3	5	4s.10p	1P	3d.4s	1D
Ca	1	387.38390	3.04e+05	8.928	5.728	3	5	4p.9s	1P	4s.7d	1D
Ca	1	387.52960	4.92e+05	8.776	5.578	3	5	4p.8s	3P	4s.6d	1D
Ca	1	389.48180	2.68e+05	8.910	5.728	3	5	4p.9s	3P	4s.7d	1D
Ca	1	389.56730	1.58e+05	8.635	5.453	3	3	4p.6d	1P	4s.7s	3S
Ca	1	399.29800	1.54e+05	8.832	5.728	3	5	4p.7d	1P	4s.7d	1D
Ca	1	399.45170	2.65e+06	9.035	5.932	3	1	4p.9d	1P	4s.11s	1S
Ca	1	399.46080	2.04e+06	6.035	2.933	5	3	4s.14d	1D	4s.4ps	1P
Ca	1	400.37980	1.40e+06	6.028	2.933	1	3	4s.15s	1S	4s.4ps	1P
Ca	1	403.02120	5.30e+05	7.756	4.681	3	5	4p.4d	3P	4s.4d	3D
Ca	1	403.09780	2.01e+05	8.803	5.728	3	5	4p.8s	1P	4s.7d	1D
Ca	1	403.12120	9.82e+05	6.007	2.933	5	3	4s.12d	1D	4s.4p	1P
Ca	1	403.24650	7.58e+05	8.255	5.181	3	1	4p.5d	1P	4p2	1S
Ca	1	403.85180	7.42e+06	8.114	5.045	3	1	4p.6s	1P	4s6s	1S
Ca	2	411.37120	3.06e+05	11.451	8.438	4	6	12d	2D	4f	2F
Ca	2	411.37120	2.92e+05	11.451	8.438	6	8	12d	2D	4f	2F
Ca	1	411.53050	1.33e+06	9.035	6.023	3	5	4p.9d	1P	4s.13d	1D
Ca	1	411.63410	9.22e+05	8.056	5.045	3	1	4p.6s	3P	4s.6s	1S
Ca	1	412.13300	1.27e+06	8.586	5.578	3	5	4p.7s	1P	4s.6d	1D
Ca	1	534.94650	2.28e+07	5.026	2.709	7	5	3d4p	1F	3d4s	1D
Ca	1	586.75620	3.06e+07	5.045	2.933	1	3	4s.6s	1S	4s.4p	1P
Ca	1	714.81500	3.59e+07	4.443	2.709	5	5	3d4p	1D	3d4s	1D
Ca	1	720.21900	1.41e+07	4.430	2.709	5	5	3d4p	3F	3d4s	1D
Ca	1	732.61500	2.94e+07	4.624	2.933	5	3	3p6.4s.4d	1D	3p6.4s.4p	1P*
Fe	1	275.89817	3.62e+05	6.668	2.176	7	7	3d7.(4F).5p	5D*	3d7.(4P).4s	a5P
Fe	1	275.97218	2.16e+06	7.509	3.018	7	7	3d6.(3F2).4s.4p.(1P*)	r 3G*	3d6.4s2	b3G
Fe	1	326.02669	1.85e+06	6.361	2.559	9	9	3d7.(2D2).4p	v 3F*	3d6.4s2	b3F2
Fe	1	326.13254	1.40e+07	7.218	3.417	5	5	3d6.4s.(4D).4d	5P	3d6.(5D).4s.4p.(3P*)	z5F*
Fe	1	542.40675	5.00e+07	6.605	4.320	15	13	3d7.(4F).4d	e 5H	3d7.(4F).4p	z5G*

Mn	2	276.54327	2.72e+07	8.408	3.926	7	7	3d5.(4G).4p	z 3F*	3d6	a3F
Mn	2	277.65244	3.16e+07	8.402	3.938	5	5	3d5.(4G).4p	z 3F*	3d6	a3F
Mn	1	280.91090	2.90e+07	6.555	2.143	8	8	(4D)sp	x6D	(5D)4s	a6D
Mn	2	283.04710	2.75e+07	9.852	5.473	5	3	a2D)4p	x3F	(2D)4s	c3D
Mn	1	283.04800	1.32e+06	8.637	4.258	10	10		v2H	(3H)4s	a4H
Mn	2	283.07190	2.04e+08	10.770	6.392	13	11	(2H)4p	y1I	(2H)4s	a1H
Mn	1	283.08000	3.35e+07	6.557	2.178	6	4	(4D)sp	x6D	(5D)4s	a6D
Mn	1	283.08000	8.69e+05	6.557	2.178	4	4	(4D)sp	x6D	(5D)4s	a6D
Mn	2	283.08370	1.66e+07	11.047	6.668	9	7	a2G)4p	3G	d6	e3F
Mn	1	283.08560	7.20e+07	6.557	2.178	2	4	(4D)sp	x6D	(5D)4s	a6D
Mn	2	283.09080	8.59e+06	10.215	5.836	7	7	(2F)4p	y3G	(2F)4s	a1F
Mn	1	283.13190	3.76e+06	7.297	2.920	6	6	7S)s12p	6P	(5D)4s	a4D
Mn	1	283.17340	6.29e+06	7.266	2.888	6	8	7S)s11p	6P	(5D)4s	a4D
Mn	1	283.17390	4.05e+07	7.750	3.373	8	6	(3G)4p	v4F	d54s2	a4P
Mn	2	283.27700	1.07e+06	11.047	6.671	9	9	a2G)4p	3G	d6	e3F
Mn	2	283.28480	1.28e+06	10.191	5.815	5	5	(4F)4p	y5G	(2D)4s	b1D
Mn	2	283.30060	1.12e+06	10.903	6.528	9	9	(2H)4p	w3H	(2G)4s	b1G
Mn	1	283.31960	2.91e+06	7.747	3.373	6	6	(3G)4p	v4F	d54s2	a4P
Mn	2	283.37140	2.18e+05	9.894	5.520	9	9	(2I)4p	y3H	(2F)4s	b3F
Mn	2	283.38770	8.63e+05	9.868	5.494	13	13	(2I)4p	y3H	(2I)4s	b1I
Mn	1	283.48780	6.93e+06	7.261	2.888	6	8	7S)s11p	8P	(5D)4s	a4D
Mn	1	283.50490	4.56e+05	8.135	3.763	8	8	(3G)4p	v2F	d54s2	b4D
Mn	2	283.53190	5.44e+05	11.285	6.913	7	7	b2F)4p	u3G	(2F)4s	c1F
Mn	2	283.54980	1.81e+07	11.042	6.671	11	9	a2G)4p	1H	d6	e3F
Mn	1	283.63160	3.52e+07	6.557	2.187	4	2	(4D)sp	x6D	(5D)4s	a6D
Mn	1	283.63710	2.10e+07	6.557	2.187	2	2	(4D)sp	x6D	(5D)4s	a6D
Mn	1	283.68560	1.61e+05	8.637	4.268	10	8		v2H	(3H)4s	a4H
Mn	1	283.69310	4.72e+06	7.747	3.378	6	4	(3G)4p	v4F	d54s2	a4P
Mn	2	283.75670	1.36e+05	8.153	3.784	13	13	(4G)4p	z5H	d6	a3H
Mn	1	283.76450	2.56e+05	7.321	2.953	4	2	7S)s13p	6P	(5D)4s	a4D
Mn	2	283.87050	2.22e+06	9.784	5.418	5	7	a2D)4p	z1D	(4F)4s	a5F
Mn	1	283.88470	1.04e+05	6.509	2.143	8	8	7S)s6p	8P	(5D)4s	a6D
Mn	2	283.95050	2.54e+06	10.859	6.493	9	7	a2G)4p	u3F	(2F)4s	d3F
Mn	1	323.66270	1.21e+07	8.023	4.194	6	6	(a2F).sp	u4D	(3P2).4s	b4P
Mn	1	323.67780	8.31e+07	5.972	2.143	10	8	(4G).sp	y6F	(5D).4s	a6D
Mn	1	323.67940	9.07e+06	6.904	3.075	8	8	(7S).s6d	h6D	(6S).sp	z6P
Mn	1	323.74440	2.64e+07	6.904	3.075	10	8	(7S).s6d	h6D	(6S).sp	z6P
Mn	1	324.85100	8.80e+07	5.979	2.164	8	6	4G)sp	y6F	(5D)4s	a6D
Mn	1	353.18270	5.34e+07	5.791	2.282	8	6	(7S).s4d	e8D	(6S).sp	z8P
Mn	1	353.19890	1.28e+08	5.791	2.282	6	6	(7S).s4d	e8D	(6S).sp	z8P
Mn	1	353.21060	1.99e+08	5.791	2.282	4	6	(7S).s4d	e8D	(6S).sp	z8P
Mn	1	353.91360	9.51e+06	7.847	4.345	8	8	(4G).sp	4F	(3F2).4s	a4F
Mn	1	354.77900	1.20e+08	5.791	2.298	10	8	(7S).s4d	e8D	(6S).sp	z8P
Mn	1	354.80190	1.25e+08	5.791	2.298	8	8	(7S).s4d	e8D	(6S).sp	z8P
Mn	1	354.81830	7.01e+07	5.791	2.298	6	8	(7S).s4d	e8D	(6S).sp	z8P
Mn	1	354.86480	6.48e+06	8.172	4.679	10	8	(3H).4p	v4G	(3G).4s	b4G
Mn	1	355.27560	1.51e+07	8.168	4.679	8	8	(3H).4p	v4G	(3G).4s	b4G
Mn	1	356.67250	1.08e+07	8.201	4.726	8	10	(3G).4p	2G	(3H).4s	a2H
Mn	1	356.94900	1.93e+08	5.792	2.319	12	10	(7S)s.4d	e8D	(6S).sp	z8P
Mn	1	356.98000	7.49e+07	5.791	2.319	10	10	(7S)s.4d	e8D	(6S).sp	z8P
Mn	1	357.00320	1.87e+07	5.791	2.319	8	10	(7S)s.4d	e8D	(6S).sp	z8P
Mn	1	388.25440	2.54e+05	8.020	4.827	4	6	a2F)sp	u4D	3F2)4s	a2F
Mn	1	388.32610	1.22e+08	8.530	5.338	16	14		z2K	(1I)4s	b2I
Mn	1	388.33130	1.28e+05	7.857	4.666	10	10	(4F)sp	6F	(3G)4s	b4G
Mn	1	388.38900	1.52e+05	7.986	4.794	8	8	a2F)sp	u4D	3F2)4s	a2F
Mn	1	388.54440	4.10e+05	7.522	4.332	10	10	(3H)4p	z2G	3F2)4s	a4F
Mn	1	388.73330	7.49e+05	7.854	4.666	10	10	a2F)sp	4G	(3G)4s	b4G
Mn	1	388.77910	3.65e+05	8.015	4.827	8	6	a2F)sp	w2G	3F2)4s	a2F
Mn	1	388.88300	4.21e+06	7.866	4.679	10	8	(4G)sp	w4H	(3G)4s	b4G
Mn	1	388.89890	2.22e+06	8.274	5.087	8	10	a1G)4p	v2G	(3G)4s	a2G
Mn	2	388.91190	3.63e+05	8.560	5.373	5	5	(4P)4p	z3P	(2D)4s	c3D
Mn	1	388.91360	3.71e+06	7.541	4.354	6	6	a2D)sp	w4F	3F2)4s	a4F
Mn	1	388.94560	3.08e+07	8.535	5.349	14	12		z2K	(1I)4s	b2I
Mn	1	388.95850	4.72e+06	7.381	4.194	4	6	a3F)4p	4D	3P2)4s	b4P
Mn	1	389.02440	1.21e+05	7.531	4.345	8	8	(3H)4p	z2G	3F2)4s	a4F
Mn	1	389.16140	1.06e+06	7.418	4.233	12	14	(3H)4p	z2I	(3H)4s	a4H
Mn	1	389.26370	4.01e+05	6.557	3.373	6	6	(4D)sp	x6D	d54s2	a4P
Mn	1	389.26370	1.68e+05	6.557	3.373	4	6	(4D)sp	x6D	d54s2	a4P
Mn	1	389.31890	2.84e+06	7.457	4.273	2	4	a3P)4p	4D	3P2)4s	b4P

Mn	1	389.47300	2.51e+06	6.555	3.373	8	6	(4D)sp	x6D	d54s2	a4P
Mn	1	389.62810	1.43e+06	7.860	4.679	8	8	(4G)sp	w4H	(3G)4s	b4G
Mn	1	389.62920	7.84e+05	7.847	4.666	8	10	(4G)sp	4F	(3G)4s	b4G
Mn	1	389.62920	4.27e+05	7.847	4.666	12	10	(3G)4p	2H	(3G)4s	b4G
Mn	1	389.67250	6.16e+05	7.375	4.194	6	6	a3P)4p	u4P	3P2)4s	b4P
Mn	1	389.67260	2.86e+05	7.541	4.360	6	4	a2D)sp	w4F	3F2)4s	a4F
Mn	2	389.76040	1.76e+06	8.560	5.380	5	7	(4P)4p	z3P	(2D)4s	c3D
Mn	2	389.80560	1.56e+06	8.747	5.567	9	7	(4G)4p	z3G	(2F)4s	b3F
Mn	1	389.83440	1.69e+07	7.373	4.194	8	6	a3P)4p	4D	3P2)4s	b4P
Mn	1	389.93130	2.36e+07	7.452	4.273	6	4	a3P)4p	4D	3P2)4s	b4P
Mn	1	389.96920	5.50e+05	6.557	3.378	4	4	(4D)sp	x6D	d54s2	a4P
Mn	1	389.96920	2.86e+05	6.557	3.378	6	4	(4D)sp	x6D	d54s2	a4P
Mn	1	389.97970	6.53e+05	6.557	3.378	2	4	(4D)sp	x6D	d54s2	a4P
Mn	1	390.10110	1.44e+05	7.522	4.345	10	8	(3H)4p	z2G	3F2)4s	a4F
Mn	2	390.23650	1.20e+05	8.743	5.567	7	7	(4G)4p	z3G	(2F)4s	b3F
Mn	1	390.35140	1.16e+06	7.854	4.679	10	8	a2F)sp	4G	(3G)4s	b4G
Mn	1	390.40980	6.56e+05	8.287	5.112	6	8	(3D)4p	u4F	(3G)4s	a2G
Mn	1	390.43020	2.46e+07	7.860	4.685	8	6	(4G)sp	w4H	(3G)4s	b4G
Mn	1	390.50710	6.72e+06	7.018	3.844	4	6		e4D	(6S)sp	z4P
Mn	1	390.52290	1.27e+07	8.261	5.087	10	10	a1G)4p	v2G	(3G)4s	a2G
Mn	1	390.57820	4.01e+06	7.533	4.360	4	4	a2D)sp	w4F	3F2)4s	a4F
Mn	1	390.85990	5.72e+05	8.305	5.133	8	6	(4D)sp	4D	7S)s5s	e6S
Mn	1	390.97610	1.00e+06	6.934	3.763	6	8	5S)s5p	4P	d54s2	b4D
Mn	1	390.99260	3.57e+07	8.257	5.087	8	10	a2F)sp	2F	(3G)4s	a2G
Mn	1	391.11330	1.29e+07	7.013	3.844	6	6		e4D	(6S)sp	z4P
Mn	1	391.14470	2.58e+07	7.363	4.194	4	6	a3P)4p	u4P	3P2)4s	b4P
Mn	1	391.22240	3.31e+05	7.828	4.660	6	4	(4G)sp	4F	3P2)4s	a2P
Mn	1	391.22960	2.82e+05	8.280	5.112	8	8	(3D)4p	u4F	(3G)4s	a2G
Mn	1	391.25470	1.37e+05	7.847	4.679	8	8	(4G)sp	4F	(3G)4s	b4G
Mn	1	391.27280	4.24e+06	7.488	4.320	4	2	a3P)4p	2D	3P2)4s	b4P
Mn	1	391.41480	1.20e+06	7.026	3.859	2	2	(5D)5s	i6D	(6S)sp	z4P
Mn	1	391.43500	6.19e+05	7.879	4.712	10	12	(3G)4p	2H	(3H)4s	a2H
Mn	1	399.06020	4.30e+05	6.869	3.763	6	8	5S)s5p	w4P	d54s2	b4D
Mn	1	399.13860	9.17e+04	7.373	4.268	8	8	a3P)4p	4D	(3H)4s	a4H
Mn	1	399.16110	2.09e+07	6.876	3.771	2	2	5S)s5p	w4P	d54s2	b4D
Mn	1	399.36690	3.66e+05	7.297	4.194	6	6	7S)s12p	6P	3P2)4s	b4P
Mn	1	399.38390	4.37e+06	6.876	3.772	2	4	5S)s5p	w4P	d54s2	b4D
Mn	2	399.41190	5.46e+06	11.233	8.129	5	5	b2F)4p	x1D	(2D)4s	c1D
Mn	2	399.53170	3.03e+05	8.483	5.380	5	7	(4P)4p	y5P	(2D)4s	c3D
Mn	1	399.60830	4.10e+06	7.375	4.273	6	4	a3P)4p	u4P	3P2)4s	b4P
Mn	1	399.77630	4.68e+06	7.347	4.247	10	12	a3F)4p	x4F	(3H)4s	a4H
Mn	1	399.95750	3.86e+05	7.357	4.258	8	10	a3F)4p	4D	(3H)4s	a4H
Mn	2	400.00330	2.84e+06	10.859	7.760	9	7	a2G)4p	u3F	(2D)4s	d3D
Mn	1	400.10030	2.45e+06	7.452	4.354	6	6	a3P)4p	4D	3F2)4s	a4F
Mn	1	400.10480	2.41e+06	6.869	3.772	6	6	5S)s5p	w4P	d54s2	b4D
Mn	1	400.20250	3.56e+06	6.869	3.772	6	4	5S)s5p	w4P	d54s2	b4D
Mn	1	400.25630	5.85e+06	7.457	4.360	2	4	a3P)4p	4D	3F2)4s	a4F
Mn	1	400.32600	1.09e+07	7.736	4.640	10	12	(3G)4p	v4F	(3G)4s	b4G
Mn	1	400.57720	2.30e+06	6.865	3.771	4	2	5S)s5p	w4P	d54s2	b4D
Mn	1	400.70360	2.22e+06	6.865	3.772	4	6	5S)s5p	w4P	d54s2	b4D
Mn	1	400.74920	3.77e+06	7.351	4.258	8	10	a3F)4p	x4F	(3H)4s	a4H
Mn	1	400.80160	4.63e+06	6.865	3.772	4	4	5S)s5p	w4P	d54s2	b4D
Mn	1	400.89080	3.98e+06	7.360	4.268	6	8	a3F)4p	x4F	(3H)4s	a4H
Mn	1	400.90360	5.02e+05	7.452	4.360	6	4	a3P)4p	4D	3F2)4s	a4F
Mn	1	403.57190	4.40e+07	5.214	2.143	6	8	(5D).4p	z6D	(5D).4s	a6D
Mn	1	534.10570	2.09e+06	4.435	2.114	8	10	(6S)sp	y6P	(5D)4s	a6D
Mn	1	534.98730	7.25e+07	7.687	5.370	14	12	(5D)4d	e6G	(5D)4p	z6F
Mn	1	537.76300	4.48e+07	6.149	3.844	4	6	(5S)s5s	e4S	(6S)sp	z4P
Mn	1	601.66730	1.87e+07	5.133	3.073	6	6	(7S)s.5s	e 6S	(6S).sp	z6P
O	2	408.92879	2.59e+08	31.737	28.706	12	10	2s2.2p2.(3P).4f G	2[5]*	2s2.2p2.(3P).3d	4F
O	2	425.38945	2.65e+08	34.233	31.319	12	10	2s2.2p2.(1D).4f H	2[5]*	2s2.2p2.(1D).3d	2G
O	2	425.41215	2.58e+08	34.233	31.320	10	8	2s2.2p2.(1D).4f H	2[5]*	2s2.2p2.(1D).3d	2G
O	2	427.31025	1.90e+06	31.758	28.857	8	6	2s2.2p2.(3P).4f F	2[4]*	2s2.2p2.(3P).3d	4D
O	2	427.42415	1.32e+07	31.758	28.858	8	8	2s2.2p2.(3P).4f F	2[4]*	2s2.2p2.(3P).3d	4D
O	2	427.55508	2.10e+08	31.757	28.858	10	8	2s2.2p2.(3P).4f F	2[4]*	2s2.2p2.(3P).3d	4D
O	2	427.59935	1.84e+07	31.756	28.857	6	4	2s2.2p2.(3P).4f F	2[3]*	2s2.2p2.(3P).3d	4D
O	2	427.62815	7.14e+06	31.756	28.857	6	6	2s2.2p2.(3P).4f F	2[3]*	2s2.2p2.(3P).3d	4D
O	2	427.66200	1.07e+08	31.729	28.831	4	4	2s2.2p2.(3P).4f D	2[1]*	2s2.2p2.(3P).3d	4P
O	2	427.67485	1.82e+08	31.755	28.857	8	6	2s2.2p2.(3P).4f F	2[3]*	2s2.2p2.(3P).3d	4D

O	2	427.74265	1.88e+06	31.756	28.858	6	8	2s2.2p2.(3P).4f F	2[3]*	2s2.2p2.(3P).3d	4D
O	2	427.74270	1.48e+08	31.750	28.853	4	2	2s2.2p2.(3P).4f F	2[2]*	2s2.2p2.(3P).3d	4D
O	2	427.78927	3.02e+07	31.755	28.858	8	8	2s2.2p2.(3P).4f F	2[3]*	2s2.2p2.(3P).3d	4D
O	2	428.13157	5.92e+07	31.717	28.822	6	6	2s2.2p2.(3P).4f D	2[2]*	2s2.2p2.(3P).3d	4P
O	2	428.29625	1.56e+08	31.751	28.857	6	4	2s2.2p2.(3P).4f F	2[2]*	2s2.2p2.(3P).3d	4D
O	2	428.32501	5.17e+07	31.751	28.857	6	6	2s2.2p2.(3P).4f F	2[2]*	2s2.2p2.(3P).3d	4D
O	2	428.37240	5.88e+07	31.750	28.857	4	4	2s2.2p2.(3P).4f F	2[2]*	2s2.2p2.(3P).3d	4D
O	2	428.88200	1.65e+08	31.729	28.839	2	2	2s2.2p2.(3P).4f D	2[1]*	2s2.2p2.(3P).3d	4P
O	2	428.88245	8.26e+07	31.729	28.839	4	2	2s2.2p2.(3P).4f D	2[1]*	2s2.2p2.(3P).3d	4P
O	2	429.12538	2.66e+07	31.710	28.822	8	6	2s2.2p2.(3P).4f G	2[3]*	2s2.2p2.(3P).3d	4P
O	2	429.47812	1.38e+08	31.717	28.831	6	4	2s2.2p2.(3P).4f D	2[2]*	2s2.2p2.(3P).3d	4P
O	2	429.49188	3.06e+07	31.717	28.831	4	4	2s2.2p2.(3P).4f D	2[2]*	2s2.2p2.(3P).3d	4P
O	2	430.28555	1.10e+06	34.200	31.319	8	10	2s2.2p2.(1D).4f G	2[4]*	2s2.2p2.(1D).3d	2G
O	2	430.28555	3.86e+07	34.200	31.319	10	10	2s2.2p2.(1D).4f G	2[4]*	2s2.2p2.(1D).3d	2G
O	2	430.30705	3.92e+07	34.200	31.320	8	8	2s2.2p2.(1D).4f G	2[4]*	2s2.2p2.(1D).3d	2G
O	2	430.36099	8.63e+07	31.738	28.858	10	8	2s2.2p2.(3P).4f G	2[5]*	2s2.2p2.(3P).3d	4D
O	2	430.38241	1.96e+08	31.702	28.822	8	6	2s2.2p2.(3P).4f D	2[3]*	2s2.2p2.(3P).3d	4P
O	2	430.72327	8.01e+07	31.717	28.839	4	2	2s2.2p2.(3P).4f D	2[2]*	2s2.2p2.(3P).3d	4P
O	2	434.20035	2.34e+08	31.738	28.883	10	8	2s2.2p2.(3P).4f G	2[5]*	2s2.2p2.(3P).3d	2F
O	2	434.28070	8.44e+07	34.228	31.374	4	4	2s2.2p2.(1D).4f D	2[2]*	2s2.2p2.(1D).3d	2D
O	2	434.28070	5.89e+06	34.228	31.374	6	4	2s2.2p2.(1D).4f D	2[2]*	2s2.2p2.(1D).3d	2D
O	2	448.81895	1.83e+08	34.228	31.466	6	4	2s2.2p2.(1D).4f D	2[2]*	2s2.2p2.(1D).3d	2P
O	2	448.81970	3.00e+07	34.228	31.466	4	4	2s2.2p2.(1D).4f D	2[2]*	2s2.2p2.(1D).3d	2P
O	1	747.64400	4.09e+07	15.781	14.123	7	5	3p	3D	3s	3P
O	1	747.72400	1.70e+07	15.782	14.124	3	3	3p	3D	3s	3P
O	1	747.90800	3.07e+07	15.782	14.124	5	3	3p	3D	3s	3P
O	1	748.06700	2.28e+07	15.782	14.125	3	1	3p	3D	3s	3P
O	1	794.31500	4.25e+06	14.100	12.539	7	7	3p	3F	3s	3D
O	1	794.71700	5.95e+06	14.100	12.541	5	5	3p	3F	3s	3D
O	1	794.75500	3.71e+07	14.099	12.539	9	7	3p	3F	3s	3D
O	1	795.08000	3.30e+07	14.100	12.541	7	5	3p	3F	3s	3D
O	1	795.21600	3.12e+07	14.100	12.542	5	3	3p	3F	3s	3D
P	2	417.84800	4.96e+07	12.601	9.635	3	5	p4p	1P	p3d	1D*
Ti	1	326.02698	1.68e+06	4.868	1.067	5	5	3d.4s2.4p	w 1D*	3d2.4s2	a3P
Ti	1	326.04044	2.88e+05	5.231	1.430	3	5	3d2.4s.(4F).5p	5D*	3d3.(4F).4s	b3F
Ti	2	368.51868	8.11e+07	3.937	0.574	4	6	3d2.(3F).4p	z 2D*	3d2.(3F).4s	a2F
Ti	2	368.51942	7.46e+07	3.971	0.607	6	8	3d2.(3F).4p	z 2D*	3d2.(3F).4s	a2F
Ti	1	430.04869	2.17e+07	5.043	2.160	5	5	3d3.(4P).4p	r 3D*	3d3.(2D2).4s	a3D
Ti	1	430.05539	1.07e+08	3.708	0.826	5	7	3d3.(4F).4p	x 5D*	3d3.(4F).4s	a5F
Ti	1	430.57402	4.11e+06	5.115	2.236	9	9	3d3.(2H).4p	3G*	3d3.(2H).4s	a3H
Ti	1	430.59077	8.94e+07	3.727	0.848	9	11	3d3.(4F).4p	x 5D*	3d3.(4F).4s	a5F
Ti	1	453.55683	6.10e+07	3.559	0.826	7	7	3d3.(4F).4p	y 5F*	3d3.(4F).4s	a5F
Ti	1	453.58437	9.11e+06	4.176	1.443	7	7	3d3.(4F).4p	w 3F*	3d3.(4F).4s	b3F
Ti	1	453.59178	5.52e+07	3.551	0.818	5	5	3d3.(4F).4p	y 5F*	3d3.(4F).4s	a5F
Ti	1	453.60402	6.81e+07	3.545	0.813	3	3	3d3.(4F).4p	y 5F*	3d3.(4F).4s	a5F
Ti	1	463.87550	4.28e+06	5.977	3.305	7	9	d2.4p2	j5F	(4F).4p	y5G
Ti	1	463.88030	4.39e+06	6.009	3.337	11	13	d2.4p2	j5F	(4F).4p	y5G
Ti	1	463.93619	5.98e+07	4.411	1.739	5	5	3d3.(4P).4p	w 5D*	3d3.(4P).4s	a5P
Ti	1	463.96609	3.42e+07	4.420	1.749	7	7	3d3.(4P).4p	w 5D*	3d3.(4P).4s	a5P
Ti	1	503.47721	1.30e+06	4.693	2.231	3	1	3d2.(3P).4s.4p.(1P*)	u 3D*	3d3.(2P).4s	b3P
Ti	1	503.53328	1.21e+06	5.570	3.108	7	7	3d3.(4F).5p	3F*	3d3.(2F).4s	3F
Ti	1	503.59030	4.35e+07	3.921	1.460	11	9	3d3.(4F).4p	w 3G*	3d3.(4F).4s	b3F
Ti	1	678.34610	4.22e+06	4.333	2.506	3	5	3d2.(3P).4s.4p.(3P*)	y 1P*	3d3.(2D2).4s	b1D

Appendix C

Two-zone Model Parameter Correlations

In Figure C.0.1, the χ^2 for different values of temperature of the inner-zone and the other parameters of the two-zone fits to the carbonate spectrum at 1000 ns can be seen. By the shape of the contours of constant χ^2 values in the plots, the correlation of the parameters can be inferred. For example, a positive correlation between the temperature and the electron density of the inner zone can be seen. The correlation comes from the Saha-equation (eq. (2.2.11) in Chapter 2), wherein an increase in temperature can be counter acted by an increase in the electron density in order to keep the degree of ionization constant. The positive correlation of the temperature and electron density was used to verify the interpretation of the temperature of the inner zone in Chapter 4.

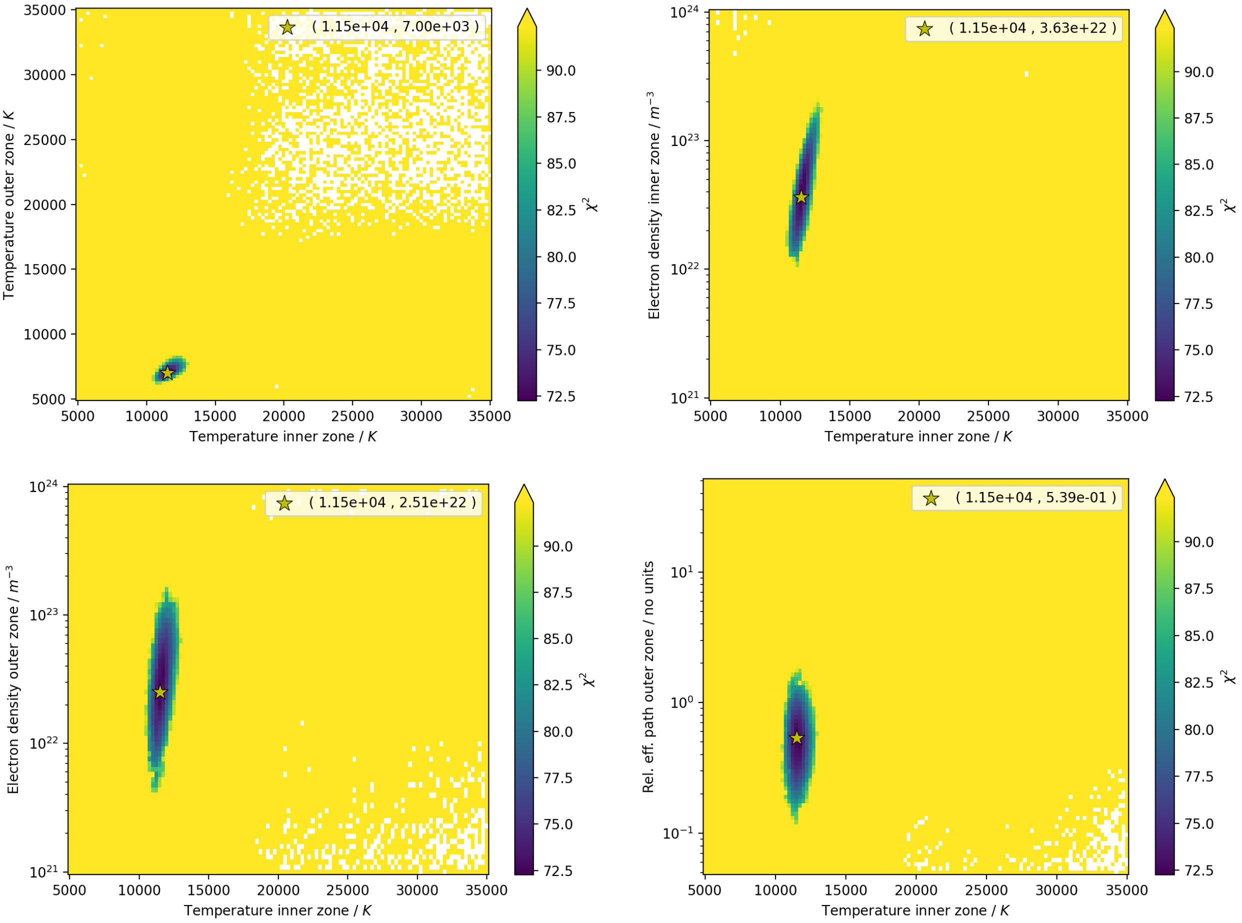

Figure C.0.1: *χ^2 for different values of temperature of the inner-zone and the other parameters of the two-zone fits to the carbonate spectrum at 1000 ns. From the figure in the upper right corner, a positive correlation between the temperature and the electron density of the inner zone can be seen.*

List of Publications

Peer-reviewed publications (first author)

- Hansen, Peder Bagge and Schröder, Susanne and Kubitza, Simon and Rammelkamp, Kristin and Vogt, David and Hübers, Heinz-Wilhelm (2021) "Modeling of time-resolved LIBS spectra obtained in Martian atmospheric conditions with a stationary plasma approach". Spectrochimica Acta Part B: Atomic Spectroscopy (178). Elsevier. doi: 10.1016/j.sab.2021.106115. ISSN 0584-8547

Peer-reviewed publications (co-author)

- Vogt, David and Schröder, Susanne and Frohmann, Sven and Hansen, Peder Bagge and Seel, Fabian and Gensch, Michael and Hübers, Heinz-Wilhelm (2021) "Spatiotemporal characterization of the laser-induced plasma plume in simulated Martian conditions". Spectrochimica Acta Part B: Atomic Spectroscopy, p. 106326. Elsevier. doi: 10.1016/j.sab.2021.106326. ISSN 0584-8547
- Kubitza, Simon and Schröder, Susanne and Dietz, Enrico and Frohmann, Sven and Hansen, Peder Bagge and Rammelkamp, Kristin and Vogt, David Sebastian and Gensch, Michael and Hübers, Heinz-Wilhelm (2020) "Detecting sulfur on the Moon: The potential of VUV-LIBS". Spectrochimica Acta Part B: Atomic Spectroscopy, p. 105990. Elsevier. doi: 10.1016/j.sab.2020.105990. ISSN 0584-8547
- Vogt, David and Schröder, Susanne and Rammelkamp, Kristin and Hansen, Peder Bagge and Kubitza, Simon and Hübers, Heinz-Wilhelm (2019) CaCl and CaF emission in LIBS under simulated martian conditions. Icarus, 335, p. 113393. Elsevier. doi: 10.1016/j.icarus.2019.113393. ISSN 0019-1035.
- Rammelkamp, Kristin and Schröder, Susanne and Kubitza, Simon and Vogt, David and Frohmann, Sven and Hansen, Peder Bagge and Böttger, Ute and Hanke, Franziska and Hübers, Heinz-Wilhelm (2019) "Low-level LIBS and Raman data fusion in the context of in situ Mars exploration". Journal of Raman Spectroscopy, pp. 1-20. Wiley. doi: 10.1002/jrs.5615. ISSN 0377-0486

Oral presentations at conferences

- Hansen, Peder Bagge and Vogt, David and Schröder, Susanne and Rammelkamp, Kristin and Kubitza, Simon and Hübers, Heinz-Wilhelm (2019) "Modeling of time-resolved LIBS spectra with a stationary plasma model for the application to Martian LIBS spectra". 11th International Conference on Laser-Induced Breakdown Spectroscopy, Virtuel
- Hansen, Peder Bagge and Vogt, David and Schröder, Susanne and Rammelkamp, Kristin and Kubitza, Simon and Hübers, Heinz-Wilhelm (2019) "Simple modeling of LIBS plasma parameters for extraterrestrial applications". European Winter Conference on Plasma Spectrochemistry, 3.-8. Feb. 2019, Pau, France.

- Hansen, Peder Bagge and Vogt, David and Schröder, Susanne and Rammelkamp, Kristin and Kubitza, Simon and Hübers, Heinz-Wilhelm (2018) ”An Implementation of Calibration-Free-LIBS for the Analysis of Spectra from Planetary Exploration”. SciX 2018, 21-26 Oct, Atlanta, GA, USA.

Poster presentations at conferences

- Hansen, Peder Bagge and Schröder, Susanne and Vogt, David and Kubitza, Simon and Rammelkamp, Kristin and Hübers, Heinz-Wilhelm (2019) ”Self-absorption in laser-induced plasmas in simulated Martian atmospheric conditions”. 10th Euro-Mediterranean Symposium onLaser-Induced Breakdown Spectroscopy, 8-13 september 2019, Brno, Czech Republic.
- Hansen, Peder Bagge and Vogt, David and Rammelkamp, Kristin and Kubitza, Simon and Schröder, Susanne and Frohmann, Sven and Hübers, Heinz-Wilhelm (2018) ”Simple modelling of Plasma Parameters to Assist the Analysis of LIBS Spectra for Planetary Exploration”. European Planetary Science Congress 2018, 16-21 Sep 2018, Berlin, Germany.

Acknowledgments

I would like to express my deepest gratitude to Prof. Dr. Heinz-Wilhelm Hübers for his support and his guidance during this thesis. His vast knowledge, critical questions, and curiosity have inspired me a lot and matured me as a researcher.

I am indebted to my supervisor Dr. Susanne Schröder. Her trust in me enabled me to do research in a field that interests me so much. Her door was always open and through guidance and thorough feedback she helped me define the scientific questions that would be of interest to planetary science and helped me to stay on track during especially the final part of my thesis. Her help and support have been indispensable.

I would like to thank the Deutsches Zentrum für Luft- und Raumfahrt (DLR) and the German Academic Exchange Service (DAAD) for giving me the opportunity to do a PhD study via the DLR-DAAD research fellowship program.

I feel lucky for having had Simon Kubitza, David Vogt, Kristin Rammelkamp, and Till Hagelschuer as colleagues and for all our exciting and fruitful scientific discussions. I also thank them for their support on the written parts of my thesis, my paper, and various conference contributions.

Finally, I would like to thank my family and friends for their support throughout my studies.

Statutory Declaration

I declare that I have completed the thesis independently using only the aids and tools specified. I have not applied for a doctor's degree in the doctoral subject elsewhere and do not hold a corresponding doctor's degree. I have taken due note of the Faculty of Mathematics and Natural Sciences PhD Regulations, published in the Official Gazette of Humboldt-Universität zu Berlin no. 42/2018 on 11/07/2018.

Copenhagen, March 12, 2022
Peder Bagge Hansen